

FACTORS INFLUENCING PRODUCT MICROSTRUCTURE AND THE
INJECTION MOLDING BEHAVIOR OF LIQUID CRYSTALLINE POLYMERS

By

• OMAR KHENNACHE

A Thesis Submitted to the Faculty of Graduate Studies
and Research in Partial Fulfilment of the
Requirements for the Degree of
Doctor of Philosophy

Department of Chemical Engineering
McGill University
Montreal

November 1990

ABSTRACT

Liquid Crystal Polymers (LCP) are a new class of polymeric materials with special molecular and solid state structures, flow characteristics and mechanical properties. Injection molded articles of rigid chain liquid crystal copolymers (LCP's) are gaining increasing commercial importance because their dimensional stability, high stiffness and strength per unit weight, make them highly attractive for aerospace structures and automotive parts, where the anisotropic nature of the materials can be exploited to achieve novel design strategies. Considerable technological importance is given to thermotropic LCP's because of their melt phase behavior and ease of processing. Because of their comparatively low viscosity, they can be injection molded with short cycle times into thin and complex shapes.

In the present work, broad range of material properties, including specific heat, thermal conductivity, thermal diffusivity, and shear viscosity of a commercial LCP injection molding resin have been determined experimentally. In addition, a detailed experimental study has been made of the crystallization kinetics of this LCP resin. The study showed that the resin undergoes two crystallization mechanisms, a fast and a slow mechanism, depending on the temperature and the cooling rates.

Various experimental techniques, to characterize the microstructure of the molded parts, including morphology, orientation, crystallinity and mechanical properties, have been developed and used. An effort is made to explain the results. Furthermore, composite theory is employed to explain the mechanical properties in

light of microstructural observations. Overall, the present work represents the most comprehensive effort to date to study and explain the processing-microstructure-property relationships for injection molded LCP's.

RESUME

Les polymères à cristaux liquides (LCP) constituent une nouvelle classe de matériaux polymériques avec une structure moléculaire, un état solide, des caractéristiques d'écoulement et de propriétés mécaniques uniques. Le moulage par injection de copolymères cristaux liquides à chaînes rigides gagne un intérêt commercial croissant, à cause de leur stabilité dimensionnelle, de leur rigidité et de leur résistance par unité de poids très élevées. Ces propriétés rendent ces matériaux très attractifs pour les applications aérospatiales et automobiles, où leur nature anisotrope peut être exploitée pour de meilleures stratégies de conception. La mésophase et la facilité de mise en forme des LCP donnent une importance technologique considérable à ces matériaux. Grâce à leur fluidité élevée, des formes à géométries complexes et des épaisseurs minces peuvent être moulées tout en maintenant des temps de cycle courts.

Dans cette étude, un nombre important de propriétés de la résine, entre autres la chaleur spécifique, la conductivité thermique, la diffusivité thermique et la viscosité en fonction du taux de cisaillement d'un polymère cristal liquide commercial ont été déterminés. En outre une étude expérimentale détaillée a été réalisée sur la cinétique de cristallisation de ce polymère. L'étude a montré que la résine passe par deux mécanismes de cristallisation, un mécanisme de cristallisation rapide et un mécanisme de cristallisation lent, dépendamment de la température et des taux de refroidissement.

Diverses techniques expérimentales pour caractériser la microstructure de pièces injectées, incluant la morphologie, l'orientation, la cristallinité et les propriétés mécaniques ont été développées et utilisées. Un effort a été fait pour expliquer ces résultats. De plus, une théorie des composites a été utilisée pour expliquer les propriétés mécaniques à l'aide des observations de la microstructure utilisant diverses techniques. En général cette étude représente l'effort le plus complet à date pour étudier et expliquer l'interaction entre la mise en forme, la microstructure et les propriétés de pièces injectées d'un polymère à cristaux liquides.

ACKNOWLEDGMENTS

I would like to express my deepest gratitude to my research director, Prof. M.R. Kamal, for his advice, encouragement and understanding during the course of this work.

I wish to thank Dr. J-M. Charrier, Dr. A. Rey, Dr. D. Grey and Dr. R. Marchessault for valuable comments and discussions.

I wish to thank my colleagues in the polymer group in particular MM. P. Singh, M. Samara, D. Abu Fara, F. Mijangos, T. Mutel, A. Haber, for their valuable discussions and comments throughout the project. A special thanks to Mr. A. Bouti from Ecole Polytechnique for helpful discussions on the composite theory.

I wish to thank Mr. A. Krish and the staff of the machine workshop for their assistance in construction of the experimental equipment. My thanks extend to Mr. J. Dumont, Mr. L. Cusmich, and Mr. N. Habib for their help in supplying the research facilities and instrumentation.

I would like to thank The Algerian Institute of Petroleum and the Ministry of Energy in Algeria for financial support in the form of a scholarship which enabled the achievement of this study.

I wish to thank Celanese Corporation, for supplying the material used in this study.

The financial support from the Department of Chemical Engineering at McGill University, the Natural Science Engineering Research Council of Canada, and the Ministère de l'Éducation du Gouvernement du Québec is also acknowledged.

Last, but certainly not least, I would like to express my deepest gratitude to my family, in particular my wife for her love, constant encouragement, and support. I can only hope that this thesis is a worthy beginning in the fulfilment of the ambitions of my late father (deceased in 1974) and my mother who passed away during the course of this work.

TABLE OF CONTENT

	Page
ABSTRACT	i
RESUME	iii
ACKNOWLEDGEMENTS	v
TABLE OF CONTENT	vii
LIST OF FIGURES	xii
LIST OF TABLES	xxi
LIST OF APPENDICES	xxii
CHAPTER I	1
1. GENERAL INTRODUCTION	1
1.1 Historical Review	1
1.2 The Liquid Crystalline State of Matter	3
1.2.1 Classification of LC Phases	3
1.2.2 Orientational Order	6
CHAPTER II	8
2. GENERAL BACKGROUND	8
2.1 Liquid Crystalline Polymers (LCP's)	8
2.2 Thermal Characteristics of LCP's	11
2.3 Structural Characteristics of LCP's	15
2.4 Rheological Properties of LCP's	19
2.5 Processing Behavior of LCP's	21
2.5.1 Injection Molding	21
2.5.2 Processing Induced Microstructure	23

	Page
2.5.2.1 Orientation	24
2.5.2.2 Morphology	27
2.5.2.3 Density and Crystallinity	27
2.5.2.4 Mechanical Properties	29
 CHAPTER III	 32
3. OBJECTIVES	32
 CHAPTER IV	 34
4 EXPERIMENTAL	34
4.1 Material	34
4.2 Thermal Properties	37
4.2.1 Specific Heat	37
4.2.2 Thermal Conductivity and Diffusivity	37
4.3 P-V-T Diagram	41
4.4 Melting and Crystallization Behavior	42
4.5 Dynamic Mechanical Behavior	43
4.6 Structural studies	45
4.6.1 Preparation of Fibers	46
4.6.2 Determination of the Transition Moment Angle ...	46
4.6.2.1 Orientation Function Using WAXD	46
4.6.2.2 Dichroic Ratio Using FTIR	47
4.7 Rheological Behavior	51
4.7.1 Shear Viscosity	51
4.7.2 Capillary Die Swell	53

	Page
4 8 Injection Molding	53
4.8.1 Injection Molding Machine	53
4.8.2 Mold Cavity	55
4.8.3 Injection Molding Variables.....	60
4.8.4 Microstructure Determination	62
4.8.4.1 Sample Preparation	62
4.8.4.2 Photomicrography	68
4.8.4.3 Scanning Electron Microscopy	70
4.8.4.4 Density Gradient Column	71
4.8.4.5 Wide-Angle X-Ray Diffraction	74
4.8.4.6 Infrared Spectroscopy (FTIR)	74
4.8.4.7 Microhardness Testing	75
4.8.4.8 Flexural Modulus	79
CHAPTER V	81
5 RESULTS AND DISCUSSION	81
5.1 Thermal Properties	81
5.1.1 Specific Heat	81
5.1.2 Thermal Conductivity and Diffusivity	83
5.2 P-V-T Diagram	86
5.3 Melting and Crystallization Behavior	86
5.3.1 Effect of cooling rates on Melting Behavior	89
5.3.2 Melting of Isothermally Melt Crystallized Samples	94
5.3.3 Kinetics of crystallization	97
5.3.3.1 Kinetics of the fast process	99
5.3.3.2 Kinetics of the slow process	103
5.4 Dynamic Mechanical Behavior	105
5.5 Rheological Properties	112

	Page
5.5.1 Shear viscosity	112
5.5.2 Capillary Die Swell	114
5.6 Injection Molding Studies	114
5.6.1 Processing Characteristics	114
5.6.2 Microstructure Development	124
5.6.2.1 Polarized light Microscopy	126
5.6.2.2 Scanning Electron Microscopy	130
5.6.2.3 Density (Crystallinity)	140
5.6.2.4 X-Ray Diffraction	142
5.6.2.5 Infrared Spectroscopy	144
5.6.2.6 Microhardness Testing	157
5.6.2.7 Flexural Modulus	165
5.7 Correlation and Integration of Results Obtained by the Various Techniques	174
5.7.1 Origin of the various layer formation	179
5.7.2 Influence of the processing conditions	183
5.8 Analysis of flexural properties	185
5.8.1 Review of Composite Theories	185
5.8.1.1 Cox-Krenchel Model	190
5.8.1.2 Halpin-Tsai Model	194
5.8.1.3 Model of Riley	195
5.8.2 Applicability to Liquid Crystalline Polymers	195
5.8.2.2 Flexural Modulus Measurements	197
5.8.2.3 Orientation and Density Distributions	197
5.8.2.4 Flexural Modulus Predictions	200

	Page
CHAPTER VI	204
6. CONCLUSION	204
6.1 Conclusions	204
6.2 Claims for Original Work	210
6.3 Recommendations for Future Work	214
REFERENCES	215
LIST OF SYMBOLS	222
APPENDICES	

LIST OF FIGURES

<u>FIGURE</u>	<u>CAPTION</u>	<u>PAGE</u>
1.1:	Classification of liquid crystal phases	5
2.1:	Differences in molecular conformation	9
2.2:	Main-chain liquid crystal polymer	10
2.3:	Side-chain liquid crystal polymer	10
2.4:	Polarized light photomicrograph of a nematic melt phase using a hot stage microscope	12
2.5:	Dynamic Mechanical Behavior of a NTP	14
2.6 A:	NPL crystals, Longitudinal matching	17
2.6 B:	NPL crystals, Lateral matching between adjacent chains	17
2.7:	Three regions of flow behavior from Onogi and Asada (49)	20
2.8:	Processing-Structure-Properties Relationship	25
2.9:	Schematic representation of the flow pattern in The advancing front during injection mold filling. (59)	26
2.10:	Photomicrograph representing the cross-sectional view of a tensile bar (73).	28
2.11:	Effect of thickness on flexural modulus and strength of PET modified with 60 mole% PHB. (12)	31

<u>FIGURE</u>	<u>CAPTION</u>	<u>PAGE</u>
4.1:	Chemical Structure of the rigid chain copolyester used in this study.	35
4.2:	Thermal Conductivity Apparatus: System arrangement and auxiliary equipment.	39
4.3:	X-ray fibre pattern.	48
4.4:	Infrared polarized absorption spectra of the fiber.	50
4.5:	Partial axial orientation: Chain distribution rotationally symmetrical about the stretching direction.	52
4.6:	Danson Metalmec Injection Molding Machine.	54
4.7:	Injection Molding Machine-Microcomputer Interface.	56
4.8:	Schematic Drawing of Mold Cavity with Pressure Transducer and Thermocouple Locations.	58
4.9:	Assigned locations of rectangular test pieces for microstructural analysis.	63
4.10:	Assigned locations of rectangular test bars for microstructural analysis	65
4.11:	The Jig used for polishing the samples and measuring the microhardness.	67
4.12:	Layer removal technique for flexural modulus measurements.	69
4.13:	Apparatus Set-Up for Density Determination	72

<u>FIGURE</u>	<u>CAPTION</u>	<u>PAGE</u>
4.14:	Calibration curve for density gradient column.	73
5.1:	Variation of specific heat as a function of temperature for different HBA/HNA compositions 58/42 and 75/25 reported by Cao and Wunderlich (88), 70/30 present study.	82
5.2:	Variation of thermal conductivity as a function of temperature.	84
5.3:	Thermal diffusivity variation as a function of temperature.	85
5.4:	Pressure-Volume-Temperature (P-V-T) Diagram	87
5.5:	DSC melting and crystallization behavior: Trace a, as received pellet; trace b, cooling at 20 deg/min from the nematic melt; trace c, remelting of the sample previously cooled at 20 deg/min.	88
5.6:	DSC melting thermograms of samples crystallized nonisothermally using a wide range of cooling rates.	90
5.7:	Thermal history effect on samples crystallized nonisothermally. Variation of heats of transition as a function of cooling rates.	92
5.8:	Variation of temperature of transition as a function of cooling rates.	93
5.9:	DSC melting thermograms of samples crystallized isothermally for 15 hours at different temperatures (T_c 's).	95

<u>FIGURE</u>	<u>CAPTION</u>	<u>PAGE</u>
5.10:	DSC melting thermograms of samples crystallized isothermally at 220°C for various times.	96
5.11:	Plot of transition temperature (corresponding to peak II, see Fig. 4.6) as a function of crystallization temperature (T_c 's).	98
5.12:	DSC exotherms of samples cooled from the nematic melt at 4, 7, and 10 deg/min.	101
5.13:	Plot of $\ln[\dot{x}/(1-x)]$ as a function of temperature for 3 different cooling rates (4, 7 and 10 deg/min).	102
5.14:	Arrhenius plot of $\ln(K)$ for 3 different cooling rates (4, 7 and 10 deg/min).	104
5.15:	Plots of heats of transition versus $\log(\text{time})$ at different crystallization temperatures (T_c 's).	106
5.16:	Arrhenius plot of $\ln(a)$.	107
5.17:	Storage Modulus, E' , from dynamic mechanical analysis.	109
5.18:	Loss Modulus, E'' , from dynamic mechanical analysis.	110
5.19:	$\text{Tan } \delta$, from dynamic mechanical analysis.	111
5.20:	Viscosity vs. shear rate at three different temperatures.	113
5.21:	Extrudate Swell of LCP at 300°C using two different shear rates.	115

<u>FIGURE</u>	<u>CAPTION</u>	<u>PAGE</u>
5.22:	Variable-Time Profiles during the injection molding process for a single run.	116
5.23:	Cavity Pressure-Time Profiles at two different locations in the mold cavity.	118
5.24:	Replicates for Nozzle- and Cavity Pressure-Time Profiles.	120
5.25:	Nozzle- and Cavity Pressure-Time Profiles obtained at two different mold temperatures.	121
5.26:	Nozzle- and Cavity Pressure-Time Profiles at two different Injection pressures.	122
5.27:	Nozzle- and Cavity Pressure-Time Profiles obtained at two different Injection speeds.	123
5.28:	Mold temperature-time profiles during the injection molding cycle.	125
5.29:	Polarized light photographs of injection molded sample microtomed in the X-Y plane	128
5.30:	Cross-Polarized Light photograph of injection molded sample microtomed in the X-Z plane.	129
5.31:	Electron photomicrograph of injection molded samples microtomed in the X-Y plane	131
5.32:	SEM photomicrograph of an injection molded sample (1L), broken in the Y-Z plane.	132
5.33:	Cross-section of an injection molded sample (1L) at higher magnification.	134

<u>FIGURE</u>	<u>CAPTION</u>	<u>PAGE</u>
5.34:	SEM photomicrograph of an injection molded sample of the center core at high magnification.	135
5.35:	SEM photomicrograph of an injection molded sample (1T) broken in the X-Z plane.	137
5.36:	SEM photomicrograph of an injection molded sample (1T) broken in the X-Z plane	138
5.37:	Electron photomicrograph of an injection molded sample (1T) broken in the X-Z plane.	139
5.38:	Density variation of microtomed sections in the depth direction of a sample molded at low mold temperature (40°C).	141
5.39:	Density variation of microtomed sections in the depth direction of a sample molded at high mold temperature (140°C).	143
5.40:	WAXS pattern for microtomies sliced at different positions across the thickness of an injection molded sample.	145
5.41:	Variation of molecular orientation in the depth direction, at different positions A, B and C along the centerline of the molded plaque.	148
5.42:	Variation of molecular orientation in the depth direction at different positions D, E and F away from the centerline near the mold wall.	151
5.43:	Variation of molecular orientation in the depth direction of an injection molded sample at two different mold temperatures.	153

<u>FIGURE</u>	<u>CAPTION</u>	<u>PAGE</u>
5.44:	Variation of molecular orientation in the depth direction of an injection molded sample at two different injection pressures.	155
5.45:	Variation of molecular orientation in the depth direction of an injection molded sample at two different injection speeds.	156
5.46:	Microhardness measurements: Effect of distance between indentations.	159
5.47:	Variation of microhardness in the depth direction, and at different positions along the centerline of the molded plaque.	160
5.48:	Replicates of microhardness measurements performed for two different samples molded under the same conditions.	162
5.49:	Variation of microhardness across the thickness of the molded sample at different mold temperatures.	163
5.50:	Variation of microhardness across the thickness of the molded sample at different injection pressures.	164
5.51:	Variation of microhardness across the thickness of the molded sample at different injection speeds.	166
5.52:	Layer Modulus Distribution in the depth direction of injection molded bars machined parallel (1L) and perpendicular (1T) to the flow direction	168
5.53:	Anisotropy Ratio of samples machined parallel (1L) and perpendicular to the flow direction (1T).	169

<u>FIGURE</u>	<u>CAPTION</u>	<u>PAGE</u>
5.54:	Layer Modulus Distribution in the depth direction of an injection molded bar (2L) as compared to sample 1L.	171
5.55:	Effect of Mold Temperature on the flexural modulus distribution in the depth direction of injection molded samples.	173
5.56:	Effect of Injection Pressure on the flexural modulus distribution in the depth direction of injection molded samples.	175
5.57:	Effect of Injection Speed on the flexural modulus distribution in the depth direction of injection molded samples.	176
5.58:	Comparison of the various distributions of properties in the depth direction of Injection Molded Liquid Crystalline Copolyester Parts .	178
5.59:	Schematic representation of different regions during the filling stage of a rectangular mold cavity.	180
5.60:	Schematic of the mold filling process and molecular orientation distributions based on experimentally obtained results.	182
5.61:	Schematic representation of the bulk structure of a polymeric liquid crystal. (1) Polydomain system, (2) degraded polydomain system, and (3) monodomain (110).	184
5.62:	Stress-strain distribution in flexure: a) Strain distribution b) Stress distribution, $\sigma(z)$ -linear isotropic; c) Stress distribution, $\sigma(z)$ -variable through thickness.	191

<u>FIGURE</u>	<u>CAPTION</u>	<u>PAGE</u>
5.63:	Predictions of flexural modulus in the depth direction of a sample machined parallel-to-flow direction (1L)	201
5.64:	Predictions of flexural modulus in the depth direction of a sample machined perpendicular-to-flow direction (1T)	202
A.13.3:	Microhardness test: Steps for microhardness measurements.	A-56
A.13.4:	The Knoop Indentor.	A-57

LIST OF TABLES

<u>TABLE</u>	<u>CAPTION</u>	<u>PAGE</u>
4.1:	Physical properties of the resin	36
4.2:	Calibration Equations for the transducers used on the Injection Molding Machine.	59
4.3:	Injection Molding Variables	61
4.4:	Calibration of Microscope Objectives	78
5.1:	Processing Parameters in the injection molding study of LCP parts; Machine settings.	127
5.2:	The effect of mold temperature on the thicknesses of the various layers formed in the molded parts.	186
5.3:	The effect of Injection Pressure on the thicknesses of the various layers formed in the molded parts.	187
5.4:	The effect of Injection Speed on the thicknesses of the various layers formed in the molded parts.	188
5.5:	Values incorporated in the model for composite theory.	198
6.1:	Previous Studies on Thermal Characterization and Crystallization Behavior of HNA/HBA Thermotropic LCP's.	212

LIST OF APPENDICES

- A.1: Thermal Properties
 - A.1.1 Specific Heat
 - A.1.2 Thermal conductivity
 - A.1.3 Thermal diffusivity
- A.2: P-V-T Diagram
- A.3: Melting and Crystallization Behavior
 - A.3.1 Melting of Isothermally Crystallized Samples
 - A.3.2 Effect of Cooling Rates on Heat of Fusion
 - A.3.3 Effect of Cooling Rates on Melting Temperature
 - A.3.4 Comparison of Data obtained experimentally
- A.4 Kinetics of Crystallization
 - A.4.1: Variation of $\ln(\bar{x}/1-x)$ with Temperature at Different Cooling Rates.
 - A.4.2: Variation of $\ln K$ with Temperature at Different Cooling Rates
 - A.4.3: Variation of $\ln(a)$ as a Function of temperature
- A.5 Dynamic Mechanical Behavior
- A.6 Rheological data
 - A.6.1 Shear viscosity data
 - A.6.2 Die swell
- A.7 Variable-time profile
- A.8: Density
- A.9: Infrared Spectroscopy
- A.10: Microhardness
- A.11: Flexural Modulus
- A.12: Flexural Modulus Predictions
- A.13: Derivations and Microhardness Figures
- A.14: Error analysis

CHAPTER I

1 INTRODUCTION

1.1 Historical Review

The existence of the liquid crystalline state was first observed in a thermotropic cholesteric small molecule, by Reinitzer (1) in 1888. The basic understanding of liquid crystal theory was then developed in the early 1920's when Friedel (2) presented the current classification of the liquid crystalline state. The interest in liquid crystal research was prompted again in the 1950's by the discovery of the possible commercial use of these materials in the field of display technology and the processing of ultra-high modulus fibres. The first theoretical prediction that accounted for the observed behavior was given by Onsager (3) in 1949. He found that solutions of highly asymmetric particles would separate into different phases, one isotropic and the other nematic of slightly higher concentration. Flory (4) in 1956, approached the problem using the simpler lattice theory of solutions. He proposed that a solution of a rodlike synthetic polymer of suitable rigidity at the appropriate concentration would form an anisotropic phase and that a polymer would be a lyotropic material. In 1965, Flory's theory was well demonstrated when Kwolek (5) discovered that wholly aromatic polyamides gave anisotropic solutions in alkylamide and alkylurea solvents. That observation led ultimately to the development of high performance Kevlar Aramid fibers.

The academic and industrial interest in liquid crystal polymers (LCP's) was sparked by the commercialization of Kevlar aromatic polyamide fiber in the early 1970's. The fiber is almost as stiff and as strong as steel, at one fifth of the density. In addition, it has good resistance to chemicals and heat. A disadvantage of Kevlar is that the polymer is a "lyotropic" liquid crystal, a polymer that has to be dissolved in an appropriate solvent for processing applications. The application of these lyotropic LCP's is limited to thin fibers and films due to removal of the solvent.

Recently, many lyotropic liquid crystalline polymers (LCP's) were reported in the literature, including polyamides (6), polyesters, polyazomethines (7), and cellulose derivatives (8-11). The aromatic polyesters have become one of the most widely studied classes of thermotropic polymers, since the publication by Jackson and Kuhfuss (12), who reported the first well characterized thermotropic liquid crystal copolyester. The polymer was an aliphatic-aromatic copolyester of poly(-ethyleneterephthalate) (PET) and parahydroxybenzoic acid (PHB). Thermotropic liquid crystalline polymers are providing substantial interest, mainly because they can be processed in the molten state. Researchers have devised ways of lowering the transition temperatures to well below the decomposition temperature, by slightly altering the linear aromatic molecular structures. While polar groups produce low degrees of the depression (13), non-polar substituents are more efficient (14). This is accomplished by introducing flexible chain units (15,16), bulky substituents (17), or kinks (18,19) into the mesogenic unit of the polymer. New liquid crystal polymers can be processed using the same equipment as for processing conventional flexible chain polymers.

To improve the modulus and strength of flexible chain polymers, a

high degree of orientation by chain extension is required. With thermotropic liquid crystal polymers, this order exists readily in the nematic state. The nematic structure is related to the presence of domains in which a high degree of molecular orientation exists. During deformation, such domains may align along the flow direction, yielding a material with exceptional physical properties.

1.2 The Liquid Crystalline State of Matter

A major requirement for the occurrence of a mesophase is that the molecule must be highly anisotropic in shape and usually rod-like (4). Phase transitions may be caused by temperature changes (Thermotropic Mesomorphism) or by concentration changes in an appropriate solvent (Lyotropic Mesomorphism).

1.2.1 Classification of Liquid Crystal Phases

LCP's can be classified into three main classes, based on their structure, as observed by Friedel (2): nematics, cholesterics and smectics (Figure 1.1a).

(a) Nematic Mesophase

The nematic mesophase allows for translational mobility of constituent molecules and has a low viscosity. Systems with one dimensional order are referred to as nematic for the threadlike morphologies seen in the polarized light microscope. Molecules are aligned in a preferred direction characterized by a unit vector n , the director (Figure 1.1a). This phase has rotational symmetry around the director n .

(b) Cholesteric Mesophase

The cholesteric phase is characterized by spatial variation of the preferred direction, leading to a periodic twisting of the nematic structure. The period is called the pitch (Figure 1.1b). If the z-axis is the helical axis, the following structure represents the vector n :

$$n_x = \cos(q_0 z + \phi) \quad (1.1)$$

$$n_y = \sin(q_0 z + \phi) \quad (1.2)$$

$$n_z = 0 \quad (1.3)$$

where q_0 is the wave vector and ϕ is the phase angle. The structure of a cholesteric phase is given by:

$$p = \pi/q_0 \quad (1.4)$$

Cholesteric phases exhibit very interesting optical properties.

(c) Smectic Mesophase

The smectic phase is characterized by one dimensional periodic structure, in which translational mobility is minimal (Figure 1.1c). From the structural point of view, all smectics are layered structures, with a well defined interlayer spacing, which can be measured by X-ray diffraction (20).

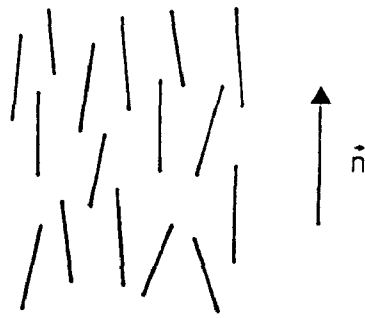


Figure 1.1.A The uniaxial Nematic Phase

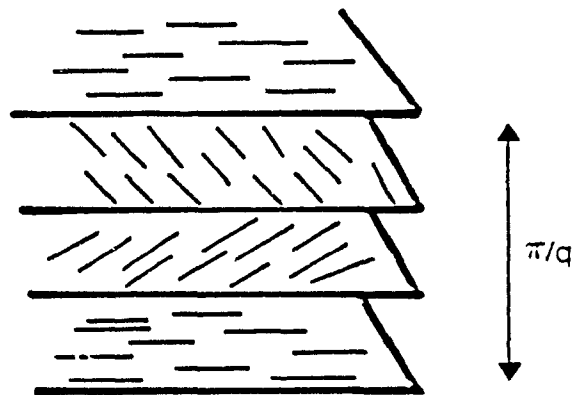


Figure 1.1 B The Helical Structure of the Cholesteric Phase

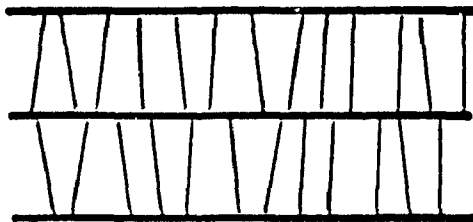


Figure 1.1.C The Smectic A Phase

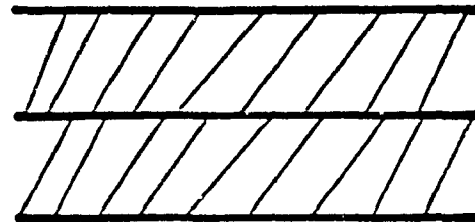


Figure 1.1.D The Smectic C Phase

FIGURE 1.1: Classification of liquid crystal phases.

1.2.2 Orientational order

The alignment of a nematic mesophase can be described by the order parameter S introduced by Mayer and Saupe (21).

$$S = 1/2 (3 \langle \cos^2 \alpha \rangle - 1) \quad (1.5)$$

Where α is the angle between the molecular longitudinal axis and some preferred direction (the director \vec{n}), and $\langle \rangle$ indicates an average value of $\cos^2 \alpha$ for all molecules. $S=0$ for random distribution of directors, as is the case with an isotropic melt, $S=1$ if all the directors are perfectly aligned along the preferred direction, and $S=-0.5$ for perpendicular alignment. The definition of S arises from the work of Zocher (22). It may be recognized as being equivalent to the Hermans orientation function (23). For nematic liquid crystals, S ranges from 0.3 to 0.8.

This thesis is divided into seven chapters. Chapters I and II deal with a historical introduction, and a general literature review on liquid crystal polymers, and review of work carried out on thermal, structural, rheological and processing characteristics of these polymers. Chapter III presents the research objectives. Chapter IV presents the experimental procedures with a detailed description of the experimental techniques. Chapter V presents the overall results and discussion of the material characterization, including the thermal and dynamic mechanical properties, melting and crystallization behavior, as well as the kinetics of crystallization. It also describes injection molding behavior and the distribution of

microstructural characteristics, as obtained by the various techniques employed in this study. Chapter VI presents a theoretical analysis to predict flexural modulus distributions using available composite theories. Finally chapter VII presents the overall conclusions, claims for original work and recommendations for future work.

CHAPTER II

2 GENERAL BACKGROUND

2.1 Liquid Crystalline Polymers (LCP's)

Anisotropic polymers consist of rigid rodlike molecules that, under the right temperature and concentration in a melt or solution, arrange themselves in domains. While the micro order parameter for describing orientation within domains is high, the macro-order parameter for describing the alignment of domains can be zero. However, aligning the domains by processing may yield a product where both molecular and domain orientations are high. The order is frozen in as the polymer cools down into a solid, yielding a product with attractive physical properties. The fiber-like internal structure of parts produced in the above manner, has led to the concept of "self-reinforcing" polymers. The early interest in rod-like molecules that form anisotropic structures is due to the fact that the properties of these highly aligned molecules can approach the calculated theoretical strength and stiffness of the molecule. In conventional polymers the entanglements (see figure 2.1) do not allow the formation of liquid crystalline structures. Liquid crystalline polymers may be synthesized using one of the following two principles: (i) by linking together suitable mesogenic monomers by condensation polymerization, leading to the formation of a backbone (Figure 2.2), or (ii) by addition polymerization of mesogenic monomers carrying a terminal group to form a backbone that carries the

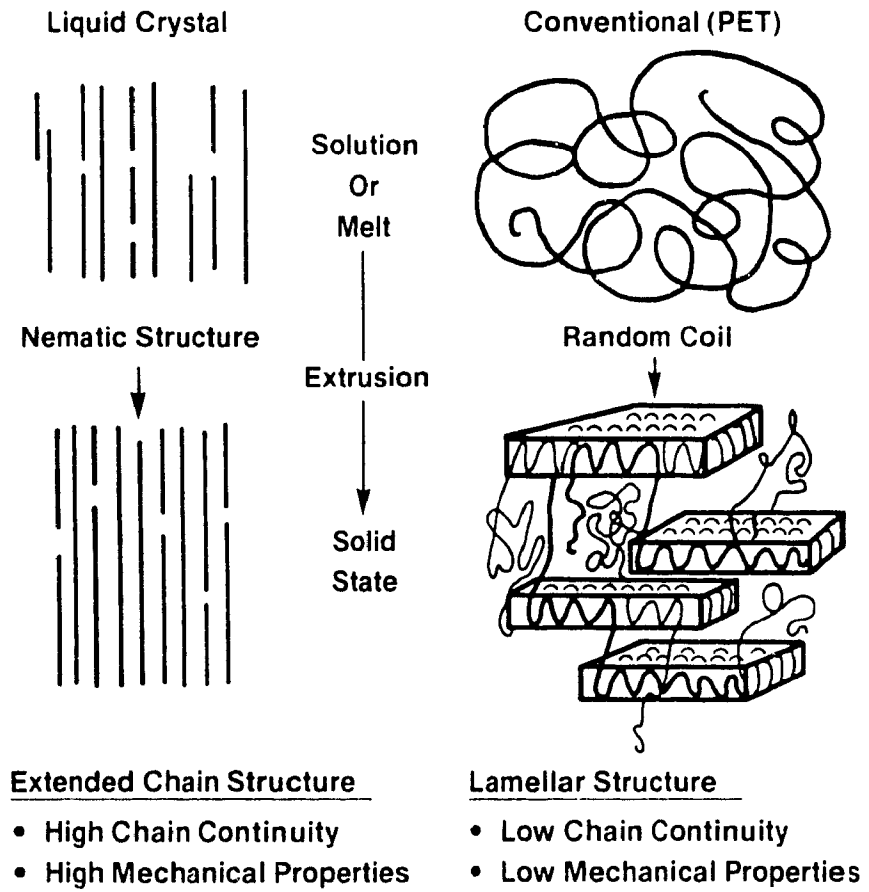


FIGURE 2.1: Differences in molecular conformation

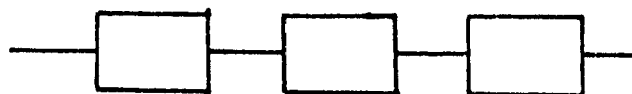


FIGURE 2.2: Main-chain liquid crystal polymer (mesogenic group in the main chain).

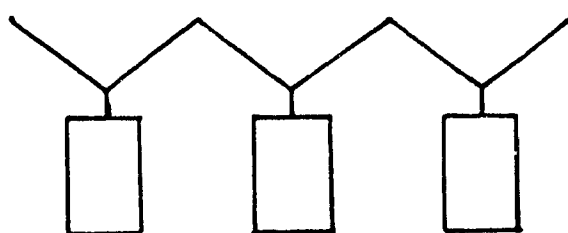


FIGURE 2.3: Side-chain liquid crystal polymer.

mesogenic units as pendant side chains, called side-chain liquid crystal polymers (Figure 2.3). The first type of polymers is of interest mainly due to their mechanical properties, while side-chain polymers display interesting optical properties. The material under study is a main chain copolyester.

2.2 Thermal Characteristics of LCP's

The thermal behavior of LCP's was studied extensively during the last decade. Grebowicz and Wunderlich (24) found that rigid chain polymers exhibit a high temperature liquid crystalline phase, usually nematic for most thermotropic copolyesters, intermediate between a partially ordered solid and an isotropic fluid state, as shown by the black "threadlike" texture or orientation boundaries observed under polarized light microscopy (Figure 2.4) (25). The transition to isotropic phase was not observed because of decomposition (24). Blundell (26) reported that because of the high transition temperatures and the low heats of transition of these copolyesters, low entropies of transition are observed with an unusually small volume change at the transitions. Bechtoldt et al. (27) reported the volume change to be of the order of 0.1 to 1%. Blundell and Buckingham (28) explained that the main motions were longitudinal translation, chain rotation and minor internal chain motions that could not alter the overall configuration. Grebowicz and Wunderlich (24) described these polymers as intermediate between the liquid crystalline and condis (conformationally disordered) crystalline state with small amount of crystallinity. Stamatoff (29) suggested that sufficiently rapid cooling could result in a polymeric glass with nematic structural order. Clements (30) confirmed that "not crystalline" does not imply amorphous, since these polymers should have at least



FIGURE 2.4: Polarized light photomicrograph of a nematic melt phase using a hot stage microscope (25).

one-dimensional (orientational) order rather than no order at all. On the other hand Bechtoldt (27) reported that the degree of crystallinity could vary between 30 and 70% depending on the thermal treatment experienced by the polymers. He also observed that thermal treatment did not affect the density. Due to the dense packing of the molecules, it is generally assumed that only cooperative motions are possible for chain rotations (rotationally ordered or disordered systems) (27). Because of the high order and the dense packing of the molecules, the thermal conductivity and diffusivity of liquid crystal polymers are higher than for flexible chain polymers. Therefore, the cooling cycles in the polymer processing operations are much shorter than for conventional polymers.

Warner and Jaffe (31), employing an isothermal method, found that the crystallization rate of liquid crystalline polymers is very fast, and the Avrami exponent n was found to be equal to 2, which corresponds to the rod-like growth from sporadic nuclei. Blundell (26) attributed this behavior to the instantaneous nucleation due to the high chain mobility of the low viscosity liquid crystalline copolymer. Butzbach et al. (32) and Bechtoldt et al. (27) observed that the crystallization process in the liquid crystalline copolymer occurred in two steps: a fast crystallization process and a slow process. They used an isothermal method to study the kinetics of the slow crystallization process and found that the degree of crystallinity increased linearly as a function of the logarithm of time.

Three different molecular processes have been observed by Calundann and Jaffe (25) in naphthalene thermotropic polyesters (NTP's) (Figure 2.5), using dynamic mechanical analysis. The high temperature α -process, occurring at about 110°C,

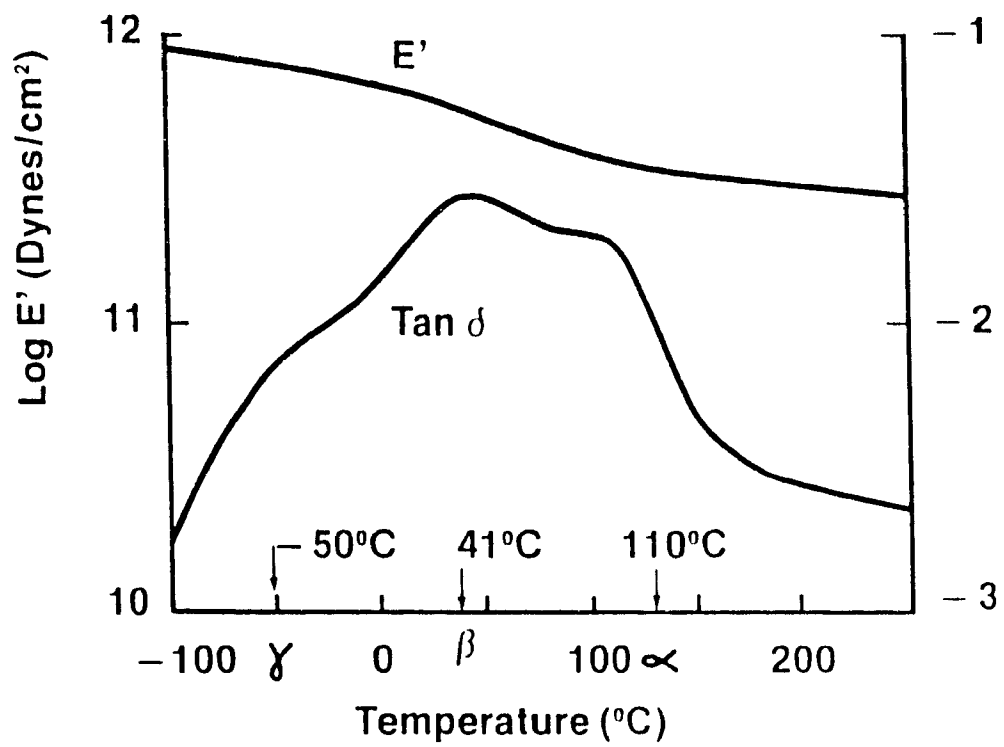


FIGURE 2.5: Dynamic Mechanical Behavior of a NTP fiber (25).

is essentially related to the glass transition temperature, T_g , associated with the onset of cooperative motions along the chain. The β -process in the region of 50°C is associated with the naphthyl moieties. Finally, they attributed the shallow γ -process at about -40°C to the onset of similar motions in the phenyl units. Recently, Blundell and Buckingham (28) focused on the β -process, and they confirmed that this process was associated with the naphthyl groups and neighbouring carbonyl groups undergoing a coordinated rotation motion about the main polymer axis.

2.3 Structural Characteristics of LCP's

The melting behavior of a copolymer consisting of a crystallizable unit, Hydroxybenzoic Acid (HBA) and a non-crystallizable unit, 2,6-Hydroxynaphthoic Acid (HNA) in the random chain is expressed by the well known Flory (4) relation:

$$\frac{1}{T_m} - \frac{1}{T_m^0} = \frac{R}{\Delta H_f} \cdot \ln(P_f) \quad (2.1)$$

Where T_m^0 is the melting temperature of the pure homopolymer, T_m is the melting temperature of the copolymer, ΔH_f is the heat of fusion per mole of crystallizable units, and R is the gas constant. P_f is the probability factor that one crystallizable unit follows another. For random chains, P_f is equal to the mole fraction of such units. The melting behavior of the naphthalene copolymers used in this work is consistent with the melting point depressions predicted by Flory's melting theory, which should not occur if the molecules are blocky. This behavior is consistent with, but not a proof of, lack of blockiness in the resulting polymers. The work of

Blackwell and Gutierrez (33), Gutierrez et al. (34) and Stamatoŕ (29), using wide-angle x-ray diffraction, offers more convincing evidence of random sequence distributions in naphthalene thermotropic copolyesters.

Hanna and Windle (35) studied the solid state order obtained upon cooling of thermotropic copolyesters from the nematic melt, thus extending the earlier work of Flory (4) and Wunderlich (36) on conventional copolymers, where only one component was considered crystallizable. The statistical approach taken was to find the largest matching sequence of similar units along the same chain (see Figure 2.6 A) and between adjacent chains for a given set of conditions, and then noting all possible secondary matches, which propagate laterally to give two dimensional crystalline regions (Figure 2.6 B). Propagation of a particular random sequence gives rise to non-periodic layer (NPL) crystals, which have been discussed previously by the same group (37). This lateral sorting is only possible for the slow crystallization process. In the case of the fast crystallization process, only longitudinal matching is possible.

Traditional methods for the morphological characterization include the entire range of microscopic instruments. Optical microscopy, generally using polarized light (PLM), is useful to observe the effects of orientation and to give an overview of structures larger than a micrometre in size. Scanning Electron Microscopy (SEM) permits a higher magnification view of 5 to 10 nm resolution of the surface of materials. Transmission Electron Microscopy (TEM) permits the observation of structures to less than 1 nm. This range of instrumental methods requires a variety of sample preparation methods which range from established methods to some developed specifically for liquid crystalline polymers.

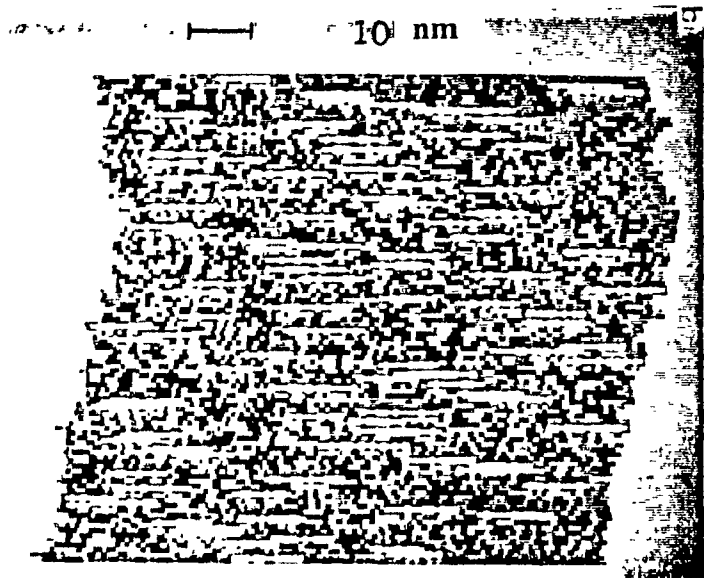


FIGURE 2.6A: Computer generated image of NPL crystals, Longitudinal matching.

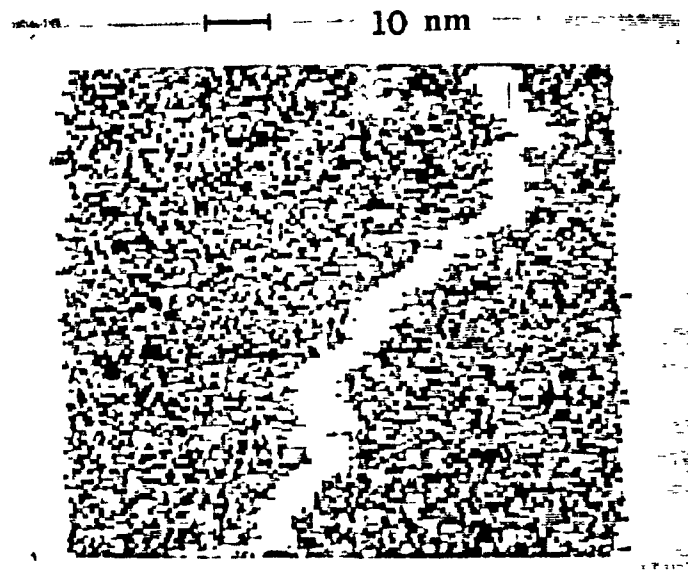


FIGURE 2.6B: Computer generated image of NPL crystals, Lateral matching between adjacent chains (35).

X-Ray diffraction is a valuable method to characterize the structure of materials. It has been used extensively to investigate the physical structure of wholly aromatic liquid crystalline copolyesters (Gutierrez et al. (34), Clements et al.(30), Jenkins et al.(38), Davies et al.(39), Troughton et al. (40), Blackwell et al. (33), Chivers and Blackwell (40), Butzbach et al.(HBA/HNA) (32), Mitchell et al. (42,43) (HBA/PET). The first x-ray work on the HBA/HNA systems was reported by Gutierrez et al. (34). They observed two relatively sharp equatorial reflections at $d = 0.45$ nm and 0.26 nm and an off-equatorial at $d = 0.33$ nm. They used an aperiodic point model to predict the positions of these reflections for a random sequence of monomers. The data were compatible with a structure consisting of an assembly of parallel chains of totally random monomer sequences. Chivers and Blackwell (40), from X-ray patterns of melt spun fiber, observed a high degree of axial orientation of the molecules, but with poor lateral order except in some highly ordered regions. Chains of this type would probably tend to form a hexagonal lattice, but with complete axial and rotational freedom in a nematic structure. The presence of off-equatorial Bragg reflections indicates the presence of some regular three-dimensional packing. They also reported that the only conformational freedom was due to torsional rotation about the aromatic-carboxy linkage bonds. Based on the molecular models, the lengths of the HBA and HNA residues were taken as 0.635 nm and 0.837 nm, respectively. Blundell (26) used the intensities of the Bragg reflections to estimate the "degree of crystallinity" which was found to be 21% in the 40/60 HBA/HNA copolymer system. He calculated, from the half-width of the diffraction peaks, the lateral size of the ordered regions to be ca. 10 nm across.

Viney et al. (44), using the X-ray diffraction method, observed pronounced molecular orientation of a specimen sectioned from a pellet, while the

micrograph taken from the same sample viewed under cross-polarized light did not confirm the X-ray results. They concluded that these LCP's have biaxial optical properties.

Windle (45) reported that Blundell's (46) conclusion about hexagonal packing was not substantiated. Windle commented that hexagonal packing implied that the first two equatorial maxima would have scattering vectors with amplitudes in the ratio of 1:1.732. The observed ratio, as stated by Blundell, was of the order of 1:1.3 (20°:26°). Windle referred to this order as being "biaxial", while Blundell observed that only after prolonged annealing, the more ordered regions moved from hexagonal packing to one possessing a degree of biaxiality.

Blundell et al. (47) studied the relationship between chain linearity and the molar fraction of HBA in the p-hydroxybenzoic acid/Isophthalic acid/Hydroquinone (HBA/IA/HQ) system. The results showed that as HBA increased, the increase in modulus was mainly a consequence of the increase in molecular orientation within the layers. They calculated Hermans orientation function f_c of the crystalline phase using the assumption that these polymers adopt a hexagonal packing.

2.4 Rheological Properties of LCP's

The rheology of polymeric liquid crystals has been reviewed by Baird (48) in 1978 and more recently an excellent review by Wissbrun (49) in 1981. Onogi and Asada (50) have proposed that the flow curves for polymeric liquid crystals have three regions: a shear thinning region at low shear rates, a region of constant viscosity, followed by another shear thinning region at high shear rates (Figure 2.7).

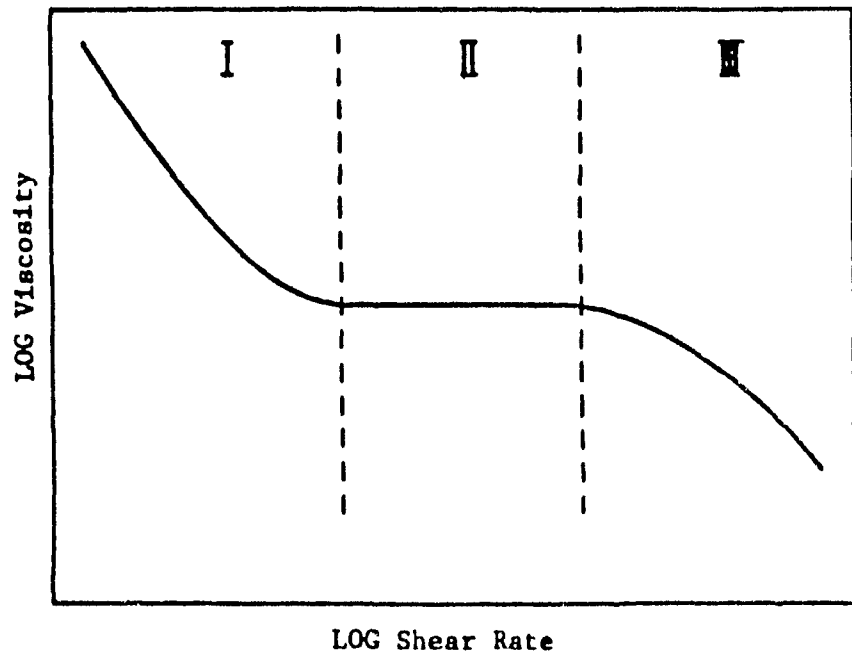


FIGURE 2.7: Three regions of flow behavior from Onogi and Asada
(50)

Wissbrun (51-53) observed that thermotropic liquid crystalline polymers show quantitative and qualitative differences when compared to semi-flexible chain polymers. Quantitatively, thermotropic polymers show a low viscosity and long relaxation times relative to those of an isotropic polymer of comparable molecular weight distribution (51). Qualitatively, shear thinning viscosity is observed in liquid crystal polymers at low shear rates, little or no extrudate swelling is displayed despite high elasticity levels in small amplitude oscillatory deformation (52,54). Occasional shear thickening behavior, transient negative normal stress difference and dependence of flow behavior on thermal and mechanical history have been reported (51,52,55-57). The rheological properties of LCP's are of particular interest to the processor. At the present time, only the nematic phase seems to be advantageous for obtaining the optimal mechanical properties with these rigid chain molecules. The flow properties of the nematic phase depend on the relative orientation of the preferred direction (of the director) and the gradient flow rate (58).

2.5 Processing Behavior of LCP's

2.5.1 Injection molding

The injection molding process involves heating solid polymeric material, usually in the form of solid pellets or powder, until it reaches a molten state; it is then injected under pressure into a cold closed mold cavity. The mold is cooled to allow the part to solidify and maintain its final shape and dimensions.

Over the past two decades, injection molding has become the major

fabrication process of plastic parts for both thermoplastic and thermosetting materials. Its outstanding versatility and ability to produce parts with intricate shapes to extremely tight specifications have been the key reasons for its widespread use. Injection molding is also highly cost effective, especially in large volume operations. The chief drawback of injection molding is the inherent difficulty of controlling the ultimate properties of the molded parts to a high degree of precision. Because of the spatial nonuniformity of the temperature and pressure fields, the complete thermo-mechanical history is unevenly distributed in the cavity, leading to structural inhomogeneity of molded parts. Although not necessarily a major concern in conventional molding, this could cause serious problems in the molding of precision parts, as for example integrated circuit boards, lenses, and fiber-optic connectors. Thus, the production of intricate parts with extremely close tolerances and high surface finish quality imposes stringent manufacturing and process control requirements.

Injection molded articles of rigid chain liquid crystal copolymers (LCP's) are gaining increasing commercial importance because of their high stiffness and strength per unit weight. These qualities make them attractive for aerospace structures and automotive parts, where the anisotropic nature of the materials can be exploited to achieve novel design strategies. Considerable technological importance is given to thermotropic LCP's because of their melt phase behavior and ease of processing. Thermotropic LCP's have excellent dimensional stability and, because of the comparatively low viscosity, can be injection molded into thin and complex shapes under appropriate processing conditions. The possibility of molding thin and intricate parts for electronic components and medical equipment has now

made them excellent candidates for these applications. The high resistance to chemicals has made LCP moldings suitable as parts in chemical processing machinery.

The processing of liquid crystalline polymers into a fiber, film, or molded article, from the melt or solution, results in structures that are highly ordered with superior mechanical properties (in the direction parallel to chain orientation) compared to conventional flexible chain polymers.

The properties of the final product are determined by the thermal and flow history experienced by the material during processing. Microstructure of the final product is the important link between the thermo-mechanical history experienced by the material and the properties of the final product. Some of the important microstructural aspects include orientation, morphology, crystallinity and frozen stresses.

Processing conditions such as the mold temperature, injection pressure and filling times are observed to affect significantly the physical properties of the end-product. Liquid crystalline polymers can be processed over a wide range of mold temperatures, generally between 30 and 150°C, with temperatures of 80 to 110°C being most common. It is observed that LCP's require lower injection pressure than other thermoplastic materials, due to the low viscosity of LCPs. The low viscosity, the low heat of transition and the high thermal conductivity result in unusually short cycle times, typically in the range of 5-30 seconds (59).

2.5.2 Processing Induced Microstructure of LCP's

Liquid crystal polymers are a new class of polymeric materials with unique molecular and solid state structures, flow characteristics and mechanical

properties. The injection molding process involves a number of variables interacting in a complex manner. The nature of interaction, when well understood, will help to control the product properties and increase process efficiency significantly. Figure 2.8 shows the variables that contribute to the interactions of the various components in the injection molding system: the material, the machine, the operating variables, and the product.

2.5.2.1 Orientation

The physical properties of the molded articles will depend upon the direction and the degree of molecular orientation. This orientation is imparted to the material as a result of elongational and shear stresses as it flows in the mold (Figure 2.9 (60)). The flow pattern in the cavity must be considered relative to the property requirements of the finished part. Generally, thin sections will be more anisotropic than thick sections (12). Several researchers (61-72) have reported skin-core morphology with layer formation along the thickness of a molded liquid crystalline specimen. Such layer formation is usually explained by the flow history during the filling stage, when the melt motion is most prominent. Ide and Ophir (62) observed that, in anisotropic melts where domains of local orientation are formed, shearing will not orient molecules if domains are stable. However, in elongational flow, each domain will be stretched out and the molecules become aligned parallel to the flow direction, yielding indistinct boundaries between domains (mono-domain structure).

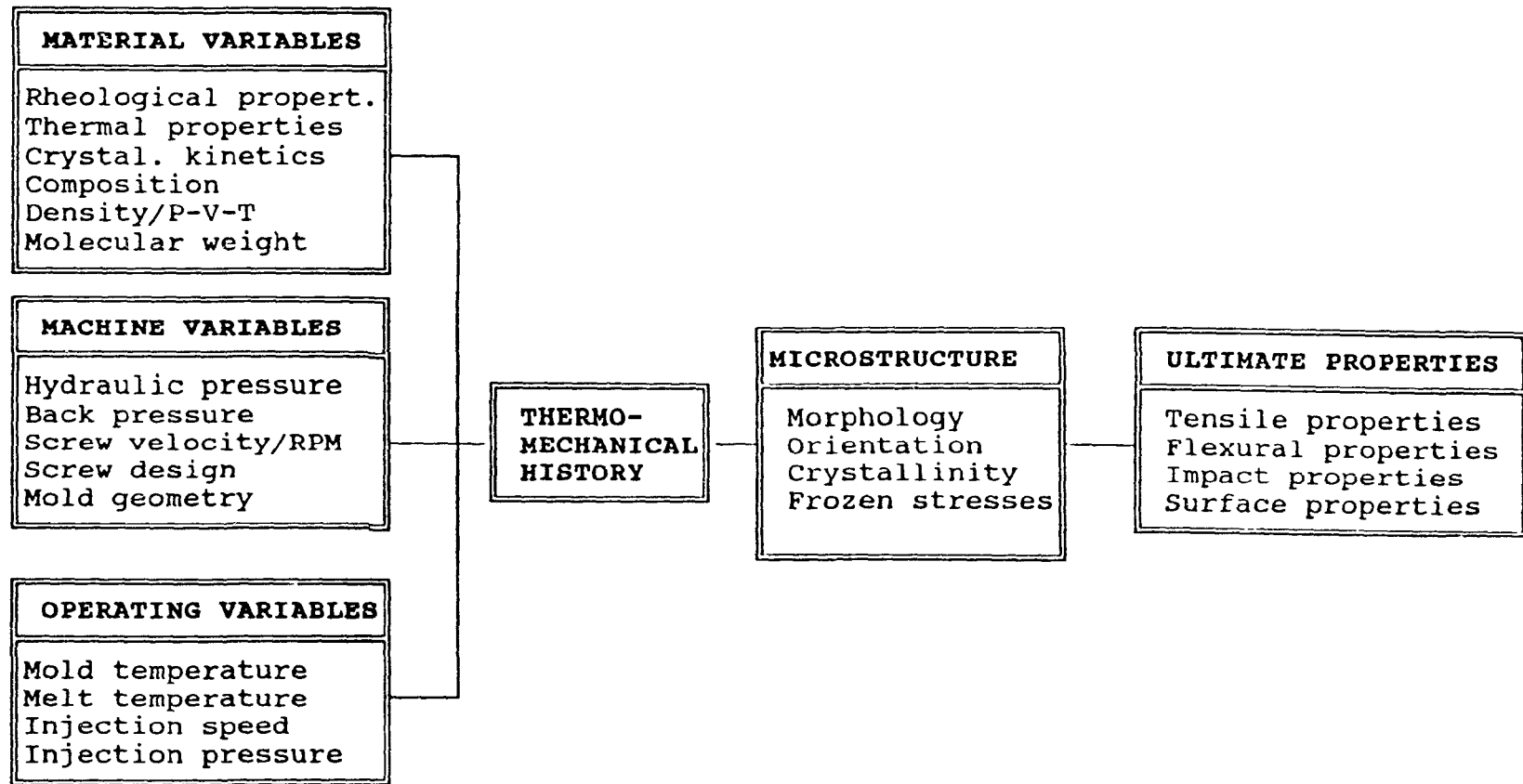


FIGURE 2.8: Processing-Structure-Properties Relationship

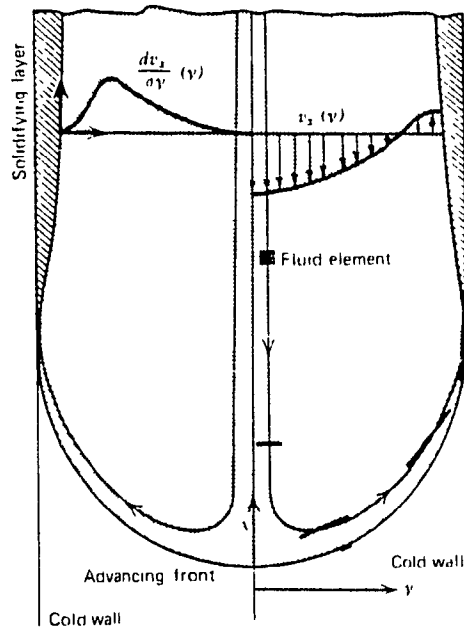


FIGURE 2.9: Schematic representation of the flow pattern in the advancing front during injection mold filling (60)

Infrared spectroscopy is a very useful tool for characterizing the molecular orientation of polymers, provided the band assignment is well established. Pirnia and Sung (73), in characterizing the molecular structure and orientation in injection molded samples of a polymer similar to that used in the present work, used three infrared bands: 1410 and 1504 cm^{-1} for the crystalline part and 1470 cm^{-1} , which is due to HNA, for the amorphous part. The transition moment angle for the above three bands was assumed to be zero.

2.5.2.2 Morphology

Many researchers observed skin-core morphology and the existence of various layer structures in injection molded liquid crystalline parts, on the basis of measurements using Polarized Light Microscopy (PLM) (25,66) and Scanning Electron Microscopy (SEM) (61,63,65,66). Skin-core morphology is also observed in injection molded bars (70,72), and in fibers (67) as well as in extruded strands (62) and extruded sheets (74,75). Ophir and Ide (72) showed a photomicrograph with four layers across the thickness (Figure 2.10). Thapar and Bevis (61) showed electron micrographs of polished surfaces and surfaces etched with sulphuric acid. They observed that there were concentric conical figures which typify the mold filling process. The fibril diameter increased from the skin region to the core, while the fibre density within each layer decreased from the skin to the core region.

2.5.2.3 Density and crystallinity

In the injection molding process, the material experiences a

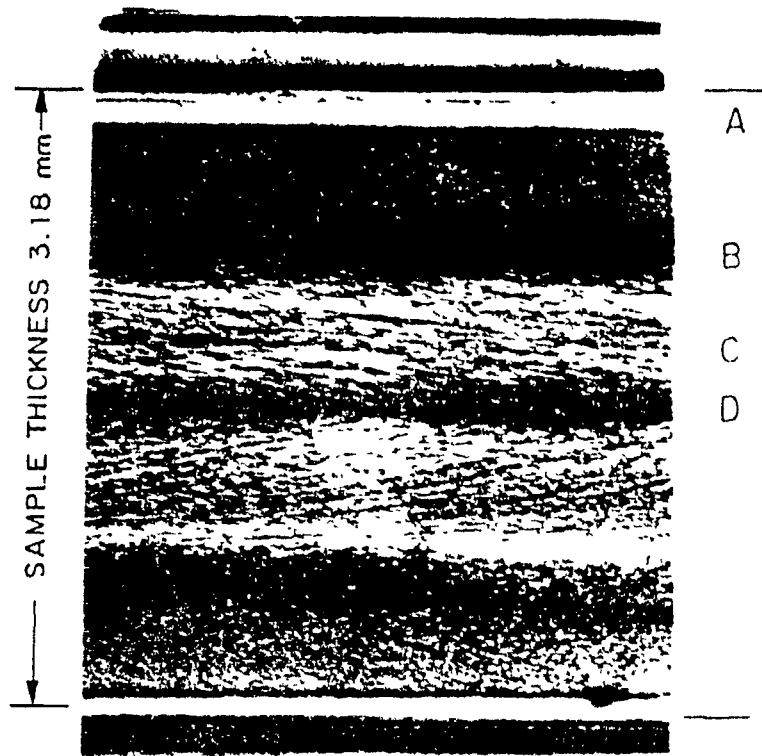


FIGURE 2.10: Photomicrograph representing the cross-sectional view of a tensile bar (72).

temperature profile where the temperature is low at the wall and high at the center of the cavity. Therefore, the crystallization rates vary across the thickness of the cavity. Since crystallinity is associated with a more compact structure, the density increases with crystallinity. In liquid crystalline polymers, only small changes in crystallinity occur during molding. Therefore, little shrinkage is observed and the dimensional stability of these materials is excellent.

In the case of rigid-chain polymers, Bechtoldt (27) observed that heat treatment increased the crystallinity but the density remained constant. Annealing below the melting point leads to the development of localized regions of enhanced order, especially in specimens with a high degree of overall orientation.

2.5.2.4 Mechanical properties

McFarlane et al.(76) reported that tensile strength and flexural moduli of injection-molded tensile bars were exceptionally large for unreinforced LCP copolyesters. The tensile strength of the bars molded from liquid crystalline melts is four to five times that obtained for the conventional polyethylene terephthalate (PET) molded under identical conditions. The tensile strength results, in part, from the high degree of molecular orientation retained in the molded article.

Data showing the significant effect of part thickness on the anisotropy of mechanical properties (Figure 2.11) were reported by Jackson and Kuhfuss (12). The distribution of mechanical properties in the thickness direction of an injection molded part was reported by Williams and Garg (71), and Garg and Kenig (77)

They observed that each of morphological zones that were observed across the thickness had distinctive mechanical properties.

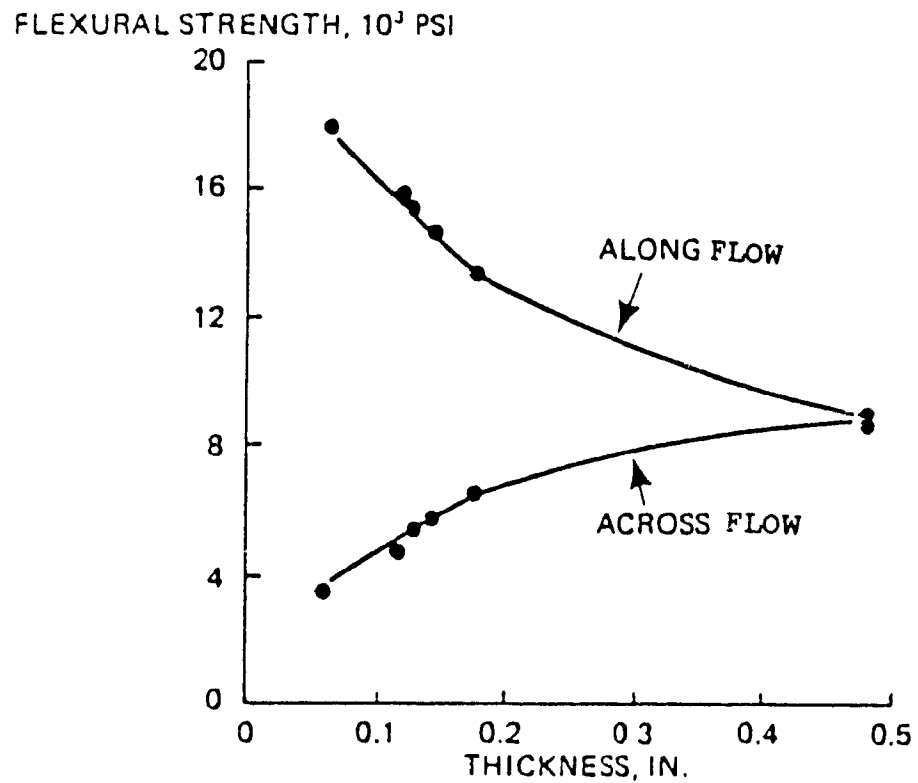
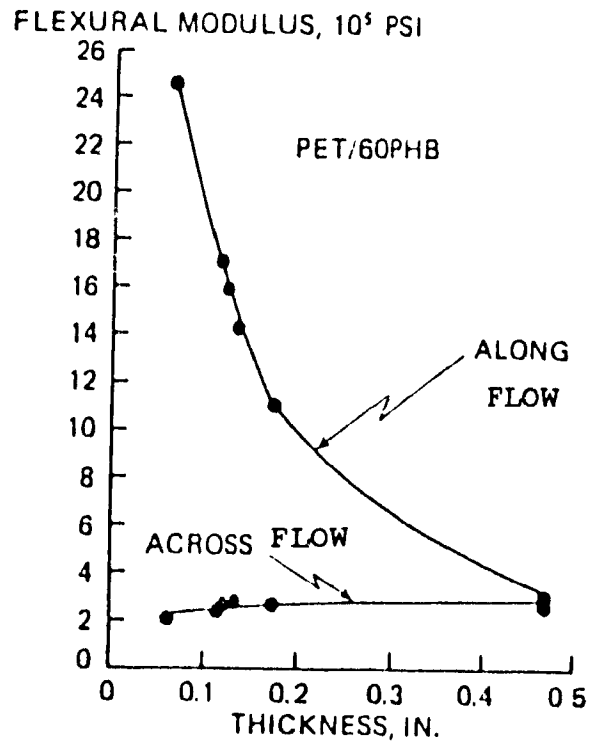


FIGURE 2.11: Effect of reduced thickness on flexural modulus and strength of PET modified with 60 mole% PHB (12).

CHAPTER III

3. OBJECTIVES

The main objective of the present work has been to obtain a better understanding of the processing behavior of thermotropic liquid crystalline polymers, with special emphasis on the injection molding process. Since the processing behavior of polymers depends strongly on the thermal, thermodynamic, and rheological properties of the material, it was also important to obtain a characterization of these properties for the liquid crystalline polymer system under consideration.

The specific objectives of the research project are outlined below.

1. Characterization of the relevant properties of the resin, including thermal properties (specific heat, thermal conductivity, and thermal diffusivity), mechanical properties (dynamic mechanical behavior), and rheological properties (viscosity-shear rate behavior and capillary die swell).
2. Evaluation of melting and crystallization behavior of the material and the crystallization kinetics over a broad range of temperatures and times.
3. Evaluation of the injection molding behavior of the liquid crystalline

polymer, including the collection and analysis of data regarding the variation of pressure and temperature under various molding conditions.

4. Analysis of the microstructure and properties of injection molded articles and the explanation of the relationships between the microstructure, properties, and processing conditions in light of the phenomena occurring during injection molding and the properties of the liquid crystalline polymer.

CHAPTER IV

4. EXPERIMENTAL

This chapter describes the material employed in the present study and the method of preparation of samples for the thermal, microstructural, mechanical and rheological characterization of the material. The preparation of the injection molded plaques under various processing conditions is also described. A detailed description of the relevant experimental apparatus and the procedures employed in this study will be presented.

4.1 Material

The rigid-chain liquid crystal copolymer used in this study, LCP-2000, consisted of about 70 mol% p-hydroxybenzoic acid (HBA) and 30 mol% 2,6-hydroxynaphthoic acid (HNA) (Figure 4.1). The resin was supplied by Celanese Research Company, New Jersey, in the form of solid pellets. The method of preparation of the copolymer was described in detail by Calundann (19). Because of the hygroscopicity of the material, the pellets were always dried overnight at 100°C in a vacuum oven, before use. Table 1 summarizes some of the important properties of the resin.

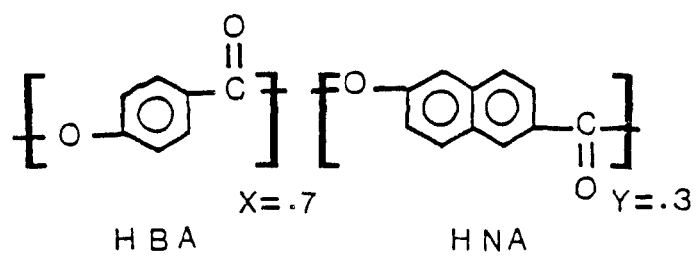


FIGURE 4.1: Chemical Structure of the rigid chain copolyester LCP-2000.

TABLE 4.1: PHYSICAL PROPERTIES OF LCP-2000

PHYSICAL PROPERTIES		SOURCE
M_w (g/mol)	30,000	(53)
M_n	15,000	(53)
Glass trans. temp.(°C)	90	
Melting range (°C)	265-280	
Average specific heat (J/K.mol)		
$C_{p,s}$	170.0	
$C_{p,l}$	243.0	
Average thermal conductivity (J/m.°C.s)		
k_s	0.237	
k_l	0.251	
Average Thermal diffusivity (m ² /s) E+7		
α_s	1.93	
α_l	1.94	
Density (kg/m ³)		
ρ_s	1.4	
ρ_l	1.3	(27)
Power law index n (300°C)	0.54	
Consistency index (300°C)	3236	

* All other data were obtained from this work.

4.2 Thermal Properties

4.2.1 Specific Heat

Specific heats of the liquid crystal copolymer (70%HBA/30%HNA) were measured over a wide range of temperatures (room temperature to 320°C at a scanning rate of 20 °C/min) using DSC (Differential Scanning Calorimetry) thermograms of the samples sliced from the skin layer of the as-received pellets. The following equation was used for the calculation of the specific heat, C_p :

$$[C_p(T)]_{\text{polymer}} = \frac{[H(T)]_{\text{polymer}}}{[H(T)]_{\text{sapphire}}} \times \frac{\text{Weight (sapphire)}}{\text{Weight (polymer)}} \times [C_p(T)]_{\text{sapphire}} \quad (4.1)$$

where $H(T)$ is the amplitude of pen deflection (heat flow) on the DSC thermogram. $[C_p(T)]_{\text{sapphire}}$ were obtained from standard tables (78).

4.2.2 Thermal Conductivity and diffusivity

The apparatus used to measure the thermal conductivity and diffusivity of the copolymer was a miniaturized version (79) of the instrument designed by Sourour and Kamal (80). It permits the measurement of thermal conductivity and diffusivity of polymeric materials in the solid as well as in the molten state. In one mode of operation, the test specimen is suddenly subjected to a thermal flux and the

velocity of the heat wave across the sample is measured for calculation of the thermal diffusivity. Maintaining the heat flux leads to a steady thermal gradient across the sample thickness from which the thermal conductivity can be determined.

The basic construction of the conductivity cell is shown in Figure 4.2. It consists of two identical stainless steel circular molds. A nichrome wire heater is sandwiched between the lower plate of the upper mold and the upper plate of the lower mold. Two molds are used to produce a uniform heat flux on both sides of the nichrome wire heater. The symmetry of the molds is verified by comparing the corresponding individual temperature signals on both sides of the molds. Copper-constantan thermocouples are used to measure the temperatures across the thickness of the specimen. Details of the system arrangement and auxiliary equipment for the measurement of current and voltage of the heater are given in an earlier paper of Kamal et al. (79). The apparatus has been interfaced with a computer for precise measurements of temperature (resolution: 0.1 °C) and time (resolution: 0.1 s).

Circular discs of 5 cm diameter and 1.6 mm thickness used to measure the thermal conductivity and diffusivity of the material were prepared by compression molding. The pellets were melted at 300°C and at an applied pressure of 200 MPa for 2 min. The moldings were allowed to cool at a rate of about 30 °C/min under pressure to room temperature.

Steady-state heat transfer by conduction through a sample confined between parallel plates follows Fourier's law:

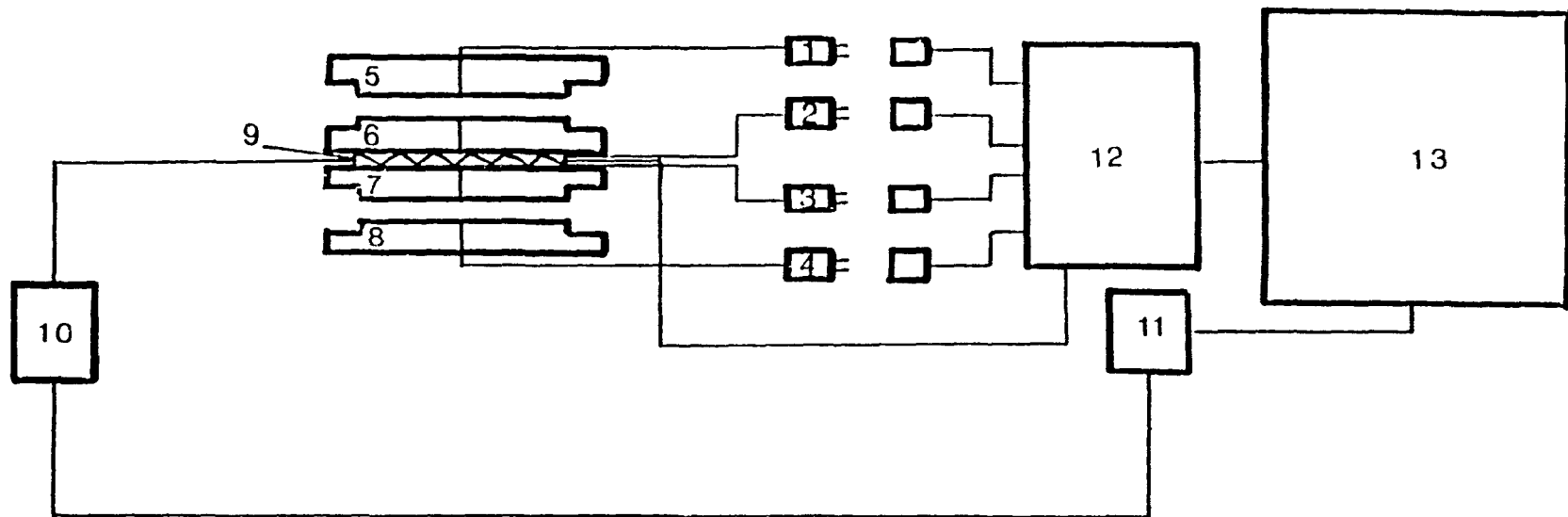


FIGURE 4.2: Thermal conductivity apparatus: system arrangement and auxiliary equipment.

- | | |
|----------------------------------|-------------------------|
| 1. Thermocouple monitoring No. 1 | 8. Bottom plate |
| 2. Thermocouple monitoring No. 2 | 9. Nichrome wire heater |
| 3. Thermocouple monitoring No. 3 | 10. D.C. Supply |
| 4. Thermocouple monitoring No. 4 | 11. D.A.C. |
| 5. Top plate | 12. A.D.C. |
| 6. Upper middle plate | 13. Computer |
| 7. Lower middle plate | |

$$k = \frac{q}{dT/dX} \quad (4.2)$$

Where q is the heat flux in the thickness direction under the influence of a temperature gradient dT/dX , and k is the thermal conductivity of the material.

Based on the assumption that equal heat flux is distributed on both sides of the conductivity cells, the thermal flux values are related to the various parameters as follows (81):

$$Q_1 = \frac{k.A. \Delta T_1}{\Delta X_1} \quad (4.3)$$

$$Q_2 = \frac{k.A. \Delta T_2}{\Delta X_2} \quad (4.4)$$

Where $Q_1 = Q_2$, are the thermal fluxes on each side of the conductivity cell, and A is equal to the heating area which is taken here as the area of the sample. ΔT_1 and ΔT_2 are the thermal gradients through thicknesses, ΔX_1 and ΔX_2 respectively. $Q = V.I$, Q is the overall power, where V is the voltage and I is the current.

The value of the thermal conductivity at each temperature can be calculated as follows:

$$k = \frac{Q_1. \Delta X_1}{A. \Delta T_1} \quad (4.5)$$

The thermal penetration time was measured by obtaining the time elapsed until a temperature change was detected in thermocouples 1 and 4 (Figure 4.2) when the external heat source used to heat the nichrome wire was applied. The value of thermal penetration time, τ , for each temperature was used to compute the thermal diffusivity employing the procedure described by Kamal et al. (79).

4.3 P-V-T Diagram

The relationship between the pressure, volume and temperature is needed in polymer processing studies, especially injection molding, due to the large thermal and pressure effects in this process and the importance of volume changes in the determination of final product properties.

The Pressure-Volume-Temperature (P-V-T) data of the liquid crystal copolyester resin were collected using the Instron Universal Testing Instrument, floor model (TT-CM-L), in conjunction with the Instron Capillary Rheometer Type MCR. The barrel temperature can be maintained within $\pm 0.5^\circ\text{C}$ of the set temperature, and the accuracy of the load weighing system is the greater of the $\pm 0.5\%$ of the indicated load or $\pm 0.25\%$ of recorded scale. The movement of the plunger could be monitored within 0.025 cm of accuracy (Instron Manual Number 10-29-1 (A) (1965)), by means of a gauge length dial. A plug resistant to high pressures, which was held in place by a clamping nut, was employed to seal off the barrel at the bottom. Teflon "O" rings were inserted around the plug and plunger to prevent the melt from leaking during compression.

The procedure involved adding pellets into the barrel, a small amount at a time, and tamping with a brass rod after each addition. Sufficient time was

allowed for the melt to reach equilibrium at the desired test temperature. Then, the volume of the melt was changed by pushing the piston at a predetermined rate to compress the polymer melt enclosed in the isothermal cylinder. Pressure was recorded as a function of temperature and volume.

4.4 Melting and Crystallization Behavior

The Perkin Elmer Differential Scanning Calorimeter (DSC-7), was used to carry out calorimetric measurements required for the evaluation of melting behavior and crystallization kinetics. Measurements of the change in enthalpy of the polymer during heating and cooling cycles were conducted. The temperature as well as the area under the peak were calibrated using Indium, Tin and Lead standards, whenever the heating/cooling rate was changed. The sample and reference compartments were purged continuously with pre-purified nitrogen at a flow rate of 20 ml/min. A baseline was run with two empty pans in both the reference and sample holders. The DSC thermograms were normalized to take into account the weight of the samples, which varied from 7 to 12 mg. The procedure of the automatic subtraction of the baseline was used for all the runs. A Cahn RG Balance was used in conjunction with the DSC to weigh polymeric samples with a precision of ± 0.0001 mg.

Microtomed sections of the skin layer (50 μm thick) were obtained from the as-received pellets for studying the melting behavior of the LC polymer.

Compression molded films of about 1mm thickness were prepared by melting the pellets at 300°C and at an applied pressure of 200 MPa for 2 min. The

melting the pellets at 300°C and at an applied pressure of 200 MPa for 2 min. The moldings were allowed to cool at a rate of about 30°C/min, while still under pressure, to room temperature. The samples of 6 mm diameter were punched out from the prepared film to fit exactly the DSC aluminum pans. These samples were melted at 320°C and held for 10 min, in order to erase any previous thermo-mechanical history developed during sample preparation. The samples were then used to study the effect of cooling rates on melting behavior and for evaluating the kinetics of crystallization.

4.5 Dynamic Mechanical Behavior

Many polymers crystallize if they are cooled from the melt. The degree of crystallinity and molecular orientation are affected by the thermal and mechanical histories experienced by the polymer during processing. These structural changes have profound effects on the dynamic mechanical properties. The changes of stiffness at temperatures below the melting point of the crystallites depend on the motion of the amorphous regions.

The dynamic modulus generally increases with increasing degree of crystallinity. The increase of crystallinity has a great effect on the α -dispersion.

The dynamic mechanical properties were measured with a Rheovibron direct reading viscoelastometer as a function of temperature at specified frequencies. This instrument is manufactured by the Toyo Measuring Instrument Co. Ltd (Tokyo).

The Rheovibron viscoelastometer has been extensively used for

During measurement, a sinusoidal tensile strain is imposed on one end of the sample, and a sinusoidal tensile stress is measured at the other end. The stress τ and strain ϵ can be expressed as follows:

$$\tau = \tau_0 \sin(\omega t + \delta) \quad (4.6)$$

$$\epsilon = \epsilon_0 \sin \omega t \quad (4.7)$$

where ω is the angular frequency, and δ is the phase angle; then:

$$\tau = \tau_0 \sin \omega t \cos \delta + \tau_0 \cos \omega t \sin \delta \quad (4.8)$$

The stress can be considered to consist of two components, one in-phase with the strain ($\tau_0 \cos \delta$) and the other 90° out-of-phase ($\tau_0 \sin \delta$). When these are divided by the strain, the modulus can be separated into an in-phase (real) and out-of-phase (imaginary) component.

$$\tau = \epsilon_0 E' \sin \omega t + \epsilon_0 E'' \cos \omega t \quad (4.9)$$

$$E' = \frac{\tau_0}{\epsilon_0} \cos \delta \quad (4.10)$$

and
$$E'' = \frac{\tau_0}{\epsilon_0} \sin \delta \quad (4.11)$$

$$\tan \delta = \frac{E''}{E'} \quad (4.12)$$

E' and E'' are the storage modulus and the loss modulus; respectively; $\tan \delta$ is the loss tangent, called also the internal friction or damping.

Compression molded films were prepared at 300°C for 2 min. and then quenched at about 30 deg/min to room temperature. Rectangular samples (5.0 x 0.3 x 0.04)cm were cut from the compression molded film. One of the samples was annealed for 10 hours at 250°C.

4.6 Structural Studies

Traditional methods for the study of polymer structure include the entire range of microscopic instruments and spectroscopic techniques. Optical microscopy, generally using polarized light (PLM), is useful to observe structures larger than a micrometre in size. Scanning Electron Microscopy (SEM) permits a higher magnification view of 5 to 10 nm resolution. Transmission Electron Microscopy (TEM) permits the observation of structures to less than 1 nm. Wide Angle X-ray Diffraction (WAXD) and Fourier Transform Infrared Spectroscopy (FTIR) are well established techniques to study the microstructure and molecular orientation. This range of instrumental methods requires a variety of sample preparation methods which range from established methods to some developed specifically for liquid crystalline polymers.

4.6.1 Preparation of fibers

A capillary rheometer with barrel temperature set at 320°C using a 0.010 in capillary diameter was used to melt extrude a strand which was hand drawn into tiny fibers. The idea was to obtain samples with uniaxial symmetry. These melt drawn fibers were arranged in parallel bundles to serve as specimens for the determination of the transition moment angle using wide-angle X-ray diffraction (WAXD) and infrared spectroscopy (FTIR).

4.6.2 Determination of the transition moment angle

4.6.2.1 Orientation Function using WAXD

Pinhole photographs of the fibers were obtained employing a Phillips X-ray generator (Model PW 1120) and a transmission pinhole camera. The Phillips X-ray generator PW 1120 features 3 kW maximum power, a 4-80 mA continuously variable tube current, and 10-60 kV continuously variable high voltage. CuK_α radiation with Ni filter was used, at a current of 20 milliamps and a voltage of 40 kV. The samples were exposed for 2 hours. Kodak medical X-ray film NS-54T, supplied by Eastman Kodak Company, was used.

The X-ray diffraction patterns were recorded on 8cms x 10.5cms photographic films. The sample-to-film distance was 5.5 cms. The intensity distributions of the various reflections, shown on the pinhole photograph in Figure 4.3, were determined using the Joyce-Loebl Automatic Recording

Microdensitometer, Model MK III C.S., supplied by Joyce, Loebel and Co., Ltd., England. The instrument incorporates a true double beam system in which the two beams arise from a single light source and terminate in a single photo-electric receiver. This makes the instrument almost independent of its own parameters and complete reproducibility of record is possible, with the range of densities specified. The azimuthal intensity distributions of the reflections were determined from 0 to 90° in increments of 1 and 2 deg., in the region of the reflection to ensure consistency. All the photographs were scanned under the same machine settings. The orientation function f was then calculated:

$$f = 1/2 (3\langle \cos^2\theta \rangle - 1) \quad (4.13)$$

For more details ref.(82) constitutes an excellent source of information.

4.6.2.2 Dichroic Ratio using FTIR

Infrared spectra were obtained using a BOMEM Michelson-100, Type TM, spectrometer. Thirty two scans were averaged and the obtained spectra were stored for data analysis. During experiments, the sample chamber was continuously purged with a flow of pre-purified nitrogen gas.

The polarized infrared measurements were obtained using a Perkin-Elmer gold wire-grid polarizer, part no. 186-0243. The parallel polarized spectra were obtained by having the sample reference direction oriented parallel to the polarization direction. The perpendicular polarized spectra were obtained by

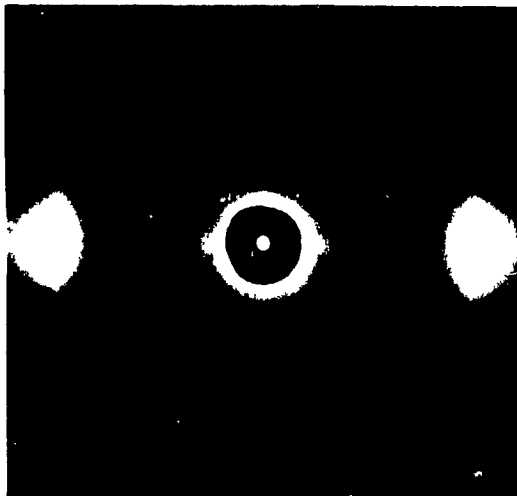


FIGURE 4.3: X-ray fibre pattern.

rotating the sample only, by 90°. The frequency range used for this study was from 400 cm⁻¹ to 4000 cm⁻¹.

Fibers drawn under the same conditions as those used for X-ray diffraction were exposed to the infrared beam to obtain the average of 32 polarized spectra parallel and perpendicular to the reference direction. From the ratio of the intensity of the 780 cm⁻¹ band, shown in Figure 4.4, of the parallel and perpendicular polarized absorption, the dichroic ratio was calculated as follows:

$$D = \frac{A_{\parallel}}{A_{\perp}} \quad (4.14)$$

where A_{\parallel} is the absorbance for linearly polarized light parallel to the chain direction and A_{\perp} is the corresponding measurement perpendicular to the chain axis. The value D can range from zero (no absorbance in the parallel direction) to infinity (no absorbance in the perpendicular direction). For an unoriented sample, no dichroism occurs and $D=1$.

Incorporating in the equation below the orientation function calculated using x-ray diffraction from section 4.6.2.1, and the dichroic ratio obtained above, D_0 can be determined.

$$f = \frac{D - 1}{D + 2} \quad \frac{D_0 + 2}{D_0 - 1} \quad (4.15)$$

as well as the transition moment angle α_t using the equation below:

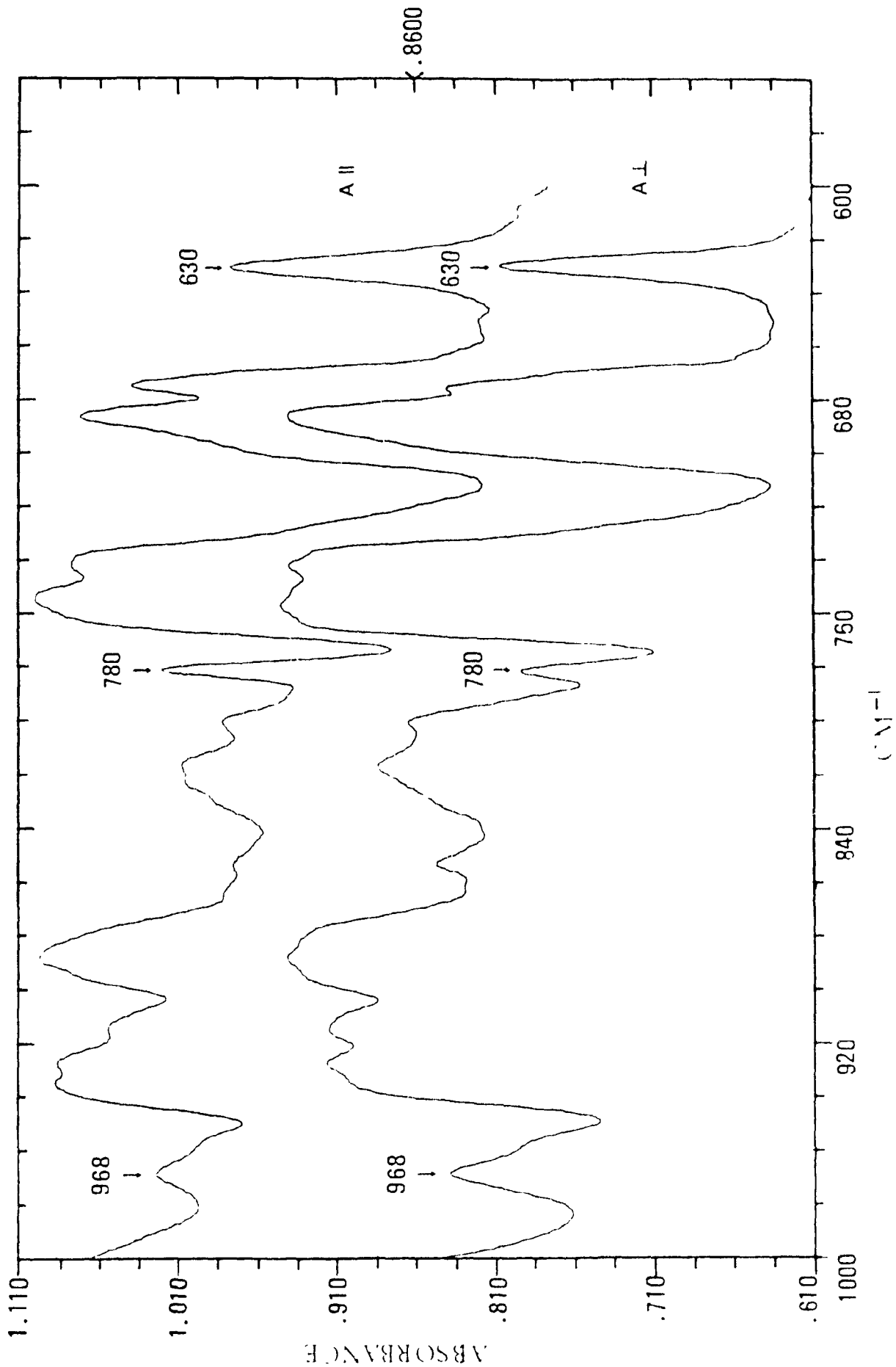


FIGURE 4.4: Infrared polarized absorption spectra of the fiber

$$D_0 = 2 \cot^2 \alpha_i \quad (4.16)$$

α_i is the angle between the chain axis and the particular absorption band considered (Figure 4.5).

4.7 Rheological Properties

4.7.1 Shear Viscosity

Rheological properties of the liquid crystal copolyester resin were measured using the Instron Universal Testing Instrument, floor model (TT-CM-L), in conjunction with the Instron Capillary Rheometer Type MCR. A broad range of cross-head speeds can be used, from 0.005 to 50 cm/min. The barrel temperature can be maintained within $\pm 0.5^\circ\text{C}$ of the set temperature, and the accuracy of the load weighing system is the greater of the $\pm 0.5\%$ of the indicated load or $\pm 0.25\%$ of the recorded scale in use. The movement of the plunger could be monitored within 0.025 cm of accuracy (Instron Manual Number 10-29-1 (A) (1965)), by means of a gauge length dial. Different Teflon "O" rings were inserted around the capillary and plunger to prevent the melt from leaking during compression. The diameter of the capillaries used was 0.030 and L/D ratios of 20, 40, 80 and 100. The shear viscosity results presented include Bagley and Rabinowitch corrections.

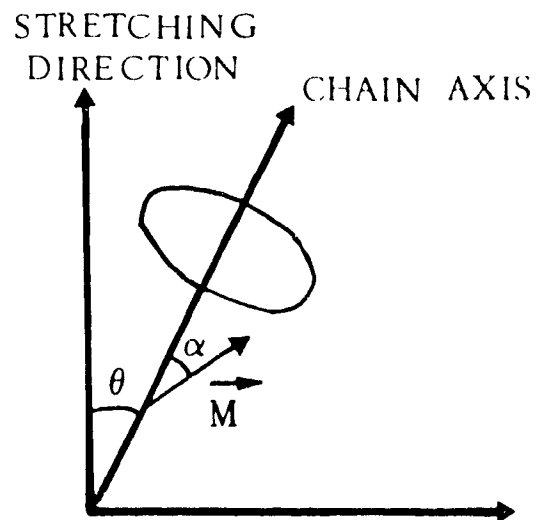


FIGURE 4.5: Partial axial orientation: Chain distribution rotationally symmetrical about the stretching direction.

4.7.2 Capillary Die Swell

Capillary extrudate swell of the liquid crystal copolyester was measured using the Instron Capillary Rheometer in conjunction with a thermostatic chamber and a detection system interfaced to a computer for acquisition and analysis of the experimental data. A detailed description of the apparatus used and the experimental procedure is given elsewhere (83). The technique permits measurement of die swell under isothermal conditions and in the absence of gravitational sagging and interfacial tension effects. The compartments of the thermostatic chamber were filled with silicone and heated up to 200 °C. The 200 fluid silicone used for this measurement was manufactured by Dow Corning and based on poly(dimethyl siloxane) with a viscosity of 20 centiStokes.

4.8 Injection Molding

4.8.1 Injection Molding Machine

The experimental work was carried out on a Danson-Metalmec reciprocating screw injection molding machine (Model 60-SR) with a shot weight of 2 1/3 oz. and a clamping force of 68 tons. The injection molding machine is shown in Figure 4.6. The machine can be operated either in the manual or semi-automatic mode. The barrel has two band heaters which divide it into two different heating zones. The temperatures of the two zones can be controlled to within $\pm 2^\circ\text{C}$. The

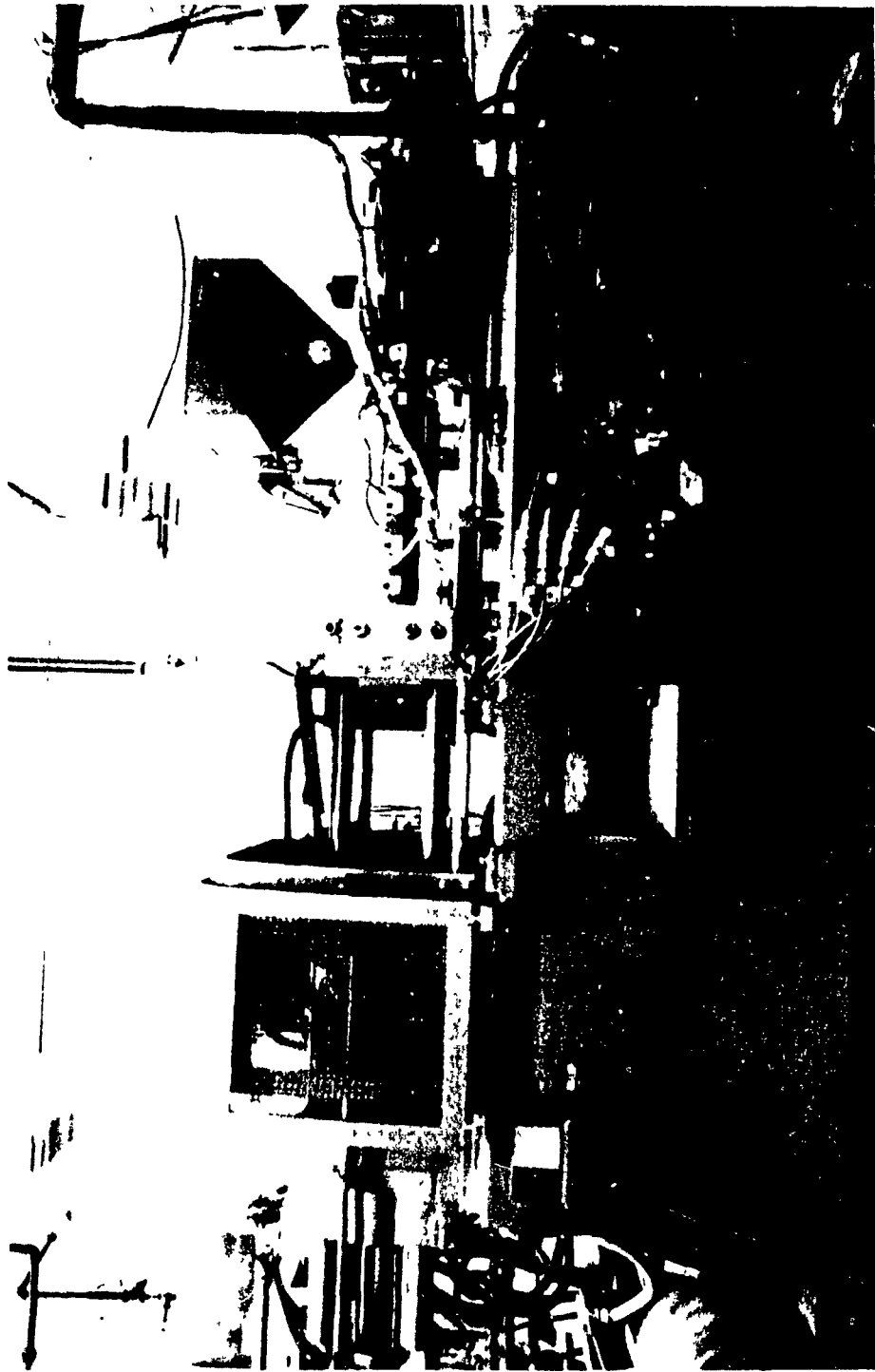


FIGURE 4.6. Diesel Motor Fuel Metering Device

injection portion of the total machine cycle is generally broken down into two pressure stages. During the first portion, the mold cavity is filled. The first stage or the injection pressure during filling is regulated by the injection speed and injection pressure control valves. During the second stage, pressure (holding pressure) is controlled by the holding pressure valve, which is the maximum pressure generated during the packing stage. The displacement of the screw is monitored with a linear displacement transducer, Model no. 4709, manufactured by Markite.

In this study the injection molding machine was interfaced with a Cromenco micro-computer to obtain information about the processing cycle for each set of conditions during each cycle, as shown in Figure 4.7. Data acquisition as well as process control could be done at a rate of up to 100 times per second using programs written in Assembly Language.

Another program was written for interfacing the microcomputer with the VAX 780 computer. The acquired data were transmitted to and stored in the VAX computer. These data were then converted from hexadecimal form to real variables, where pressure was given in psi and temperature in °C, by using a Fortran program.

4.8.2 Mold Cavity

The rectangular mold cavity, with the geometry shown in Figure 4.8, was employed to injection mold rectangular test plaques. The geometry of the mold cavity was simple, in order to facilitate the interpretation of data and the predictions of fluid and heat flow during the molding cycle. The cavity dimensions were 10 cm x 6.5 cm x 3.18 mm. The low viscosity of the melt and the lack of extrudate swell

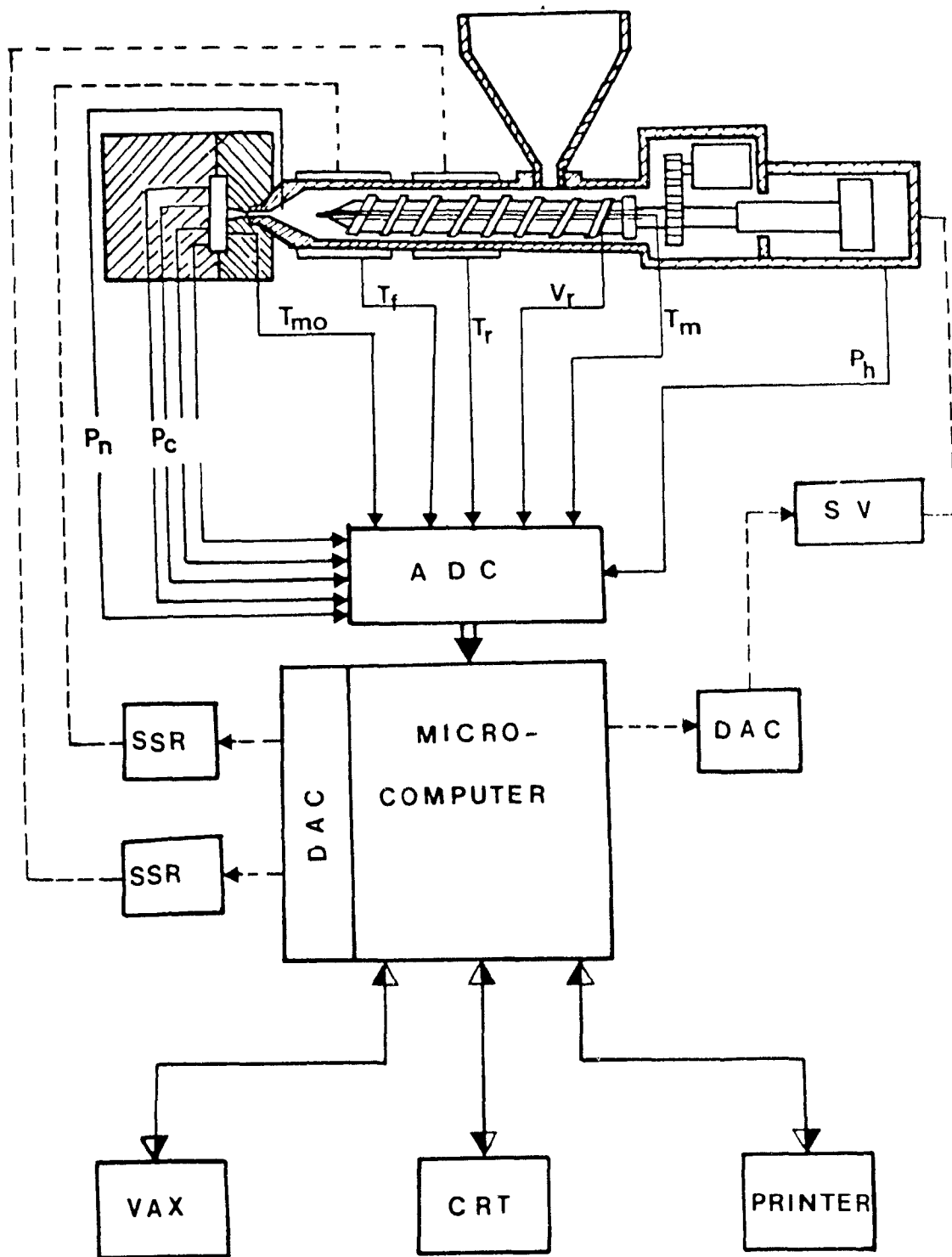


FIGURE 4.7: Injection Molding Machine-Microcomputer Interface

differentiate liquid crystal polymers (47,48) from conventional polymers. Oda et al. (84), based on their experiments, hypothesized that the occurrence of jetting was related to extrudate swell. In order to avoid jetting, a fan gate, expanding to the whole thickness of the cavity was chosen. The fan gate had an angle of 150° , while expanding to the whole width of the cavity as shown in Figure 4.8. Tadmor (60) and Ide and Ophir (62) reported that fan type and side type gates reduce "jetting" phenomena.

A Sterlco heating-cooling unit, Model 7000, using circulating water, was used to cool the mold. The temperature in the mold was controlled within $\pm 1^\circ\text{C}$. The high mold temperature (140°C) was achieved by joining the mold connections of the cooling channels to the main steam line. The selected temperature was adjusted by setting the proper pressure with the help of a servovalve. Two servovalves were connected to the steamline connection. One for the low pressure range and the second for the high pressure range. The high pressure range servovalve was used to obtain 52.4 lb/in^2 steam pressure, which corresponds to a mold temperature of 140°C .

Four Dynisco pressure transducers and four thermocouples were installed in the mold cavity, as depicted in Figure 4.8, to measure the temperature, pressure and temperature and pressure gradient(s) in the mold cavity. All the transducers were calibrated prior to installation to verify their gauge factors and linearity. The calibration equations for the pressure transducers are given in Table 4.2.

A thermocouple with a grounded junction was installed for melt temperature measurement. The thermocouple positioned at the tip of the screw,

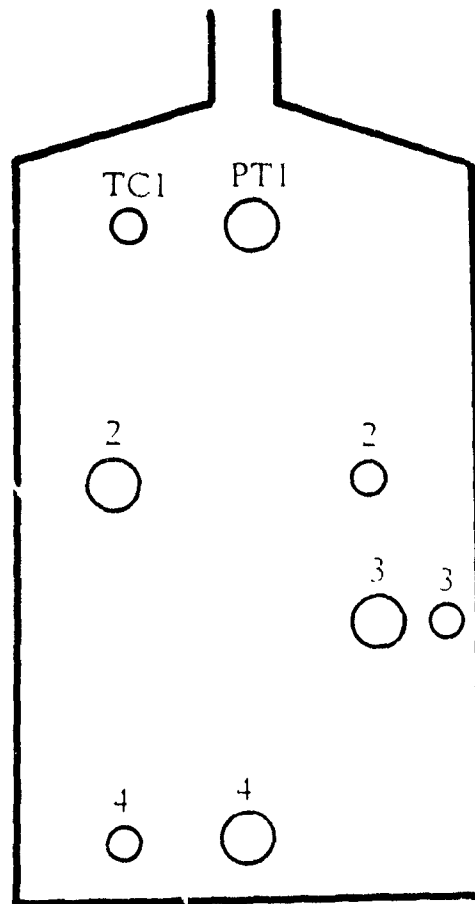


FIGURE 4.8: Schematic Drawing of Mold Cavity with Pressure Transducer and Thermocouple Locations

TABLE 4.2: CALIBRATION EQUATIONS FOR THE TRANSDUCERS

TRANSDUCER	EQUATION
HYDRAULIC PRESSURE	$P = 43.24 X \text{ (mV)} - 27.15 \text{ psi}$
NOZZLE PRESSURE	$P = 462.92 X \text{ (mV)} - 51.2 \text{ psi}$
CAVITY PRESSURE (1)	$P = 284.33 X \text{ (mV)} - 133.24 \text{ psi}$
CAVITY PRESSURE (2)	$P = 424.34 X \text{ (mV)} - 208.04 \text{ psi}$
LINEAR DISPLACEMENT	$L = 0.6147 X \text{ (mV)} - 1.2265 \text{ cm}$

through the bottom core, was parallel to the flow direction. It was in direct contact with the polymer melt from the screw tip (85). The mold temperature was measured by two thermocouples flush mounted in the mold cavity at the positions shown in Figure 4.8. The thermocouples were previously calibrated for two temperatures (0°C in ice water and 100°C in boiling water).

4.8.3 Injection Molding Variables

In this study, the injection cycle variables such as injection pressure and injection speed, holding pressure and holding time were controlled on the machine timers and control box. The computer in this work was employed only for data acquisition.

Process variables are those variables experienced by the material during the process, such as melt pressure at the nozzle, melt temperature at the nozzle, cavity pressure, injection speed, cavity pressure gradient, and mold temperature. During the preparation of the molded plaques, only one independent parameter was varied at each time, while the other independent parameters were kept constant. The injection molding parameters are given in Table 4.3. In this study, four parameters were varied, melt and mold temperatures and injection pressure and speed. The last two variables are interrelated. The molded plaques were prepared under the molding conditions given in Table 4.3. Ten molded plaques were prepared at each particular condition. The samples were stored in an environmental chamber where a temperature of 23°C and a relative humidity of 50% were maintained.

TABLE 4.3: INJECTION MOLDING VARIABLES

PROCESSING PARAMETER	VALUES USED	
MOLD TEMPERATURE (°C)	40	140
MELT TEMPERATURE (°C)	300	330
CAVITY PRESSURE (psi)	1600	2200
INJECTION SPEED (cm ³ s ⁻¹)	9	18

To study the microstructure of the rectangular plaques obtained at various molding conditions, samples were taken from the environmental chamber to prepare the specimens required by the particular test.

4.8.4 Microstructure Determination

4.8.4.1 Sample Preparation

A molded plaque, representing a particular set of molding conditions, was chosen from a series exhibiting similar processing characteristics, particularly reproducible cavity pressure-time profiles. These profiles, under similar thermal and injection conditions, reflect the processing conditions experienced by the material during cavity filling.

(a) Microtoming

Rectangular test pieces were cut from six different positions in the injection molded plaque, as shown in Figure 4.9, using a fine-tooth coping saw. The sample cutting operation was carried out carefully to minimize heat generation during cutting. These samples were used to obtain microtomed sections for microstructure characterization, using infrared spectroscopy, x-ray diffractometry, density measurements and polarizing microscopy.

The above rectangular test pieces were glued on a acrylic sample holder with a cyanoacrylate adhesive (Krazy glue). The sample holder was fitted in an "Om E" sledge microtome, manufactured by Reichert, and steel knives supplied

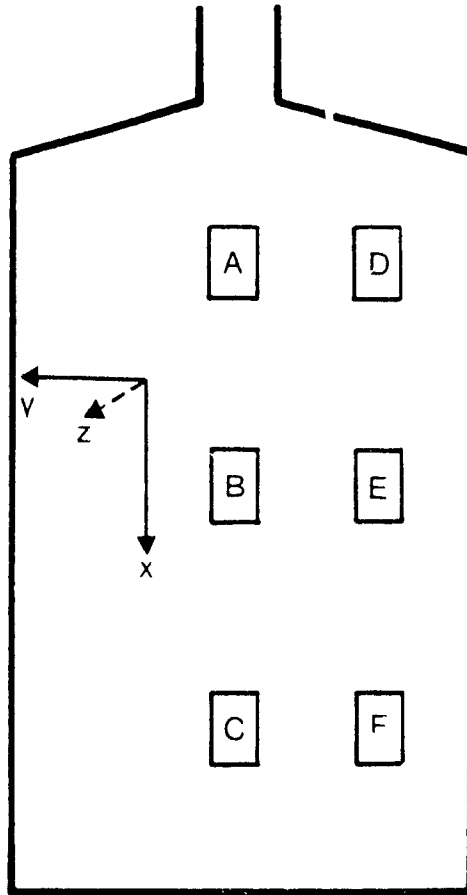


FIGURE 4.9: Assigned locations of rectangular test pieces for microstructural analysis.

Optical Co. The microtome was used to slice sections in the X-Y plane from the surface to the center of the thickness of the rectangular piece.

The angle between the knife cutting plane and the microtomed surface plane (X-Y plane) is chosen to suit the type of material to be microtomed. The section thicknesses of the material may be adjusted automatically or manually. Usually 32 slices of 50 μm each were obtained from the surface to the center across the thickness of the samples (in the Z-direction). The 32 specimens were divided into 16 odd and 16 even specimens displaying a good representation of the microstructure across the thickness. These sections were put between glass slides and stored in a desiccator for later use in microstructure characterization.

(b) Rectangular test bars

Rectangular test bars were machined from four different positions of an injection molded rectangular plaque as shown in Figure 4.10. Two were cut in the parallel-to-flow direction, one from the centerline position (1L) and the second away from the centerline near the mold wall (2L), and two other rectangular bars were cut in the perpendicular-to-flow direction, one from the region near the gate (1T) and the second sample further away from the gate (2T). These rectangular bars with dimensions of (5.8 x 1.2 x 0.32) cms, were used for microhardness testing, by polishing the X-Z plane for the sample (1L). Furthermore the same samples were broken in liquid nitrogen, in order to examine the morphological texture developed across the thickness of the fractured surface, using a Scanning Electron Microscope (SEM). Finally the same rectangular bars were also used in conjunction with a layer removal technique for the determination of the distribution of mechanical properties.

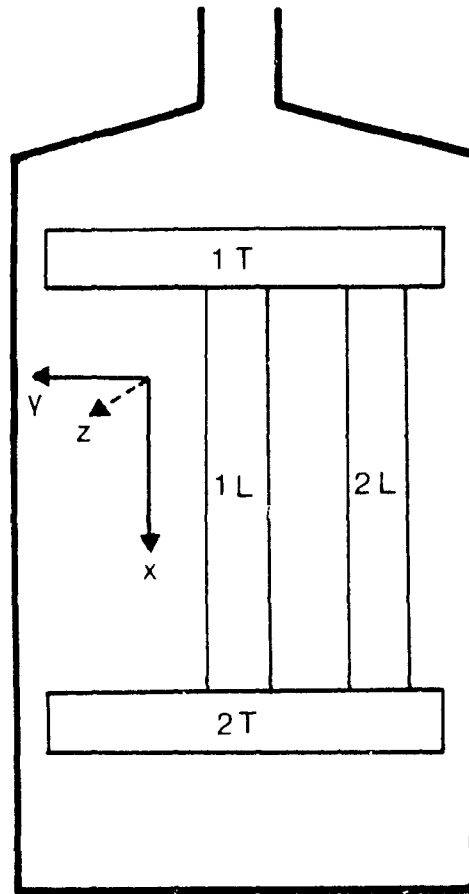


FIGURE 4.10: Assigned locations of rectangular test bars for microstructural analysis.

along the thickness of the samples using an Instron Tensometer. These samples were stored in a desiccator prior to the experiments.

(c) Polishing Technique

Sample preparation is important in Microhardness measurements, and great care must be taken to ensure that the hardness recorded is representative of the microstructure under study. Careful attention must be given to: a) edge effects, b) the method of specimen mounting, c) the problem of illumination and viewing, and d) possible interactions.

The rectangular test bars cut from the injection molded plaques, shown in Figure 4.10, were employed to measure the microhardness distribution in the X-Z plane. These bars were mounted on the polishing jig shown in Figure 4.11, to prepare the sample surface for testing, over the X-Z plane across the thickness of the rectangular bar. The bevel or groove at the top of the polishing jig reduces the compressive stresses present at the top surface. Polishing of the samples was carried out in the polishing jig starting with 400 emery sand paper and finishing with 1 μm alumina paste. The jig containing the polished sample was placed on the sample holder of the Tukon microhardness tester so that the long diagonal of the indentations made in the plastic was aligned parallel to the flow direction (X-direction).

(d) Fracture surface preparation

Rectangular bars (1L) and (1T), obtained as displayed in Figure 4.10,

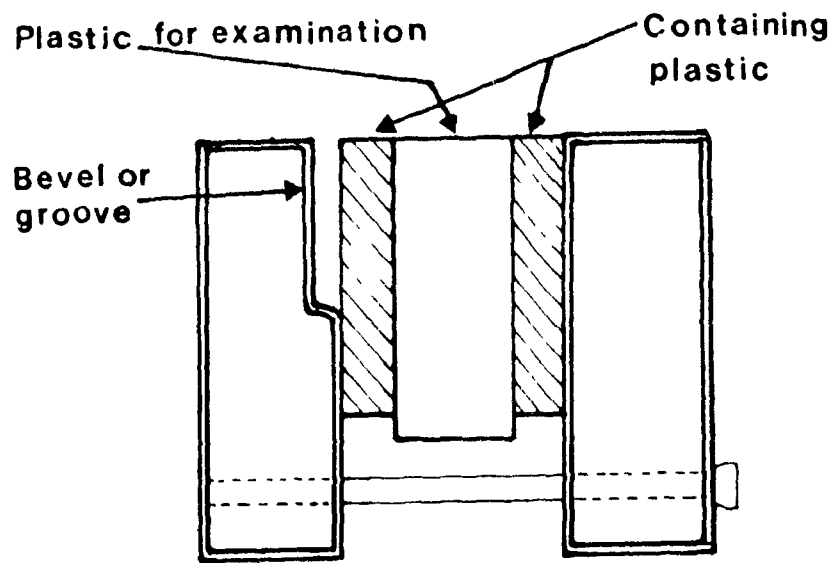


FIGURE 4.11: The jig used for polishing the samples and measuring the microhardness.

were immersed in liquid nitrogen for a period of about 5 minutes, in order to freeze the structure and obtain brittle fracture. Subsequently, the rectangular bars were broken in the middle. Fractured surfaces were obtained in the Y-Z plane for the sample 1L and in the X-Z plane for the sample 1T. Broken pieces were cut from the other side to reduce the length of the sample, which was then glued on small copper cylinders along the side opposite to the fractured surface. The fractured surface was metallized by a Polaron sputtering apparatus with gold-palladium alloy, to enhance the viewing of the sample microstructure by Scanning Electron Microscopy (SEM).

(e) Layer Removal Technique

A layer removal technique was used by milling away $100\mu\text{m}$ from both sides (X-Y plane) of the rectangular samples, as indicated in Figure 4.12, using a fly type cutter in a milling machine. The milling operation was done carefully so as not to generate excessive heat that would affect the original morphology. The layer removal operation was repeated after performing the three point bending test on the newly reduced sample thickness. The measurement of the bulk flexural modulus was obtained in this manner for the samples with different thicknesses

4.8.4.2 Photomicrography

A Reichert Zetopan-Pol Polarization Microscope was used to carry out the optical photomicrography. The microscope was equipped with a large circular rotating stage, a polarization body fitted with a Bertrand lens and an iris diaphragm,

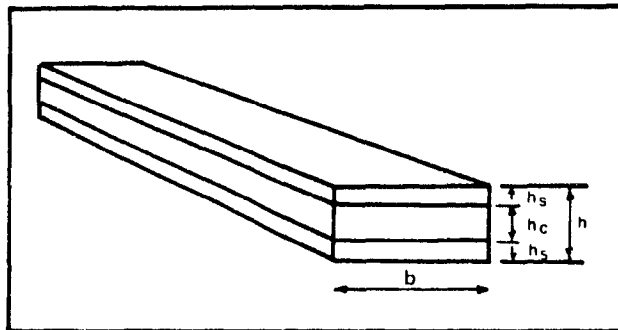


FIGURE 4.12: Layer removal technique for flexural modulus measurements.

a filter analyzer (which could be rotated 360°), transmitted light and incident light objectives mounted in a slide, and a transmitted light filter polarizer which could be rotated 360° in increments of 5° . The magnification capability is from 45 to 630 times the original area.

Since each of the polarizing plates, polarizer and analyzer has the property that only a specific component of polarization of the incident beam can penetrate the plate, then, if the polarization directions of the two polarizing plates are set at 90° to each other, there will be no light passing through the two plates in the absence of a sample. If an anisotropic substance is placed between the two polarizing plates and rotated, a position of maximum darkness (extinction) is observed. A position of maximum brightness is obtained by rotating 45° from extinction. In this work, Polaroid photographs were taken at maximum brightness for microstructure evaluation. Specimens microtomed in the X-Z plane approximately 5 microns thick each, were used. The procedure described above was used to visualize the morphology developed during the injection molding process. The opacity of the liquid crystal copolymer under study rendered the observation very difficult. This was complicated by the need to obtain very thin slices. The microtomed sections curled easily and it was difficult to uncurl the specimens without damage.

4.8.4.3 Electron Microscopy (SEM)

A Jeol JSM-T300 Scanning Electron Microscope (SEM) was used to view the fractured surfaces in the X-Z and Y-Z planes at various magnifications. Polaroid photographs were obtained across the thickness of the molded samples.

4.8.4.4 Density Gradient Column

The densities of the samples were determined using a glass density gradient column built according to the ASTM standard procedure D-1505-68 (86). This method is based on observing the level to which a test specimen settles in a liquid density gradient column, which also contains standards of known density. The column employed a mixture of tetrachloromethylene and xylene. The experimental arrangement is shown in Figure 4.13.

A number of colored calibration glass floats of known density were lowered into the column at 1 cm/min. The floats left the basket one by one as the proper density level was reached. The density gradient was represented by the eight colored floats ranging from 1.15 to 1.5 g/cm³. The calibration curve was linear, as shown in Figure 4.14.

In order to study the density distribution in injection molded liquid crystalline polymer moldings, sections were microtomed in the X-Y plane from the surface to the center of the test pieces, as described in section 4.8.4.1. To determine the density of the microtomed layers, the specimens were placed in the column and were allowed to settle to an equilibrium level. After twelve hours, the relative heights of each specimen, along with the heights of the floats immediately above and below it, were measured using a cathetometer. The density of the specimen was calculated by linear interpolation through the relation:

$$\rho_s = \rho_a + (\rho_b - \rho_a) (h_s - h_a) / (h_b - h_a) \quad (4.17)$$

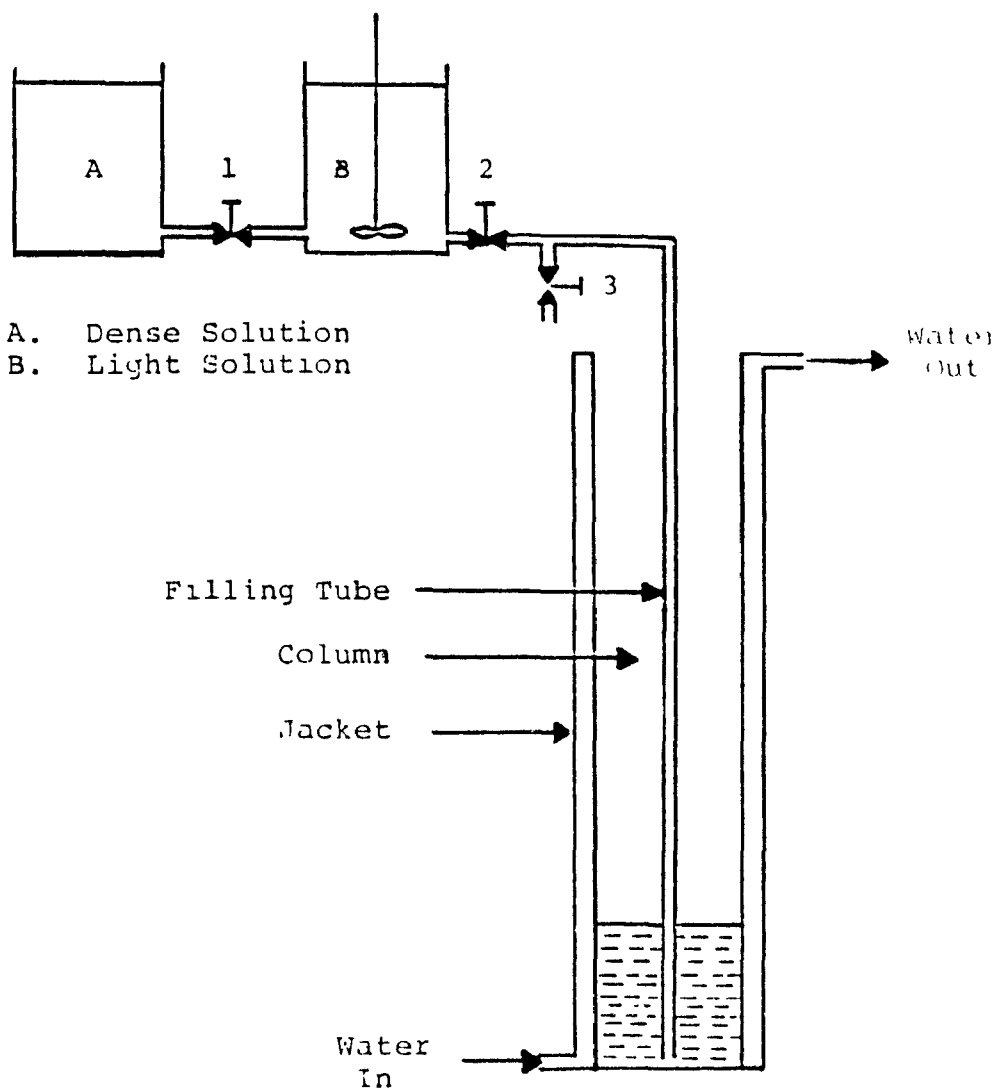


FIGURE 4.13: Apparatus Set-Up for Density Determination

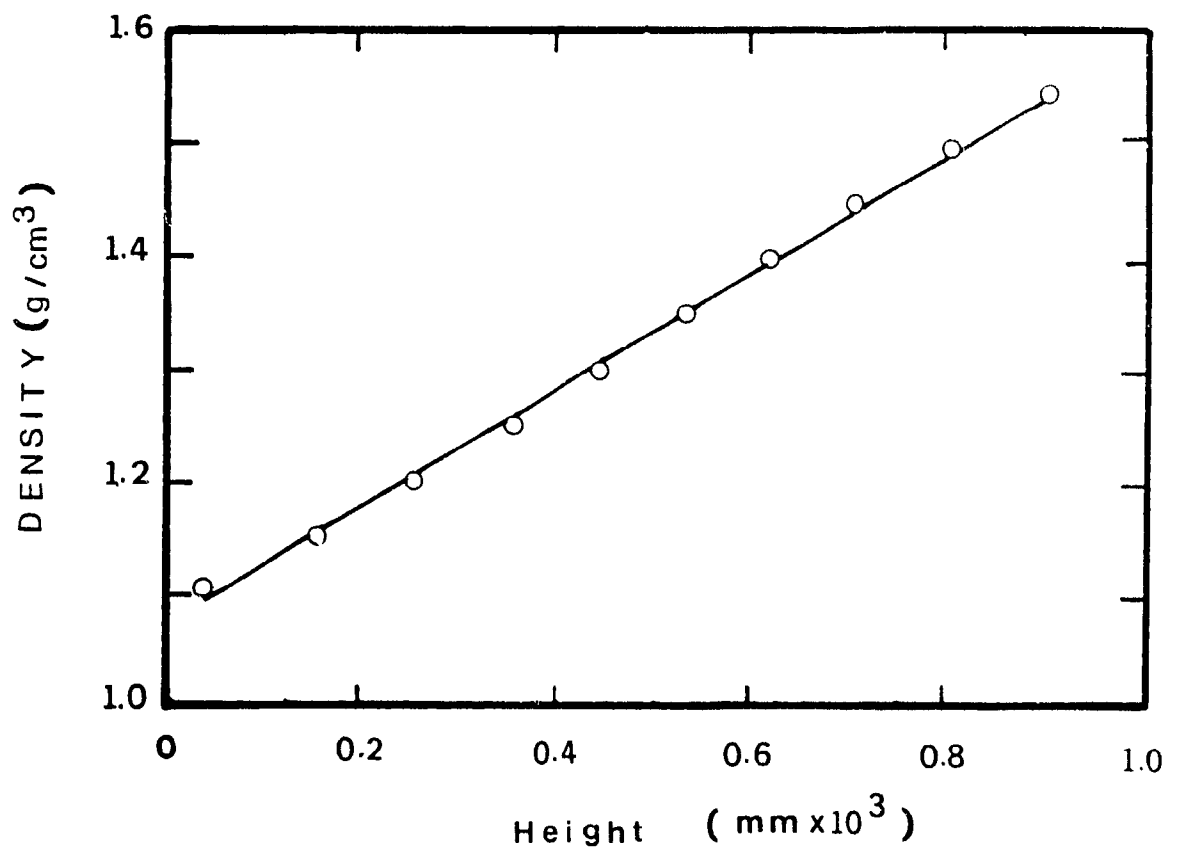


FIGURE 4.14: Calibration curve for density gradient column

Where ρ = Density
s = Specimen
a = Float immediately above the specimen
b = Float immediately below the specimen
h = Height as measured by cathetometer

4.8.4.5 Wide-Angle X-Ray Diffraction

The x-ray diffraction apparatus used in this study was described in section 4.6.2.1. To examine the orientation distribution using x-ray diffraction, microtomed samples were prepared as explained in section 4.8.4.1. Each sample was exposed for two hours. Pinhole photographs were obtained for the microtomed samples, across the thickness, from the surface to the center region of the molded plaque.

4.8.4.6 Infrared Spectroscopy

The 16 odd microtomed specimens obtained as explained in section 4.8.4.1, were used to evaluate the molecular orientation. The specimens were placed in sample holders made to fit perfectly in the proper location of the infrared apparatus. Particular attention was paid to identify the direction of alignment of the microtomed specimens. The reference direction was taken to be the flow direction (X-direction). A Bomem Michelson-100, Type TM, Spectrometer in conjunction with a Perkin-Elmer Wire-Grid Polarizer was used to obtain linearly polarized absorption spectra parallel to the flow direction. The polarized absorption spectra obtained for the region of 600 to 1000 cm^{-1} permitted calculation of the dichroic ratio as explained earlier (see section 4.6.2.2). The 780 band, which represents the group-

CH out-of-plane was used for this purpose.

Two spectra were acquired for each microtomed layer, one spectrum was obtained with the sample reference direction parallel to the polarization direction and the other spectrum with the sample reference direction perpendicular to the polarization direction. The peak height absorbance values were used in this study to calculate the dichroic ratios for each absorption band (See Figure 4.4). The resulting Hermans orientation functions were plotted as a function of distance from the surface to the center core of the sample across the thickness.

4.8.4.7 Microhardness Testing

Microhardness measurements were performed with a "MO" Tukon Microhardness Tester. A Knoop rhombic-based pyramidal diamond was used to make indentations (Figure A.13.4). A micrometer microscope eyepiece was used to measure the dimensions of the indentations, within $\pm 0.5\mu\text{m}$, after load removal. A Bausch and Lomb Microscope tube was fitted with a triple revolving nosepiece carrying three Balcoated and par-focaled objective lenses; 16 mm., 0.25 N.A., 14X; 10.25 mm., 0.40 N.A., 22X; and 4 mm., 0.85 N.A., 60X. The experimental procedure for carrying out the microhardness testing is described below (see also Figure A.13.3):

- (i) The dash-pot oil must be at room temperature before starting.
- (ii) The needle valve should be adjusted so that the piston reaches the dash pot cap in 30 seconds.
- (iii) The indenter descends at a rate of 1 mm/min, after turning

crank H.

- (iv) The telltale light goes out after 5-7 seconds.
- (v) The indenter contacts the specimen approximately 15 seconds after the start of the test.
- (vi) The indenter remains in contact for a standard time of approximately 15 seconds.
- (vii) The indenter is mechanically pick-off the specimen by action of yoke D.
- (viii) When telltale light relights, the test is complete and the indenter is removed from the indentation.
- (ix) The microton can now be placed under the microscope for measurement of the indentation.

The Knoop hardness number, HK, is computed from the following equation:

$$HK = P_L / A_p = P_L / d^2 c_1 = P_L / 0.07028 d^2 \quad (4.17)$$

$$HK = 14.229 P_L / d^2 \quad (4.18)$$

where:

P_L = Load, kgf,

A_p = Projected area of indentation, mm²,

d = Length of long diagonal, mm,

c_1 = Indenter constant relating projected area of the indentation to the square of the length of the long diagonal.

Since the units normally used are grams-force and micrometers, the Knoop hardness number can be expressed conveniently as:

$$HK = 14229 P_V / d^2 \quad (4.19)$$

Sample preparation is important in microhardness testing, and great care must be taken to ensure that the hardness recorded is representative of the material and microstructure. Consideration is given to (a) possible edge effects, (b) the method of specimen mounting, (c) the problem of illumination and viewing, and (d) possible interactions.

The rectangular bars cut from the injection molded plaques, as indicated in Figure 4.10, were used to measure the microhardness. The jig containing the polished sample was placed on the sample holder of the Tukon microhardness tester, so that the indentations in the plastic were made with the long diagonal aligned parallel to the machine direction. Several indentations (every 150 μm) were then be made along the 3.2 mm thick sample, from the surface to the central region of the sample using a 10 g load. The measurements were made at three different positions along the rectangular bar, in the X-Z plane. The readings from the eyepiece were expressed in Filar units, which were converted to μm by multiplying the objective factor obtained from the calibration of the microscope objectives for each lens given in Table 4.4. The calibration was carried out using a stage micrometer, graduated in 0.1 mm., which had been calibrated by the National Bureau of Standards. In this study, the 10.25 mm microscope objective was used for measuring the length of the long diagonal by the indenter after removal of the load. A standard stainless steel sample was first used to calibrate the indentation size and reproducibility. The indentation size should correspond to the value reported on the standard sample specification (Figure A.13.4).

TABLE 4.4: CALIBRATION OF MICROSCOPE OBJECTIVES

LENS	OBJECTIVE FACTOR
4.00 mm	0.1667
10.25 mm	0.4583
16.00 mm	0.7106

4.8.4.8 Flexural Properties

The flexural modulus was measured according to ASTM D-790, using the three point bending test on a rectangular bar obtained from the molded plaque, as shown in Figure 4.10. The dimensions of the bars were 5.8 cm long, 1.2 cm wide and 0.32 cm thick. The Instron Universal Tester was used to carry out the experiments at a constant crosshead speed of 0.5 mm/min. All the flexural experiments were carried out at 23°C. The deflection of the rectangular bars was kept as low as possible to avoid irreversible damage in the material, thus allowing the same test-bars to be subsequently utilized for making other measurements (max. strain = .3). A test of reversibility was conducted for each test-piece by turning it over and carrying out the bending test again. The average of both measurements was used to calculate the flexural modulus.

The initial slope of the load-deflection test record was used to calculate the flexural modulus E_f as follows:

$$E_f = \frac{1}{4} \left(\frac{F}{Y} \right) \frac{S_p^3}{b h^3} \quad (4.20)$$

Where (F/Y) is the initial slope of the load-deflection record, S_p is the support span (50 mm), and b and h are the width and the thickness of the test piece, respectively.

The strain varies linearly across the sample thickness, being maximum at the surface and decreasing towards zero at the neutral axis. Thus, with the three point

bending test, the skin layer contributes the most to the flexural modulus value. A layer removal technique (see section 4.8.4.1) was used to obtain the distribution of the bulk flexural modulus in this manner along the thickness of the rectangular sample.

Using the rule of mixtures for a sandwich material (87), the tensile modulus for the whole material, E_t , is given by the formula:

$$E_t = E_c \varphi + E_s (1 - \varphi) \quad (4.21)$$

where $\varphi = h_c/h$, with h and h_c are the thicknesses of the beam and the core, respectively; E_s and E_c are the Young's moduli for the skin and core layers, respectively. The above implies that the skin and core contribute to the tensile stiffness in proportion to their thicknesses.

The effective flexural modulus E_f of the sandwich beam is then calculated (87) by assuming that classical bending theory is applicable to the sandwich beam (See Appendix A.13.2):

$$E_f = E_c \varphi^3 + E_s (1 - \varphi^3) \quad (4.22)$$

CHAPTER 5

5. RESULTS AND DISCUSSION

In this chapter, we present and discuss the experimental results obtained in the study. Initially, the data relating to the processing behavior of the material under various processing conditions are summarized and explained. Subsequently, data regarding the microstructure and the properties of the injection molded articles are analyzed. The data include results obtained with optical microscopy, scanning electron microscopy, infrared spectroscopy, x-ray diffraction, microhardness and flexural testing. The data are given in subsequent appendices. Finally, an effort is made to integrate the various results in light of some theoretical considerations.

5.1 Thermal Properties

5.1.1. Specific Heat

Figure 5.1 shows the variation of specific heat, C_p , as a function of temperature. The DSC trace shows a second order transition at about 90°C, which corresponds to the glass transition temperature T_g . Values of C_p reported by Cao and Wunderlich (88) for two different HBA/HNA compositions are also plotted in the same figure for comparison. It is seen that, below the solid-to-nematic melt transition, the values of C_p are in good agreement with those obtained by Cao and

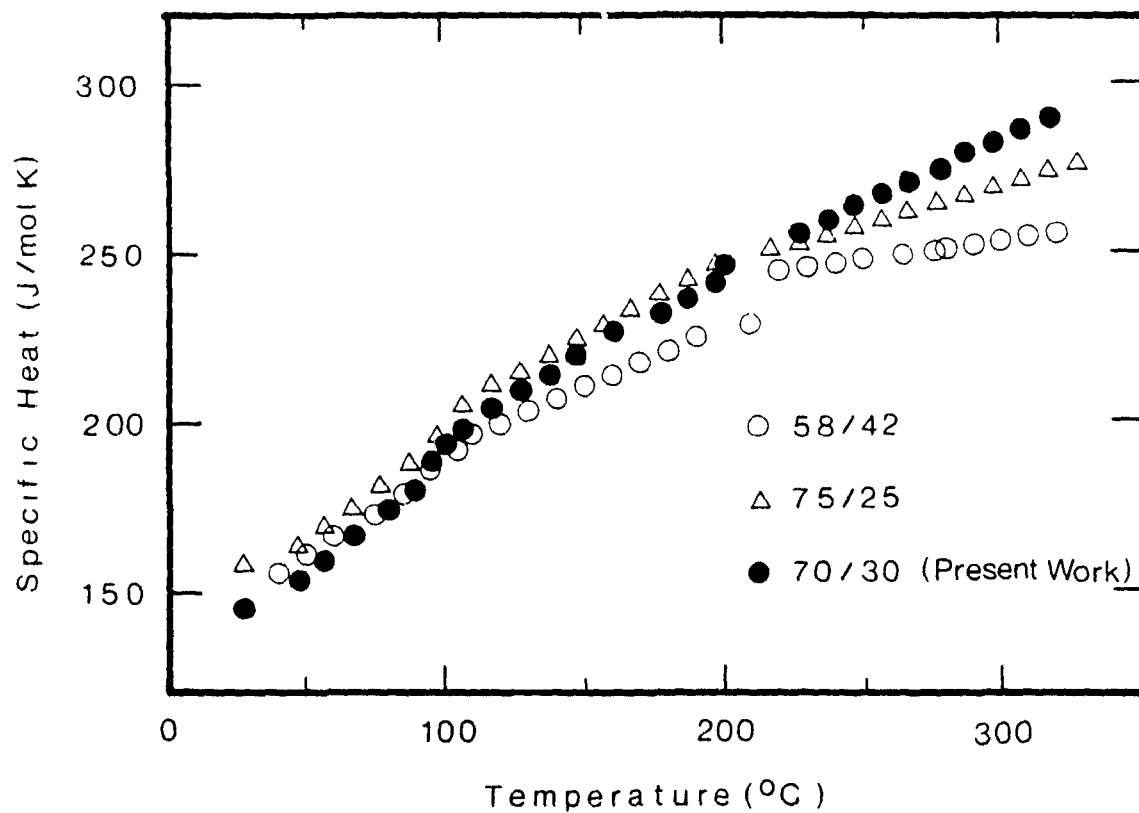


FIGURE 5.1: Variation of specific heat as a function of temperature for different HBA/HNA compositions 58/42 and 75/25 reported by Cao and Wunderlich (88), 70/30 present study.

Wunderlich (88). However, in the solid-to-nematic melt transition range, the values of C_p obtained in the present work are slightly higher than those reported previously (88). These differences may be due to the different thermo-mechanical history of the melt extruded pellets used in the present work. The rise in the magnitude of specific heat, ΔC_p , at the glass transition temperature, T_g , is found to be equal to about (28 ± 2) [J/(mol.K)], which is in agreement with theoretically estimated values of ΔC_p by Cao and Wunderlich (88).

5.1.2 Thermal Conductivity and Diffusivity

Thermal conductivity k and diffusivity α of the copolymer were measured over a wide range of temperatures, using compression molded samples of 5 cm diameter and 1.6 mm thickness. Figures 5.2 and 5.3 show the variation of thermal conductivity and diffusivity as a function of temperature. It is seen from Figures 5.2 and 5.3 that the values of k and α first increase as the temperature is raised from room temperature to about 90°C, which corresponds to the glass transition temperature, T_g , and then decrease slightly between T_g (90°C) and 120°C. This behavior may be due to the increased free volume and segmental mobility of molecules in the glass transition region. A slight increase in values of k and α is observed between 120°C and the solid-to-nematic melt transition temperature (280°C), which may be due to more ordered structures formed by annealing of the samples (kept for about 1 hour to achieve equilibrium) in this range of temperatures. Since more ordered portions conduct energy better than amorphous phases (89), the effect of annealing will tend to increase values of k and α . Above the solid-to-nematic melt transition temperature, a slight drop in values of k and

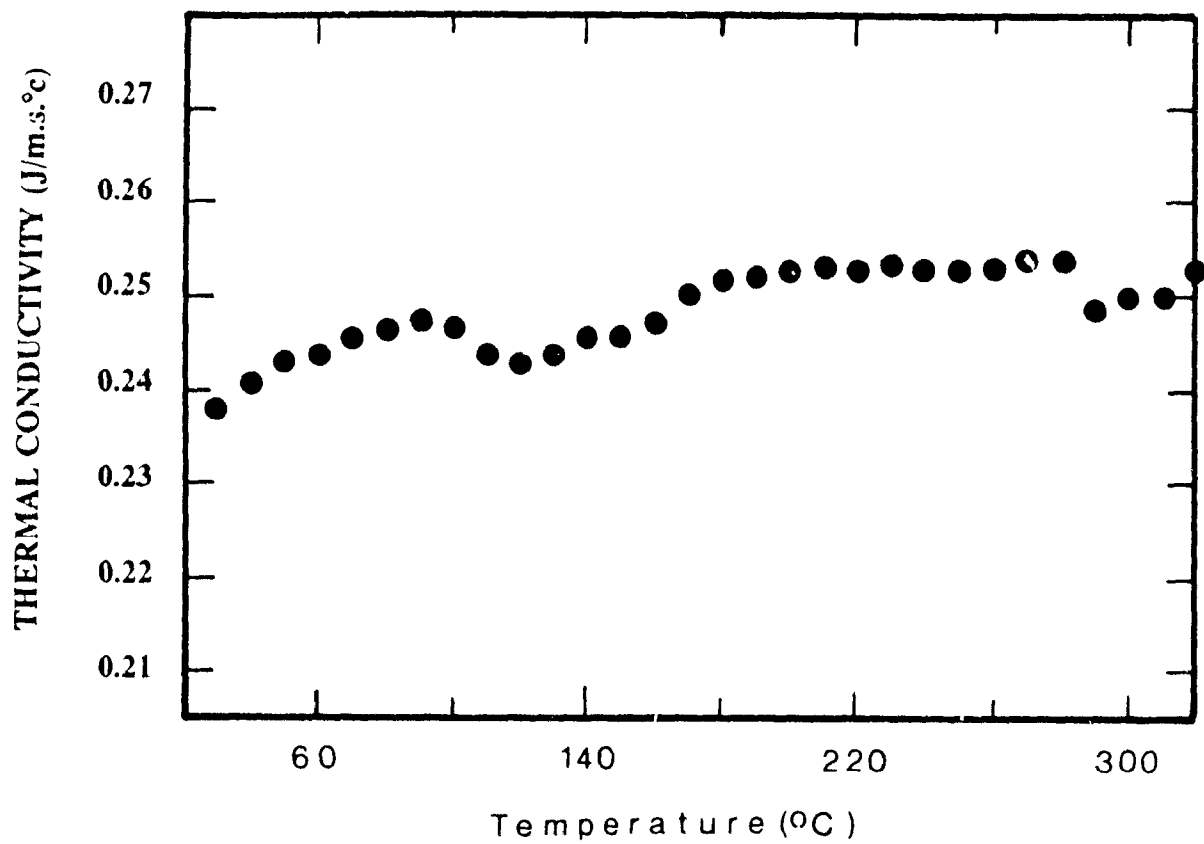


FIGURE 5.2: Variation of thermal conductivity as a function of temperature.

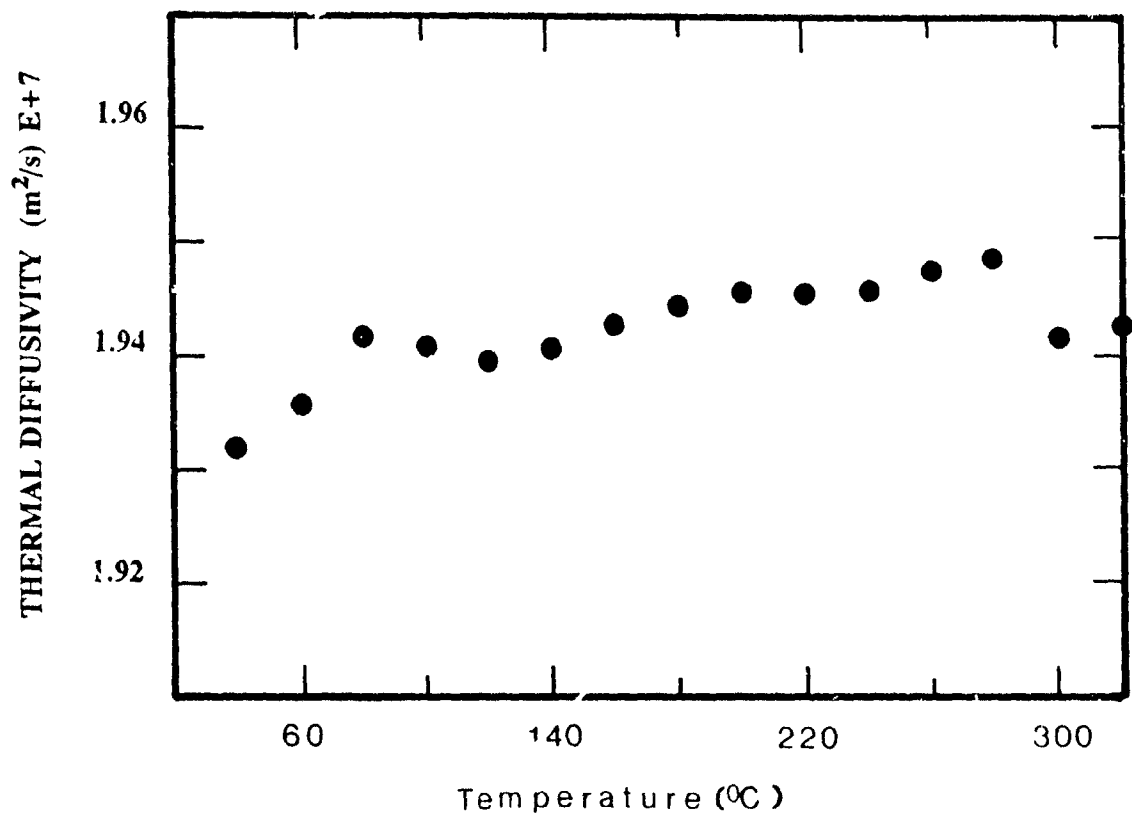


FIGURE 5.3: Thermal diffusivity variation as a function of temperature.

α is observed which may be because of the loss of ordered regions. It is interesting to note that the thermal conductivity and diffusivity plots as a function of temperature give a sharper indication of both T_g and T_m , in comparison with transitions obtained with the DSC.

5.2. P-V-T Diagram

The variation of density with temperature and pressure for the liquid crystalline polymer resin, designated as LCP2000 is shown in Figure 5.4. The results show that the density increases approximately linearly with increasing pressure. It should be pointed out that the P-V-T data given here are approximate and do not reflect thermodynamic equilibrium properties due to the nature of the measurement.

5.3 Melting and crystallization behavior

Figure 5.5 shows three typical thermograms for the liquid crystal copolymer (70% HBA/30% HNA) employed in the present study. The melting curve from room temperature to 320°C at a scanning rate of 20°C/min is shown as DSC trace (a) in Figure 5.5 for the sample sliced from the skin layer of the as-received melt extruded pellet. This DSC trace shows a second order transition (glass transition) temperature, T_g , at about 90°C. Twenty traces were obtained using skin layers from different pellets, which showed a value of T_g within ± 4 °C. The value of T_g reported by Cao and Wunderlich (88) varied from 104°C to 152°C for different HBA/HNA compositions. However, no certain relationship was observed between T_g and copolymer composition.

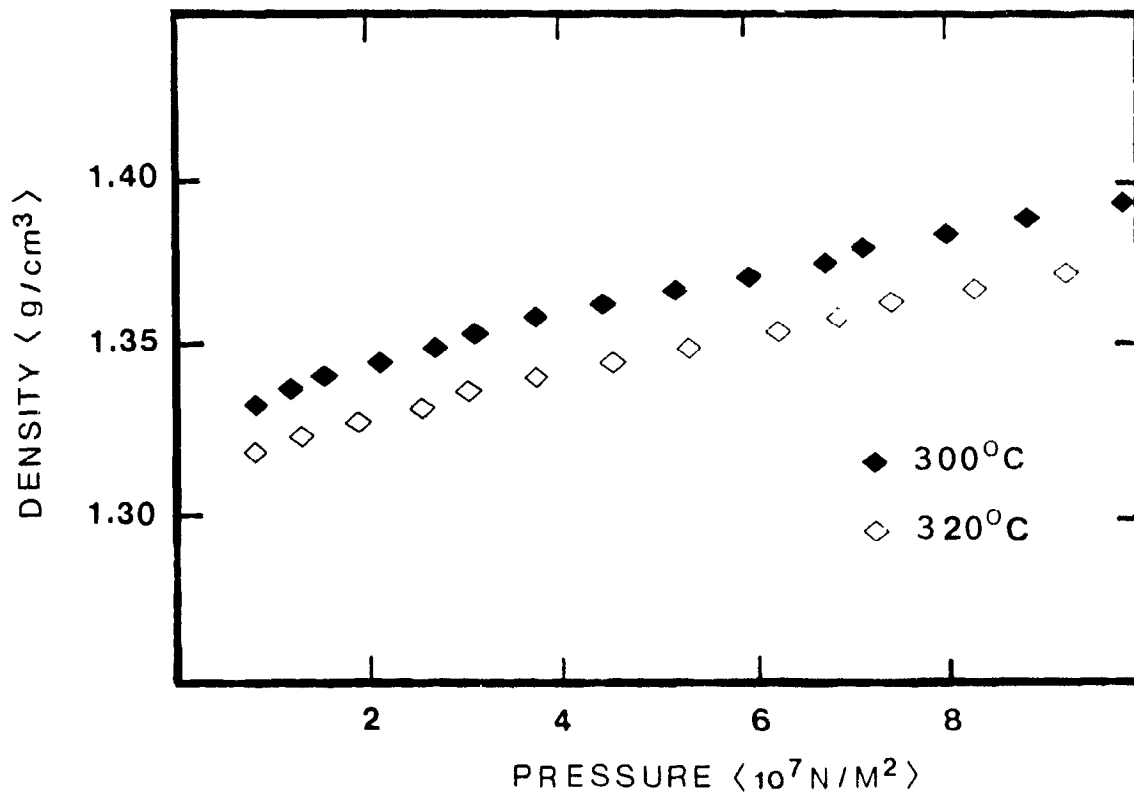


FIGURE 5.4: Pressure-Volume-Temperature (P-V-T) Diagram.

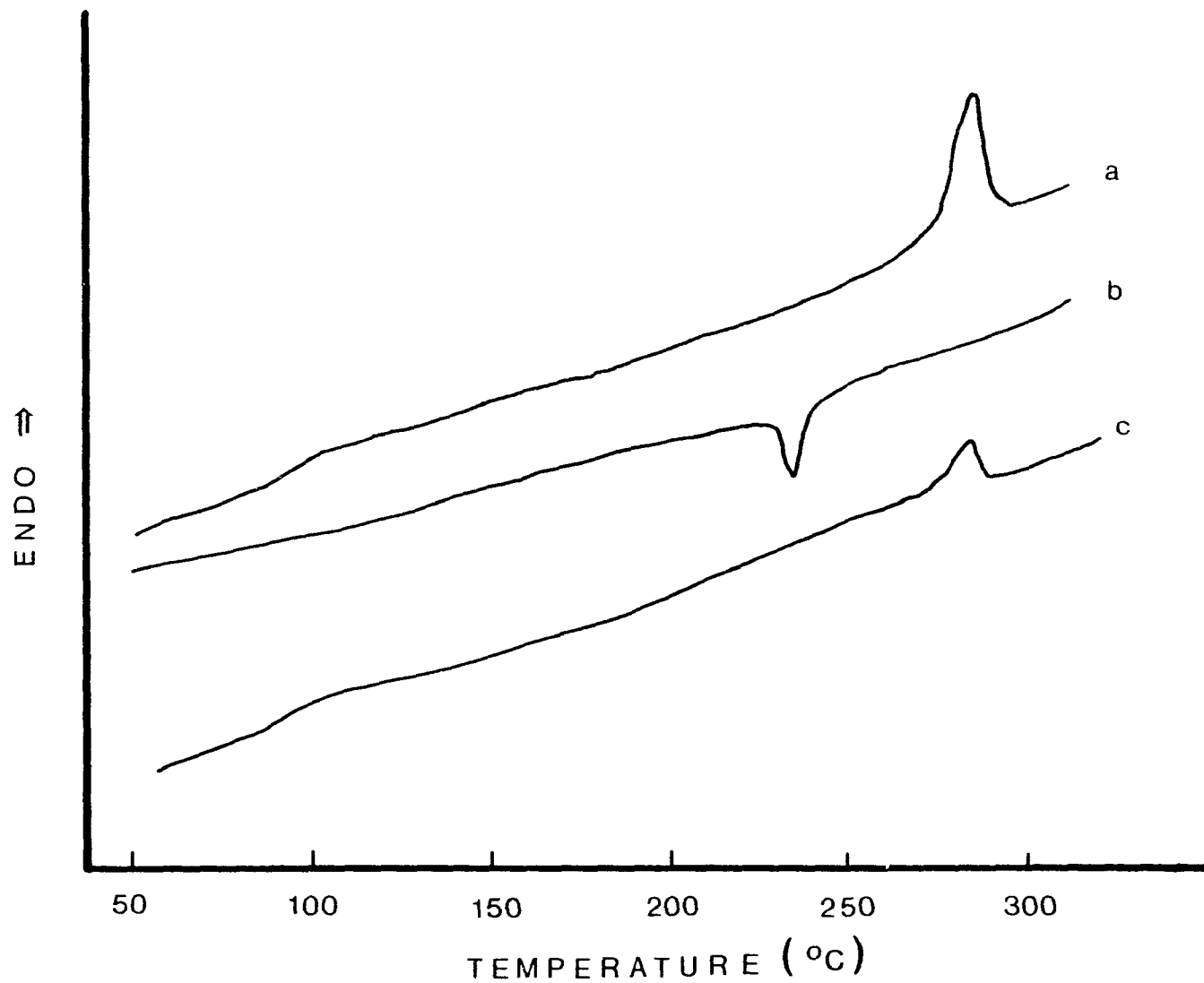


FIGURE 5.5: DSC melting and crystallization behavior: Trace a, as-received pellet; Trace b, cooling at 20 deg/min. from the nematic melt; Trace c, remelting of the sample previously cooled at 20 deg/min.

Trace (a) in Figure 5.5 shows that an endothermic peak appears at about 275°C which corresponds to the solid crystalline-to-nematic melt transition. In some samples, multiple melting peaks were observed in the solid crystalline-to-nematic melt transition range. The same sample was then kept for 10 min. in the nematic melt state at 320°C. Upon cooling at the same scanning rate as that used for heating, an exothermic peak is observed at about 50°C below the solid crystalline-to-nematic melt transition temperature, as shown by DSC trace (b) in Figure 5.5. On remelting the same sample (trace (c) in Figure 5.5), the glass transition as well as the solid-to-nematic melt transition occur again at about the same temperatures as observed for the as-received pellets. However, the heat of transition (area under the endothermic peak) of the remelted sample is about one third of that obtained for the as-received pellet. This is probably due to the effect of stress-induced crystallization obtained during the manufacturing of the melt extruded pellets.

5.3.1 Effect of cooling rates on melting behavior

Various non-isothermally crystallized samples were prepared by cooling the copolymer from the nematic melt state to room temperature using a wide range of scanning rates (0.1 to 102.4°C/min). These samples were remelted at a scanning rate of 10°C/min. Figure 5.6 shows the thermograms of the remelted samples prepared at different cooling rates. It is observed that the sample quenched in liquid nitrogen shows a very small heat of transition. The samples cooled at scanning rates ranging from 3.2 to 102.4°C/min show single peaks with an appreciable amount of heat of transition ΔH_m . There is no significant difference in

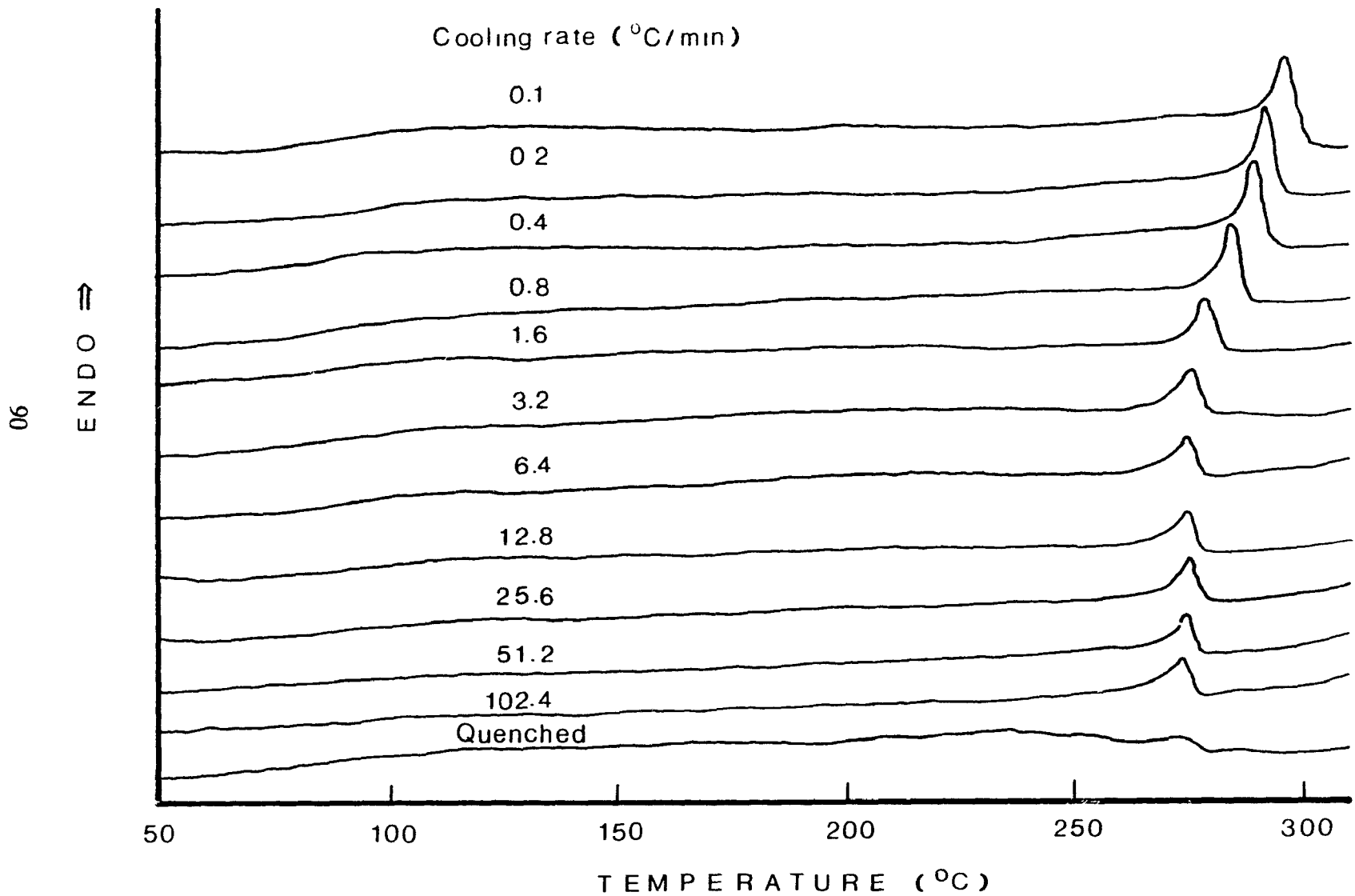


FIGURE 5.6: DSC melting thermograms of samples crystallized nonisothermally using a wide range of cooling rates.

the values of ΔH_{n} and the transition temperatures T_{n} measured in this range of cooling rates. This observation indicates that a fast crystallization process occurred at cooling rates above $3.2^{\circ}\text{C}/\text{min}$. At cooling rates below $3.2^{\circ}\text{C}/\text{min}$, a steady increase in the heat and temperature of transition is observed. This is shown in Figures 5.7 and 5.8, respectively. The steady increase in the heat and temperature of transition at lower cooling rates indicates that a secondary slow crystallization process occurs in the samples which are allowed to crystallize for longer times. A similar two-step crystallization process was observed by Butzbach et al. (32), although they employed a different experimental procedure with annealed samples at various temperatures and times.

The data shown in Figures 5.7 and 5.8 and a procedure similar to that employed by Liberti and Wunderlich (90) were used to estimate the temperature (T°_{n}) and the heat of transition ($\Delta H^{\circ}_{\text{n}}$) for the samples crystallized at zero-cooling-rate. The calculated values were 300.5°C and 13.59 J/g , respectively. The value of $\Delta H^{\circ}_{\text{n}}$ obtained from wide-angle x-ray diffraction by Butzbach et al. (91) for HBA/HNA composition of 58/42 was 12.91 J/g , which is in reasonable agreement with the above value. The entropy of transition to the nematic melt was calculated from the relationship,

$$\Delta S_{\text{n}} = \Delta H^{\circ}_{\text{n}} / T^{\circ}_{\text{n}} \quad (5.1)$$

and it was found to be equal to $3.2 \text{ J}/(\text{mol.K})$, which is again in agreement with the value of $3.19 \text{ J}/(\text{mol.K})$ reported previously (91).

The surface free energy for the copolymer employed in the present

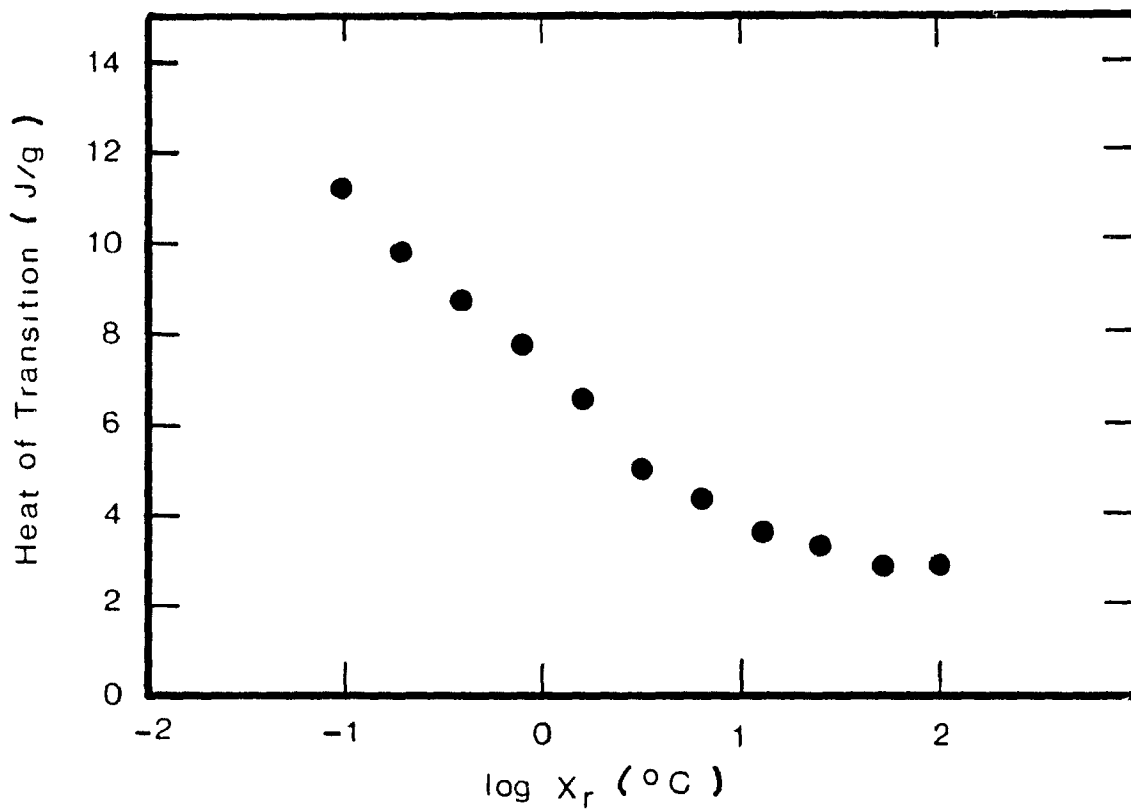


FIGURE 5.7: Thermal history effect on samples crystallized nonisothermally. Variation of heats of transition as a function of cooling rates.

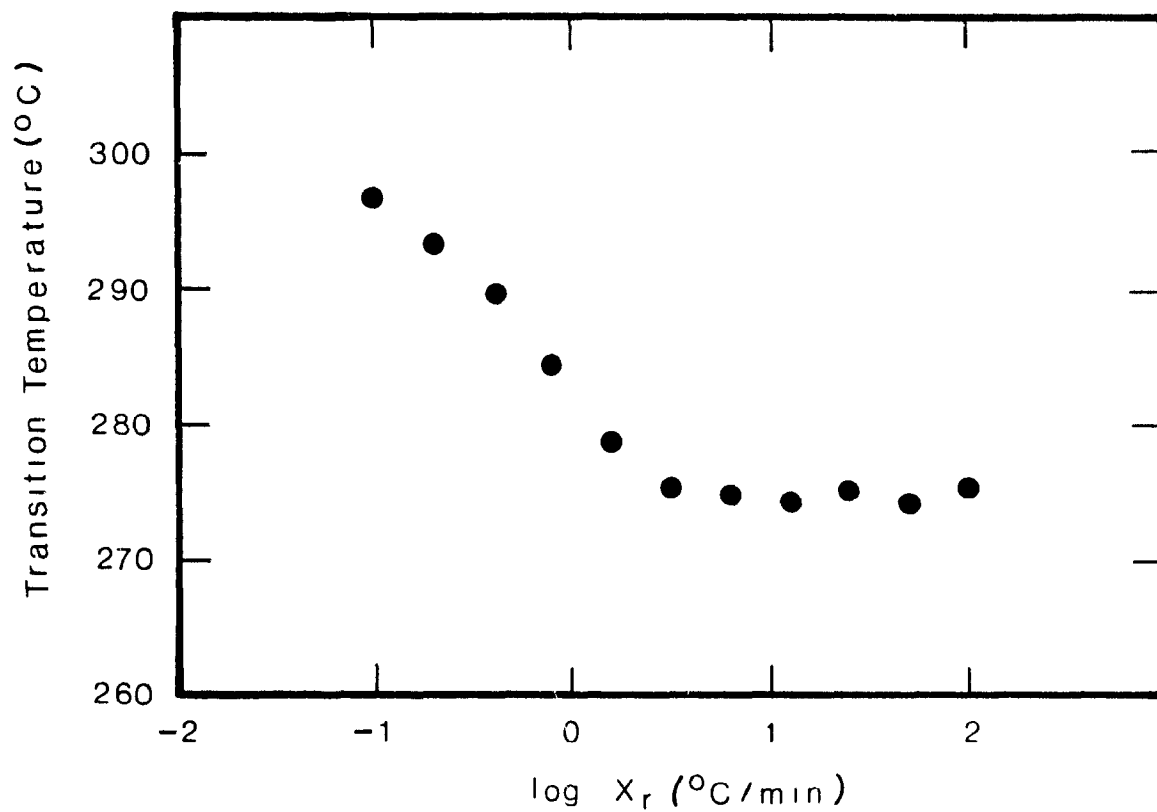


FIGURE 5.8: Thermal history effect on samples crystallized nonisothermally. Variation of temperature of transition as a function of cooling rates.

study may be calculated using the Thompson equation (92).

$$\sigma_s = \frac{\Delta H^{\circ}_m L \rho}{2} \left(\frac{T^{\circ}_m - T_m}{T^{\circ}_m} \right) \quad (5.2)$$

where σ_s is the surface free energy, T°_m and ΔH°_m , the temperature and heat of transition, respectively, of the sample crystallized at zero-cooling-rate; T_m is the observed transition temperature; L is the dimension of the ordered entities and ρ is the density. Using $L=100 \text{ \AA}$ (93), the value of σ_s was calculated to be 4.2 ergs/cm^2 . This value is reasonable considering the morphology of liquid crystal polymers which show no significant change in the general configuration of molecules as a result of melting (26).

5.3.2 Melting Behavior of Isothermally Melt Crystallized Samples

In order to study the effect of crystallization temperature and time on melting behavior, isothermally melt crystallized samples were prepared using either the crystallization temperature T_c constant and varying the crystallization time t_c or vice-versa. Figures 5.9 and 5.10 show remelting thermograms of samples which were isothermally crystallized at different temperatures (for a constant period of 15 hours) and times (at a constant temperature of 220°C), respectively. It is seen from Figures 5.9 and 5.10 that, at lower crystallization temperatures ($150^{\circ}\text{C} < T_c < 230^{\circ}\text{C}$) and times ($1 < t_c < 1200 \text{ min}$), two endothermic peaks appear in the DSC traces. Peaks shown as I in these figures seem to correspond to the crystallization associated with

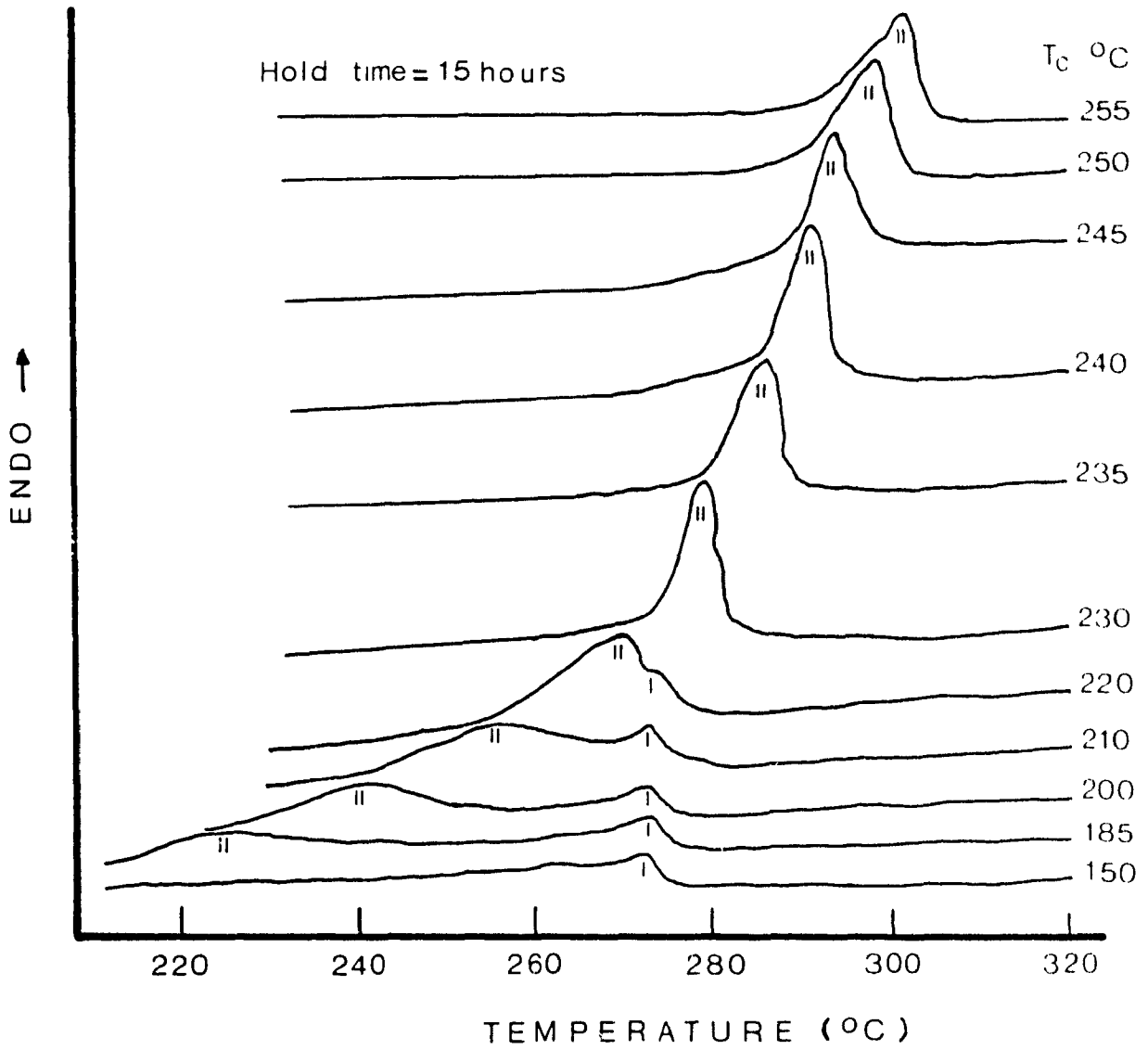


FIGURE 5.9: DSC melting thermograms of samples crystallized isothermally for 15 hours at different temperatures (T_c 's).

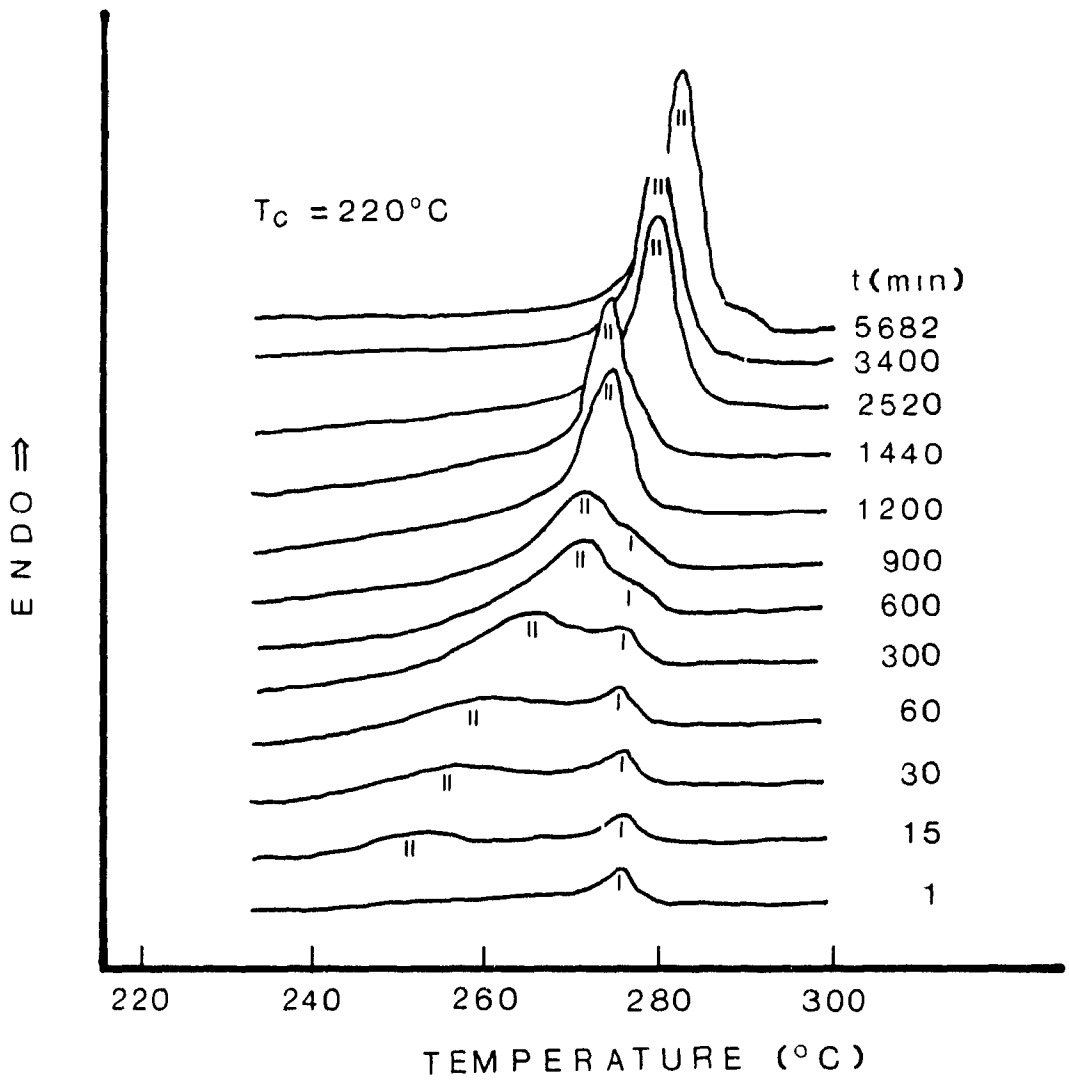


FIGURE 5.10: DSC melting thermograms of samples crystallized isothermally at 220°C for various times.

a fast crystallization process. Furthermore, it is observed that the peaks shown as I remain at the same position on the temperature axis, while peaks depicted as II show an increase in both the heat and temperature of transition with an increase in crystallization temperature or time. Peaks II seem to correspond to a slow crystallization process which leads to more ordered structures at higher crystallization temperature.

In order to determine the equilibrium melting point, T_m^* , which corresponds to the melting of perfectly crystallized samples (92), a plot of final melting temperature T_m versus crystallization temperature T_c was made, as shown in Figure 5.11. Extrapolation of the T_m versus T_c line (for peaks II) up to $T_m = T_c$ yields an equilibrium melting point of 372°C.

5.3.3 Kinetics of Crystallization

As described above, the crystallization process in the liquid crystalline copolymer used in the present work occurs in two steps: a fast crystallization process and a slow process. The kinetics of the fast crystallization process cannot be determined using the isothermal crystallization technique, since the fast process occurs in the range of the transient response of the DSC equipment. It was found from experiments conducted using an intracooler that the crystallization peak overlapped with the transient response of DSC even at cooling rates of 250°C/min. This is probably because of the instantaneous nucleation due to the high chain

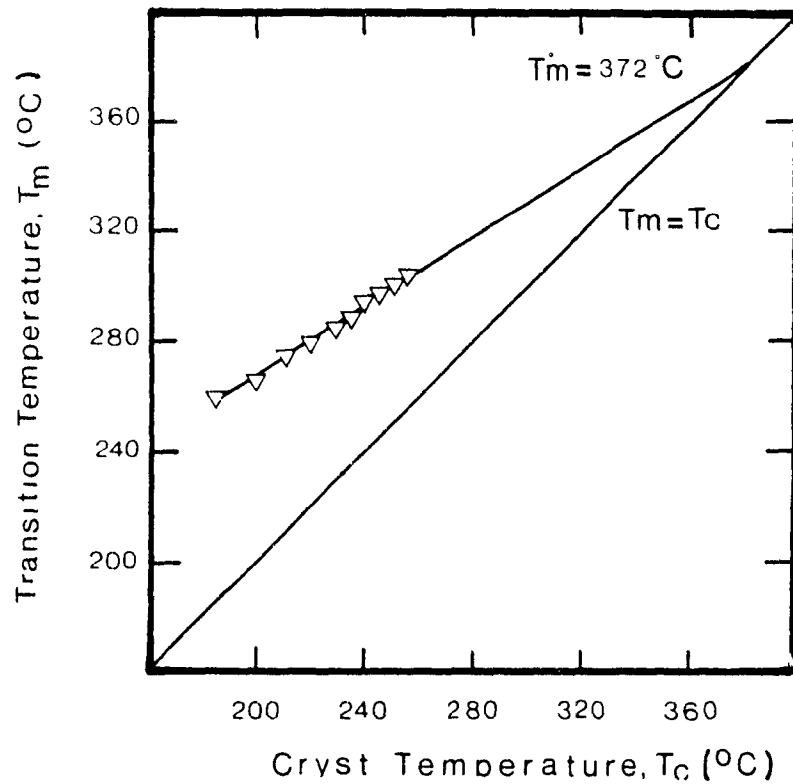


FIGURE 5.11: Plot of transition temperature (corresponding to peak II, see Fig. 5.9) as a function of crystallization temperature (T_c 's).

mobility of the low viscosity liquid crystalline copolymer (31). However, the kinetics of the fast process can be determined using a non-isothermal crystallization technique recently developed by Harnisch and Muschik (94). This technique can be used to determine the kinetics of growth of polymers crystallized from the molten state.

The isothermal crystallization technique can be used for determining the kinetics of the slow crystallization process, since the slow process can be easily monitored at different crystallization temperatures and times.

5.3.3.1 Kinetics of the fast crystallization process

The kinetics of the fast crystallization process may be described by the Avrami equation:

$$x(t) = 1 - \exp(-Kt^n) \quad (5.3)$$

Where $x(t)$ is the degree of crystallinity at time t , K is the crystallization rate constant and n is the Avrami exponent.

For polymers crystallizing from the melt under non-isothermal conditions, Equation [5.3] can be rewritten as follows (94):

$$\ln \frac{\dot{x}}{1-x} = (n-1) \cdot \ln t + \ln(nK) \quad (T=T_c) \quad (5.4)$$

where $x = dx/dt$ is the rate of crystallization. Analyzing the data, using two different cooling rates, the factor $\ln(nK)$ in Equation [5.4] can be eliminated and the Avrami exponent n can be obtained from the following equation (94):

$$n = 1 + \left[\ln \frac{\dot{x}_1}{1 - x_1} - \ln \frac{\dot{x}_2}{1 - x_2} \right] / \ln(\beta_2/\beta_1) \quad (T=T_c) \quad (5.5)$$

where β_1 and β_2 are the cooling rates, yielding crystallinity levels x_1 and x_2 , respectively.

Figure 5.12 shows exothermic peaks of samples cooled from nematic melt at three different cooling rates (4, 7 and 10°C/min). These peaks correspond to the fast crystallization process under non-isothermal conditions. The degree of crystallinity x at different temperatures can be determined from the partial areas between the onset of crystallization and different temperatures along the exothermic peak (94) as shown in Figure 5.12. The rate of crystallization $\dot{x} = dx/dt$ can be determined from the change in partial areas with respect to temperature (time) as described by Harnisch and Muschik (94).

Figure 5.13 shows the variation of $\ln[\dot{x}/(1-x)]$ with temperature T_c for three different cooling rates corresponding to the fast crystallization process. The quantity $[\dot{x}/(1-x)]$ represents the ratio of the rate of crystallization and the volume fraction of amorphous polymer in the sample. It is seen from Figure 5.13 that $\ln[\dot{x}/(1-x)]$ increases linearly as the crystallization temperature decreases. The Avrami

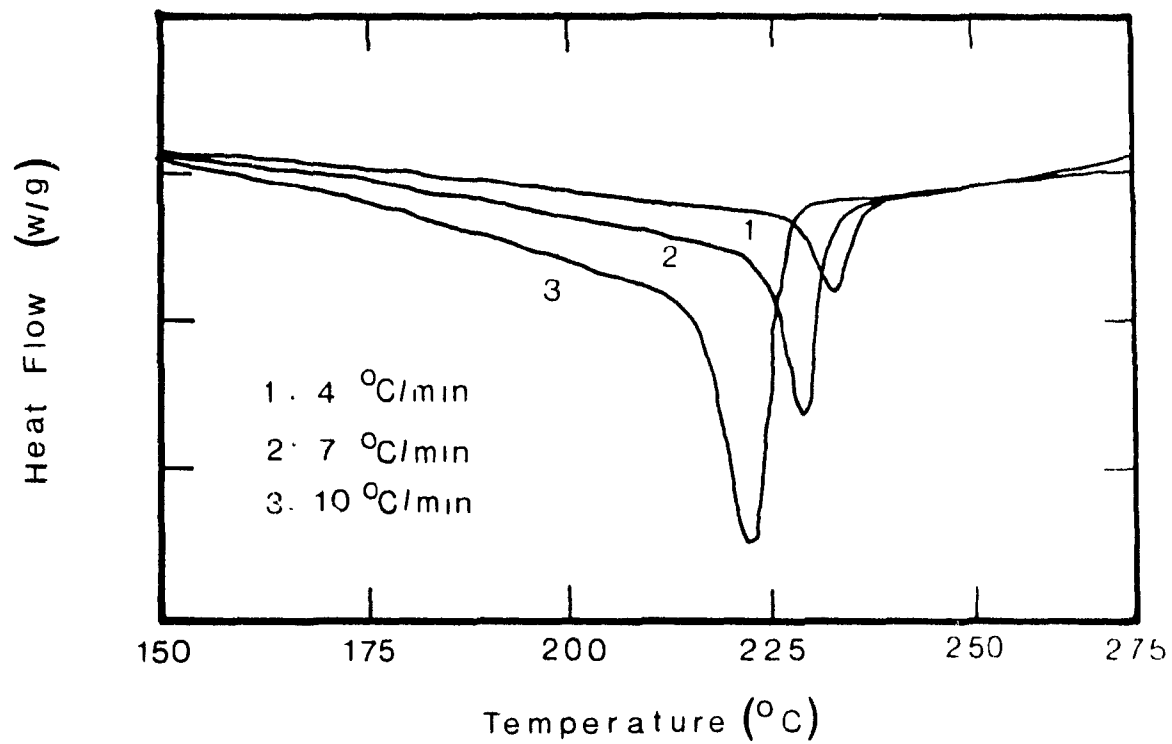


FIGURE 5.12: DSC exotherms of samples cooled from the nematic melt at 4, 7, and 10 deg/min.

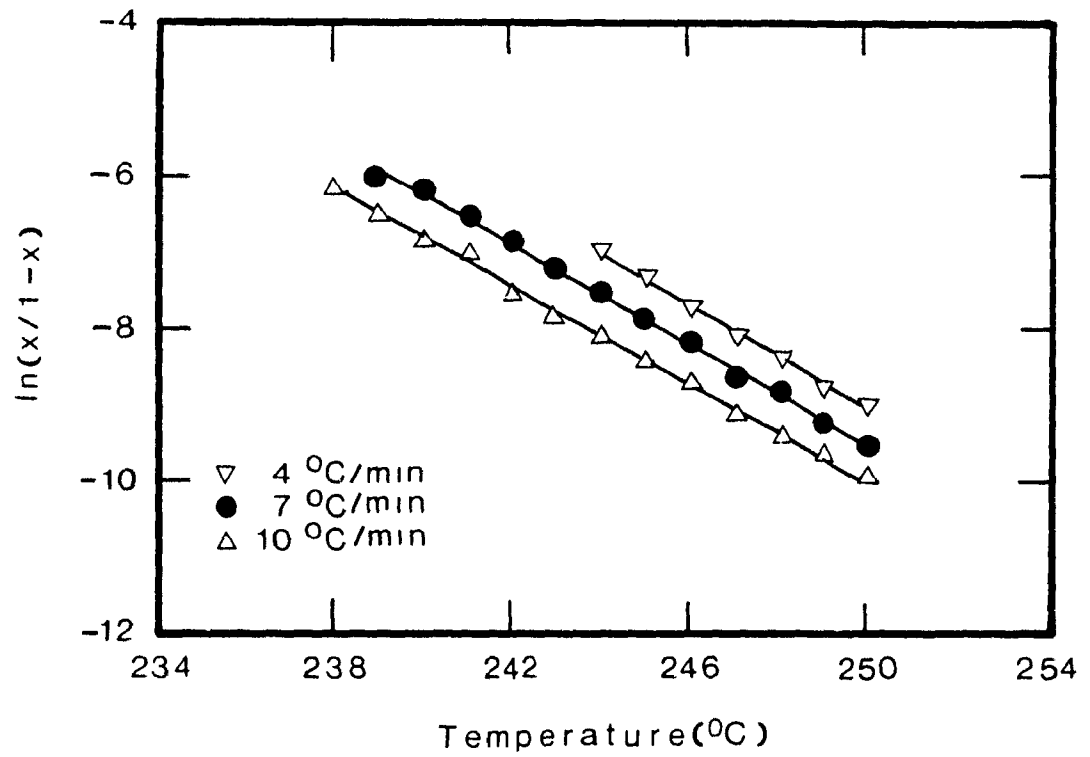


FIGURE 5.13: Plot of $\ln[\dot{x}/(1-x)]$ as a function of temperature for 3 different cooling rates (4, 7 and 10 deg/min).

exponent n for the fast crystallization process was calculated from Equation [5.5], using three different pairs of cooling rates (4 and 7, 7 and 10, and 4 and 10 °C/min) and the value of n was found to be always equal to 2 which corresponds to the rod like growth from sporadic nuclei (31). The crystallization rate coefficient K was evaluated from Equation [5.4], at different temperatures using various cooling rates.

Figure 5.14 depicts variation of $\ln(K)$ with the inverse absolute temperature. The decrease of $\ln(K)$ with $1/T$ is approximately linear, especially at high temperatures, when the fast crystallization process predominates.

5.3.3.2 Kinetics of the slow crystallization process

An isothermal crystallization method was used to study the kinetics of the slow crystallization process. Each sample was first heated up to 320°C to obtain the nematic melt, where it was held for 10 minutes. Subsequently, it was quenched at the rate of 80 °C/min to a predetermined isothermal crystallization temperature T_c . The material was allowed to crystallize isothermally for different times. The samples were then remelted at 10 °C/min to record the heat of transition which corresponds to the amount of crystallinity developed under isothermal conditions. The variation of heat of transition with respect to time can be represented as follows (32):

$$\Delta H_m(T_c, t_c) = a(T_c) \ln(t_c/t_0) \quad (5.6)$$

where $a(T_c)$ is the measure of the rate of transformation at different crystallization

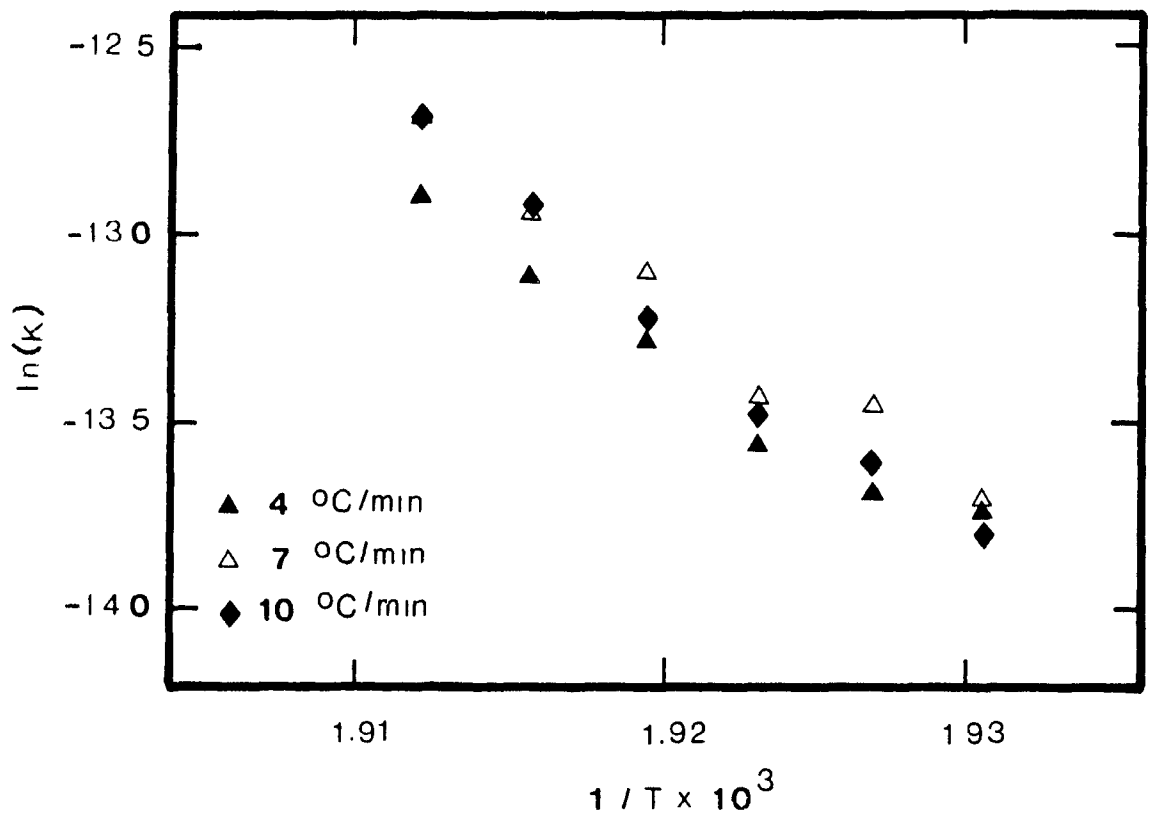


FIGURE 5.14: Arrhenius plot of $\ln(K)$ for 3 different cooling rates (4, 7 and 10 deg/min).

temperatures. Figure 5.15 shows a plot of heat of transition ΔH_m versus $\log(\text{time})$ at six different crystallization temperatures. This Figure shows that the heat of transition (degree of liquid crystallinity) varies linearly with $\log(\text{time})$. The rates of transformation can be calculated at different crystallization temperatures from the slopes of the lines plotted in Figure 5.15.

Figure 5.16 shows the variation of the logarithm of the rate of transformation with inverse absolute temperature. This Arrhenius plot yields a linear relationship in the low temperature range, when the slow crystallization process predominates.

5.4 Dynamic Mechanical Behavior

The results of dynamic measurements are shown in Figures 5.17, 5.18 and 5.19. E' , E'' and $\tan\delta$ are plotted against temperature for a quenched and annealed samples at 11 Hz. The obtained data at two frequencies, 3.5 and 11 Hz are given in Appendix A.5.

The storage modulus of the annealed sample is significantly higher than that of the quenched sample for the low temperature range (-110°C to 50°C), but the difference decreases somewhat above 50°C , and both samples show the same modulus above 120°C .

The loss modulus shows the effect of increase in crystallinity on the

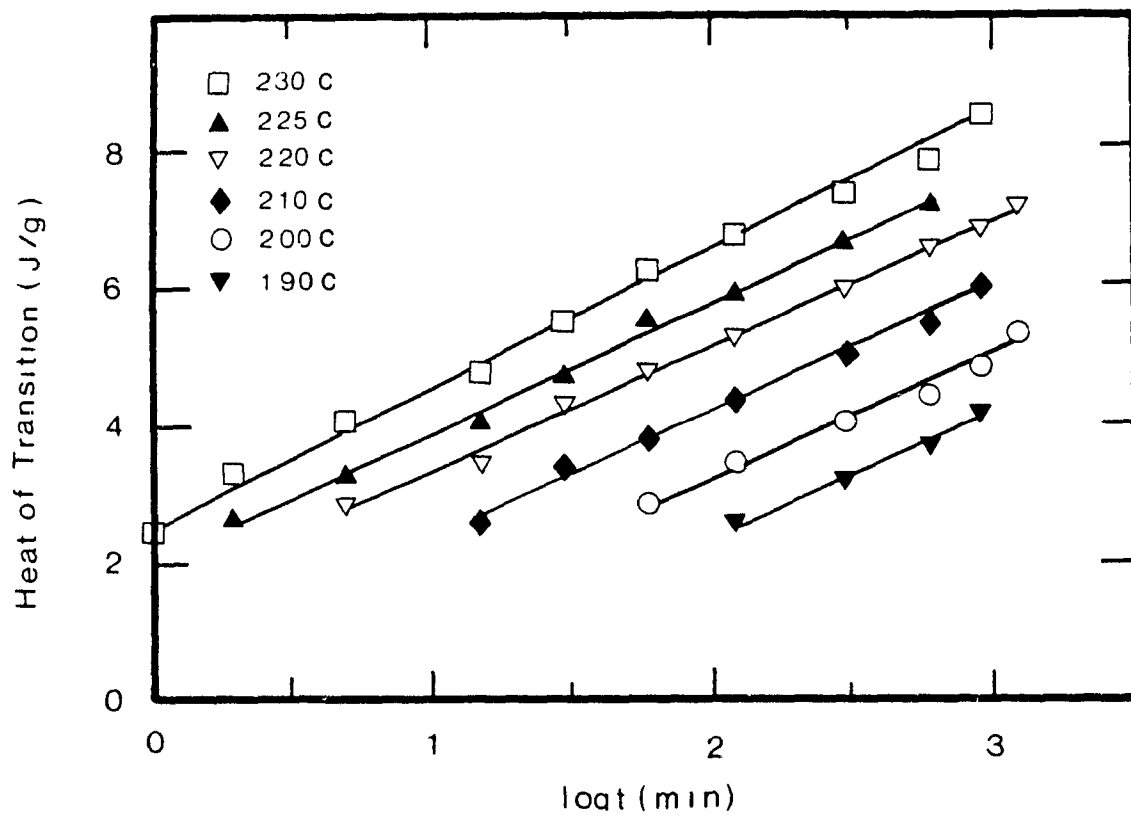


FIGURE 5.15: Plots of heats of transition versus log(time) at different crystallization temperatures (T_c 's).

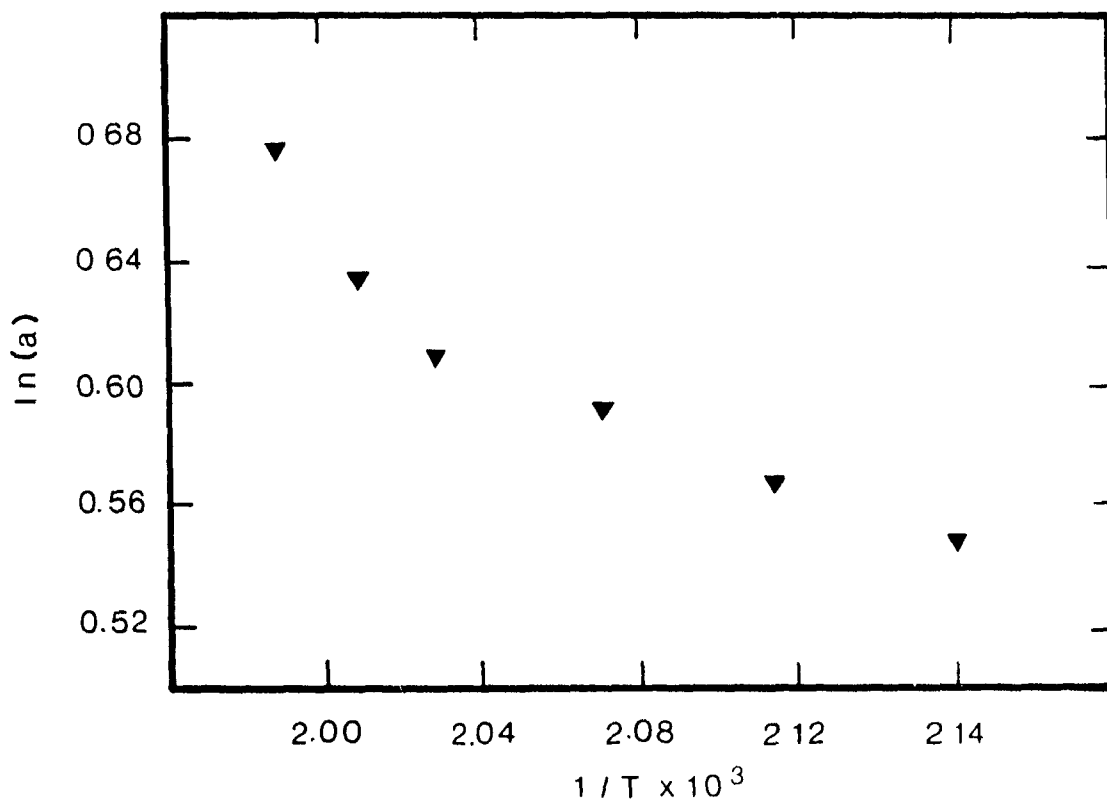


FIGURE 5.16: Arrhenius plot of $\ln(a)$.

α - and β - loss peaks. The δ - loss peak was not affected by the change in crystallinity. The position of the α - loss peak for the annealed sample with respect to the quenched one did not change with annealing, as was reported for PET samples with different degrees of crystallinity (95). This means that the segmental motion occurring near the glass transition temperature, T_g , is not affected by the increase of the degree of crystallinity. The higher loss modulus values observed for the annealed sample are attributed to the increased interfacial area between the amorphous and the crystalline regions, without affecting the internal friction of both components. This behavior can be corroborated by observing that the storage modulus of the annealed sample is larger than the one obtained for the quenched sample.

From the $\tan\delta$ plot, three clear transitions are observed: The α - processes at 110°C, at the glass transition temperature, the β - processes around 50°C attributed to rotation of naphthyl moieties around the ester links, and the δ - processes at about -40°C normally assigned to the reorganizational motion of the phenyl units. When the $\tan\delta$ plots are compared, the effect of annealing is observed mainly on the T_g loss peak, where it shows a higher value for the annealed sample than for the quenched sample. The effect of frequency change is not significant in this case, because of proximity of frequencies (3.5 and 11 Hz).

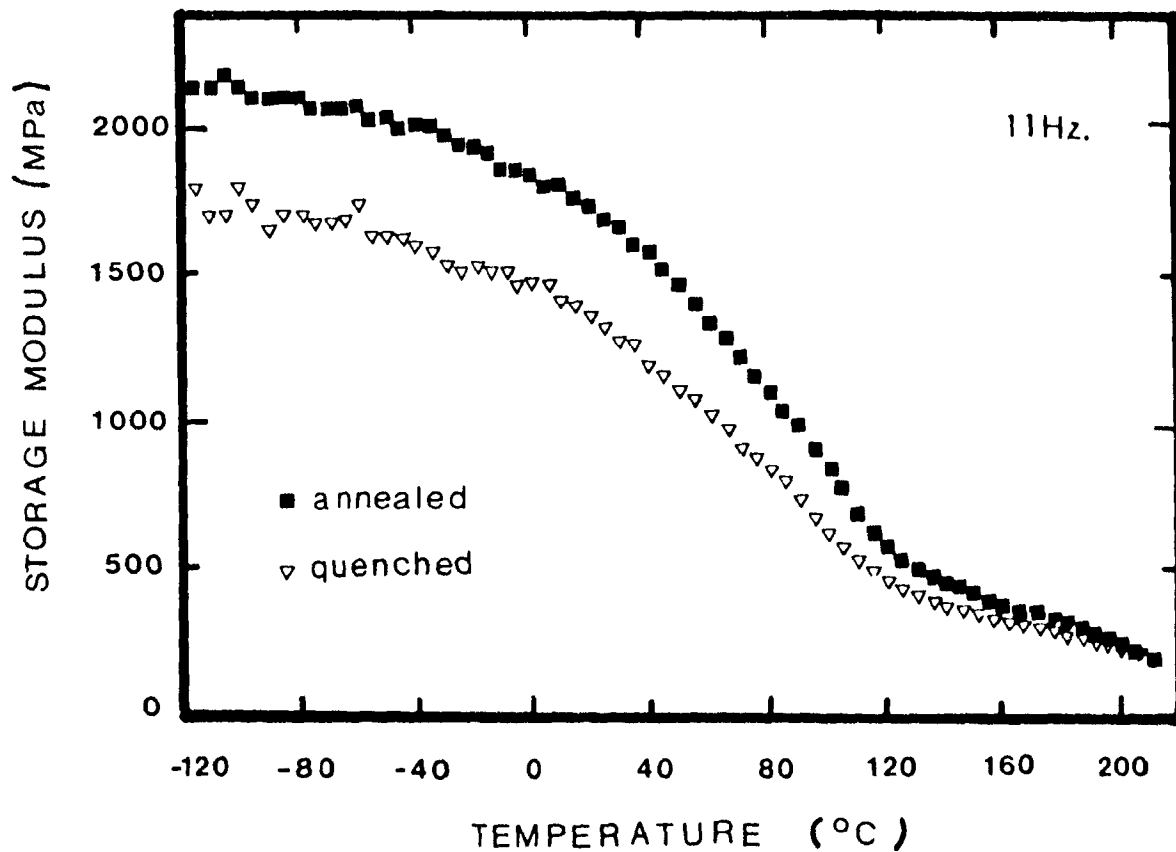


FIGURE 5.17: Storage Modulus, E' , from dynamic mechanical analysis.

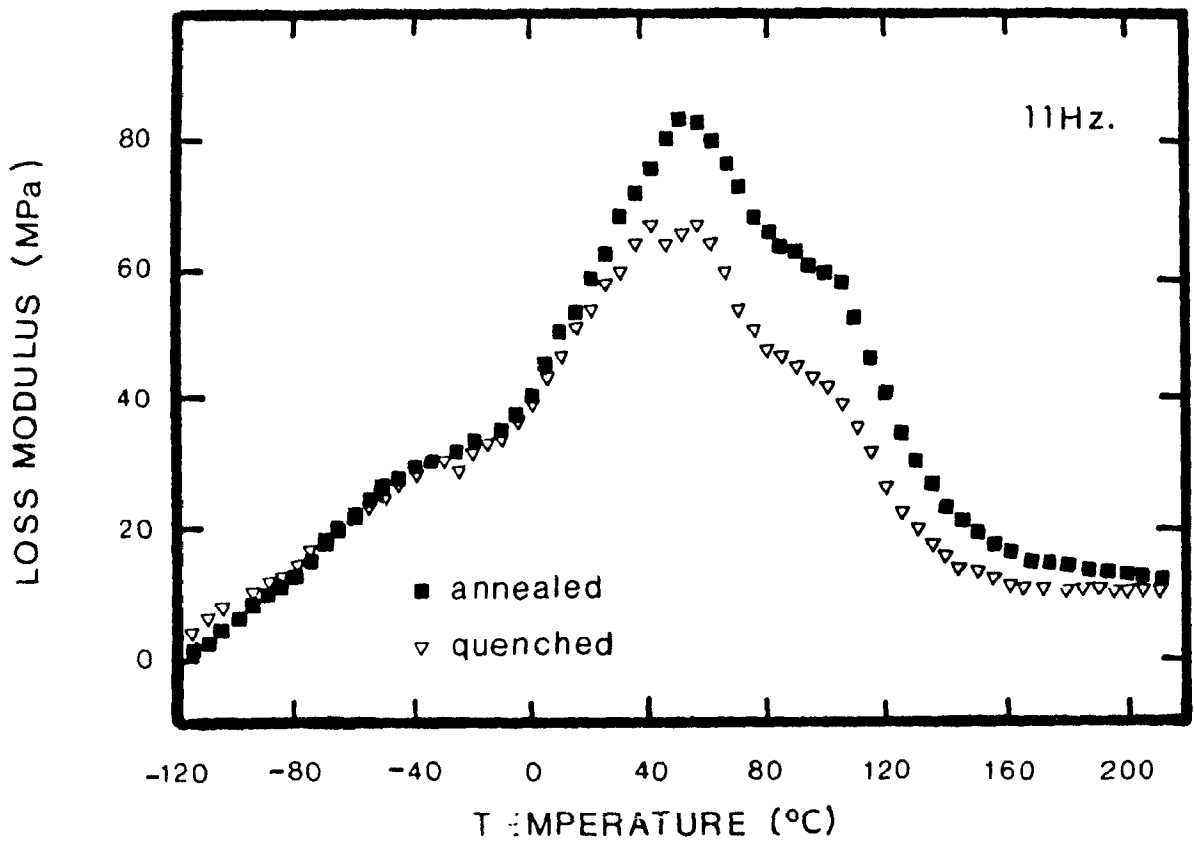


FIGURE 5.18: Loss Modulus, E'' , from dynamic mechanical analysis.

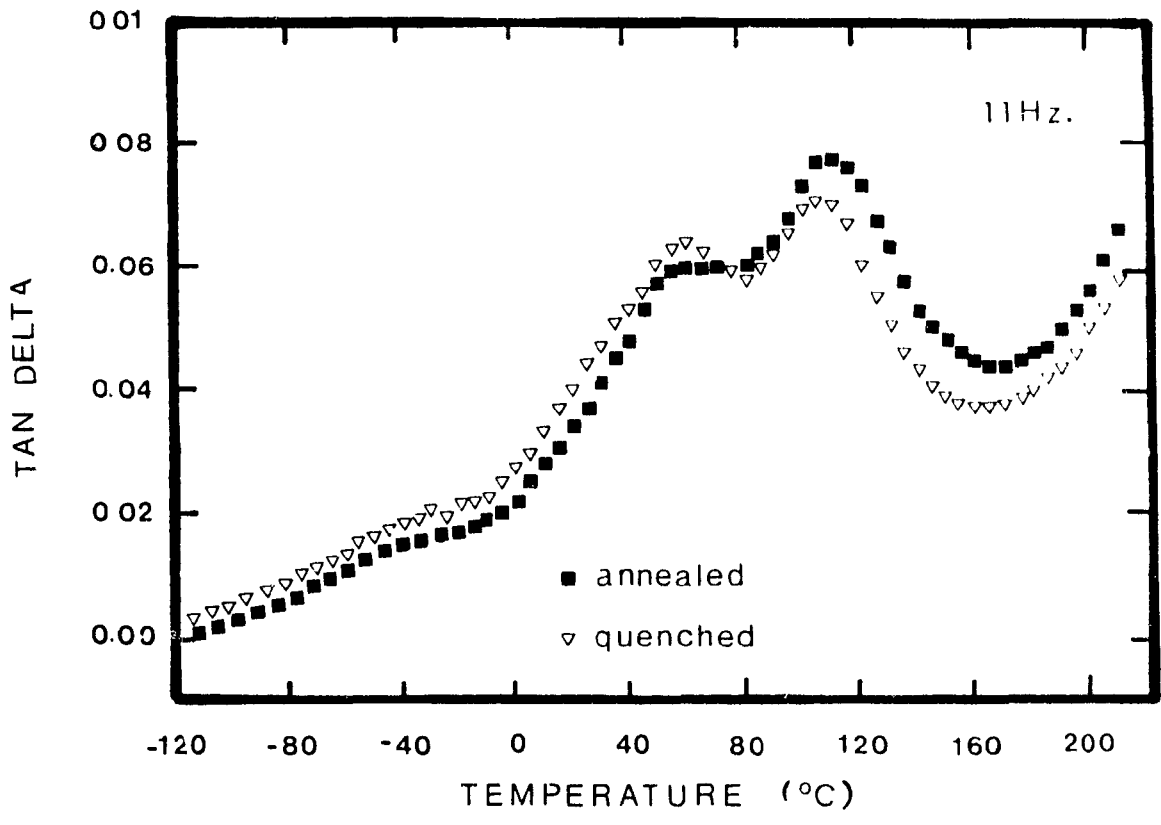


FIGURE 5.19: Tan δ , from dynamic mechanical analysis

5.5 Rheological properties

5.5.1 Shear Viscosity

The true shear viscosity of the liquid crystalline copolyester used in this study, as a function of true shear rate and temperature, is plotted on log-log scale in Figure 5.20. The shear rate dependence of viscosity, over the range of ca. 10 to 1000 sec^{-1} , was measured at three different temperatures of 300, 310 and 320°C. The flow curves show a viscosity decrease with increasing temperature. The power law exponent range from 0.50 to 0.55 over the temperature and shear rates ranges under study. A sharp break is observed in the viscosity-temperature curve at 310°C. This phenomenon can be explained by the existence of some unmelted order which effectively crosslinks the polymer melt (53). The viscosity was observed to be very sensitive to the amount of this residual order. Wissbrun et al. (53) reported that for a similar LCP resin, the activation energy above 300°C was equal to 10 kcal/mole, while below 300°C the activation energy increased enormously to about 40-50 kcal/mole.

The shear rate dependence of the viscosity is very close to power-law form over a wide shear rate range. Figure 5.20 indicates that shear thinning persists at low shear rates. This behavior is different from that of isotropic polymers, where the viscosity approaches a constant value at low shear rates.

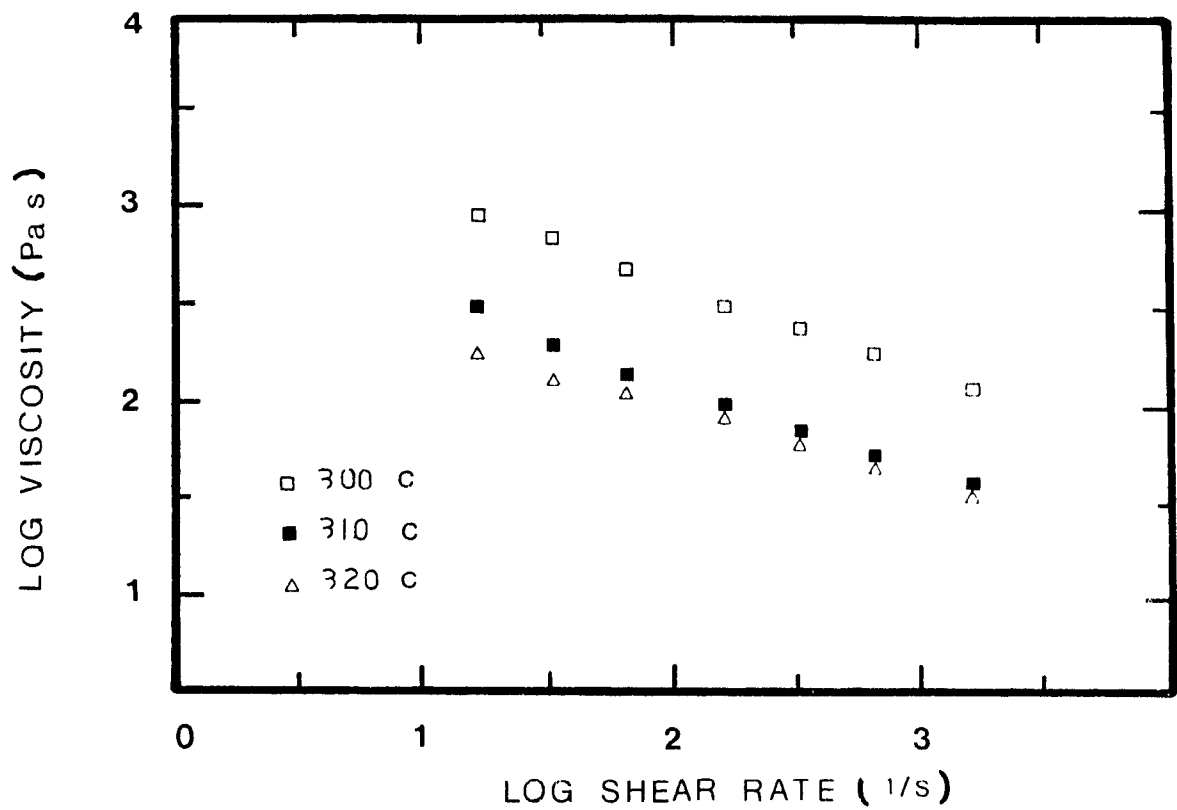


FIGURE 5.20: Viscosity vs. shear rate at three different temperatures.

5.5.2 Capillary Die Swell

Extrudate swell was measured (83) at 300 °C using two different shear rates 26 s⁻¹ and 104 s⁻¹. The results are shown in Figure 5.21. The data are also reported in Appendix A.6.2. It is observed that no extrudate swell occurs at both shear rates by the liquid crystalline copolyester, which is in general agreement with results obtained by several workers (52,54). White (96) and Samara (83) noted that the absence of extrudate swell in liquid crystalline melts is similar to the swell behavior of short fiber-filled melts.

5.6 Injection Molding Studies

5.6.1 Processing Characteristics

Pressure and temperature-time profiles obtained for a typical single run are displayed in Figure 5.22, (Data are given in Appendix A.7). Profiles for nozzle, cavity and hydraulic pressures, melt and mold temperatures, as well as screw displacement, are shown.

The cavity pressure is the most interesting variable, since it is closely related to the flow behavior of the polymer melt during all stages of the injection molding cycle. Pressure profiles span the filling, packing, holding and cooling stages. During the filling, the pressure rises slowly, as the molten polymer flows into the cold mold cavity from the delivery channels, including the sprue, runners and through the gate. When the flow front impinges against the far end of the cavity, at the end of the filling stage, more melt is packed into the cavity to compensate for

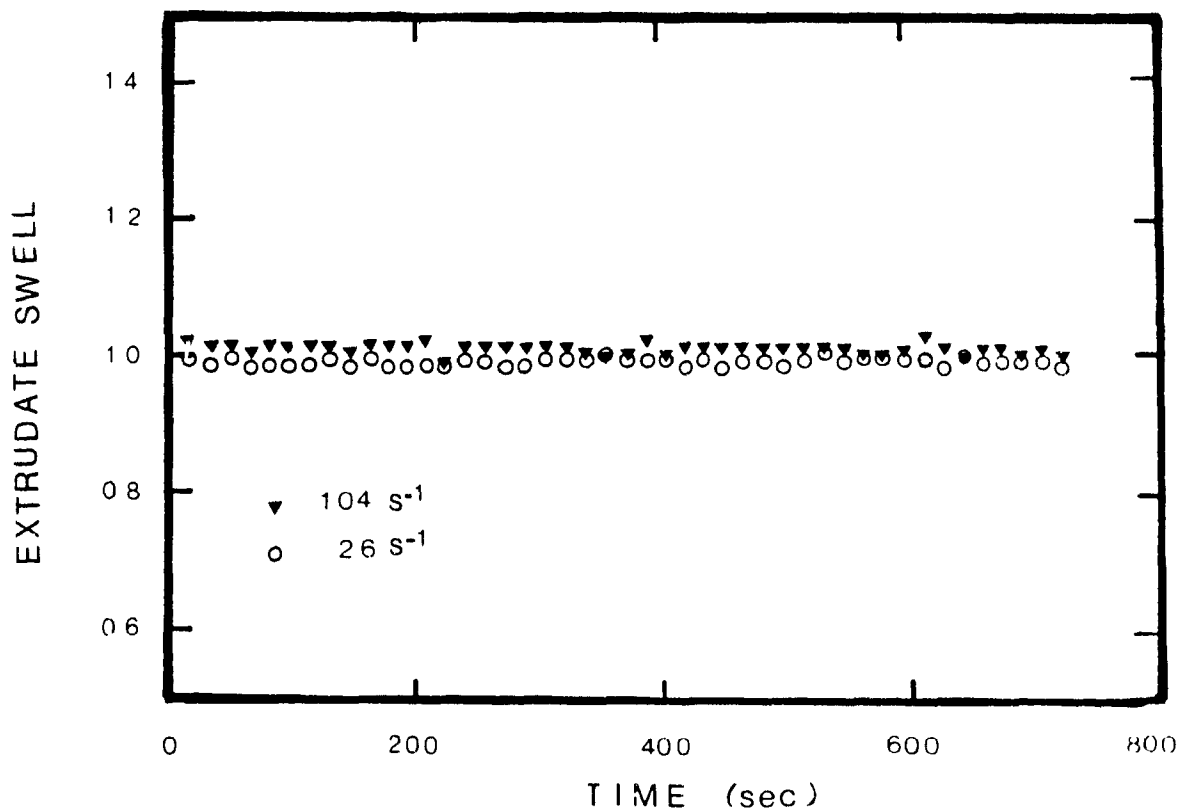


FIGURE 5.21: Extrudate Swell of LCP at 300°C at two different shear rates (83)

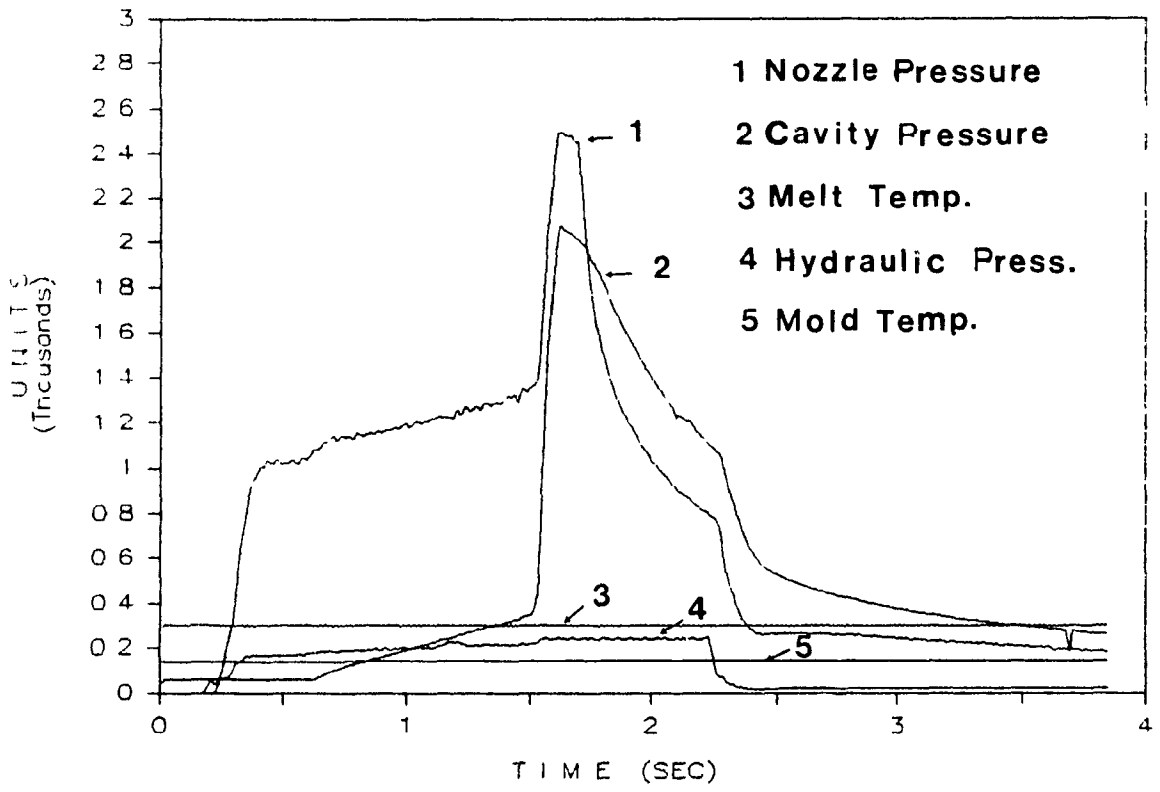


FIGURE 5.22: Variable-Time Profiles during the injection molding process for a single run.

the shrinkage of the material, due to cooling and crystallization. During packing, the pressure in the cavity rises sharply within a short interval of time to reach a maximum. Sometimes, the pressure is maintained at the same level or allowed to decrease slowly, during the holding stage, which follows the packing stage. In the cooling stage, a continuous decrease in cavity pressure is observed. No flow should take place during this stage, as a result of the freezing of the gate. The rate of cooling usually plays an important role in determining the final properties of the molded article.

The theoretical models for the various stages of the injection molding cycle attempt to predict the distributions of melt pressure, temperature, and velocity in the barrel and cavity and their dependence on resin properties, gate and cavity shape, screw design and processing conditions. Some of these models can also yield information regarding the relationships between resin properties and machine and molding variables on one side, the microstructure and the ultimate properties of the molded article on the other side. The resulting equations are very complex and numerical solutions are usually required with considerable computational effort.

Previous studies regarding the structure of injection molding liquid crystalline polymers (LCP's) have evaluated microstructure under limited processing conditions. In this study, the effects of four different processing variables were considered. These included melt and mold temperature, injection pressure and injection speed.

Figure 5.23 displays the variation of cavity pressure at two different locations in the mold, one near the gate (PT1) and the second in the middle of the cavity (PT2). The pressure increase during the packing stage is equal to 2000 psi for

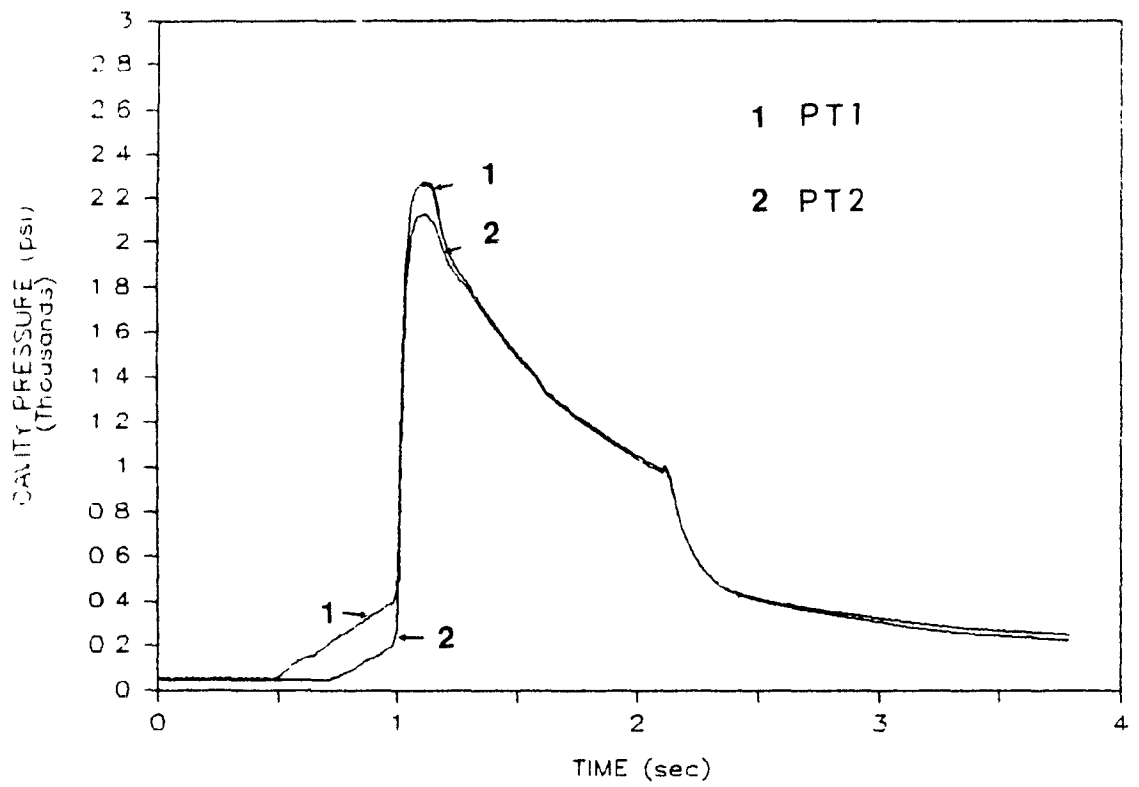


FIGURE 5.23: Cavity Pressure-Time Profiles at two different locations in the mold cavity.

both transducers. The peak cavity pressure is higher for the PT1, because of higher initial pressure value. During the cooling stage no difference is observed at both positions, suggesting the freezing of the gate in the early stages of the holding stage.

Figure 5.24 shows replicates of nozzle and cavity pressure-time profiles for 3 samples molded under the same conditions. The reproducibility of the runs is excellent, suggesting that errors due to sample-to-sample variability are small.

Figure 5.25 depicts the nozzle and cavity pressure-time profiles obtained for two different mold temperatures. The main differences are observed in the peak pressure and the cooling stage. At low mold temperature, the nozzle and cavity pressures are higher than at the higher mold temperature, due to the higher viscosity of the melt at the lower mold temperature.

Figure 5.26 shows the nozzle and cavity pressure-time profiles obtained for two different injection pressures. Higher injection pressure resulted in an increase of the peak pressure in the nozzle as well as in the mold cavity. Thus, the differences in microstructure will be induced mostly by the higher packing and cooling pressure. The above differences may be reflected in the differences of the dimensional stability (e.g. shrinkage) of the moldings. It has been reported (12) that, due to the high molecular ordering of the liquid crystal copolyester under study, the dimensional stability is excellent.

Figure 5.27 shows the nozzle and cavity pressure-time profiles obtained for two different injection speeds. The faster filling rates shorten the

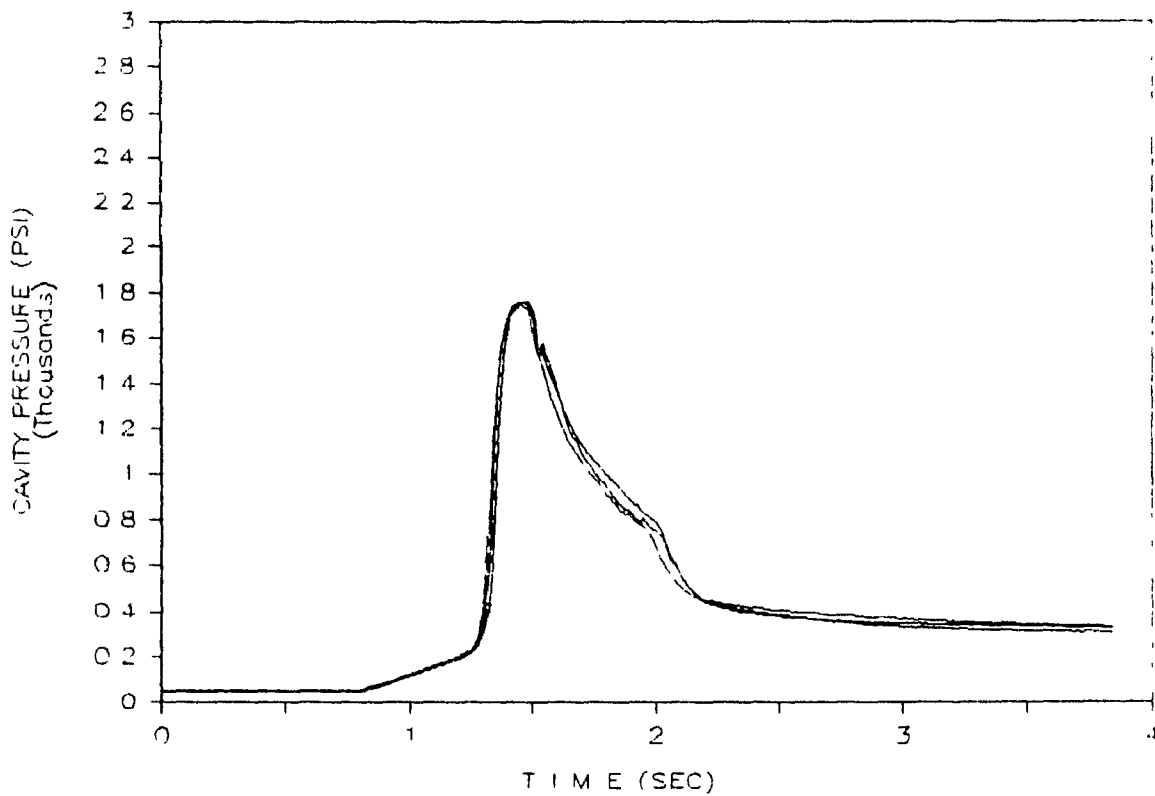
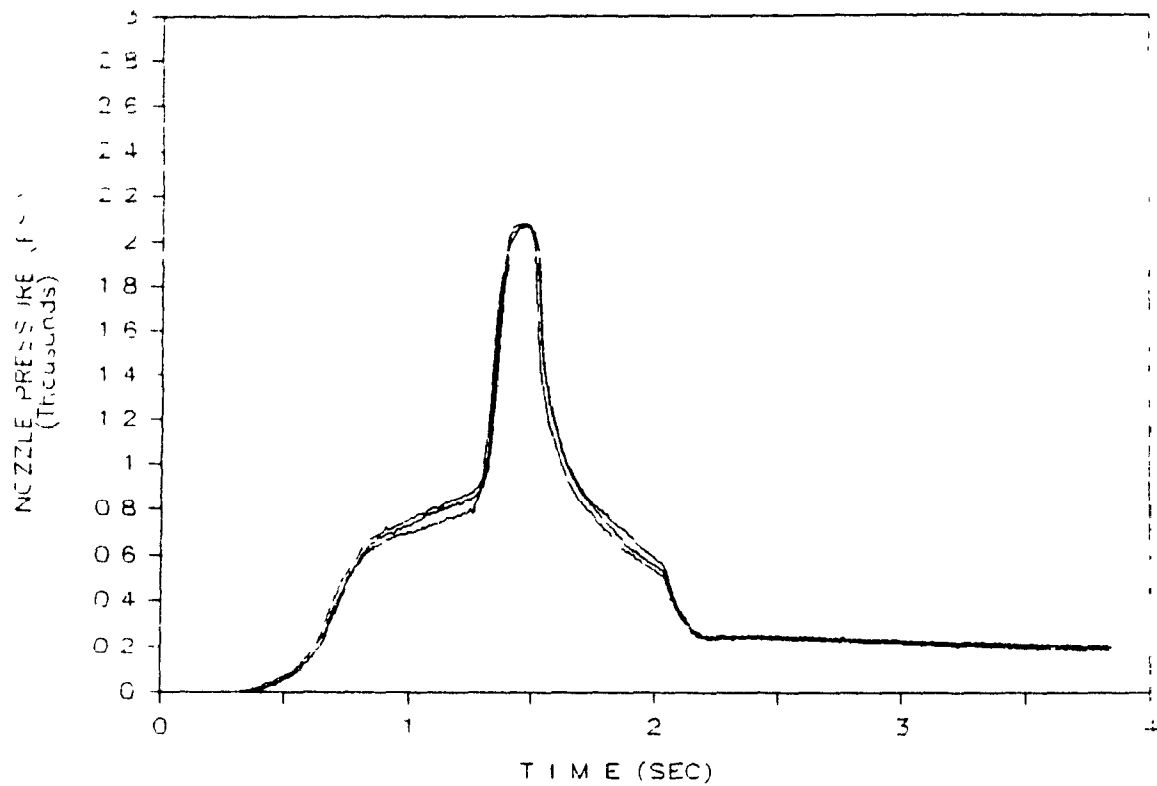


FIGURE 5.24: Replicates for Nozzle- and Cavity Pressure-Time Profiles.

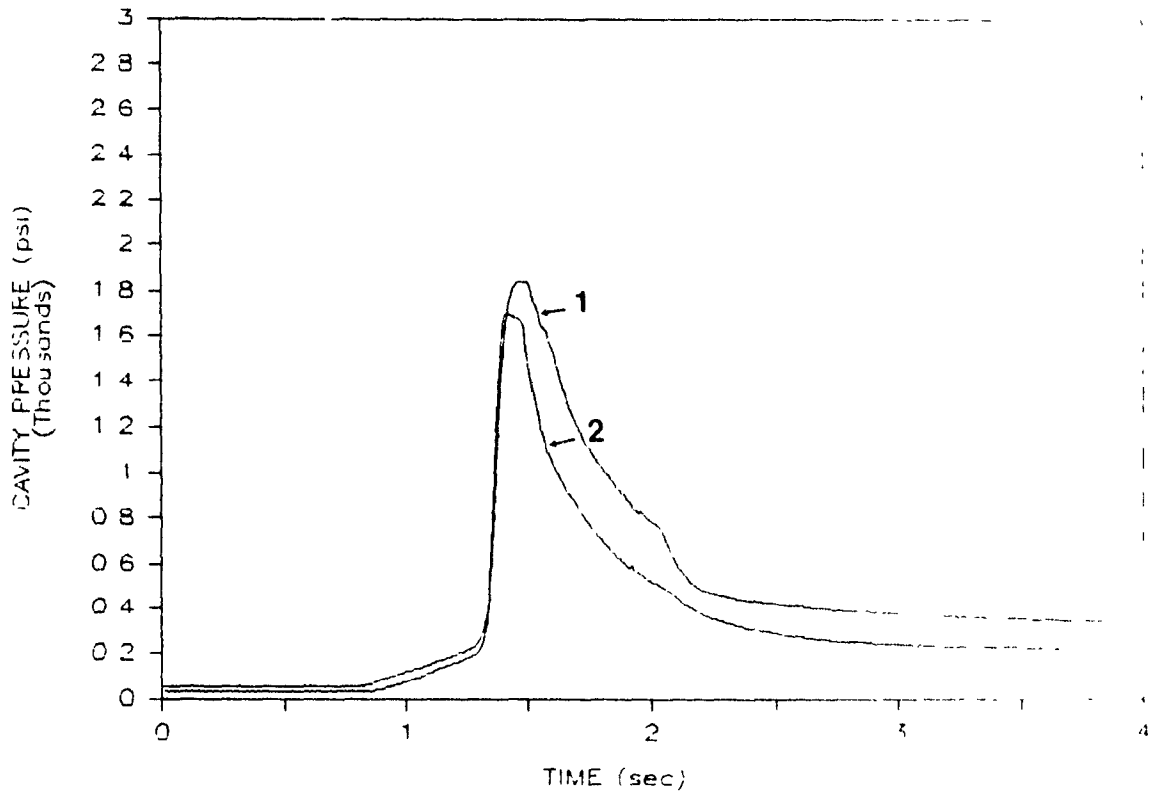
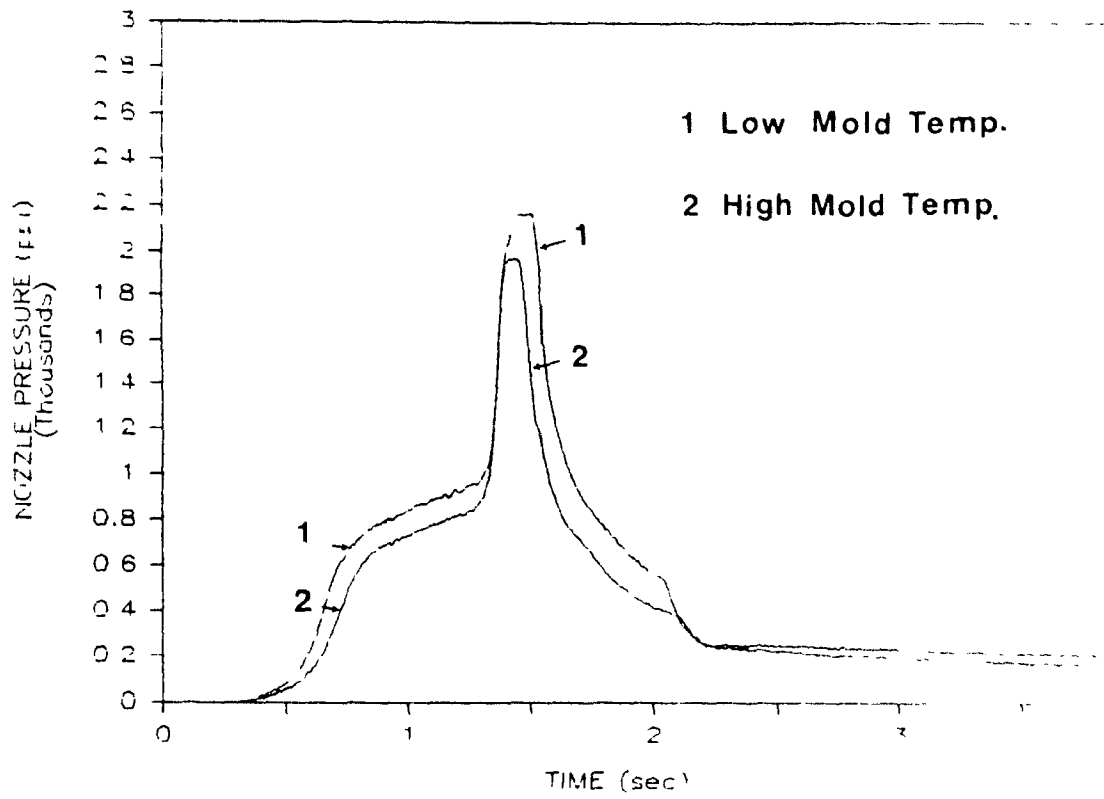


FIGURE 5.25: Nozzle- and Cavity Pressure-Time Profiles obtained at two different mold temperatures.

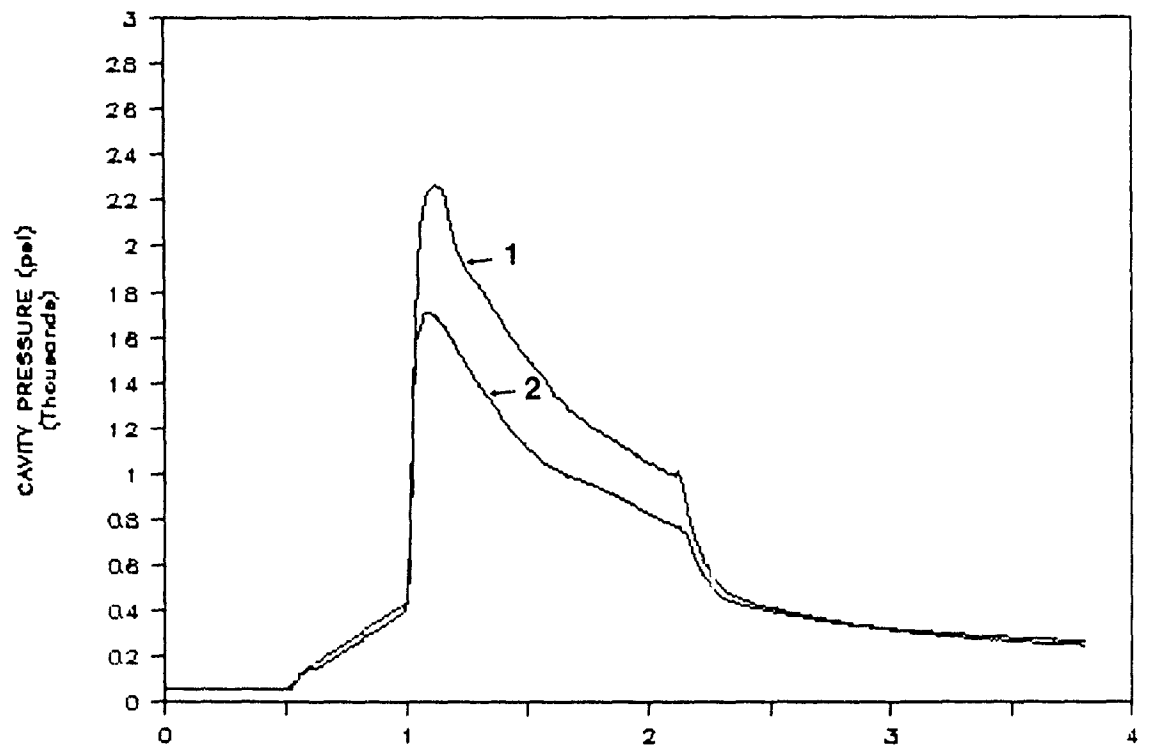
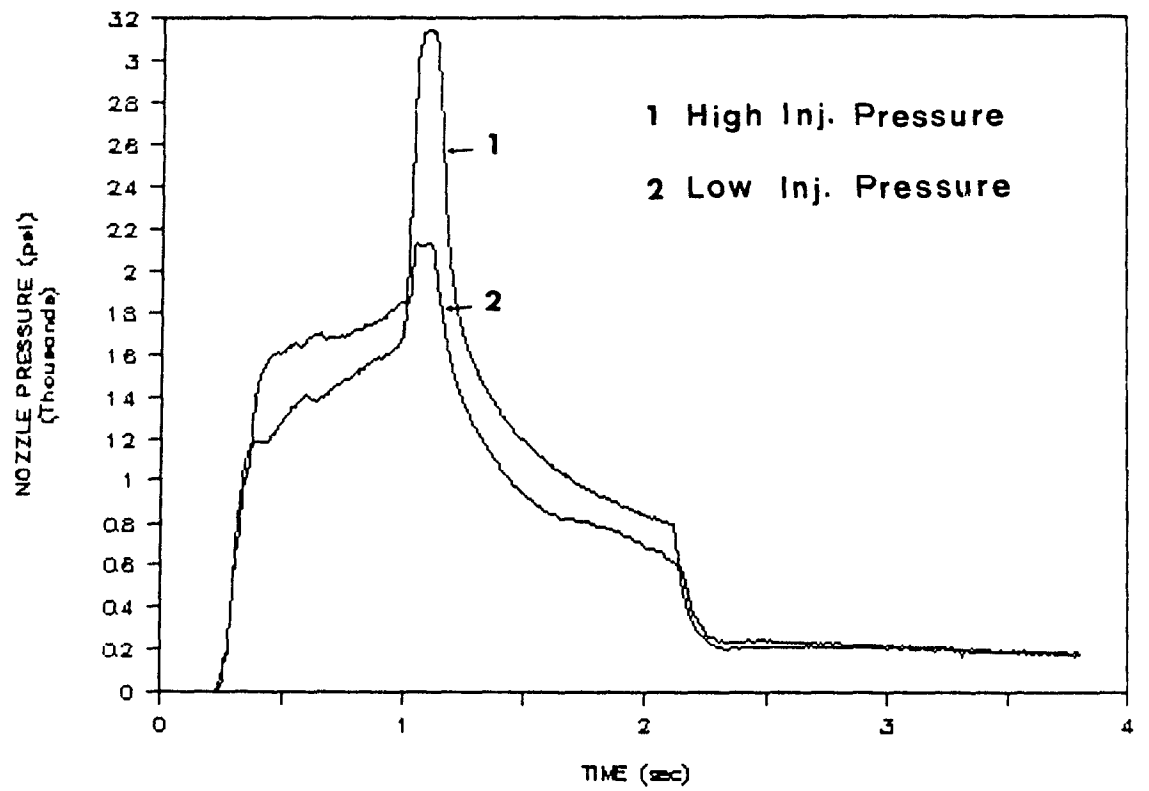


FIGURE 5.26: Nozzle- and Cavity Pressure-Time Profiles at two different injection pressures.

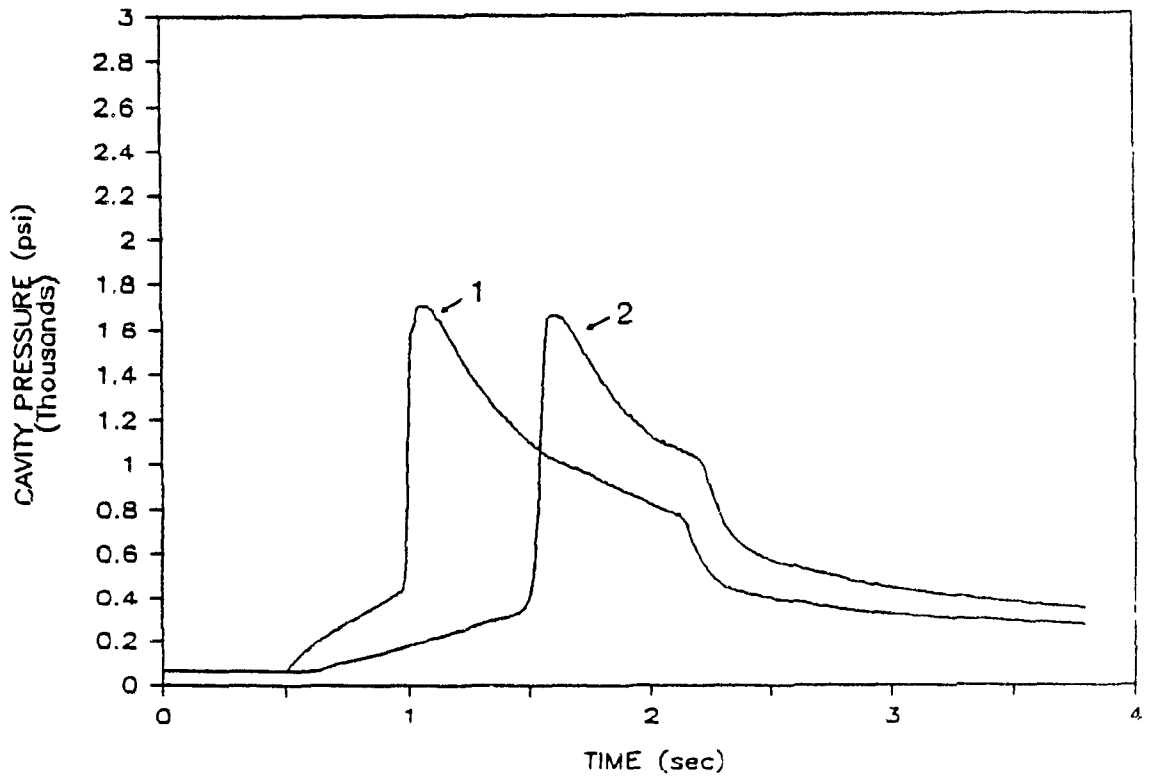
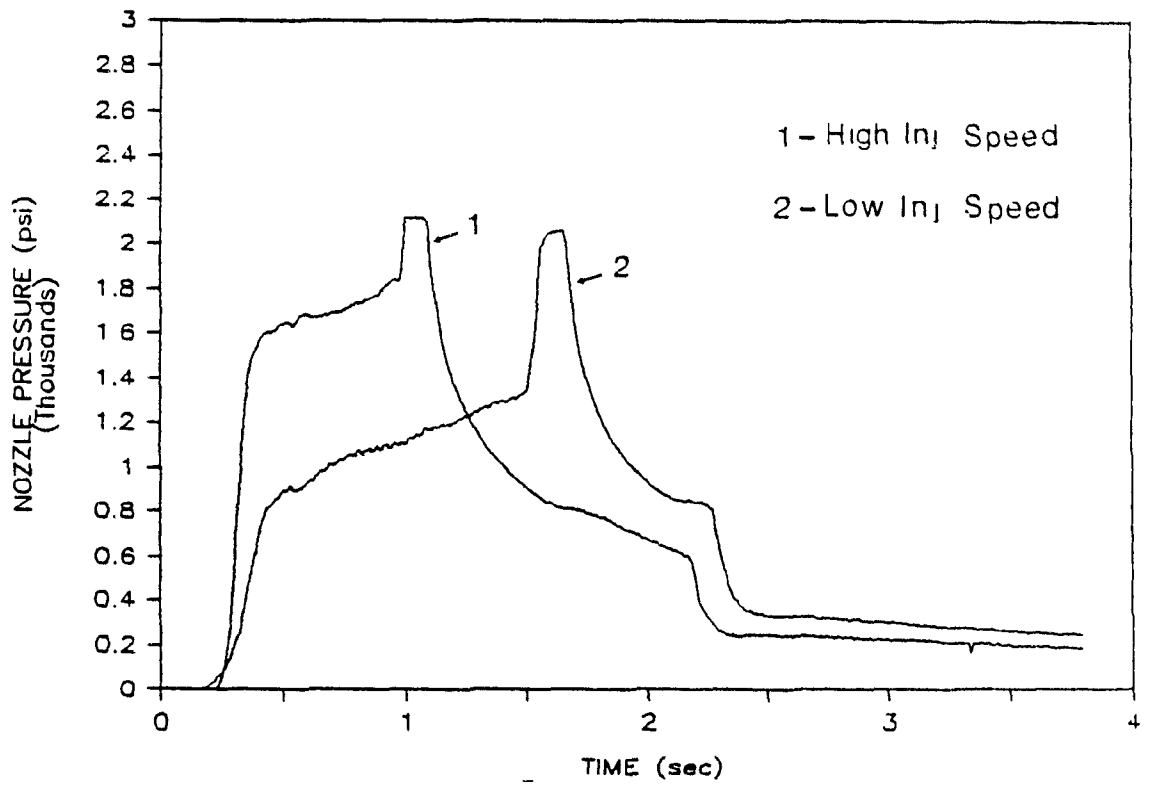


FIGURE 5.27: Nozzle- and Cavity Pressure-Time Profiles obtained at two different injection speeds.

overall cycle time, but the viscous forces are very high. When shorter filling times are present, there is an increased shearing occurring in the gate area and against the cold mold wall. The nozzle pressure, at two different injection speeds, indicates a pressure difference of about 900 psi during the filling stage. The higher pressure induces higher stresses during cavity filling, and the expectation is that the effect on the product microstructure will be significant. At lower injection speed, the time needed to fill the cavity is longer.

Figure 5.28 shows the temperature-time profiles at the mold surface, for two different mold temperatures during the injection molding cycle. Figure 5.28a shows that at a mold temperature of 40 °C, after the molten polymer (320°C) was injected into the cavity, the mold temperature increased by 15°C within 1.25 seconds. Figure 5.28b shows that when the mold temperature is set at 140°C, the equilibrium mold temperature is reached within 0.75 sec, with an increase of 10°C. The driving force for cooling is higher than at lower mold temperature.

In brief, the pressure-time profiles obtained during the injection molding cycle give significant insight regarding the injection molding process. They should be helpful in the understanding of the microstructure and ultimate properties of molded articles.

5.6.2 Microstructure Development

In order to study the microstructure of the samples prepared under different molding conditions, ten samples from each particular processing condition

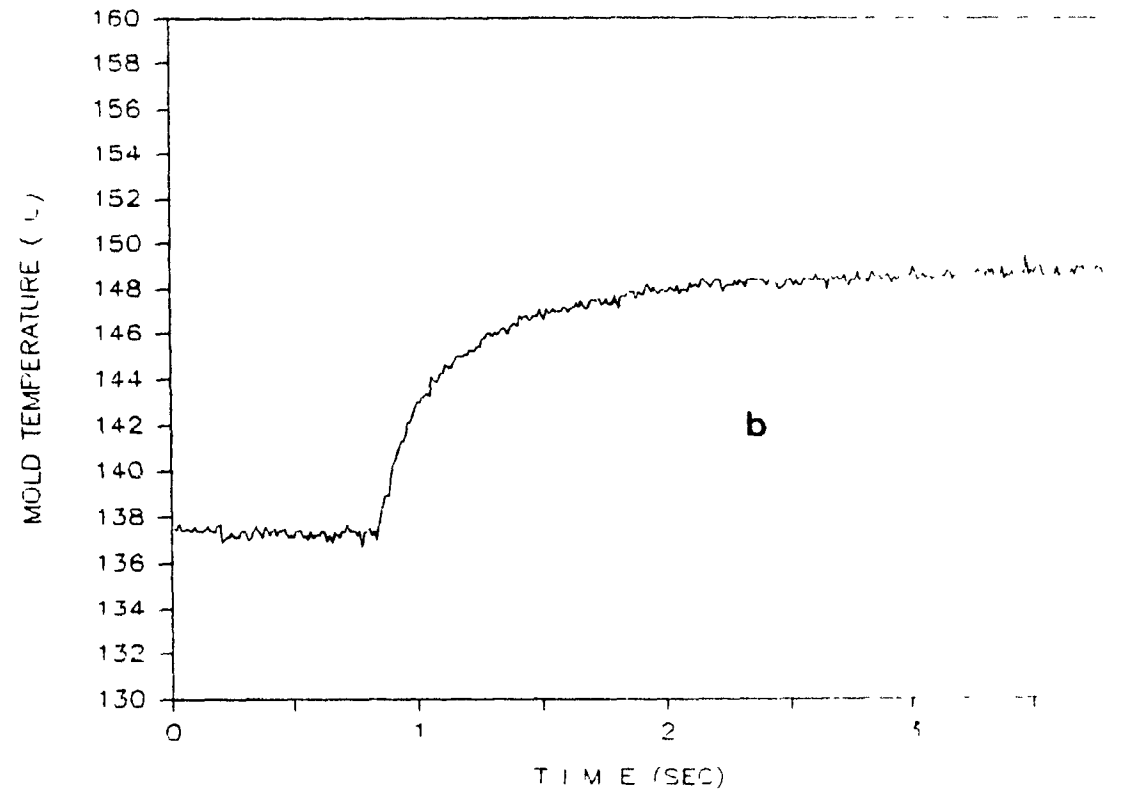
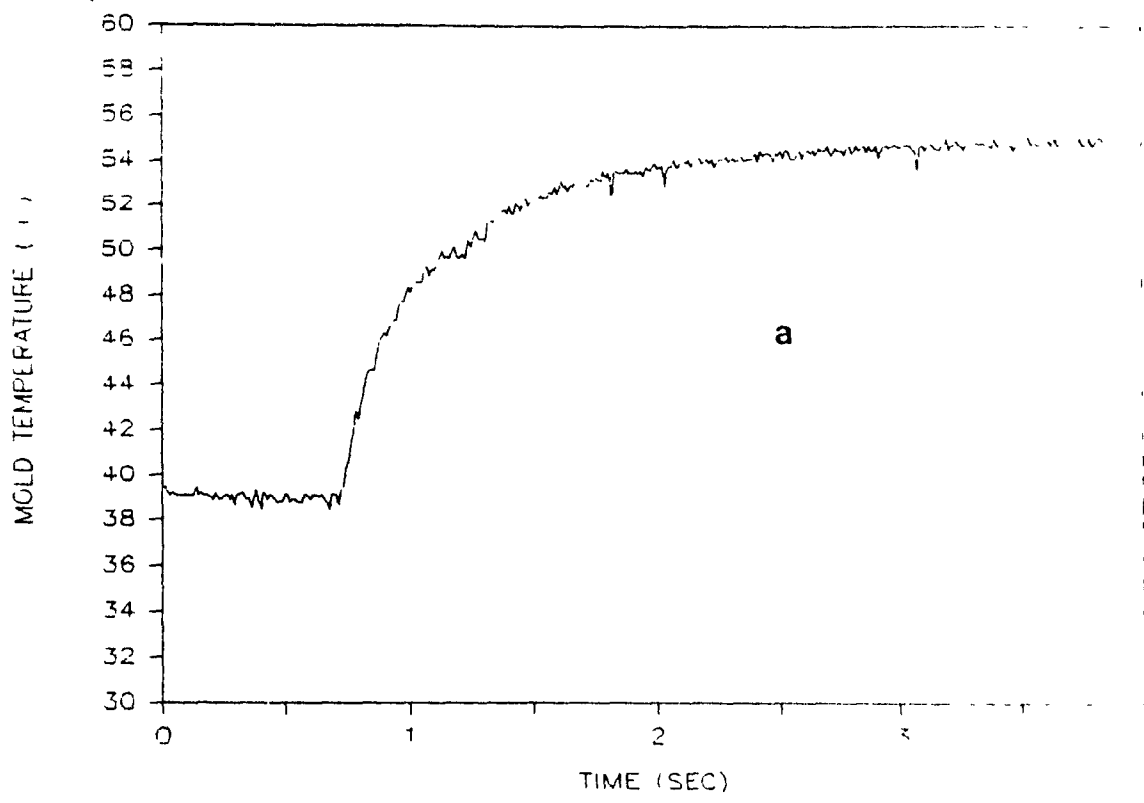


FIGURE 5.28: Mold temperature-time profiles during the injection molding cycle.

were obtained. These samples were then properly labelled and stored in a desiccator for microstructural characterization. The particular processing parameters are given in the Table 5.1.

5.6.2.1 Polarized Light Microscopy

Cross-polarized light photomicrographs were taken using a Reichert microscope in conjunction with a Polaroid camera. The specimens were very thin layers microtomed in the X-Y plane, with thicknesses of about 2 to 3 microns. The photomicrographs are shown in Figure 5.29. The top picture represents a microtomed section from the surface layer (skin) of the molded sample. The bottom picture represents a microtomed section from the center region (core) of the test piece taken from region A near the gate (see Figure 4.9). The skin layer shows clearly ordered regions elongated along the flow direction. The bottom photomicrograph representing the central core region, shows no preferred orientation along any of the axes.

Figure 5.30 illustrates a cross-polarized photomicrograph taken from a sample microtomed in the X-Z direction, across the thickness of a test piece taken from the position B as shown in Figure 4.9. The type of morphological texture observed in this picture is the well known skin-core morphology, displaying four layers from the surface to the center of the molded sample. A skin layer representing the surface layer, a sub-skin layer, an intermediate layer and a core layer representing the middle of the sample thickness. We can also observe that there is symmetry around the central core region. The picture shows that the skin

**TABLE 5.1: PROCESSING PARAMETERS IN THE INJECTION
MOLDING STUDY OF LCP PARTS; MACHINE
SETTINGS**

	LMdT	HMdT	LP	HP	LIS	HIS
1	40	140	140	140	140	140
2	330	330	330	330	300	300
3	1600	1600	1600	2200	1600	1600
4	18	18	9	9	9	18

- 1: Mold Temperature (MdT) (°C)
- 2: Melt Temperature (MtT) (°C)
- 3: Cavity Pressure (P) (Psi)
- 4: Injection Speed (IS) (cm³/sec)

LMdT: Low Mold Temperature
 HMdT: High Mold Temperature
 LP: Low Cavity Pressure
 HP: High Cavity Injection
 LIS: Low Injection Speed
 HIS: High Injection Speed

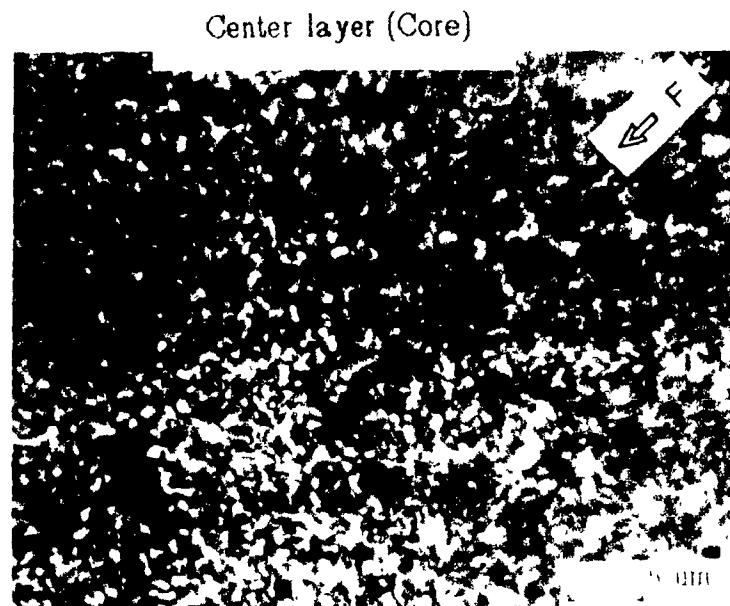
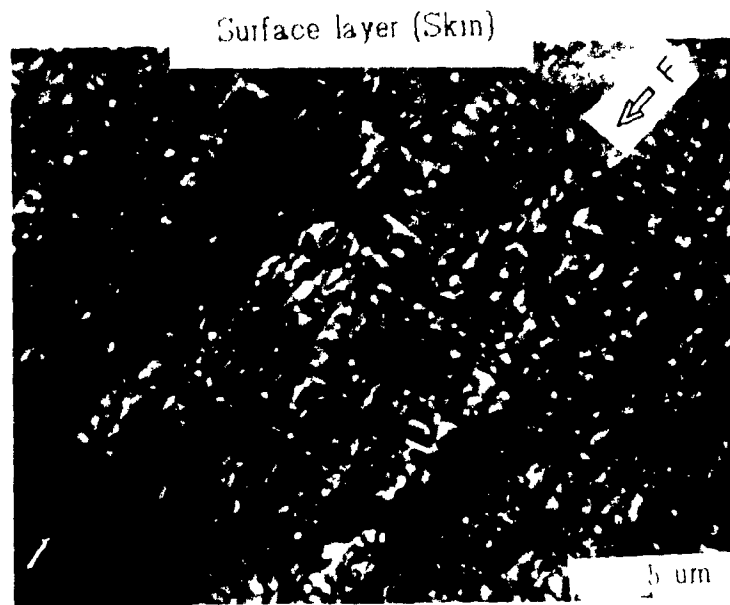


FIGURE 5.29: Polarized light photographs of injection molded sample microtomed in the X-Y plane.

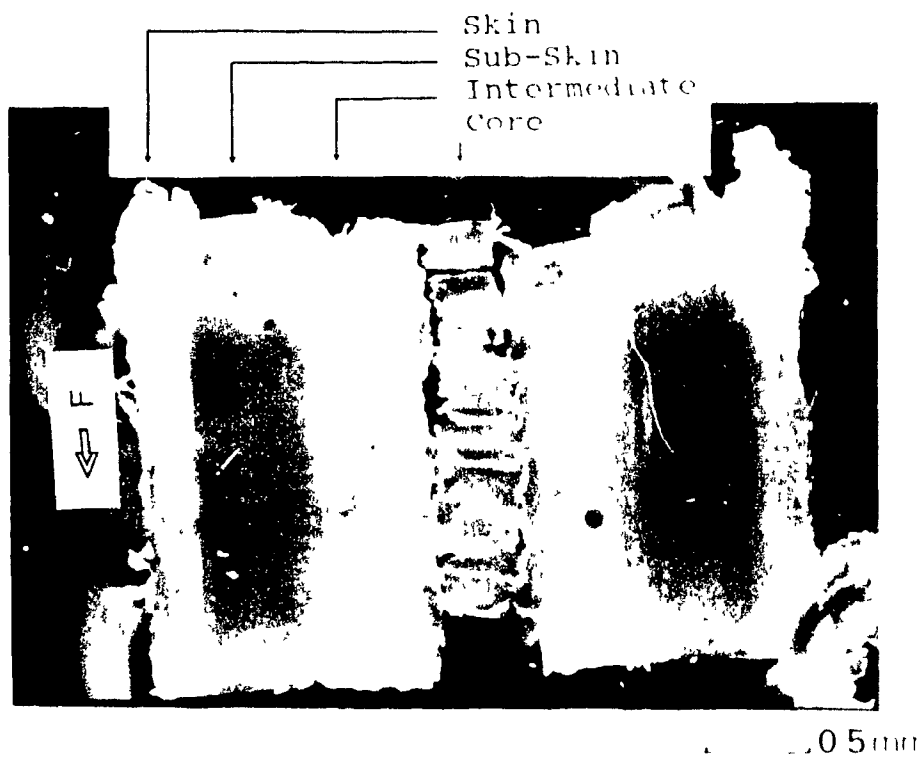


FIGURE 5.30: Cross-Polarized Light photograph of injection molded sample microtomed in the X-Z plane.

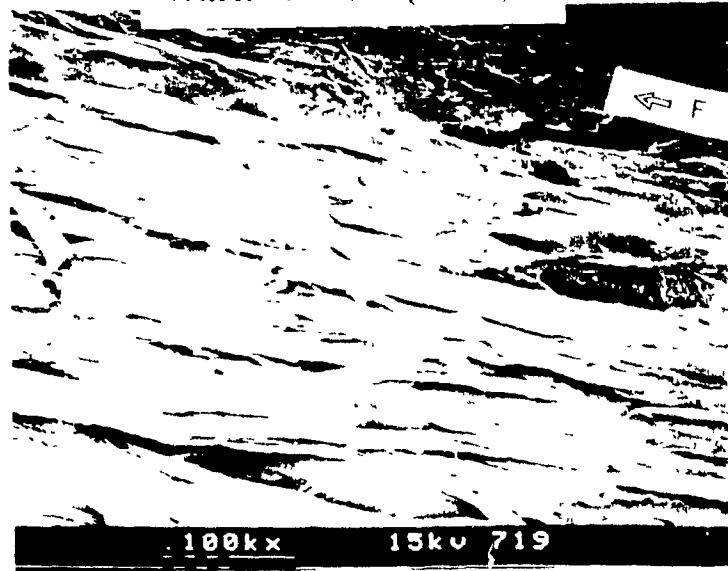
layer is oriented parallel to the flow direction (X-direction), the sub-skin layer is less ordered, the intermediate zone is oriented along the flow direction, and the core layer shows less ordered structure in relation to the flow direction. The microtomed surface in the core layer suggests that the orientation might be perpendicular to the flow direction. The crackled surface in this layer is similar to that obtained by microtoming a glass-fibre reinforced polymer sample, which is oriented transverse to the flow direction (97). As a result, it is suggested that the orientation in the core layer is transverse to the flow direction.

5.6.2.2 Scanning Electron Microscopy

Scanning Electron Microscopy (SEM) was used in conjunction with a Polaroid camera to obtain photomicrographs of microtomed samples from the surface to the center of the test piece obtained from the position A near the gate region in the X-Y plane, as shown in Figure 4.9. The Polaroid photomicrographs shown in Figure 5.31 display skin-core morphology. The top photomicrograph illustrates the structure observed for the surface layer, while the bottom photomicrograph illustrates the surface structure of the core layer. It is observed that the skin layer is fibrous in nature and highly oriented along the flow direction as indicated by the top photomicrograph, while the bottom photomicrograph shows a core layer with less order. The photomicrographs shown display very clearly the skin-core morphology of the injection molded part.

Figure 5.32 shows a photomicrograph of the fractured surface of the sample (1L) (see Figure 4.10) broken perpendicular to the flow direction in the Y-Z

Surface layer (Skin)



Center layer (Core)

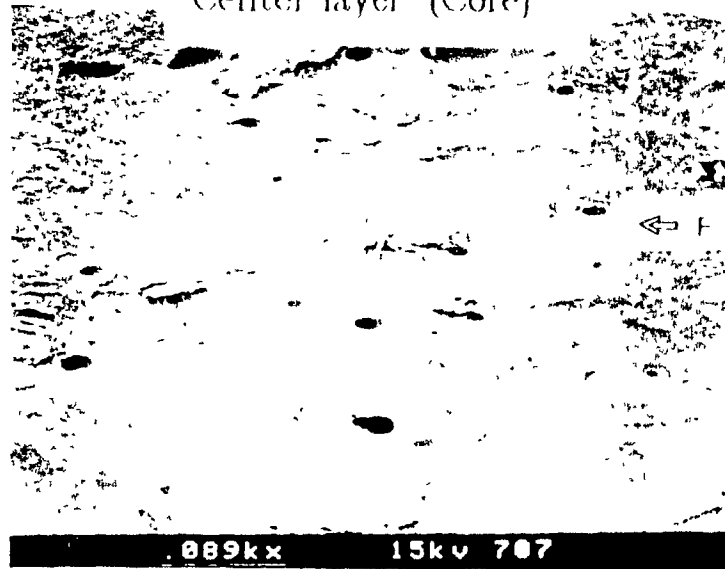


FIGURE 5.31: Electron photomicrograph of injection molded samples microtomed in the X-Y plane.

FLOW \perp TO THE PLANE
OF THE PICTURE



FIGURE 5.32: SEM photomicrograph of an injection molded sample (1L), broken in the Y-Z plane.

plane. The photomicrograph shows the overall sample thickness area. The flow direction is perpendicular to the plane of the picture. The electron micrograph shows a skin-core morphology. The skin layer is oriented parallel to the flow direction as shown by the fibers pulled off from original positions at the surface layer. While the neat fracture surface of the central region of the micrograph suggests that the orientation is perpendicular to the flow direction. The area of the core region, measured from the picture, represents about 30% of the total sample thickness area.

Figure 5.33 shows a higher magnification of the skin and intermediate layers of the previous photomicrograph. The surface skin layer displays a fibrous texture oriented parallel to the flow direction, as the fibers are torn off their original place or pointing perpendicular to the plane of the photomicrograph.

At much higher magnification, a detailed microstructure of the central core region is obtained, as shown in Figure 5.34. The photomicrograph indicates the presence of very thin fibers. This type of fibers or fibrils, indicated by the arrows on the picture, has been observed by many workers (61,65-67). Thapar and Bevis (61) examined etched surfaces of similar injection molded LCP samples, with the scanning electron microscope, and reported that the diameter of the fibrils in the surface skin layer is equal to $0.1 \mu\text{m}$, while in the core layer it increases to about $0.3 \mu\text{m}$. From the fractured surface of the sample under study, the fibril diameter observed in the core layer of the photomicrograph shown in Figure 5.34 is equal to $0.1 \mu\text{m}$, which is not in agreement with what has been reported by the previous workers (61). The direction of preferred orientation of the fibrils observed in this

FLOW ↓ TO THE PLANE
OF THE PICTURE

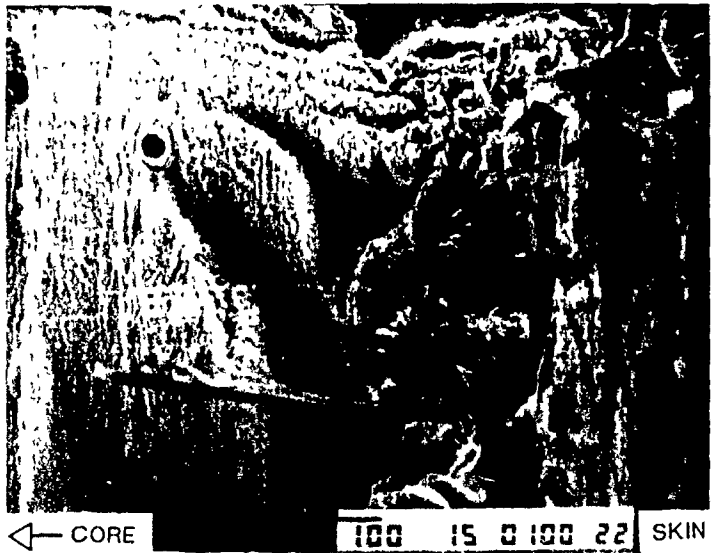


FIGURE 5.33: Cross-section of an injection molded sample (1L) at higher magnification.

FLOW ↓ TO THE PLANE
OF THE PICTURE

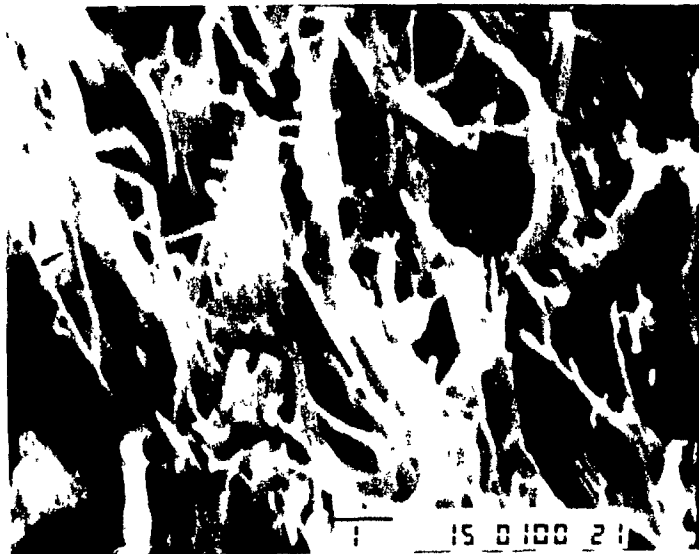


FIGURE 5.34: SEM photomicrograph of an injection molded sample of the center core at high magnification

core layer is perpendicular to the flow direction.

Figure 5.35 shows a photomicrograph of the fractured surface across the thickness of the sample (1T). The fractured surface under observation represents the X-Z plane. The flow direction (X-direction) is indicated by the arrow. Clear transitions are observed between the skin, sub-skin and intermediate layers. The center core layer of this sample is not shown in this photomicrograph. Figure 5.35 displays a fibrous and highly oriented skin layer in the direction parallel to the flow axis. The intermediate layer displays a preferred orientation along the flow direction but less ordered than the skin layer. The thicknesses of the three layers are observed to be comparable in magnitude.

At higher magnification, the details of the morphological texture observed are shown in Figure 5.36. The skin region contains macrofibers with a diameter equal to 3-5 μm . Macrofibers of the same diameter have been observed, and reported in the literature by Sawyer and Jaffe (67).

Figure 5.37 shows a photomicrograph taken from the core region of the same sample displayed in Figure 5.35. Typical flow lines are observed, in addition to possible fountain flow effect near the wall. The photomicrograph suggests how the material in the flow front is elongated and reoriented along the flow direction near the surface, when it solidifies, forming a highly oriented skin layer in the flow direction.

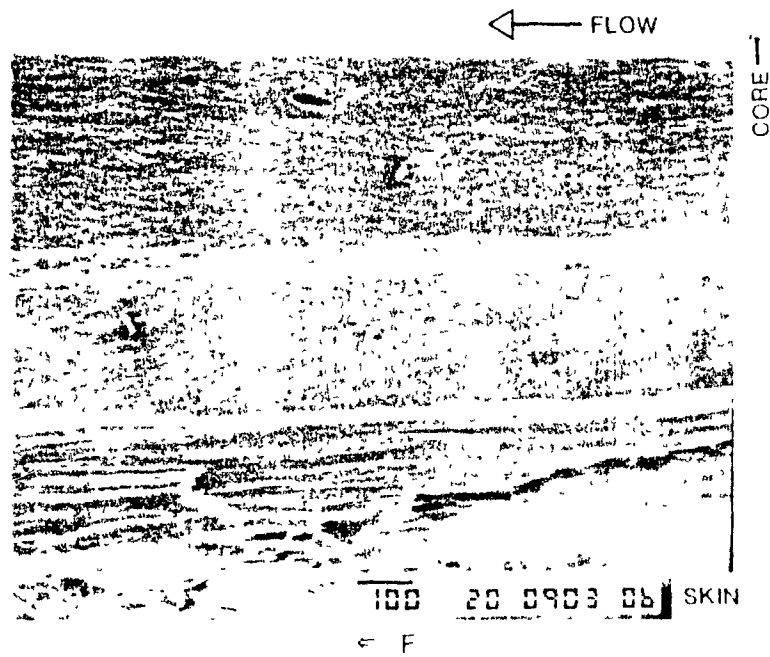


FIGURE 5.35: SEM photomicrograph of an injection molded sample (1T) broken in the X-Z plane.

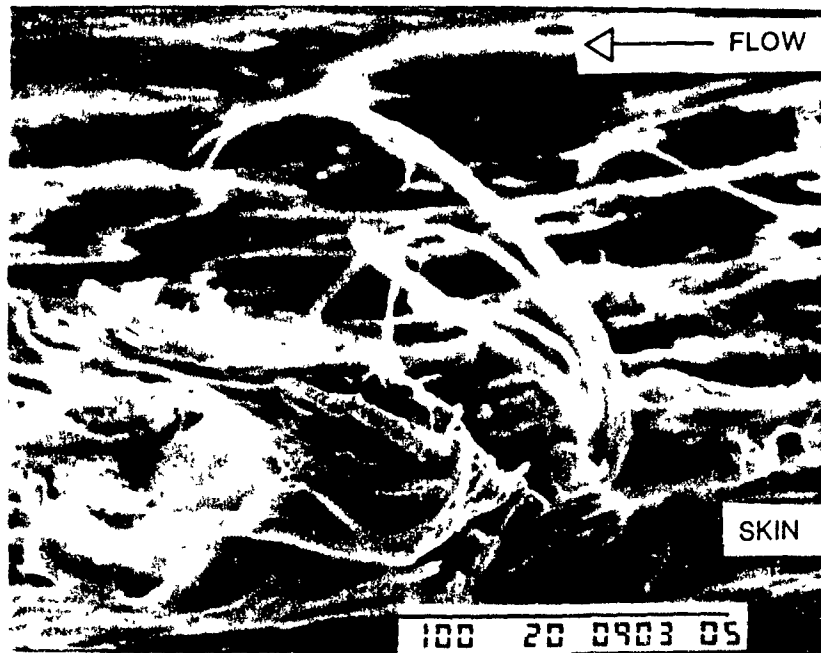


FIGURE 5.36: SEM photomicrograph of an injection molded sample (1T) broken in the X-Z plane

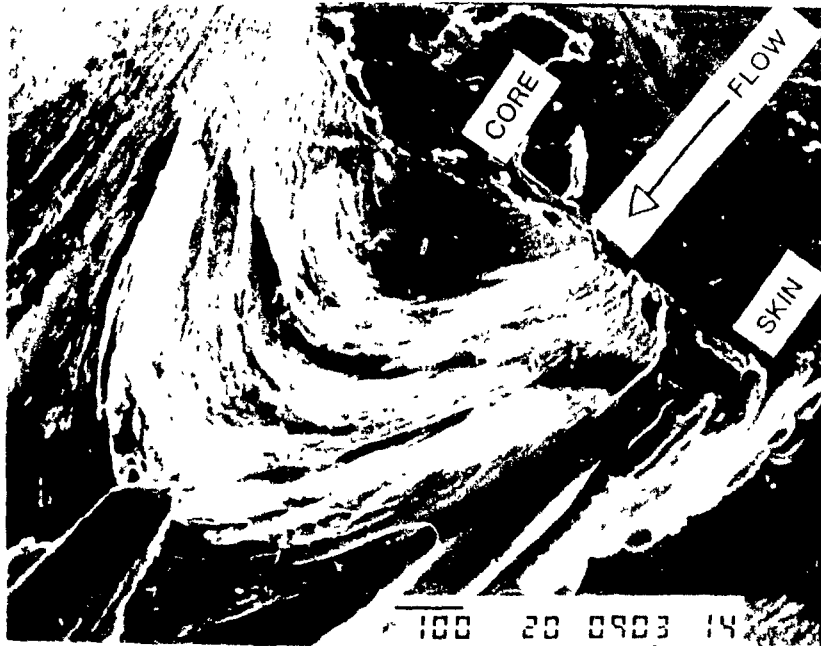


FIGURE 5.37: Electron photomicrograph of an injection molded sample (1T) broken in the X-Z plane.

5.6.2.3 Density (Crystallinity)

The variation of liquid crystalline copolyester density (crystallinity) across the thickness of a molded part is related to the crystallization phenomena occurring during the injection molding process. The variation of the density as a function of distance from the surface, for sections microtomed in the X-Y plane, is shown in Figures 5.38 and 5.39, for mold temperatures of 40°C and 140°C. The density data are given in appendix A.8. The rectangular test piece was obtained from the position B of the molded plaque (as illustrated in Figure 4.9 of section 4.8.4.1),

For the low mold temperature, the density is observed to be almost constant across the thickness. The quenching process obtained when the hot melt touches the cold mold wall does not allow sufficient time for the growth of the liquid crystalline order. These results are in qualitative agreement with data obtained using Differential Scanning Calorimetry (DSC) on similar specimens. The DSC results are not reported here because of lack of consistency. It has been found that there are two different crystallization processes: a fast and slow crystallization process (see section 5.3.1). The fast process occurs instantaneously and the degree of crystallinity is independent of cooling rates, for the range between 102.4 to 3.2°C/min. In the lower range of cooling rates below 3.2°C/min, the degree of crystallinity increases linearly with cooling rates. The cooling rates involved during the molding operation are, very high, so that the fast crystallization process is the only process occurring during molding.

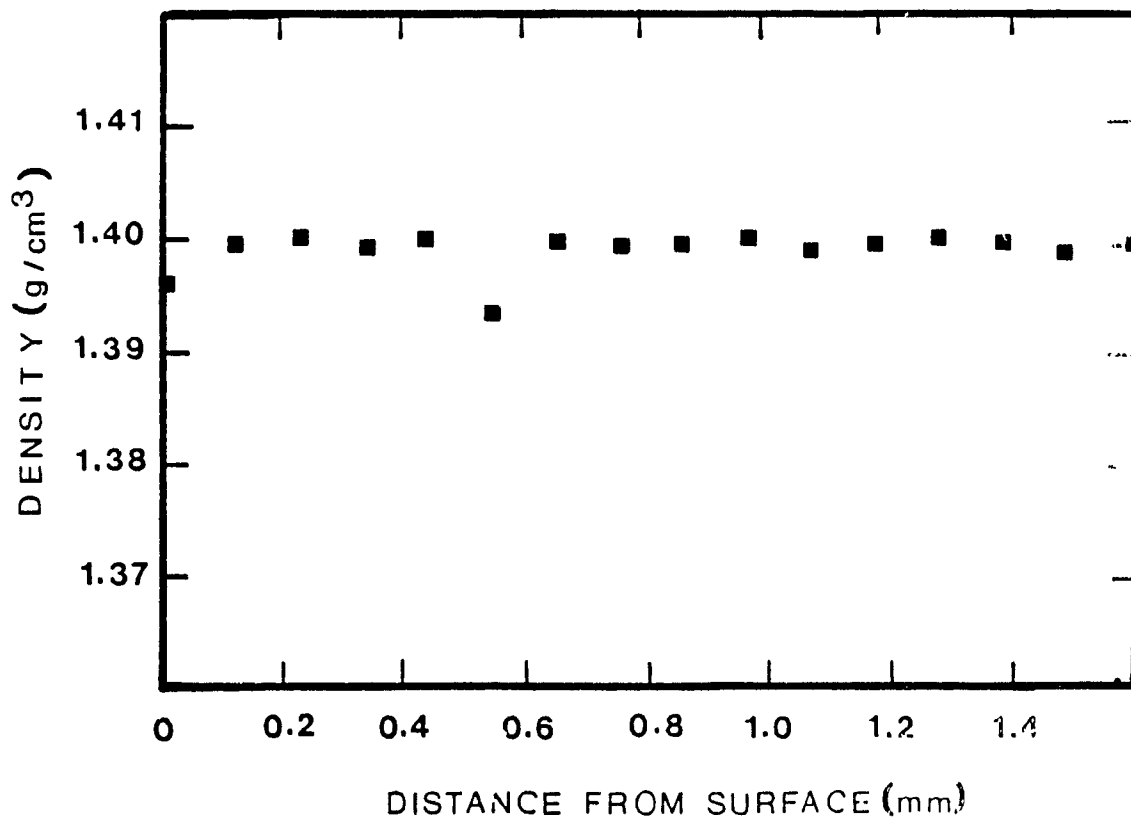


FIGURE 5.38: Density variation of microtomed sections in the depth direction of a sample molded at low mold temperature (40°C).

The results at the higher wall temperature, 140°C, shown in Figure 5.39, indicate that the density is lower at some intermediate layer between the skin and core layers. It is suggested that the low density in this region is associated with higher orientation obtained due to the higher shear stresses in that zone. Density in these materials tends to be inversely proportional to orientation.

5.6.2.4 X-Ray Diffraction

X-Ray Diffraction is a useful technique for microstructure characterization. It gives insight regarding the crystalline orientation and molecular ordering. Joseph et al. (98) reported the first x-ray study on thin slices microtomed in the depth direction of injection molded liquid crystalline copolyester samples. they observed a skin-core morphology with three different layers across the thickness; a skin layer oriented parallel to the flow direction and intermediate and core layers exhibiting much less orientation. The rather indistinct WAXS pattern indicated a low degree of crystallinity. Blundell et al. (46), focusing on the variations that could be produced by changing the characteristics of the polymer, at a molecular level, explored how a change in the molecular linearity of a chain affected the degree of orientation and general layer structure in a molding. Furthermore, they established a quantitative relationship between orientation in the moldings and the measured modulus. They concluded that the observed modulus increase with increased chain linearity is essentially a consequence of higher orientation. Recently, Hedmark et al. (99) reported results of $\langle \cos^2\theta \rangle$ as a function of distance from the surface for two molded samples with 2.9 and 5.8 mm thickness. Three and five different layers were

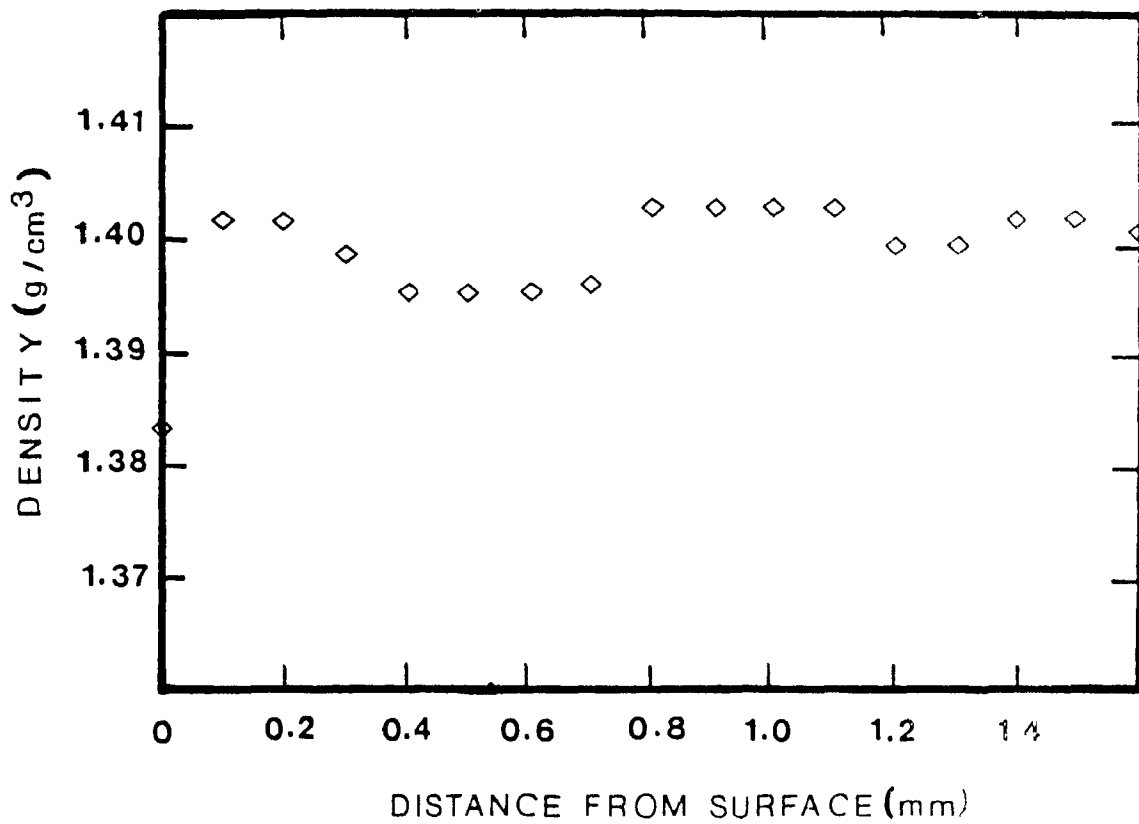


FIGURE 5.39: Density variation of microtomed sections in the depth direction of a sample molded at high mold temperature (140°C).

observed for the 2.9 and 5.8 mm thick samples, respectively.

X-Ray diffraction was carried out in this work to reveal chain orientation in the different morphological layers as observed in the microscopic studies discussed above. One of the main purposes of these studies was also to determine if these morphological layers have an internally uniform chain orientation, as revealed by the SEM.

The WAXS patterns for the layers are shown in Figure 5.40. In the same Figure, corresponding Hermans orientation function values for the same sections, obtained with infrared spectroscopy (FTIR) are given for comparison. It is clearly shown that there are at least four different morphological zones. A surface layer oriented parallel to the flow direction, the next layer below the surface with much less oriented material, and the third layer is oriented again parallel to the flow direction. Finally the fourth layer, which represents the center of the sample thickness, is observed to be oriented transverse to the flow direction.

5.6.2.5 Infrared Spectroscopy

The mechanical properties are greatly influenced by the state of orientation present in the molded part. In conventional polymers, crystallization occurs simultaneously with orientational flow, inducing an axial orientation parallel to the flow direction. If this orientation is frozen-in, the effect will produce anisotropic properties of the end-product.

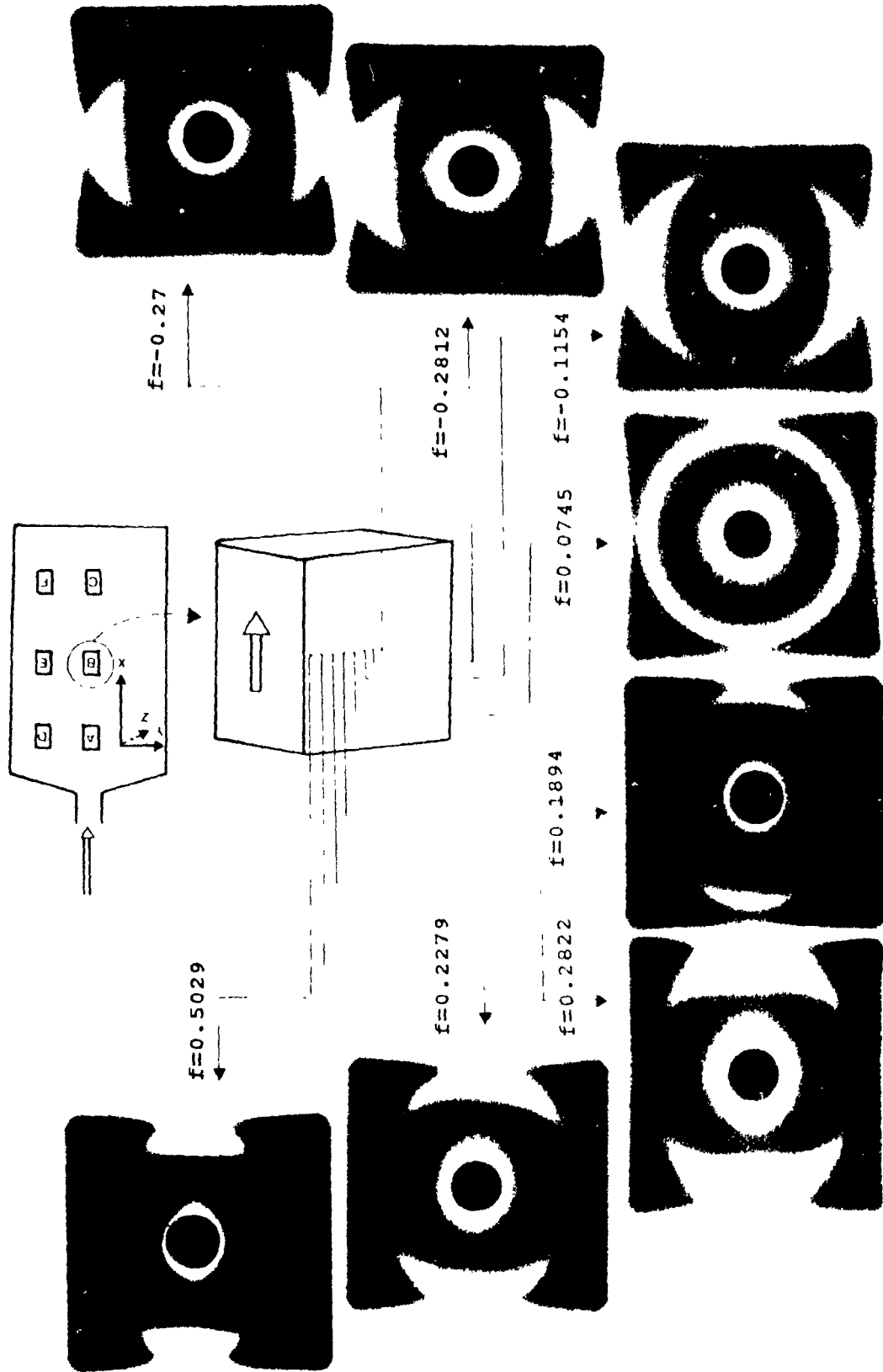


FIGURE 5.40. WAVELENGTHS: 1.0000; DISTANCE: 1.0000

In the case of the polymer liquid crystalline copolyester of the type under study, the crystallization rate is very rapid (see results obtained from the study on thermal behavior reported in section 5.3.1). The driving force for cooling the material from the molten state (330°C) to below the glass transition temperature (100°C) is very high. Thus, the part freezes almost immediately. Consequently, only the fast crystallization process will occur due to the high cooling rates present during the molding process. As a result, the molded parts will have almost constant crystallinity across the thickness, as suggested in the previous sections. However, molecular orientation varies across the thickness, depending on the type of predominant flow during molding. The filling stage induces most of the orientation obtained in the molded part, since, in the packing stage the melt motion is significantly reduced. Because of long relaxation times and high crystallization rates associated with these materials, most of the orientation developed during the filling stage is retained. Hence, flow phenomena occurring during the filling stage effectively determine the final state of orientation obtained in the molded article.

Molecular orientation was evaluated employing a method reported by Kissin et al. (100). The technique employs measurements of infrared absorbance of microtomed sections along mutually perpendicular axes. The vibrations with transition moments perpendicular to the polarized infrared beam appear with enhanced intensity, whereas the vibrations with transition moments parallel to the polarized infrared beam interact little. Thus, the method estimates the proportion of polymer molecules with their chain axes aligned in each of the respective directions. In the following discussion, the orientation of the molecular chains is described relative to the X axis i.e. the flow direction.

The orientation function used in conjunction with this technique is a Hermans type function f . The orientation functions f calculated from the dichroic ratios were obtained for the microtomed sections, as explained in section 4.6.2.2. Orientation functions are plotted as functions of distance from the surface (Z-direction). A value of f equal to 1 implies that all the molecules are perfectly aligned parallel to the flow direction. When f is equal to 0, the molecular orientation is random, and when f is equal to -0.5, all the molecules are oriented transverse to the flow direction.

(a) Orientation Distribution in Moldings

Figure 5.41 depicts the variation of orientation functions in the depth direction of microtomed sections from the test pieces obtained at the three different positions along the centerline of the molded plaque (A, B and C as represented in Figure 4.9, in section 4.8.4.1). The data are given in appendix A.9. Inspection of cross-sections machined in the transverse direction (Y-direction) of the test piece reveals that these polymers have layered structure, with layer thicknesses visible to the naked eye, as observed earlier by Weng et al. (65) and Ophir and Ide (72). Four layers can be distinguished from the surface to the center of the molding, which are believed to be associated with differences in the thermo-mechanical history experienced by the different layers. The surface layer or the skin, is oriented parallel to the flow direction. It is probably formed under the influence of elongational stretching at the flow front, in the presence of fountain flow, coupled with the quenching effect of the mold wall, as described by Tadmor (60). The melt in the

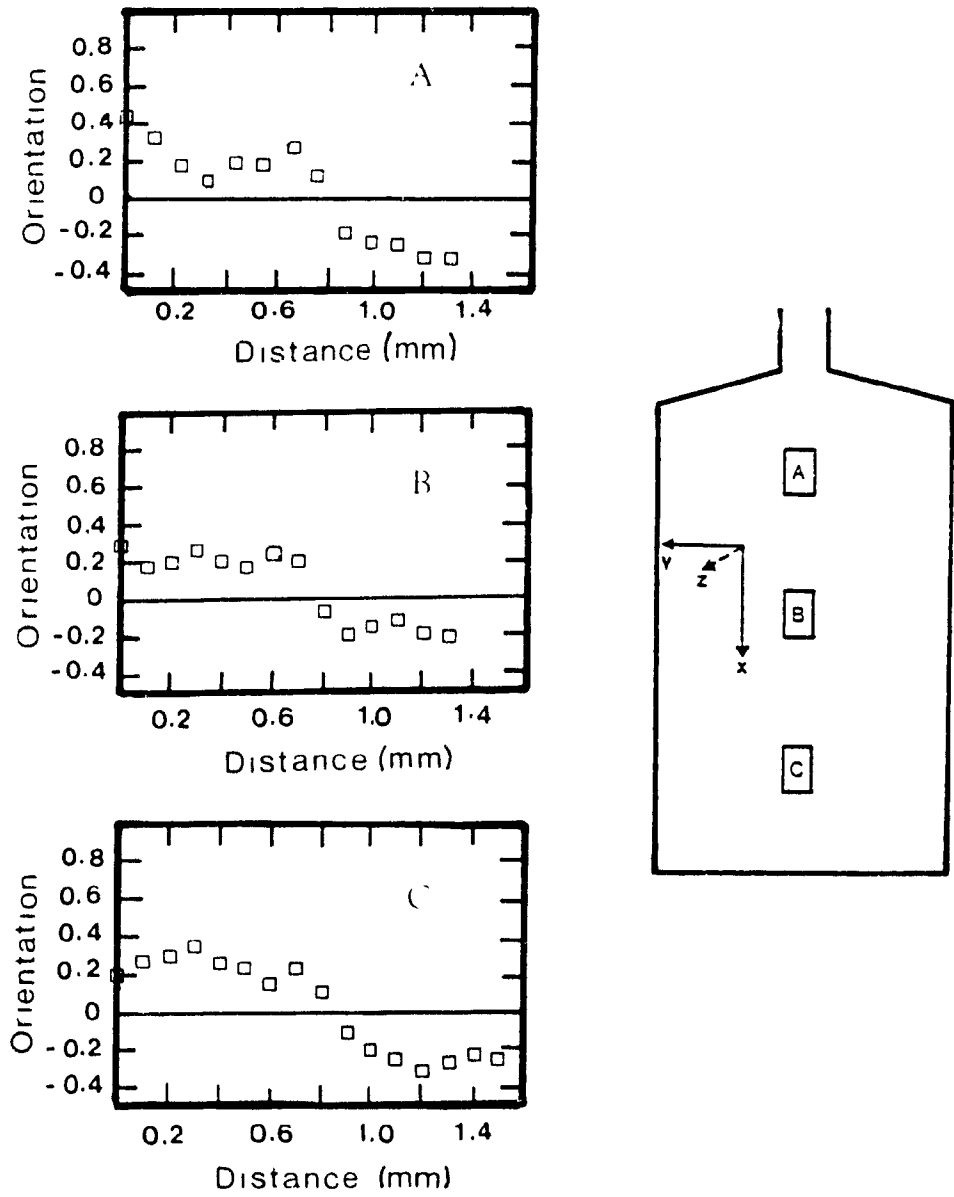


FIGURE 5.41: Variation of molecular orientation in the depth direction, at different positions A, B and C along the centerline of the molded plaque.

flow front region undergoes fountain flow from the core towards the wall, where it experiences strong elongational flow; the oriented melt is deposited at or near the wall, freezing almost instantaneously to form a highly oriented skin layer. The second layer or the sub-skin layer involves material behind the flow front which did not experience significant stretching in the flow direction and was frozen-in in a less ordered state, as compared to the skin layer. The third layer or the intermediate layer is oriented again parallel to the flow direction. It originates in the high shear zone next to the frozen skin and sub-skin layers. Normally, the developing frozen layer causes a narrowing of the flow channel, and thus contributes to raising the shear rate at the solid-melt boundary. This high shear rate produces a local maximum in the orientation within the intermediate zone. Finally, the fourth layer is in the center region of the molding or the core. It generally exhibits orientation perpendicular to the flow direction. The low shear rate in the core and the transverse stretching of the melt in the core as the material emerges from the gate into the cavity contribute to the transverse orientation in this zone (101). Effectively, the same trends are observed at the three positions A, B, and C. Figure 5.41 suggests that the thickness of the skin layer decreases with increasing distance from the gate, while the intermediate zone tends to grow. Similar observations were reported by Boldizar (102) on the basis of data relating to the mechanical properties of injection molded samples of the same material. For the positions B and C, the maximum orientation for the skin layer is lower than that of position A. This is similar to observations reported by Singh and Kamal (103) for short-fiber filled polypropylene moldings. Furthermore, the sub-skin layers for the samples B and C are more oriented than in sample A near the gate. The amount of orientation observed for the sub-skin layers in samples B and C is equivalent to that observed

for the intermediate zone, which might be due to a thicker solidified layer away from the gate. Liquid crystalline polymers (LCPs) have been shown to behave similarly to short-fiber polymer composites, where fiber orientation is mainly controlled by hydrodynamic forces (101). In elongational flow, both LCPs and short fiber moldings exhibit almost perfect orientation in the flow direction. Consequently, enhanced mechanical properties develop in the orientation direction.

Figure 5.42 shows the variation of molecular orientation as a function of distance from the surface for microtomed sections at positions D, E and F of a molded plaque, as shown in Figure 4.4. Orientation functions for the position D indicate a skin layer with a preferred orientation along the flow direction (X-direction). Furthermore, relatively low order is observed in the intermediate and core layers. Similar trends are observed for the position E. However, none of the three positions shows transverse orientation in the core region, in contrast to the samples taken from the centerline (A, B and C). This is due to the spreading flow of the polymer melt at the gate and reorientation of the melt towards the flow direction (X-direction) away from the centerline and especially close to the side mold walls. Similar behavior was reported for injection molded short-fiber reinforced polypropylene (103).

(b) Effect of Processing Conditions

The effect of processing conditions has been investigated by other workers (68,70-72,102,104,105). However, only sketchy results have been reported. It is known that the processing conditions have a marked influence on the

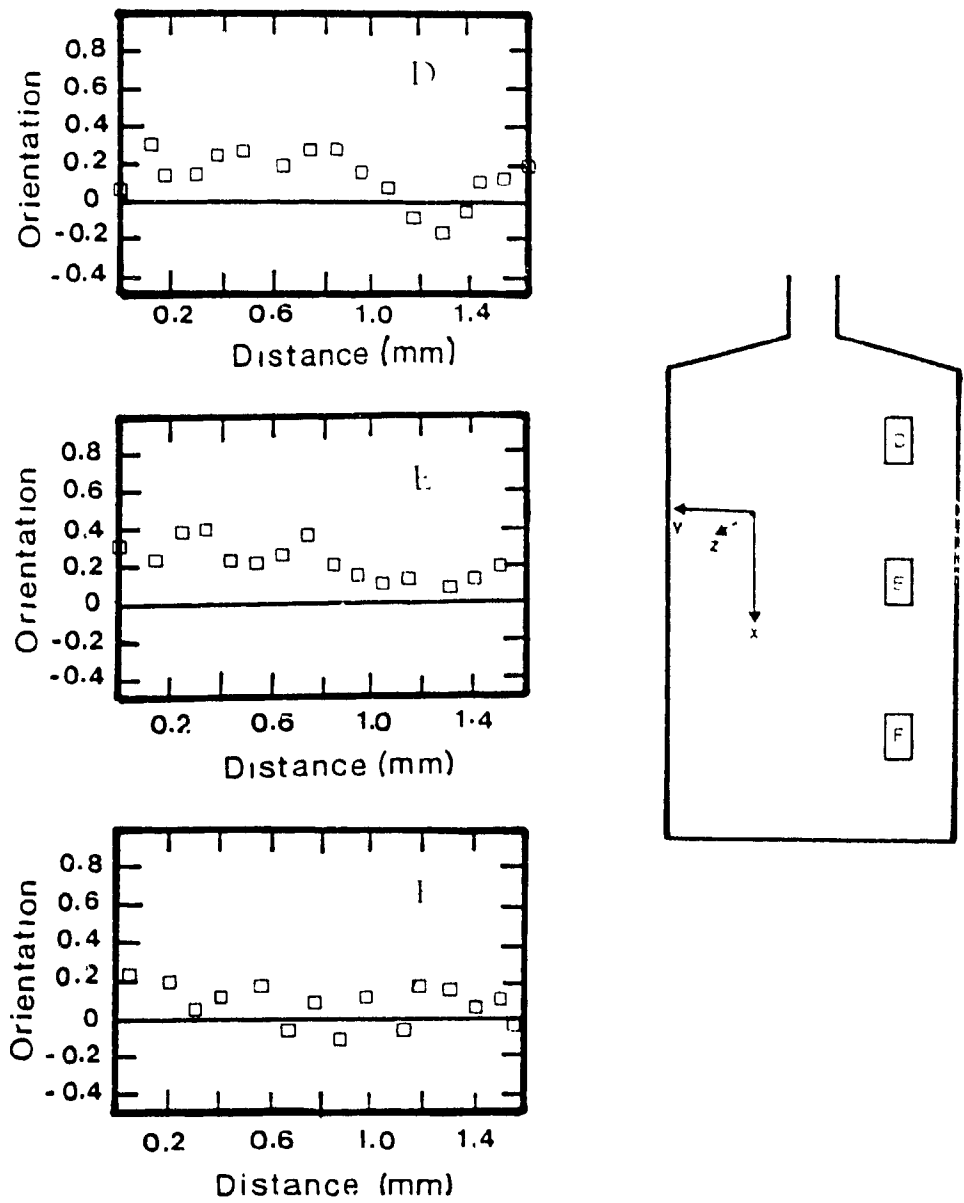


FIGURE 5.42: Variation of molecular orientation in the depth direction at different positions D, E and F away from the centerline near the mold wall.

properties of the injection molded thermoplastic parts, and the same can be expected for liquid crystalline polymers. Since liquid crystalline polymers exhibit substantial anisotropy, as indicated in the last section, it appears possible to manipulate the extent and distribution of this anisotropy by variations in processing conditions and design parameters, as reported by Jackson and Kuhfuss (12) and Ophir and Ide (72).

Position B, in the center of the molded plaque was chosen to study the influence of processing conditions on molecular orientation. Microtomed sections were obtained in the depth direction of the rectangular test piece representing the position B.

The effect of mold temperature on molecular orientation distribution as a function of distance from the surface is shown in Figure 5.43. It is observed that, at low mold temperature (40°C), the surface layer is thicker and more oriented along the flow direction (X-direction) compared to that obtained for the high mold temperature (140°C). Furthermore, at lower mold temperature, the intermediate layer shows an orientation parallel to the flow direction, as explained earlier in this section. This is probably due to the high shearing action, at the solid-melt interface of the frozen layers on both sides of the mold walls. The mold temperature affects mostly the thickness of the third layer, as it was reported recently by Suokas (105), for photomicrographs obtained by optical and scanning electron microscopy. He observed that the thickness of the surface layer decreased slightly with increasing mold temperature, and the third layer expanded at the expense of the fourth layer. The rise in mold temperature results in a reduced heat conduction rate, which increases the thickness of the intermediate layer, while the sub-skin and core layers

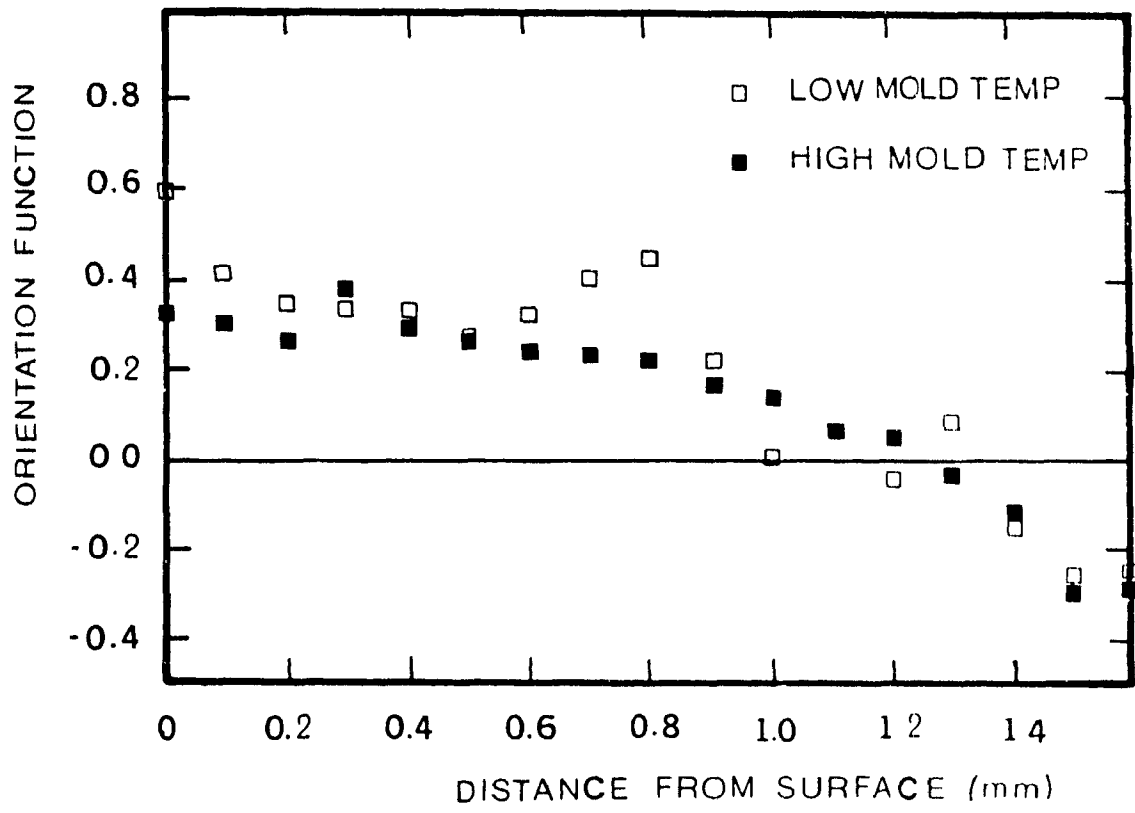


FIGURE 5.43: Variation of molecular orientation in the depth direction of an injection molded sample at two different mold temperatures.

remain almost unaltered. This finding is in good agreement with what has been reported by Duska (105) and Suokas et al. (70).

Figure 5.44 shows the effect of injection pressure on the properties of the molded parts. Differences are observed in the skin, intermediate and core layers. The surface layer of the sample molded at lower injection pressure is more oriented parallel to the flow direction than that molded at higher injection pressure. This finding is in concordance with results reported by Duska (105) on similar LCP molded samples. At higher injection pressure, the intermediate layer shows a higher orientation in the flow direction. The amount of viscous heat dissipation at higher injection pressure increases, especially in the intermediate zone. Therefore, the polymer viscosity will decrease as the injection pressure increases.

Figure 5.45 depicts the variation of molecular orientation at two different injection speeds. Lower injection speed induces higher orientation in the skin and intermediate layers compared to that obtained at higher injection speed. However, the core layer is not significantly affected by the change in the injection speed. The thickness of the skin layer is significantly affected by the cooling and heat transfer that takes place during the filling stage of the cavity (106). Slower filling produces a thicker skin layer, due to the higher degree of cooling during the filling stage. Lower injection velocity causes less viscous dissipation in the intermediate zone on both sides of the solidified skin layers at the walls of the mold. Therefore, the internal stream of molten polymer flowing to fill the remainder of the mold cavity experiences higher orientation in the intermediate zone. The core layer is not affected significantly by the change in injection speed.

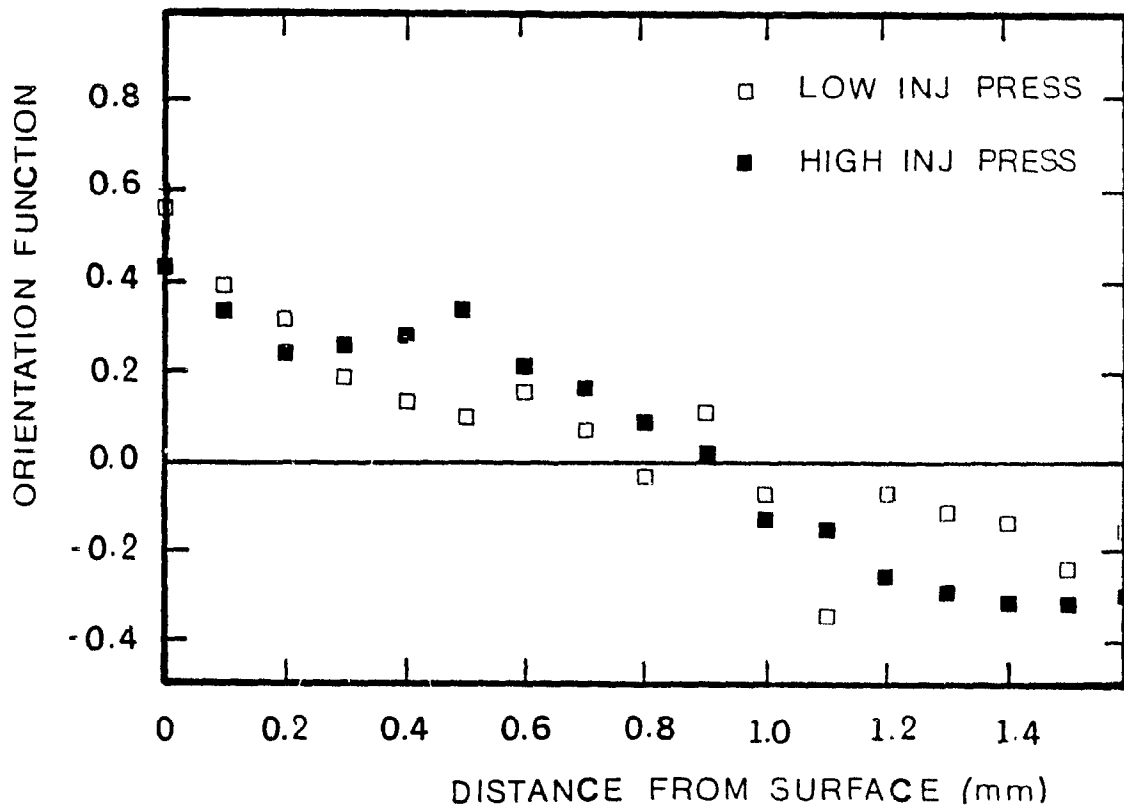


FIGURE 5.44: Variation of molecular orientation in the depth direction of an injection molded sample at two different injection pressures

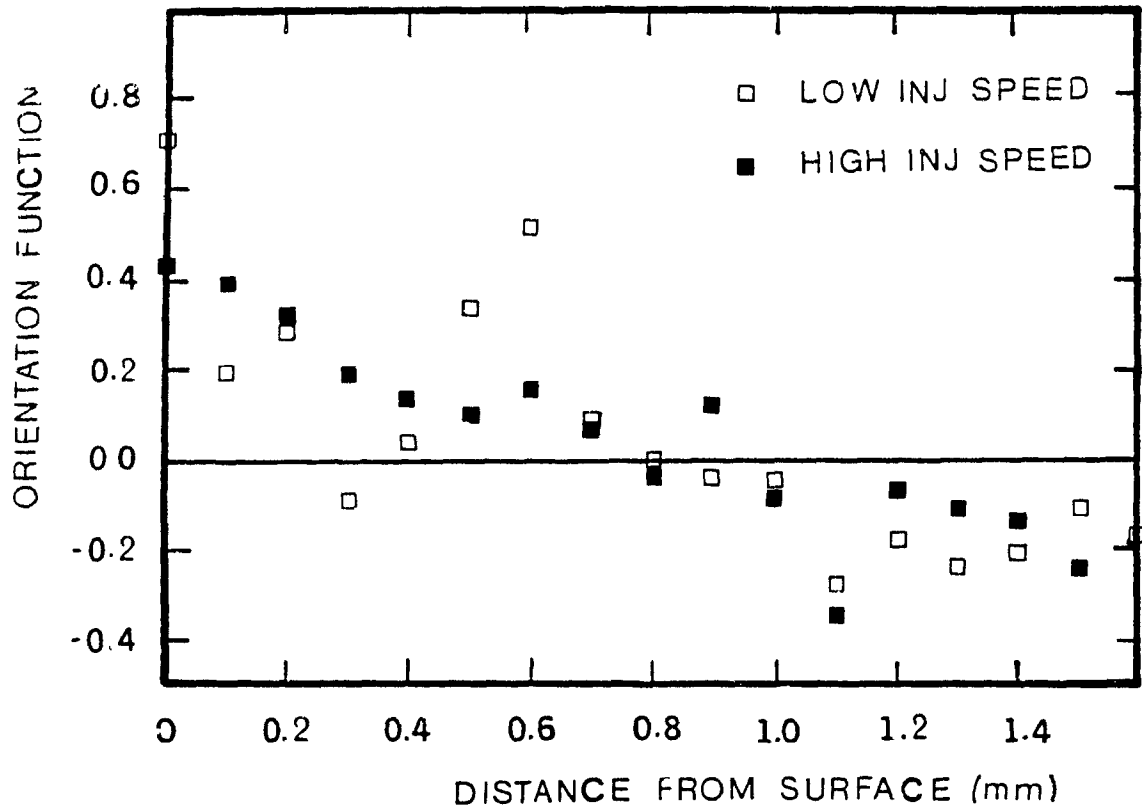


FIGURE 5.45: Variation of molecular orientation in the depth direction of an injection molded sample at two different injection speeds

5.6.2.6 Microhardness Testing

The purpose of this experiment was to evaluate the possibility of using microhardness as a technique to differentiate between the morphological zones across the thickness of injection molded samples, by comparing microhardness data with the results obtained using other techniques such as infrared spectroscopy and three-point bending.

The principle of the test is reported in more detail in section 4.8.1.7. The indenter is applied on the X-Z plane with the long diagonal being parallel to the flow direction (X-direction). Measurement with the diagonal parallel to the injection direction, yields data regarding variation of microhardness in the depth direction of injection molded samples. The indenter length (long diagonal) varies according to the molecular orientation. The value of the length of the long diagonal is higher when the molecules are oriented parallel to the direction of measurement, which is the machine direction. The value of the microhardness is inversely proportional to the indenter diagonal. For the sake of simplicity, and also for easier comparison of results obtained with other techniques, the indenter length is plotted as a function of distance from the surface of the molded specimen in contact with the mold.

The variation of the indenter length as a function of distance from the surface depends mainly on molecular orientation, since observations, based on the DSC and density results, reported in sections 5.3.1 and 5.6.2.3, respectively, have

shown that the crystallinity/density change across the thickness (Z-direction) is negligible. Bowman and Bevis (107,108) have evaluated the microstructure of molded parts using the Vickers microhardness test and concluded that the microhardness of injection molded samples can be used to determine the relationships between structure and processing conditions.

In order to have a detailed description of the variation of microhardness across the thickness of the molded sample, the measurements were made every 150 μm . Microhardness measurements were also made every 300 μm and 450 μm . The data are shown in Figure 5.46, which shows that the results are identical, thus indicating that up to 150 μm , the effect of spacing between the measurement is negligible.

(a) Microhardness Measurements

The variation of microhardness as a function of distance from the surface to the middle of the cross-section of the sample (1L) is shown in Figure 5.47. The results show that the value of the indentation length, obtained by measuring the long diagonal, near the surface, is higher at all three positions A, B and C, and decreases towards the center of the thickness. A second maximum is observed in the intermediate layer, which, as discussed previously in section 5.6.2.5, may be due to the high shear stresses in the constricted channel at both sides of the frozen skin near the wall of the mold cavity. The orientation of the skin layer is higher near the gate and decreases towards the end of the mold. The proportion of oriented material parallel to the flow direction is higher for the position B (representing the

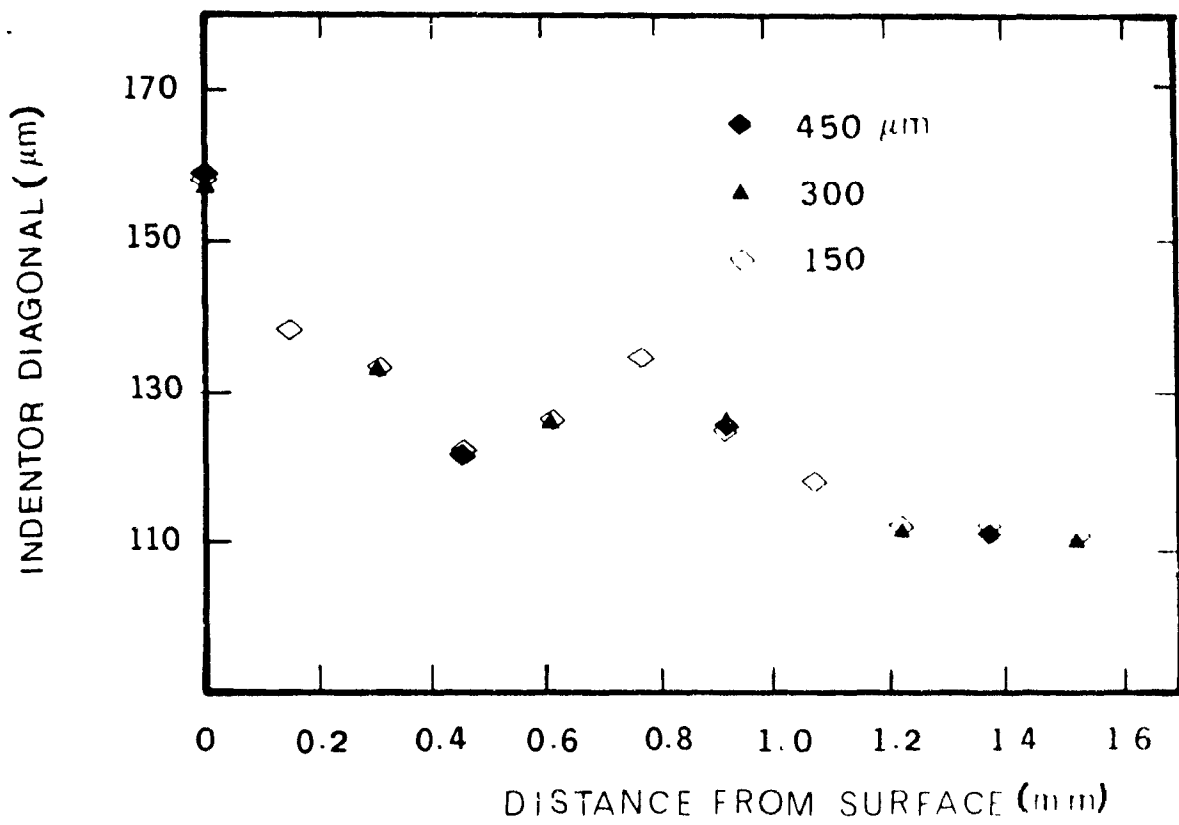


FIGURE 5.46: Effect of distance between indentations

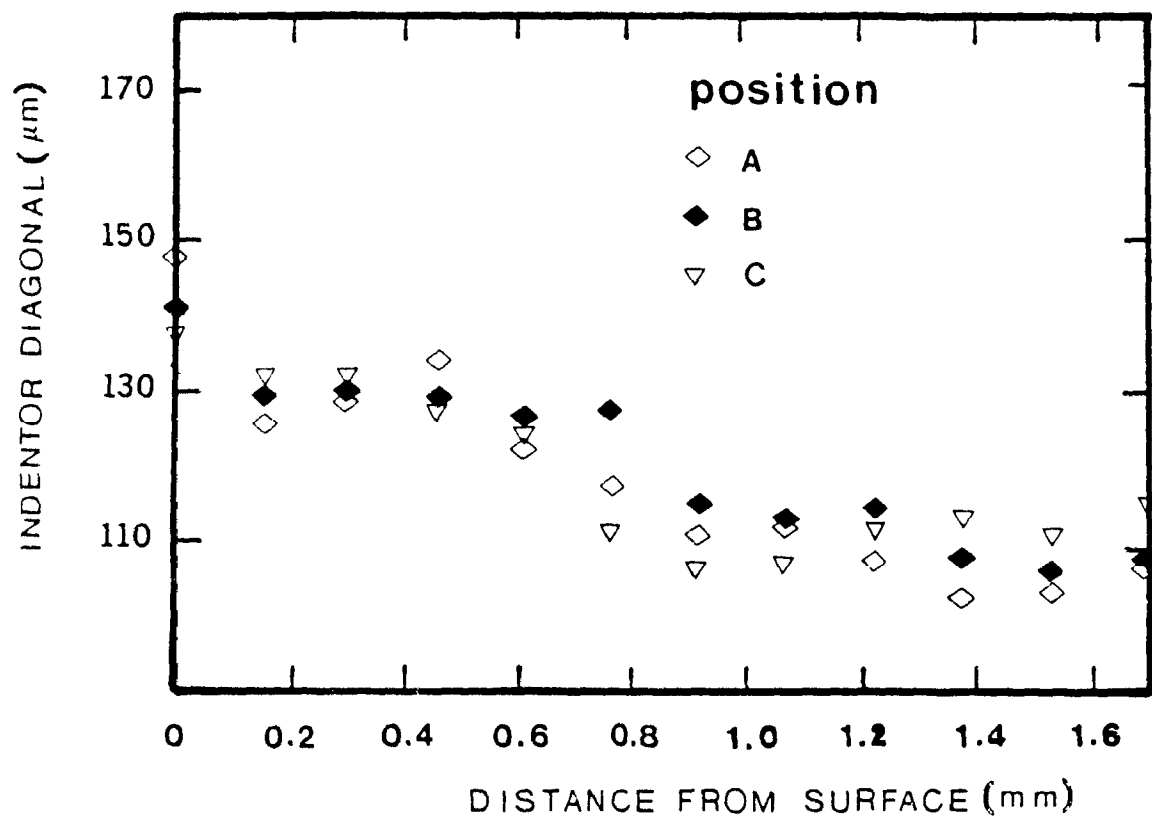


FIGURE 5.47: Variation of microhardness in the depth direction, and at different positions along the centerline of the molded plaque.

center of the plaque). The orientation is maximum at the surface near the gate and at the end of the mold where, in both cases, the frozen layer is the thinnest.

Figure 5.48 shows microhardness distribution in the depth direction of two samples molded under the same processing conditions in order to evaluate the sample-to-sample consistency. The results show that, for two samples molded under the same conditions, as illustrated by the replicates of cavity and nozzle pressure-time profiles in Figure 5.24, the repeatability is good.

(b) Effect of Processing Conditions

Figure 5.49 depicts the variation of microhardness across the thickness of samples molded at two different mold temperatures. The skin layer exhibits slightly higher orientation in the flow direction at lower mold temperature. Also, at lower mold temperature, the intermediate layer shows more orientation in the flow direction, probably due to the high shearing action at the solid-melt interface in the narrow channel caused by the solidified polymer layer. The mold temperature affects mostly the thickness of the intermediate layer. This observation is in good agreement with orientation data obtained with infrared measurements.

The variation of microhardness along the thickness of samples molded at two different injection pressures is shown in Figure 5.50. Lower injection pressure causes higher orientation in the flow direction in the skin layer. Higher injection pressure has the tendency to cause higher orientation in the sub-skin and the intermediate layers parallel to the flow direction. The microhardness in the centre

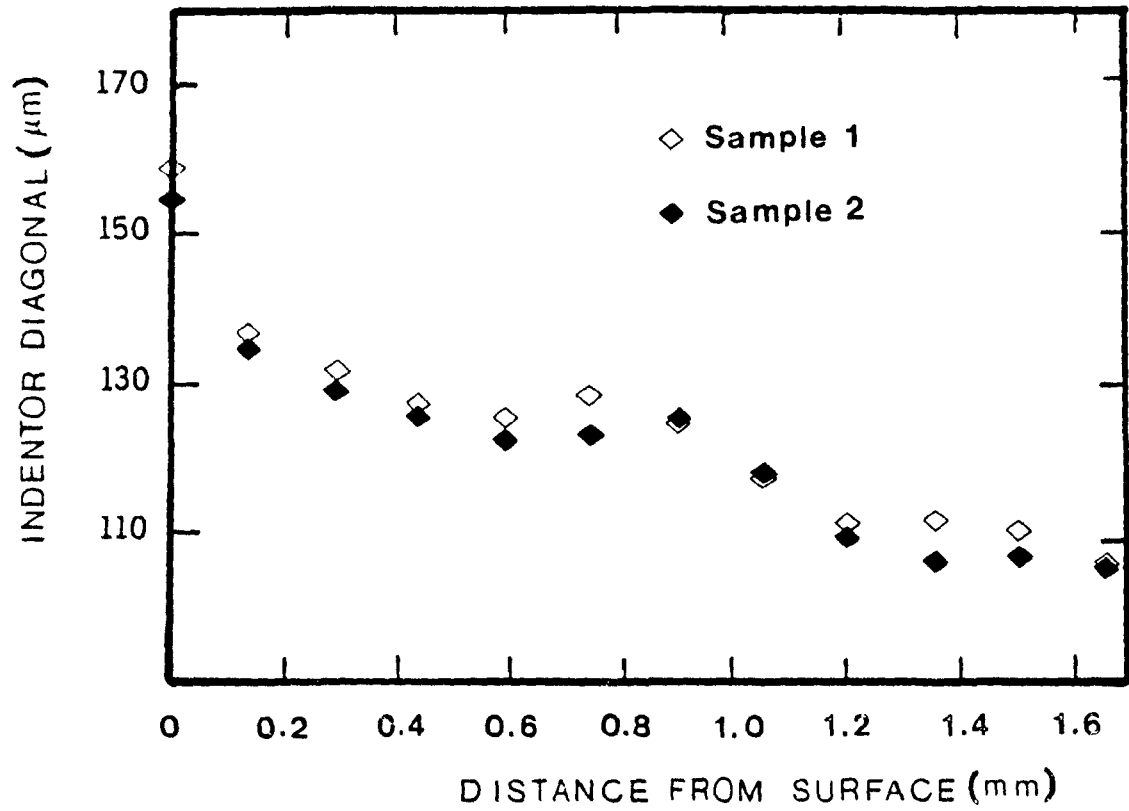


FIGURE 5.48: Replicates of microhardness measurements performed for two different samples molded under the same conditions.

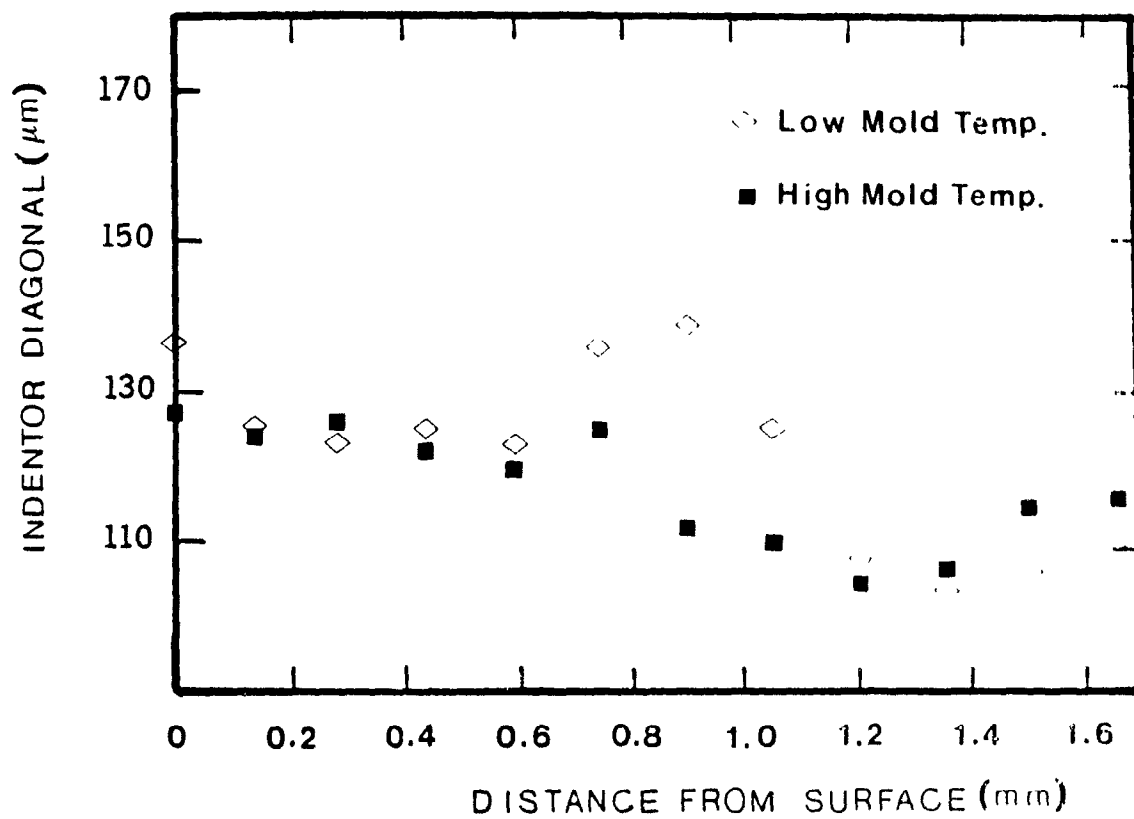


FIGURE 5.49: Variation of microhardness across the thickness of the molded sample at different mold temperatures.

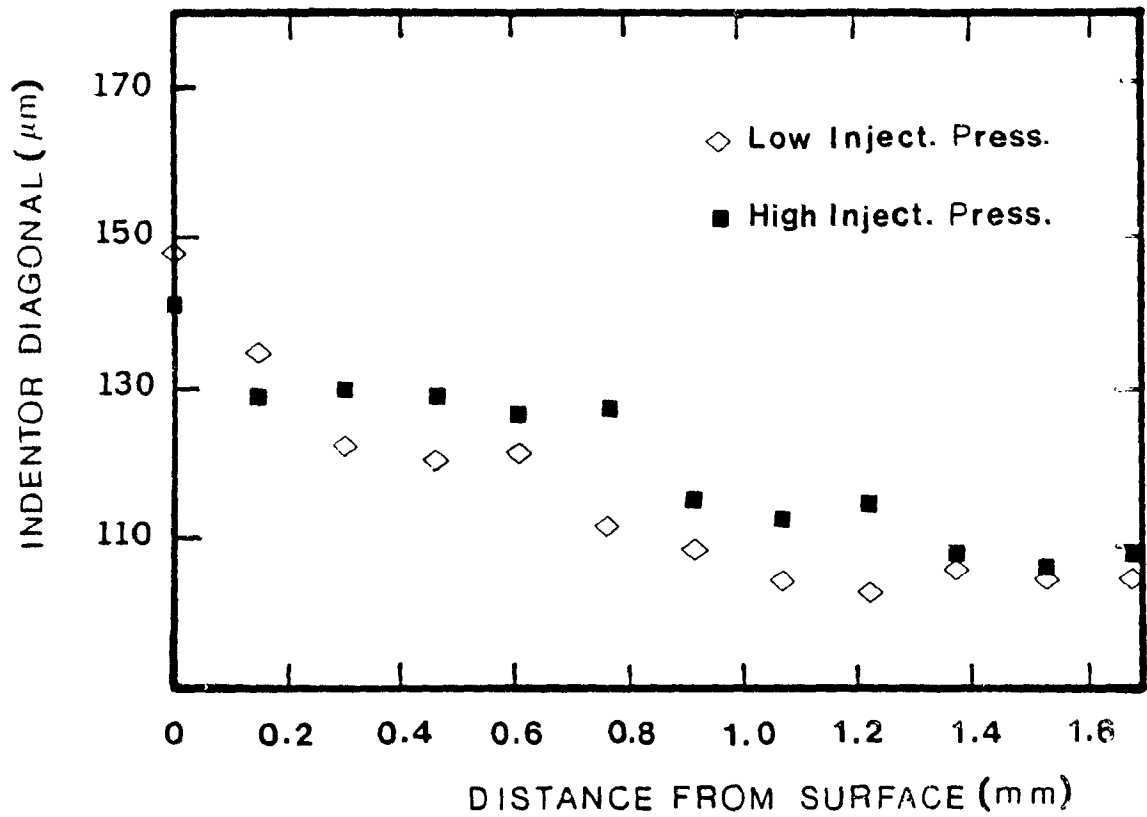


FIGURE 5.50: Variation of microhardness across the thickness of the molded sample at different injection pressures.

core region is not significantly affected by the change in injection pressure.

Figure 5.51 illustrates the variation of microhardness as a function of distance from the surface in samples molded at two different injection speeds. The skin and intermediate layers are more oriented along the flow direction at low injection speed. This is in agreement with the results of Duska (105), who suggests that lower injection velocity decreases the amount of viscous heat generated between the already solidified skin layers and the molten polymer stream, thus producing a thicker skin layer.

5.6.2.7 Flexural Modulus

The flexural modulus distribution along the depth direction gives a good indication of the overall strength of the part. The major contribution to strength in the flow direction is provided by all the layers showing parallel orientation to the flow direction, mostly the skin and the intermediate layer. By increasing the thickness of the skin, relative to the core, the strength will increase. Therefore, if higher mechanical strength is desired in the flow direction, the part must have a larger skin to core thickness ratio. Duska (68,105) discussed the contributions of the skin and core to the tensile strength of the molded part and the role played by the processing conditions in this regard.

(a) Flexural Modulus Distributions

Figure 5.52 depicts the variation of flexural modulus in the depth

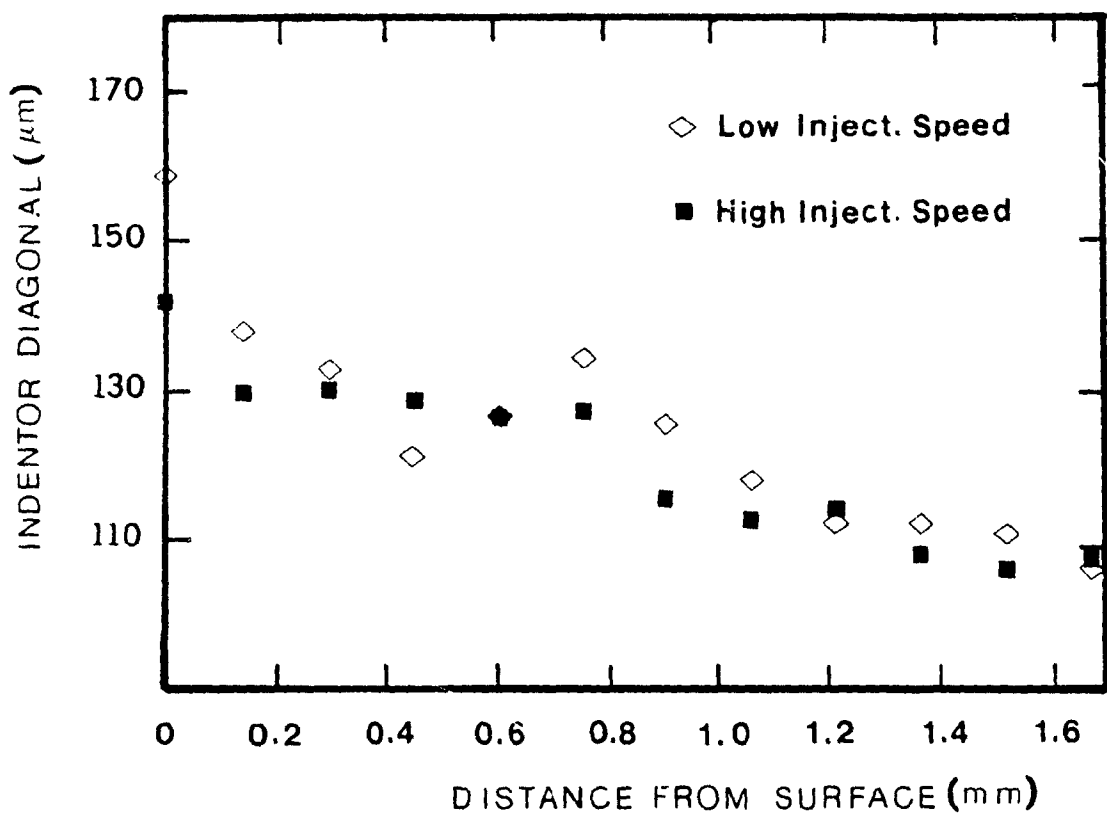


FIGURE 5.51: Variation of microhardness across the thickness of the molded sample at different injection speeds.

direction of an injection molded rectangular bar machined parallel to the flow direction (1L) and perpendicular to the flow direction (1T) (see Figure 4.10). A characteristic skin-core morphology is observed. High orientation occurs at the surface and decreases towards the center. However, a secondary maximum, occurs in the intermediate layer at half distance between the skin and the core region. This intermediate layer is also called the shear zone. It is believed that the high modulus exhibited by this layer is a result of the high shearing action of the molten polymer at the solid-melt interface on both sides of the solidified polymer layer.

The variation of flexural modulus in the depth direction for the sample machined perpendicular to the flow direction (1T) is also shown in Figure 5.52. It is observed that a low modulus value occurs at the surface skin, but the modulus increases to exhibit the highest value near the core of the sample. The modulus in the core region of the transverse sample is comparable to the modulus in the surface layer of the longitudinal sample. This suggests that the core of the longitudinal sample is oriented perpendicular to the flow direction.

Figure 5.53 shows the variation of the anisotropy ratio, defined as the ratio of the modulus of the longitudinal sample (1L) to that of the transverse sample (1T), as a function of distance from the surface. The results show that the skin layer is highly oriented in the flow direction, while the core is oriented transverse to the flow direction. An anisotropy ratio equal to 1 indicates that the molecular orientation is random in the corresponding region. The modulus of the core region of the transverse sample is very close to the modulus value of the surface layer of the longitudinal sample. This suggests that the core of the longitudinal sample is

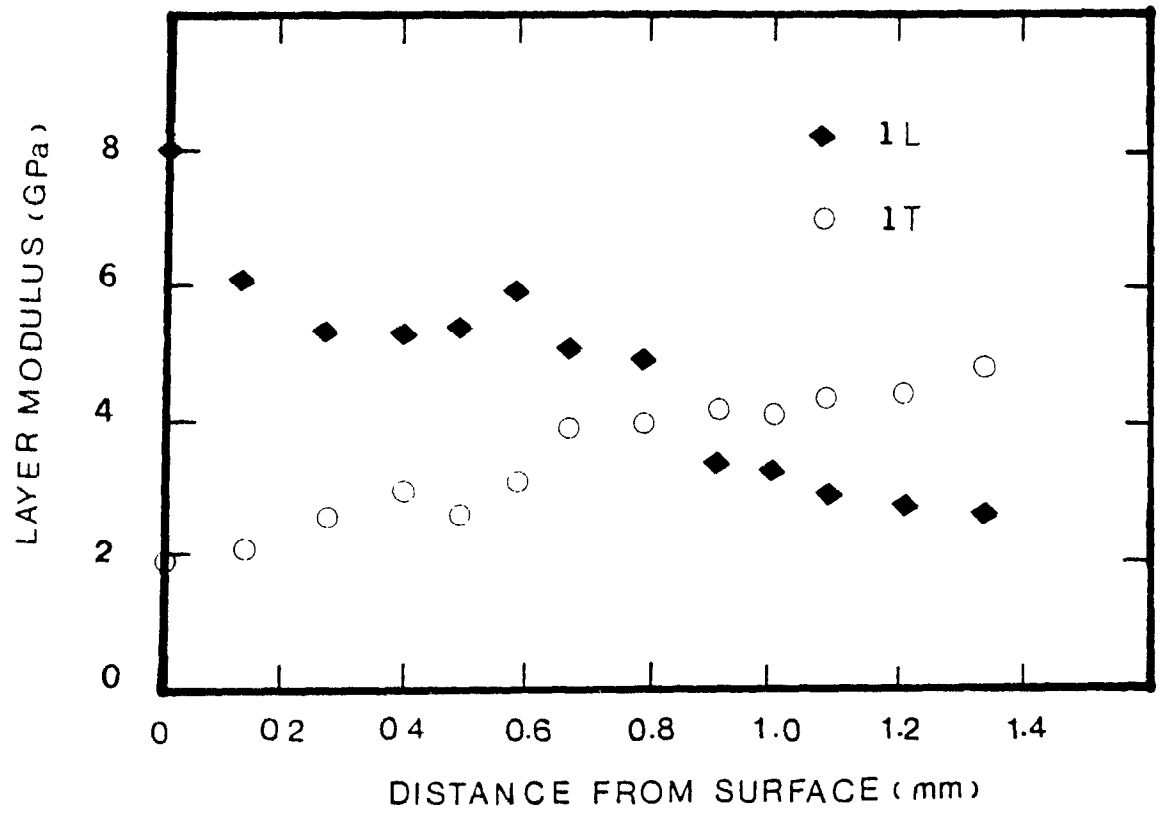


FIGURE 5.52: Layer Modulus Distribution in the depth direction of injection molded bars machined parallel (1L) and perpendicular (1T) to the flow direction

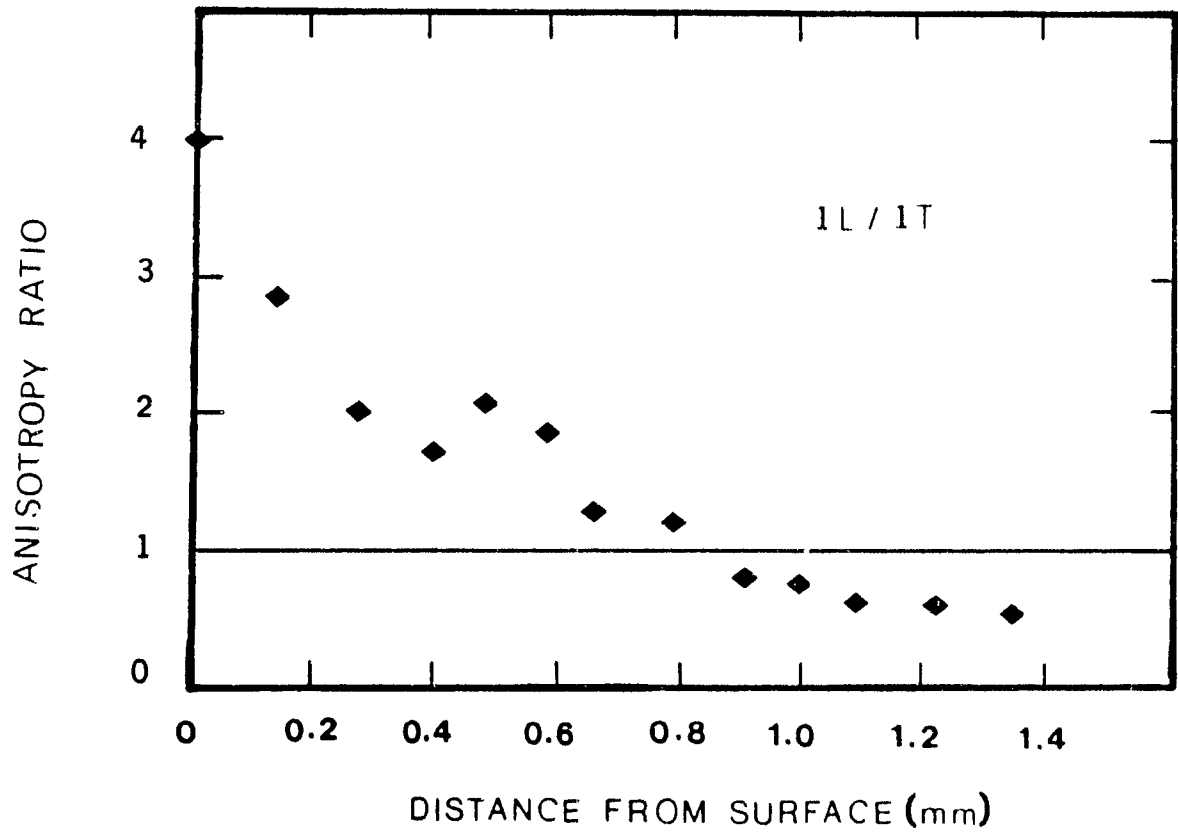


FIGURE 5.53: Anisotropy Ratio of samples machined parallel (1L) and perpendicular to the flow direction (1T).

oriented perpendicular to the flow direction.

The variation of the flexural modulus, as a function of distance from the surface, for the samples machined from the positions 2L and 1L is illustrated in Figure 5.54. Both samples showed similar trends, but the sample 2L exhibited less pronounced variation of the modulus in the depth direction. Sample 2L did not show transverse orientation in the core region according to the molecular orientation results obtained at position E, and shown in Figure 5.42 of section 5.6.2.5, using the infrared technique.

The sample 2T did not show significant differences as compared to sample 1T. These results support the orientation distribution data based on infrared measurements at positions A, B and C. The three samples exhibited similar orientation distributions, which is in agreement with the above results obtained on flexural modulus distribution. Although samples 1T and 2T were measured in the X-Z plan, transverse to the flow direction, the results would be similar to what has been obtained for the orientation distribution profiles in the X-Y plane if the samples were rotated by 90°. Both tests were performed in the centerline of the molded plaque.

(b) Effect of Processing Conditions

The mold temperature affects mostly the thickness of the third layer, as reported recently by Suokas (104) using Optical and Scanning Electron Microscopy studies. He also showed that notched Izod impact strength and tensile

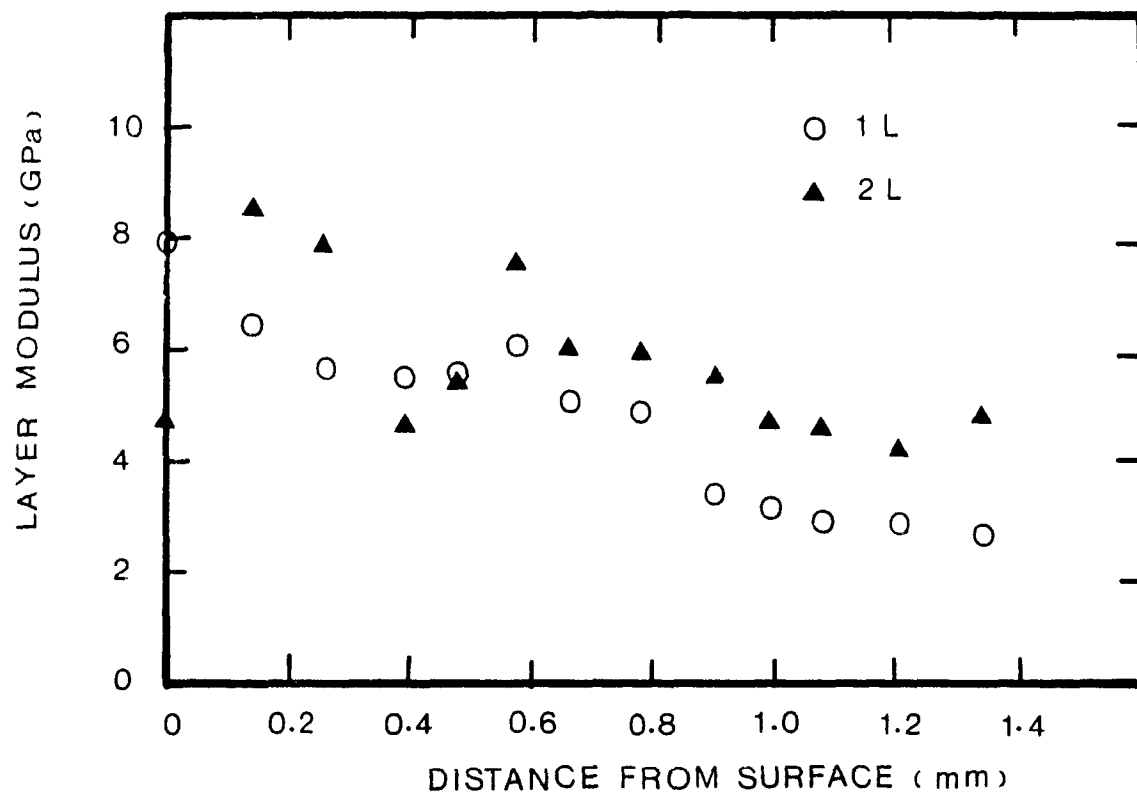


FIGURE 5.54: Layer Modulus Distribution in the depth direction of an injection molded bar (2L) as compared to sample 1L.

and flexural moduli are all orientation-sensitive. He observed that the holding pressure reduced the tensile modulus while it was beneficial for flexural modulus. The best values for Izod impact strength were obtained with the highest mold temperature. Recently Duska (105) reported that the highest values of tensile strength were obtained at low injection speed, low injection pressure and low mold temperature. Ophir and Ide (72) also reported that a lower injection rate could be beneficial with regard to the mechanical properties, although this point was not examined in detail in their work. Boldizar (102) made an attempt to estimate the variation of mechanical properties of a 3 mm thick test bar over its cross-section by machining off the surface layers and then testing the remaining part. He found that the mechanical properties varied substantially over the cross-section caused probably by the inhomogeneous degree of orientation. The author reported that a maximum in strength occurred about 0.5 mm under the surface. However, with this method, he could not estimate the mechanical properties of the skin layer.

The effect of mold temperature on the distribution of flexural modulus from the surface to the center of sample (1L) cut along the centerline is shown in Figure 5.55. The profiles displayed in this Figure show that the rise in mold temperature resulted in a slightly higher modulus of the skin layer. However, the thicknesses of the skin and the intermediate layers were higher at lower mold temperature. The lower mold temperature induces more orientation in the flow direction, because of higher shear rates occurring against the frozen skin layers. The flexural modulus distributions in the core layer was not affected by the mold temperature change. The major differences were only observed in the skin and intermediate layers.

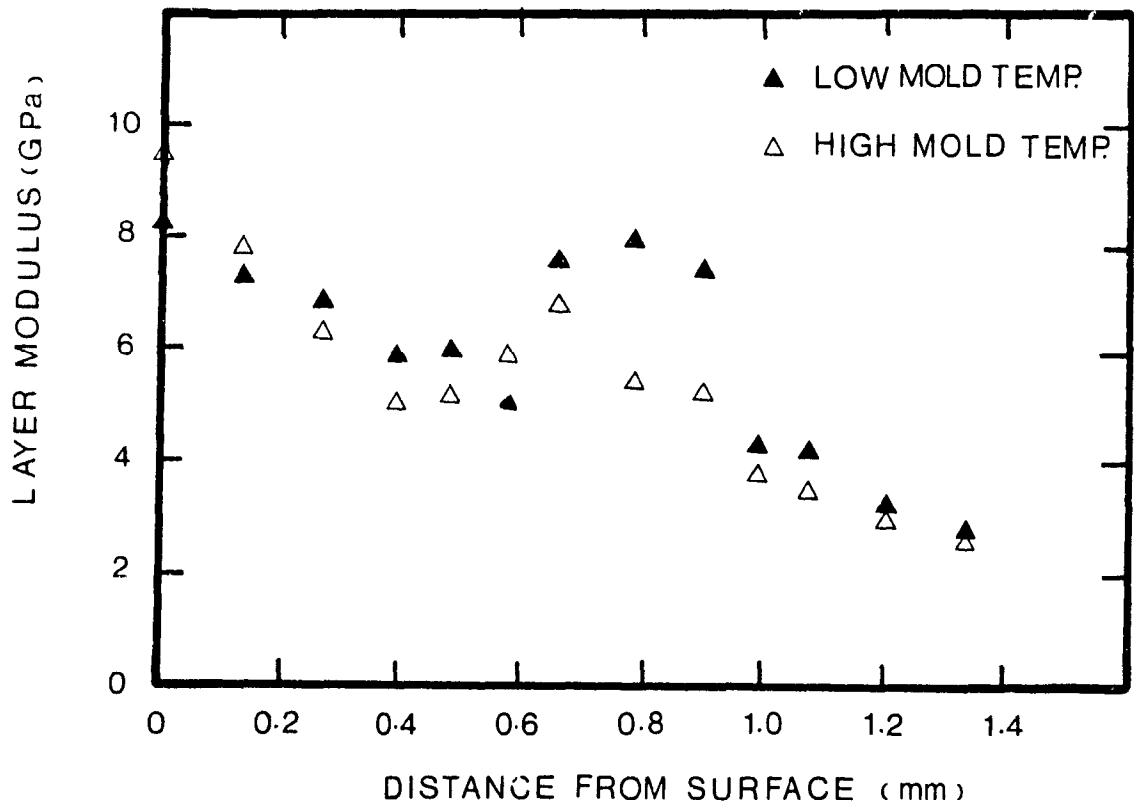


FIGURE 5.55: Effect of Mold Temperature on the flexural modulus distribution in the depth direction of injection molded samples.

Figure 5.56 shows the influence of injection pressure on the properties of the molded parts. Lower injection pressure induces more orientation along the flow direction, in the skin layer. Furthermore, a thicker core region is obtained at lower injection pressure. However higher injection pressure produces higher molecular orientation in the sub-skin and intermediate layers, resulting in higher flexural modulus values. In the central core region no significant changes were observed.

Figure 5.57 depicts the variation of flexural modulus in the depth direction of an injection molded sample obtained at two different injection speeds. It is observed that, at lower injection speed, a thicker skin layer with a higher amount of preferred orientation in the flow direction is obtained. Furthermore, a higher value of the flexural modulus due, probably to a marked shear zone in the intermediate layer, is observed. In the central core, the change in the injection speed did not affect the distribution of the flexural modulus.

5.7 Correlation and Integration of Results Obtained by Various Techniques.

Various techniques were employed to study the microstructure of injection molded articles and the effect of thermo-mechanical history during molding on microstructure.

- (1) Polarizing and Scanning Electron Microscopy clarified most of the hierarchical morphological structure that resulted from the complex

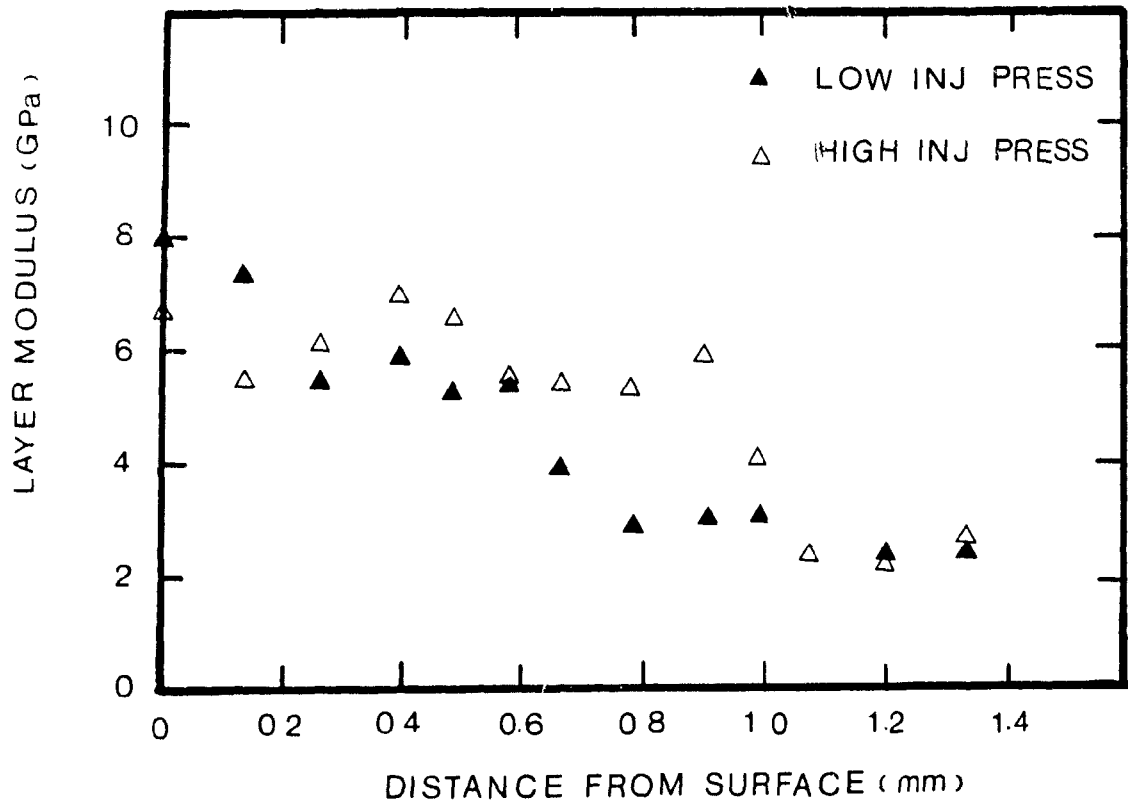


FIGURE 5.56: Effect of Injection Pressure on the flexural modulus distribution in the depth direction of injection molded samples.

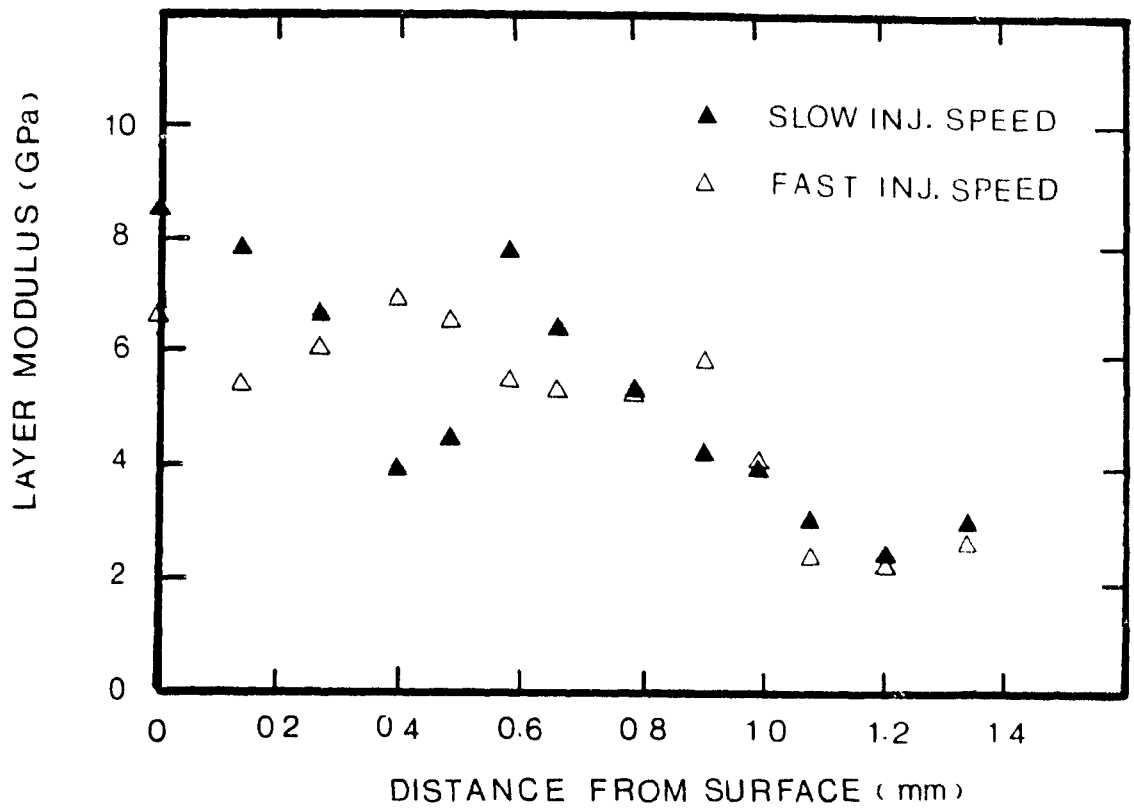


FIGURE 5.57: Effect of Injection Speed on the flexural modulus distribution in the depth direction of injection molded samples.

- flow patterns prevailing during the injection molding of LCP parts;
- (2) The density/crystallinity measurements elucidated the effect of thermal history on the molded parts, during the solidification stage;
 - (3) Wide-Angle X-Ray Diffraction and Infrared Spectroscopy permitted a characterization of orientation distribution across the thickness of the molded parts;
 - (4) The Microhardness technique was evaluated, as a new method for microstructure characterization, to confirm orientation distribution results;
 - (5) The three point bending technique was used to determine the distribution of flexural modulus across the thickness of molded samples.

Figure 5.58 shows a typical comparison of the various techniques used to determine the distributions of properties in the depth direction of the molded LCP parts. The case shown in Figure 5.58 corresponds to the condition LMdT given in Table 5.1.

The trends of the distributions of orientation functions, indenter length and layer modulus correspond very well to the morphological layer distribution shown in the photomicrograph displaying the cross-section of a molded sample taken from position B along the centerline. The photomicrograph shows clearly four different layers across the thickness. A highly oriented surface layer parallel to the flow direction (X-direction), a less oriented sub-skin layer, an intermediate layer oriented again in the flow direction and a core layer oriented transverse to the flow

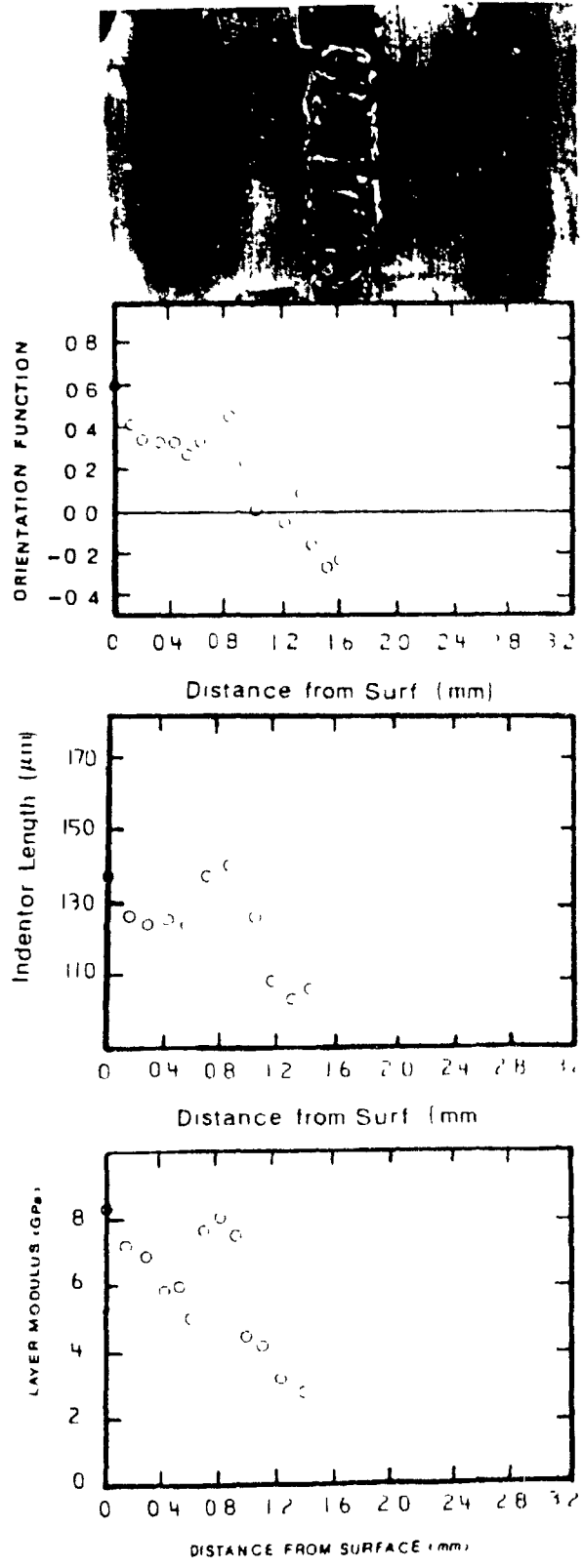


FIGURE 5.58: Comparison of the various distributions of properties in the depth direction of Injection Molded Liquid Crystalline Copolyester Parts .

direction (Y-direction), as shown by the FTIR and flexural modulus results. The results shown in Figure 5.58, which are typical of the results obtained in this study, show surprisingly excellent agreement between the findings of the different experimental techniques. Similar results of cross-sectional bands and layer structure formation were reported for glass-fiber reinforced systems by Kalishe and Seifert (109). They observed again four layers, with more or less similar orientation patterns as observed with liquid crystalline polymers. Singh (96) obtained similar results on fiber-filled polypropylene moldings.

5.7.1 Origin of the various layers

Figure 5.59 depicts the flow of polymer melt during the filling stage. As the melt leaves the narrow gate and enters the cavity, it experiences spreading radial flow, causing the orientation transverse to the main flow direction (Y-direction).

The skin of the plastic in contact with the cold mold freezes very rapidly while the central core remains molten. As further material is injected, it flows into this central region displacing the material already there which then forms a new "front", as depicted in Figure 5.59. The flow of the displaced material is a combination of forward and outward flow, the outward flow contacts the wall, freezes and forms the next section of skin, while the flow forward forms the new molten core. Further material entering the mold flows along a channel lined with frozen walls of plastic. The flow described above, in the region of the advancing melt front, is usually called "fountain flow". It contributes to orienting the surface layer in the flow direction.

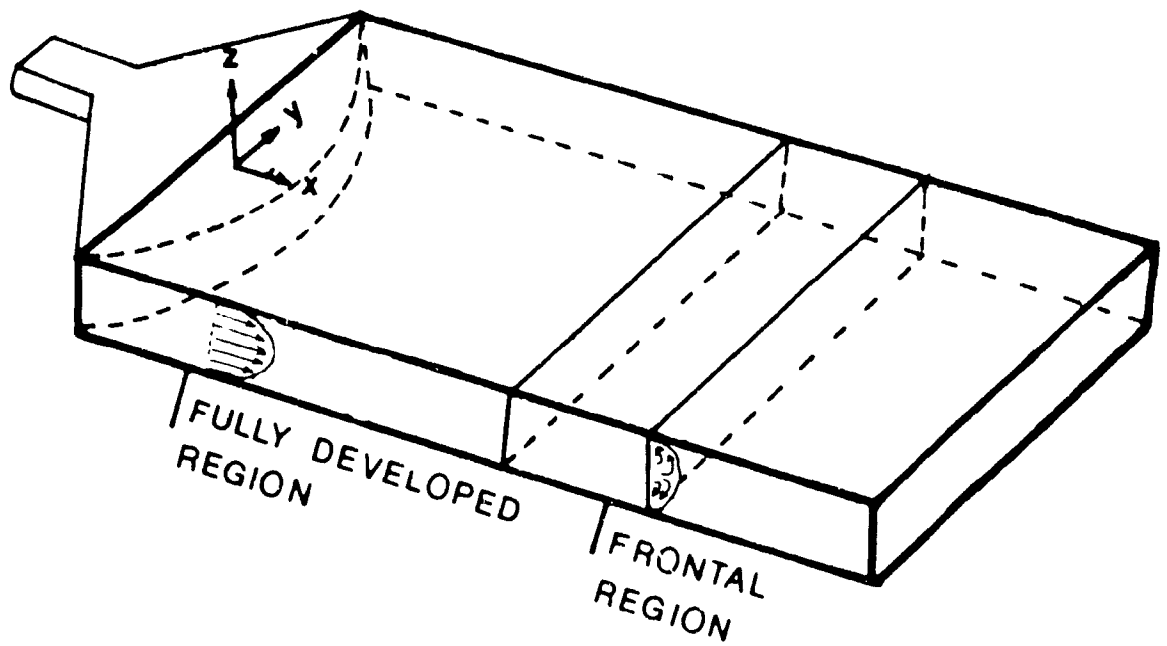


FIGURE 5.59: Schematic representation of different regions during the filling stage of a rectangular mold cavity.

Initially, the frozen layer is very thin; so, heat is lost very rapidly, due also to the cold surface of the mold. The layer becomes thicker, as the melt flows downstream in the cavity, as a result of the continuing cooling effect. However, as a result of fountain flow, hot melt is pumped from the center towards the walls. Thus, the thickness in the zone of the front will decrease again. This suggests that the thickness of the frozen layer during filling will be a maximum somewhere in the middle of the cavity, as observed experimentally. The flow channel is narrowest in this zone, leading to high shear rates at the solid-melt interface. Thus, orientation tends to be high at the solid-melt boundary, at some distance from the wall, as shown in Figure 5.59. The combination of the above effects, i.e. fountain flow and the formation of the solid layer explains the complicated orientation patterns, and consequently, the mechanical properties which were measured in the molded specimens.

Recently, Boldizar (102) observed that the injection molded liquid crystalline polymer parts exhibit layered structures. He observed four distinct layers, and the thickness of each layer was measured for tensile bars, using an optical microscope.

The rectangular test bars machined from the molded plaque, as shown in Figure 4.10 in section 4.8.4.1, while being polished for the microhardness testing, showed patterns, visible to the naked eye, of flow lines and clear and dark regions. These patterns reflect the flow lines during filling. The results obtained by the various techniques employed in this study combined with an examination of the flow patterns observed in the polished samples with clear and dark regions, have suggested the schematic of the mold filling process and orientation distributions illustrated in Figure 5.60.

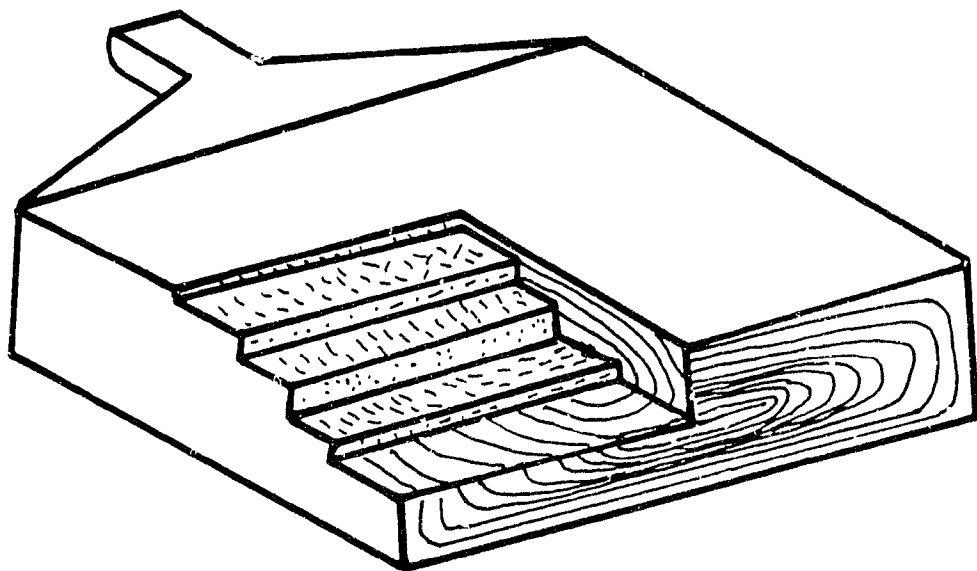


FIGURE 5.60: Schematic of the mold filling process and molecular orientation distributions based on experimentally obtained results.

5.7.2 Influence of the processing conditions

In the injection molding of liquid crystalline copolyester, the development of crystallinity/density, orientation, and mechanical properties depends greatly on the processing conditions as well as on gate and cavity geometries. The material flow involved in the cavity filling is pressure-driven. The nematic melt could be homogeneous or polydomain. The high shear rates present in injection molding probably turn a nematic melt into a homogeneous state (110) (Figure 5.61). This homogeneous state has been confirmed experimentally using microscopic techniques, as evident from the overall sheet-like microstructure and homogeneous layer orientation indicated by infrared spectroscopy.

The dimensions of the intermediate layer depend strongly on temperature and pressure. A reduction in the mold temperature causes it to expand at the expense of the inner core layer. On the other hand, this layer becomes thinner at high injection pressure. The solidification rate is relatively slow in the intermediate layer; thus, the molecules have more time to relax. Slow injection speeds favor a formation of a thicker frozen skin. As a result of low shear rates, the transverse orientation of the incoming melt is maintained beyond the core. Appreciable shear only occurs as the channel thickness is constricted by the frozen layer. At higher injection speeds, the frozen skin growth would be limited. Also, viscous heating could play a significant role.

A semi-quantitative analysis of the percentage of the area occupied by the various layers has been estimated from the results of flexural modulus distributions, obtained at three different processing conditions (see Figures 5.55-

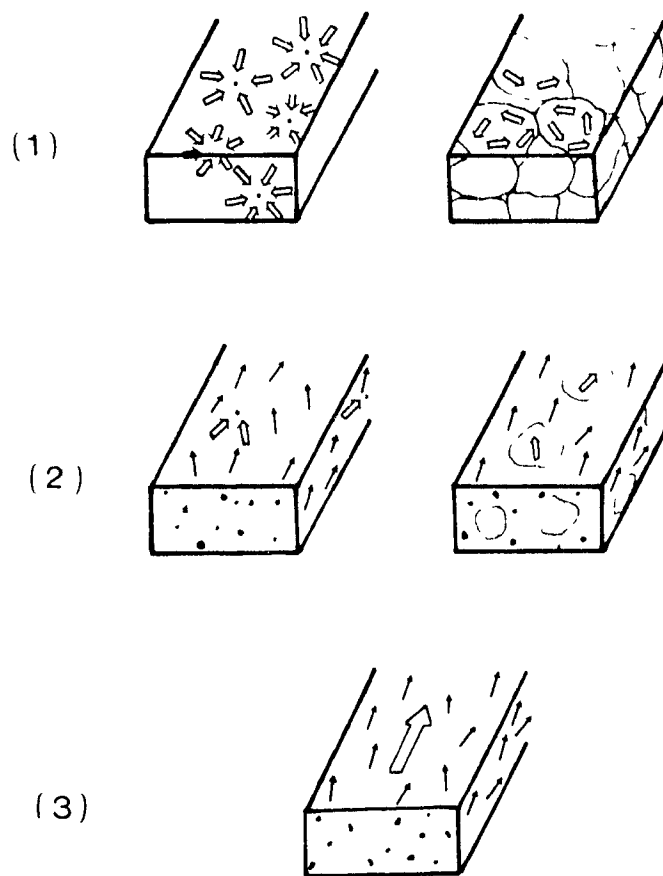


FIGURE 5.61: Schematic representation of the bulk structure of a polymeric liquid crystal. (1) Polydomain system, (2) degraded polydomain system, and (3) monodomain (110).

5.57). These results are in general agreement with results obtained with other techniques.

At low mold temperature (40°C), the area occupied by the skin layer is 50% higher than at higher mold temperature (140°C), as shown in Table 5.2. The effect of mold temperature is quite significant in the intermediate and core layers. The intermediate layer is thicker at low mold temperature.

Table 5.3 shows the effect of injection pressure on the percentage area occupied by the different layers across the thickness of the molded samples. The area of the skin layer at low pressure is thicker and exhibits high orientation along the flow direction. At the low pressure, the core layer represents about 50% of the total thickness.

Table 5.4 shows that, at the high injection speed, the area occupied by the surface layer is more than two times its value at the high injection speed. However, the reverse effect is observed in the sub-skin layer. The intermediate layer becomes more oriented along the flow direction and slightly thicker than at the higher injection speed.

5.8 Analysis of flexural properties

5.8.1 Review of Composite Theories

Variations in microstructure from part to part or within the same part result in differences in mechanical properties. Microstructure, and, as a result,

TABLE 5.2: The effect of mold temperature on the thicknesses of the various layers formed in the molded parts.

LAYER	LAYER THICKNESS (%)	
	LMdT	HMdT
Skin	15	10+
Sub-Skin	20	25
Intermediate	41+	23
Core	24	42

+ Higher Modulus values along the flow direction

TABLE 5.3: The effect of Injection Pressure on the thicknesses of the various layers formed in the molded parts.

LAYER	LAYER THICKNESS (%)	
	LP	HP
Skin	16+	11
Sub-Skin	4+	9
Intermediate	34	44+
Core	46	36

+ Higher Modulus values along the flow direction

TABLE 5.4: The effect of Injection Speed on the thicknesses of the various layers formed in the molded parts.

LAYER	LAYER THICKNESS (%)	
	LIS	HIS
Skin	17+	8
Sub-Skin	9	19+
Intermediate	36+	30
Core	38	43

+ Higher Modulus values along the flow direction

mechanical properties depend on the thermo-mechanical history experienced by the sample during processing. Most previous studies on injection molding of LCP parts have dealt with bulk mechanical properties, mainly tensile modulus and strength. Little or no data are available on bulk flexural modulus and layer flexural modulus across the thickness of molded liquid crystalline copolyester parts.

Data showing the significant effect of part thickness on the anisotropy of mechanical properties were reported by Jackson and Kuhfuss (12). The distribution of mechanical properties in the thickness direction of injection molded liquid crystalline parts suggests that the skin layers contribute the most to the high flexural modulus and strength. Duska (105) reported, based on tests performed on liquid crystalline polymers, that the highest tensile strength value occurred with a part molded at low injection speed, low injection pressure, and low mold temperature.

Morphological studies on injection molded parts of LCPs' have been reviewed by Frayer (111). He classified the reported results into two groups: One group (61,63,97,112,113) showing no preferred orientation in the core, and another group (64,65,67,72) reporting transverse core orientation. Recent research (68,69,70) has been in agreement with the latter group. The dimensions of the layers and the level of orientation were observed to be a function of gate and cavity geometries and of the processing conditions (102,105). It was found also that the thickness of

the skin layer was very dependent on the molding conditions. Suokas et al. (70) made a semi-quantitative analysis of layer thicknesses. They observed that the layer thicknesses varied with processing conditions. Based on these findings they presented a flow model of the cavity filling. Recently Boldizar (102) evaluated the tensile properties of a molded liquid crystalline copolyester, similar to the resin used in this study. Inspection of cross sections cut in the transverse direction (perpendicular to the flow direction), with an optical microscope revealed four different layers from the surface to the center of the thickness.

In this part of the present study, the use of theoretical models developed for fiber reinforced composite systems to predict elastic properties of LCP molded parts is investigated.

5.8.1.1 Cox-Krenchel Model

Assuming that the polymer matrix is linear, i.e. exhibiting a linear stress distribution (Figure 5.62):

$$M = \int_A \sigma(z) z \, dA \quad (5.7)$$

where M is the bending moment, σ is the stress and z is the coordinate in the

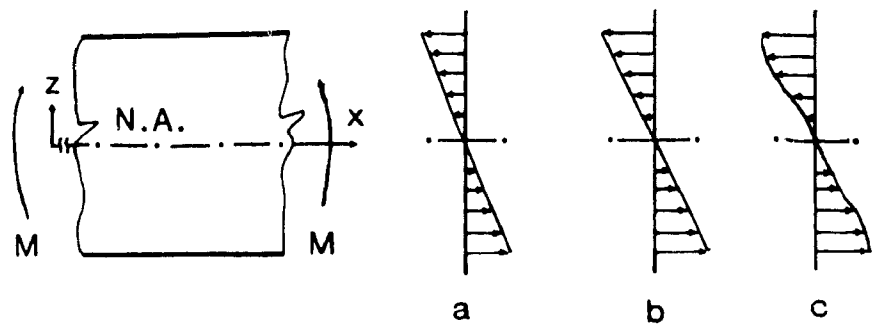


FIGURE 5.62: Stress-strain distribution in flexure:

- a) Strain distribution
- b) Stress distribution, $\sigma(z)$ -linear isotropic;
- c) Stress distribution, $\sigma(z)$ -variable through thickness.

thickness direction. Since $\sigma = E z/\rho$, where $1/\rho$ is the curvature (114), the flexural modulus of the composite, E_c , is given by the following equation:

$$E_c = \frac{M \rho}{I} = \frac{1}{I} \int_A E(z) z^2 dA \quad (5.8)$$

where $dA = wdz$, w is the displacement of the neutral axis in the z -direction and I is the second moment area. $E(z)$ is the tensile modulus of the composite.

The local composite modulus E_c is given by the so-called "law of mixtures" equation, valid for continuous fibers:

$$E_c = E_m (1-V_f) + E_f V_f \quad (5.9)$$

where E_f and E_m are the fiber and matrix moduli, respectively, and V_f is the fiber volume fraction. Cox (115) first modified the Law of Mixtures by adding a fiber length correction factor in order to calculate the elastic modulus of the fiber reinforced composite in one direction. This model considered the reinforcing fiber isolated and long, with an aspect ratio higher than 100, neglecting the interactions with other fibers. This Model was also called the "Shear Lag Model". Later Krenchel (116) added another term to take into account the orientation of the fibers.

$$E_c = E_m (1 - V_f) + \eta_o \eta_L E_f V_f \quad (5.10)$$

where η_L is the Cox fiber-length efficiency factor, and η_o is the Krenchel fiber

orientation efficiency factor.

$$\eta_L = 1 - \frac{\tanh (\beta L / 2)}{(\beta L / 2)} \quad (5.11)$$

where L is the fibre length, and β is given in the following equation:

$$\beta = \left[\frac{D}{E A} \right]^{1/2} \quad (5.12)$$

where E is the Young's modulus and A is the cross-sectional area of the fiber, and

$$D = \frac{2 \pi G}{\ln (R_1 / R_0)} \quad (5.13)$$

In the above, R_1 is the mean distance between the fibers, R_0 is the fiber radius and G is the shear modulus of the matrix.

The Krenchel fiber orientation efficiency factor, η_α , with respect to the direction for which η_α is being calculated, is given by the following equation:

$$\eta_\alpha = \frac{1}{\sum_{u=1} a_u} \langle \cos^4 \theta_u \rangle \quad (5.14)$$

where a_u is the fraction of the fibers in ply u , θ_u is the average angle indicating the orientation of the aligned fibres in ply u with respect to the direction for which E_α is

being calculated, l is the number of fiber plies.

Combining Equations [5.10] and [5.14] yields:

$$E_{flex} = E_M (1 - V_F) + \frac{1}{I} \eta_L E_F V_F \int_A \eta_a z^2 dA \quad (5.15)$$

5.8.1.2 Halpin-Tsai Model

Starting from the work of Hill (117) and Hermann (118), Halpin and Tsai (119) developed a model for the prediction of mechanical properties of fiber reinforced materials, also called the "Self Consistent Model". They proposed the following equation

$$E = E_M \frac{1 + A B V_F}{1 - B V_F} \quad (5.16)$$

with

$$B = \frac{E_F/E_M - 1}{E_F/E_M + A} \quad (5.17)$$

Where V_F is the volume fraction of the fibers and E_F and E_M are the moduli of the fiber and matrix, respectively, A is a constant for a particular case. In the case of longitudinal module:

$$A = \frac{L}{R_1} \quad (5.18)$$

where L is the fiber length and R_1 is the mean distance between fibers

5.8.1.3 Model of Riley

Riley (120) took into consideration the fiber interactions in the case of short-fiber reinforced composites. The fiber length efficiency factor is given as:

$$\eta_L = 1 - \frac{\ln(U + 1)}{U} \quad (5.19)$$

with

$$U = \frac{L}{R_1} \left[\frac{G}{E_f} \right]^{1/2} \left[\frac{1 - \nu_f}{\nu_f} \right]^{1/2} \quad (5.20)$$

where L is the fiber length and R_1 is the mean distance between fibers and G is the shear modulus.

5.8.2 Applicability to Liquid Crystalline Polymers

Liquid crystalline polymers possessing special molecular configurations may be considered as self-reinforcing composites due to the composite-like structure observed under the microscope (25).

Ide and Chung (74) observed that the mechanical properties of liquid crystal polymers, for the case of extruded sheets, follow the general equations for fiber-reinforced

composites. They reported that the angular dependence of the tensile strength of the extruded LCP sheets obeyed the Tsai-Hill theory (121), while the angular dependence of the initial modulus follows the Lees equation (122). Catani et al. (75) studied the microstructure of extruded sheets in order to control the anisotropy. They observed skin-core morphology, with the skin layer highly oriented in the flow direction and the core layer possibly oriented transverse to the flow direction with a particular die geometry

Applicability of fibre reinforced composite theory to liquid crystalline polymers requires the definition of the basic units and parameters used with composites in terms of the LCP structure. The molecules of the copolymer, which consists of crystallizable units (HBA) and non-crystallizable units (HNA) of chains, tend to pack in a hexagonal lattice, but with complete axial and rotational freedom in a nematic structure (41). The fiber in this analysis is the microcrystal as defined by Blundell (26) and may be described by the statistical approach of Hanna and Windle (35). During the injection molding process, the cooling rates are very high, thus allowing only for the fast crystallization process to occur (see section 5.3.1). It is assumed in this analysis that only longitudinal matching (See Figure 2.6.A) is possible, because of the fast cooling rates. The diameter of the basic crystallizable HBA unit is 0.637 nm. The length of the crystal would be equal to about 10 nm (93). This is the same as the value obtained from the statistical approach of Hanna and Windle (35). They found that the length would be based on 17 HBA units along the chain, so the basic unit considered is the rigid crystalline rod formed by a match of about 17 HBA unit. Table 5.5 summarizes the material parameters obtained in the following calculation.

In this part of the present work, experimental data obtained regarding the

TABLE 5.5: VALUES INCORPORATED IN THE MODEL

<u>Macroscopic data</u>	
Modulus at 0° (E_{\max})	100 GPa (46)
Modulus at 90° (E_{\min})	2 GPa (46)
Shear Modulus	1 GPa (46)
Volume fraction of crystals (Vf)	0.21 (27)
<u>Microscopic data</u>	
Length of a crystal (L)	10 nm (27,93)
Radius of a crystal (R_0)	0.32 nm
Mean distance between crystals (R_1)	0.45 nm

variation of the bulk flexural modulus along the thickness direction of the molded part in conjunction with a layer removal technique (114) were compared to predictions of the layer modulus distribution. The predictions were made using the theory for a sandwich beam, assuming that the molded part has distinct layer structures. The relevant data regarding material parameters employed in the calculations are summarized in Table 5.5.

5.8.2.1 Flexural Modulus Measurements

The flexural modulus was measured according to ASTM D-790, using the three point bending test on a rectangular bar (56x8x3.2)mm., with the Instron Universal Tester, at a constant crosshead speed of 0.5 mm/min. The details of the experimental procedure is given in section 4.8.4.8.

The measured flexural modulus data were discussed and reported in section 5.6.2.7.

5.8.2.2 Orientation and Density Distributions

The distribution of the orientation functions obtained experimentally from the microtomed samples is shown in Figure 5.42. A detailed discussion of the results is given in section 5.6.2.5.

The same microtomed specimens used to measure the orientation functions were used to measure the density distribution along the thickness of the molded part. The results are shown in Figure 5.39, and discussed in detail in section 5.6.2.3. It was observed that the density did not vary significantly across the

thickness. In other words, crystallinity was not a significant factor in influencing the distribution of mechanical properties across the thickness of the molded sample. The values of the orientation functions and the crystallinity measurements along the thickness of the molded part were utilized to estimate the distribution of the mechanical properties using the above composite theory.

The quantity $\langle \cos^2 \theta \rangle$ obtained from infrared spectroscopy, has to be expressed in the form of $\langle \cos^4 \theta \rangle$, in order to allow the calculation of η_a from Equation [5.14], reported previously.

The moments of the axial distribution (123), $\langle \cos^m \theta \rangle_p$, are given by:

$$\langle \cos^m \theta \rangle_p = \int_0^{\pi/2} n_p(\theta) \cos^m \theta \sin \theta d\theta \quad (5.21)$$

$$= \frac{\int_0^{\pi/2} I_p(\theta) \cos^m \theta \sin \theta d\theta}{\int_0^{\pi/2} I_p(\theta) \sin \theta d\theta} \quad (5.22)$$

where $I_p(\theta)$ is an axial orientation function specifying the number of chain axes directions in the crystalline phase ($I_c(\theta)$) and amorphous phase ($I_a(\theta)$) at an angle θ with respect to the draw direction (122). A similar definition can be given to n_p which is a normalized density function. The subscript p signifies the crystalline or amorphous phase (pth phase).

Introducing orientation parameters, f_p and g_p :

$$f_p = 1/2 [3 \langle \cos^2 \theta \rangle_p - 1]; \quad -1/2 \leq f_p \leq 1 \quad (5.23)$$

$$g_p = 1/4 [5 \langle \cos^4 \theta \rangle_p - 1]; \quad -1/4 \leq g_p \leq 1 \quad (5.24)$$

Assuming that the axial orientation distribution function is of the form $I(\theta) = K \cos^m \theta$, then

$$g_p = \frac{(3f_p)}{(5 - 2f_p)} \quad (5.25)$$

The derivation of Equation [5.25] is given in Appendix A.13.1.

5.8.2.3 Flexural Modulus Predictions

The predictions of the distributions of mechanical properties along the thickness direction are shown in Figures 5.63 and 5.64. The predictions of the flexural modulus as a function of distance from the surface for the sample (1L), machined longitudinal to the flow direction along the centerline are shown in Figure 5.63. The data are reported in Appendix A.12. It is observed that Riley's theory is in very good agreement with the experimental results. As discussed in section 5.8, Riley's theory applies to composite systems reinforced with short fibers having an aspect ratio less than 100. In addition, interaction between the fibers is taken into account. Cox's theory does not take into account interactions between fibers. The

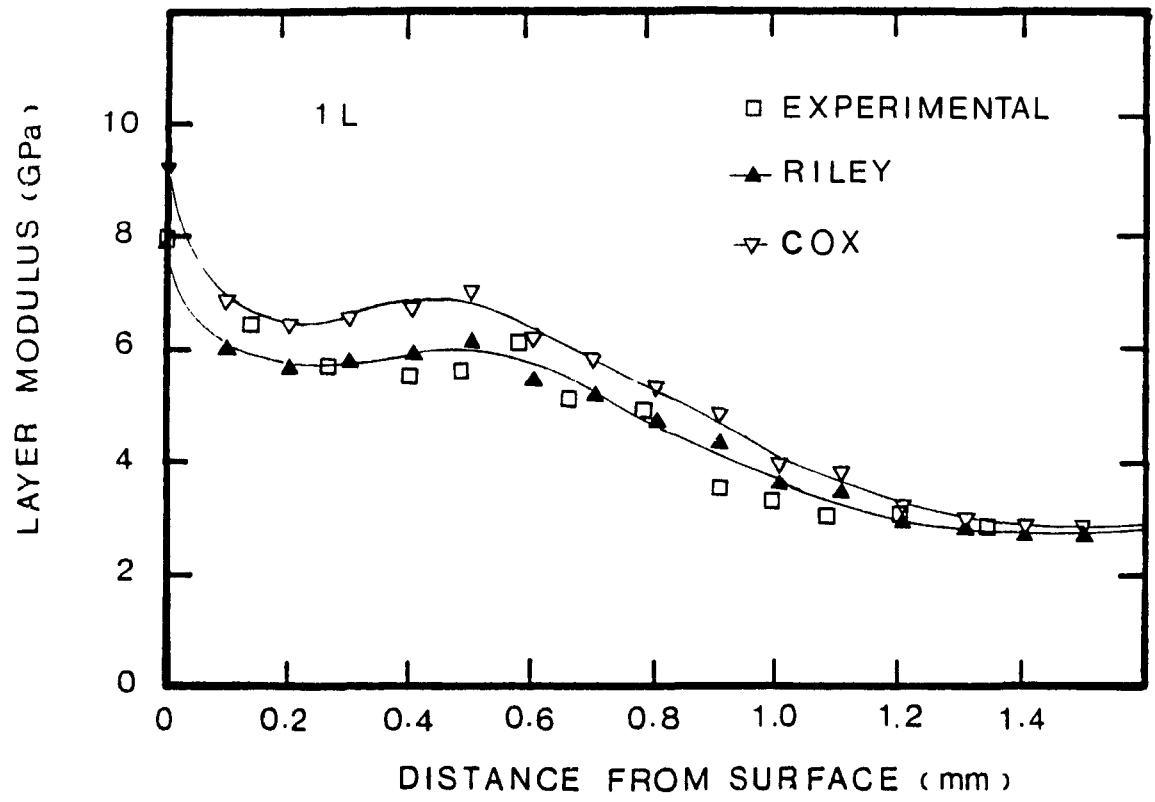


FIGURE 5.63: Predictions of flexural modulus in the depth direction of a sample machined parallel-to-flow direction (1L)

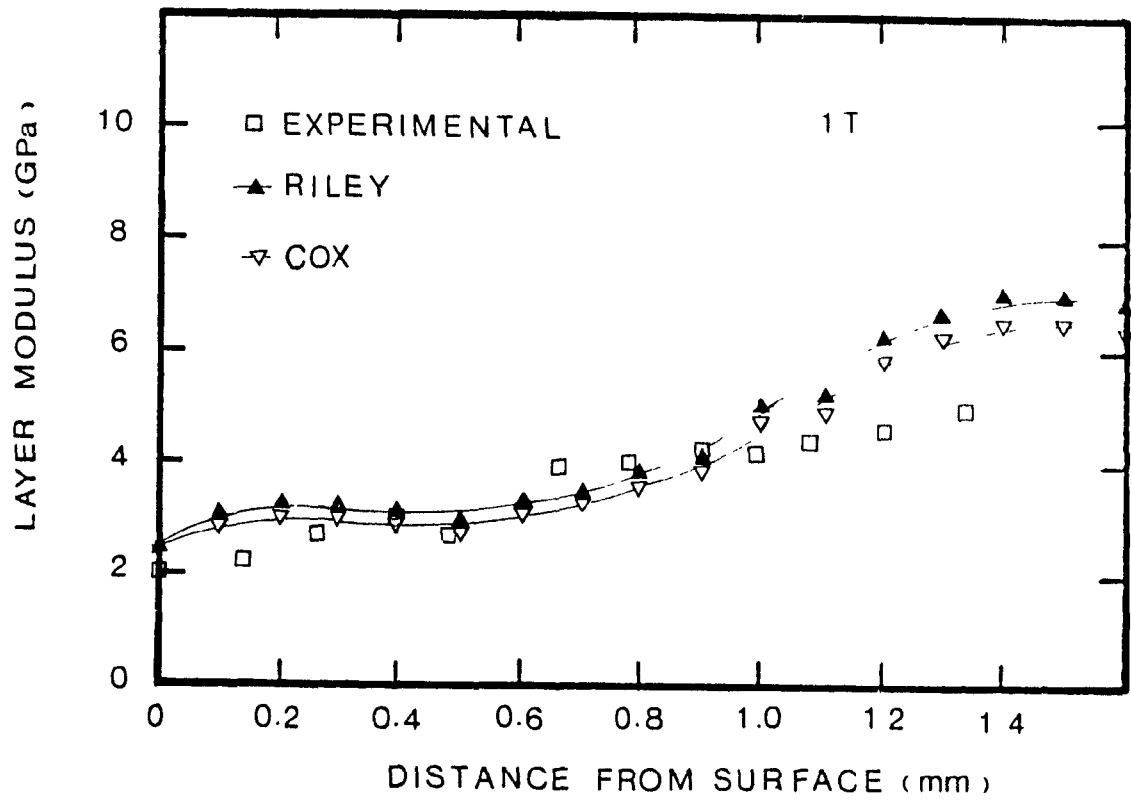


FIGURE 5.64: Predictions of flexural modulus in the depth direction of a sample machined perpendicular-to-flow direction (1T).

latter theory applies better when continuous fibers with an aspect ratio higher than 100 are used. Therefore, Cox's predictions are observed to produce higher predictions than experimental data. The predictions of the distribution of flexural modulus as a function of distance from the surface, for the sample (1T), machined near the gate transverse to the flow direction, are shown in Figure 5.64. It is observed for this particular sample that both theories are in good agreement with experimental data. Cox's theory slightly underestimates the experimental results obtained for the sample (1T), due to the assumption of continuous fibers oriented transverse to the flow direction.

CHAPTER VI

6. CONCLUSION

6.1 Conclusions

The work presented in this thesis is the result of a very comprehensive study on the properties and injection molding behavior of liquid crystalline copolyester resins. The work consists of three major parts:

- (i) a comprehensive study of LCP resin properties.
- (ii) a study of microstructure development in LCP injection molding and the effect of molding conditions on microstructure and product properties.
- (iii) Utilization of material parameters and molding information to predict some of the properties of final parts, especially flexural modulus distribution in injection molded LCP.

Some of the important conclusions of the present work are outlined below.

- (1) The HBA/HNA based thermotropic liquid crystalline copolyester studied in this work has been recently commercialized by the Celanese Corporation-(now Hoechst-Celanese). A variety of techniques were employed to characterize the thermodynamic, thermal and dynamic mechanical properties of the resin. The crystallization behavior was

investigated using isothermal and non-isothermal methods. The viscosity and die swell at different temperatures and shear rates were also measured.

- (2) Values of C_p obtained in the present work are in reasonable agreement with those reported previously on similar LCP materials but with different HBA/HNA compositions (88). The variation in the values of k and α over a wide range of temperatures was found to be smaller than that reported for conventional flexible chain polymers (79). This can be probably attributed to the packing configuration of the rigid rodlike molecules. The values of various thermodynamic properties such as ΔH°_m , ΔS°_m and σ_e were found to be much smaller than those reported for flexible chain polymers. However, these values are considered to be reasonable for liquid crystalline polymers because of their different morphology.

- (3) The kinetics of the fast crystallization process, evaluated using a non-isothermal method, indicate a two-dimensional rod-like morphological growth characterized by an Avrami exponent of 2, which is in agreement with the rodlike nature of the molecular conformation. The kinetics of the slow crystallization process, which were studied using an isothermal method, showed that the degree of crystallinity varies linearly with $\log(\text{time})$ and the logarithm of the rate of crystallization increases linearly with the inverse absolute temperature in the low temperature range.

- (4) Dynamic mechanical measurements showed three clear transitions: α -processes at 110°C, corresponding to the glass transition temperature; β -processes around 50°C, attributed to rotation of naphthyl moieties around the ester link, and finally the δ -process occurring at about -40°C, the latter is assigned to the reorganizational motion of the phenyl units.
- (5) The viscosity as a function of shear rates at three different temperatures was measured. The results show that the LCP2000 has shear viscosity profiles similar to those observed for conventional thermoplastics; but shows about 2 order of magnitude lower viscosity. This low viscosity reflects the high alignment of the rigid rodlike molecules. The resin studied did not show die swell at 300°C, for both shear rates used.
- (6) Infrared spectroscopy (FTIR) and X-ray diffraction techniques were used to determine the transition moment angle in order to allow for the calculation of Hermans orientation functions. Infrared spectra and X-ray patterns were obtained on the same drawn fibers. The dichroic ratio using FTIR and the Hermans orientation functions using X-ray diffraction permitted the calculation of the transition moment angle.
- (7) A variety of experimental techniques have been developed and used for evaluating microstructure of the molded liquid crystalline copolyester parts. The distributions of the various properties are

affected by the development of morphological structure and layer formation in the depth direction of the moldings. Injection molded articles exhibit a skin-core structure with four layers from the surface to the center of the thickness. The skin layer, oriented parallel to the flow direction, is probably due to the combination of fountain flow and freezing layers at the walls. The core layer is oriented transverse to the flow direction as a result of diverging flow at the entry of the cavity. The sub-skin layer formed between the skin and core, is probably a transition zone. The intermediate layer oriented parallel to the flow direction, is the result of the shearing action against the frozen surface layer during the filling stage.

- (8) Crystallinity does not vary significantly within the LCP molding since only the fast crystallization process occurs, because of the rapid cooling rates observed in injection molding process. Thus the effect of crystallinity on product variability and anisotropy is small.
- (9) A hierarchical morphology was observed from the microstructure of injection molded samples. A detailed microstructure was observed using microscopic techniques. The nematic melt turn to a homogeneous state, after being elongated or sheared. This homogeneous state has been confirmed with the experimental results of this work, using microscopic and infrared spectroscopic techniques. Three different fibrillar species were observed on molded LCP samples with SEM: microfibrils of about 0.05 to 0.1 μm , fibrils of

about 0.3 to 0.5 μm and the macrofibers about 3 to 5 μm . Based on morphological substructures, a descriptive model given in Figure 6.40 is proposed. The gradient of structure could be directly related to the flow characteristics of a molecular composite reminiscent of short-fiber reinforced systems. This model can serve as the basis for understanding the mechanical behavior.

- (10) The microhardness technique was evaluated as a method to characterize the microstructure of the molded parts. It was found that microhardness data were in very good agreement with those obtained using other techniques employed in this study.

- (11) The effect of injection molding parameters was analyzed by performing a systematic experimental study on the microstructure of the naphthalene-based liquid crystalline copolyester moldings. Four symmetric layers were observed across the thickness. The third layer was found to be very strongly dependent on the molding conditions utilized, such as the mold temperature, injection pressure and speed. However, the effects are smaller in the core region. Mold temperature and injection speed have the most profound influence. Lower mold temperature was observed to increase the thickness of the intermediate layer at the expense of the core layer. Lower injection speed showed sharper transitions between differently oriented layers. The orientation in the intermediate layer, obtained by shear, was of the same magnitude as in the skin layer, obtained by elongation.

- (12) The composite-like nature of injection molded liquid crystalline parts makes them comparable to fiber-reinforced systems. Theoretical models used in composite systems to predict elastic properties of molded parts have been analyzed for applicability in liquid crystalline copolyesters. The predictions were compared with experimentally measured data on samples machined in the flow direction and perpendicular to the flow direction. It was found that the predictions were in good agreement with experiments. Riley's theory was found to fit the experimental data better, probably because rigid rodlike molecules behave like short-fibers with an aspect ratio less than 100. Also, the interaction between the fibers is taken into account. Cox's theory does not take into account the interaction between fibers. The latter theory works better with continuous fiber-reinforced composites having an aspect ratio higher than 100. Cox's predictions are observed to overestimate our experimental data which is in agreement with Cox's projections.

6.2 Claims to Original Contributions

The totality of the work presented in this thesis can be claimed to represent a significant contribution to the study of the liquid crystalline polymer resin properties, the understanding of microstructure developed in LCP injection molded parts, and the elucidation of relationship between processing variables, microstructure and properties in liquid crystalline polymer injection molding. It also represents a significant step towards the development of suitable mathematical models for the simulation of the morphological development and the predictions of ultimate mechanical properties in injection molding of LCP products.

The specific original contributions claimed in this work, can be summarized as follows:

- (1) Comprehensive data were obtained regarding the thermal properties of the LCP resin, including specific heat , thermal conductivity and thermal diffusivity at different temperatures from the solid to the melt state.
- (2) The kinetics of crystallization for the slow crystallization process were determined using an isothermal method. The kinetics for the fast

crystallization process were obtained using a non-isothermal method (see Table 6.1).

- (3) The determination of the transition moment angle, using infrared spectroscopic and x-ray diffraction techniques to calculate the Hermans functions of orientation, represents, to our knowledge, the first set of data reported concerning the orientation functions of the crystallographic axes of the unit cell of the injection molded liquid crystalline copolyester under study.
- (4) This work represents a comprehensive study of the injection molding behavior and microstructure characterization of the molded LCP parts. Specific findings include layer formation, the details and characteristics of the morphology obtained during the molding process, and the interaction between the processing conditions, microstructure and product properties.
- (5) The microhardness results represent the first such data reported for microstructure characterization in injection molded liquid crystalline copolyesters.

TABLE 6.1: Studies on Thermal Characterization and Crystallization Behavior of HN.VIIB.A Thermotropic LCP's

REFERENCE	THERMODYNAMIC PROPERTIES			THERMAL PROPERTIES			
	ΔH_m^0	ΔS_m^0	σ_c	C_p	k	α	Cryst. Kinet
Blundell (26)	Yes	Yes	No	No	No	No	No
Cao & Wunderlich(88)	Yes	Yes	No	Yes	No	No	No
Butzbach et al. (91)	Yes	Yes	No	No	No	No	No
Butzbach et al. (32)	Yes	No	No	No	No	No	For Slow Cryst. Process
Present Work	Yes	Yes	Yes	Yes	Yes	Yes	For Slow & Fast Cryst. Process

- (6) This work represents the first attempt to measure the layer flexural modulus distributions in the depth direction of injection molded liquid crystalline copolyester parts. It is also the first attempt to predict the mechanical properties using available composite theories by incorporating experimentally microstructural data, such as orientation and crystallinity/density distributions across the thickness of injection molded parts.

6.3 Recommendations for Future Work

- (1) The data acquired through the numerous measurements obtained in the present study would be useful for the development of mathematical models for the simulation of microstructure developed in injection molded liquid crystalline copolyester parts. The flow pattern within the mold has a pronounced effect on the quality of the finished part. It is necessary to evaluate carefully the contributions of both shear and elongational flow to orientation. The roles of heat transfer and layer formation in the molded parts should be also considered. Thus, a realistic computer simulation of the injection molding process, as it relates to LCP resins, would be very valuable.

- (2) This work can be extended to a more systematic study of the effect of gate type and size on microstructure and morphology development and, in future on the ultimate properties of molded LCP articles.

REFERENCES

1. F. Reinitzer, *Monatsh. Chem.*, **9**, 421 (1888)
2. G. Friedel, *Annal. Phys. (Paris)* [9], **18**, 273 (1922)
3. L. Onsager, *Ann. N. Y. Acad. Sci.* **51**, 627 (1949)
4. P.J. Flory, *Proc. R. Soc.*, **A234**, 73 (1956)
5. S.L. Kwolek, U.S. patent, 3,600,350 (1971)
6. P.W. Morgan, *Macromolecules*, **10**, 1381 (1977)
7. D.R. Wilson and R.S. Jones, Sixteenth-of-the-Art Symposium, Div. of Ind & Eng. Chem., Am. Chem. Soc., Washington, D.C., June 9-11, 1980.
8. R.S. Werbowyj and D.G. Gray, *Mol. Cryst. Liq. Cryst.*, **34**, 97 (1976)
9. R.S. Werbowyj and D.G. Gray, *Macromolecules*, **13**, 69, (1980)
10. M. Panar and O.B. Willcox, German Patent 2,705,382 (1977).
11. S.M. Aharoni, *Mol. Cryst. Liq. Cryst.*, **56**, 237 (1980).
12. H.F. Jackson and W.J. Kuhfuss, *J. Polym. Sci. Polym. Chem. Ed.*, **14**, 2043 (1976)
13. Qi-Feng Zhou and R.W. Lenz, *ACS Polym. Prep.*, **12**, 255 (1983)
14. J.J. Kleinschuster, US patent No. 3,991,014 (1976)
15. H.F. Jackson and W.J. Kuhfuss, U.S. Pat. No. 3,804,805 (1974)
16. F.E. McFarlane and T.G. Davis, US patent No. 3,804,
17. T.C. Pletcher, US patent No. 3,991,013 (1976)
18. G. Calundann, US patent No. 4,067,852 (1978)
19. G. Calundann, US patent No. 4,184,996 (1980)

20. A.C. Griffin and S.J.Havens, *J. Polym. Sci. Polym. Phys.*, **19**, 951 (1981)
21. W. Mayer and A. Saupe, *Z. Naturforsch*, **A13**, 564 (1958)
22. H. Zocher, *Trans.Fraday Soc.*, **29**, 945 (1933)
23. P.H. Hermans and P. Platzek, *Kolloid Z.*, **88**, 68 (1939)
24. J. Grebowicz and B. Wunderlich, *J. Mol. Cryst. Liq. Cryst.*, **76**, 287 (1981)
25. G.W. Calundann and M. Jaffe, Reprinted from the proceeding of The Robert A. Welch Conf. on Chem. Resear., 247 (1982)
26. D.J. Blundell, *Polymer*, **23**, 359 (1982)
27. H. Bechtoldt, J.H. Wendorff, H.J. Zimmermann, *Makromol.Chem.*, **188**, 651 (1987).
28. D. J. Blundell and K. A. Buckingham, *Polymer*, **26**, 1623 (1985)
29. J.B. Stamatoff, *Mol. Cryst. Liq. Cryst.*, **110**, 75 (1984)
30. J. Clements, J. Humphreys and I.M. Ward, *J. Polym. Sci., Polym .Phys. Ed.*, **24**, 2293 (1986)
31. S.B. Warner and M. Jaffe, *J.Cryst.Growth*, **48**, 148 (1980)
32. G.D. Butzbach, J.H. Wendorff, H.J. Zimmermann, *Polymer*,**27**, 1337 (1986).
33. J. Blackwell and G.A. Gutierrez, *Polymer*, **23**, 671 (1982)
34. G.A. Gutierrez, R.A. Chivers, J. Blackwell, J.B. Stamatoff and H. Yoon, *Polymer*, **24**, 937 (1983)
35. S. Hanna and A.H. Windle, *Polymer*, **29**, 207 (1988)
36. B. Wunderlich, *J. Chem. Phys.*, **29**, 1395 (1958)
37. A.H. Windle, C. Viney, R. Golombok, A.M. Donald and G.R. Mitchell, *Faraday Discuss. Chem. Soc.*, **79**, 55 (1985)
38. J.C. Jenkins and G.M. Jenkins, *J. Mater. Sci.*, **22**, 3784 (1987)
39. G.R. Davis and R. Jakeways, *Polym. Comm.*, **26**, 9 (1985)

40. M.J. Troughton, A.P. Unwin, G.R. Davies and I.M. Ward, *Polymer*, **29**, 1389 (1988)
41. R.A. Chivers and J. Blackwell, *Polymer*, **26**, 997 (1985)
42. G.R. Mitchell and A.H. Windle, *Polymer*, **23**, 1269 (1982)
43. G.R. Mitchell and A.H. Windle, *Polymer*, **24**, 1513 (1983)
44. C. Viney, G.R. Mitchell, A.H. Windle, *Polym. Commun.*, **24**, 145 (1983).
45. A.H. Windle, *Faraday Discuss. Chem. Soc.*, **79**, 112 (1985)
46. D.J. Blundell, *Faraday Discuss. Chem. Soc.*, **79**, 109 (1985)
47. D.J. Blundell, R.A. Chivers, A.D. Curson, J.C. Love and W.A. MacDonald, *Polymer*, **29**, 1459 (1988)
48. D.G. Baird, in *Liquid Crystalline Order in Polymers*, A. Blumstein Ed., Academic Press, New York, Chap.7 (1978)
49. K.F. Wissbrun, *J. Rheol.*, **25**, 6, 619 (1981)
50. S. Onogi and T. Asada, in *Rheology, Vol. I*, G. Marrucci, and L. Nicolais, Eds. (Papers presented at Eighth International Congress on Rheology, Naples, 1980), Plenum, New York, 1980.
51. K.F. Wissbrun and A.C. Griffin, *J. Polym. Sci. Polym. Phys.*, **20**, 1835 (1982)
52. K.F. Wissbrun, *Brit. Polym. J.*, **12**, 163 (1980)
53. K.F. Wissbrun, G. Kiss, and F.N. Cogswell, Paper presented at LC workshop in Montreal, April 5-8, 1986, to be published in *Chem. Eng. Commun.*
54. R.E. Jerman and D.G. Baird, *J. Rheol.*, **25**, 275 (1981)
55. F.N. Cogswell, *Brit. Polym. J.*, **12**, 170 (1980)
56. C.R. Gochanour and M. Weinberg, *J. Rheol.*, **30**, 1, 101 (1986)
57. G. Kiss, *J. Rheol.*, **30**, 3, 585 (1986)
58. J.H. Wendorff, *Kunststoffe*, **73**, 9 (1983)

59. F.C. Jaarsma, 44th SPE Antec, 726, (1986)
60. Z. Tadmor, J. Appl. Polym. Sci., 18, 1753 (1974)
61. H. Thapar and M. Bevis, J.Mat.Sci., Lett.Eds., 2, 733 (1983)
62. Y. Ide, Z. Ophir, Polym. Eng. Sci., 23, 5 261 (1983)
63. E.G. Joseph, G.L. Wilkes and D.G. Baird, Polymer, 26, 689 (1985)
64. J.J. Duska, N.D. Field and F. Scardiglia, Polymer Processing Society Conference, Montreal (April 1986)
65. T. Weng, A. Hiltner, and E. Baer, J. Mat. Sci., 21, 744 (1986)
66. H. Voss, K. Friedrich, J. Mat. Sci., 21, 2889 (1986)
67. L.C. Sawyer, M. Jaffe, J. Mat. Sci., 21, 1897 (1986)
68. J.J. Duska, Plastics Engineering , 12, 39 (1986)
69. G. Menges, T. Schacht, H. Becker, S. Ott, Intern. Polym. Proces., 2, 2, 77 (1987)
70. E. Suokas, J. Sarlin, and P. Tormälä, Mol. Cryst. Liq. Cryst., 153, 515 (1987)
71. G.E. Williams and S.K. Garg, Paper presented at Japan-U.S. Polymer Symposium, Kyoto, Japan, 1985
72. Z. Ophir and Y. Ide, Polym. Eng. Sci., 23, 14, 792 (1983)
73. A. Pirnia and C.S.P. Sung, ACS Polymer Preprints, 9 (1987)
74. Y. Ide and T.-S. Chung, J. Macrom. Sci., Phys.Eds., B23 (45), 497 (1984)
75. A. Catani, C. de Grandpre, J.M. Charrier and R.V. Ciplijauskas, 46th SPE Antec, 1988.
76. F.E McFarlane, V.A. Nicely and T.G. Davis,"Contemporary Topics in Polymer Science", Vol.2, E.M. Pearce and J.R. Shaefgan, Ed., Plenum Publishing Corp., New York (1982)
77. S.K. Garg and S. Kenig, Paper presented at Liquid Crystal Workshop, Montreal, (April 5-8,1986)

78. Certificate Stand. Ref. Material 720, NBS (1970).
79. M.R. Kamal, V. Tan, F. Kashani, Adv. Polym. Sci. Technol., 3, 89 (1983)
80. S. Sourour, M.R. Kamal, Polym.Eng.Sci., 16, 480 (1976)
81. M. Weber, Summer Project, McGill University, 1986
82. R.J. Samuels, Structured Polymer Properties, J. Wiley & Sons (1974)
83. M. Samara, M. Eng. Thesis, Mc Gill University, Montreal (1985)
84. K. Oda, J.L. White and E.S. Clark, Polym. Eng. Sci., 16, 585 (1976)
85. V. Gomes, M. Eng. Thesis, McGill University, 1985
86. ASTM D-1505-68, American Society for Testing and Materials, 35 (1978)
87. A.F. Johnson, G.D. Sims, Composites, 17, 4, 321 (1986)
88. M.Y. Cao, B. Wunderlich, J. Polym. Phys. Ed., 23, 521 (1985).
89. L.N. Cherkasova, Russ. J. Phys. Chem., 33, 9, 224 (1959)
90. F.N. Liberti, B. Wunderlich, J. Polym. Sci.: Part A-2, 6, 833 (1968).
91. G.D. Butzbach, J.H. Wendorff, and H.J. Zimmermann, Makromol. Chem., Rapid Commun., 6, 821 (1985)
92. J.D. Hoffmann, J.J. Weeks, J. Research of NBS-A Phys. Chemistry, 66A, 1, 13 (1962).
93. D.J. Blundell, Faraday Discuss. Chem. Soc., 79, 109 (1985)
94. K. Harnisch, H. Muschik, Colloid Polym. Sci., 261, 908 (1983).
95. J.P Bell and T. Murayama, J. Polym. Sci.: PART A-2, 7, 1059 (1969.)
96. J.L. White, J. Rheol., 22, 507 (1978)
97. P. Singh, Ph.D. Thesis, McGill University, Montreal, 1989
98. E.G. Joseph, G.L. Wilkes and D.G. Baird, Polym. Eng. Sci., 7, 25, 377 (1985)

99. P.G. Hedmark, J.M. Rego Lopez, M. Westdahl, P-E Werner, J-F Jansen and U.W. Gedde, *Polym. Eng. Sci.*, **28**, 19, 1248 (1988)
100. Y.V. Kissin, I.A. Lekaye, Y.A. Chernova, N.A. Davydova, N.M. Chirkov, *Kysokomol Soyed.*, **A16**, 3, 667 (1974).
101. S. Kenig, *Polym. Compos.*, **7**, 50 (1986)
102. A. Boldizar, *Plastics and Rubber Processing and Applications*, **10**, 73 (1988).
103. P. Singh and M.R. Kamal, presented at the 8th annual NRCC/IMRI symposium "Composites-'88", 12/1 (1988).
104. E. Suokas, *Polymer*, **30**, 1105 (1989)
105. J. Duska, *SPI/SPE Journal* 153 (1986)
106. S. Kenig, B. Trattner, and H. Anderman, *Polym. Compos.* **9**, 1, (1988)
107. J. Bohman, N. Harris and M. Bevis, *J. Mater. Sci.*, **10**, 63 (1975)
108. J. Bohman and M. Bevis, *Colloid and Polym. Sci.*, **255**, 954 (1977)
109. G. Kalishe and H. Seifert, *Plaste Kautschuk*, **22**, 837 (1973)
110. T. Asada, in *Polymer Liquid Crystals*, A. Ciferri, W.R. Krigbaum and R.B. Meyer Eds., Academic Press., p. 247 (1982)
111. P.D. Frayer, *Polymer Composites*, **8**, 6, 379 (1987)
112. G.G. Viola, D.G. Baird and G.L. Wilkes, *Polym. Eng. Sci.*, **25**, 888 (1985)
113. J.L. White, *J. Appl. Polym. Sci., Appl. Polym. Symp.*, **41**, 241 (1985)
114. G.R. Smith, M.W. Darlington, and D. McCammond, *J. Strain Analysis*, **13**, 4, 221 (1978)
115. H.L. Cox, *British J. Appl. Phys.*, **3**, 73 (1952)
116. H. Krenchel, *Fibre reinforcement 1964* (Akademisk Forlag, Copenhagen).
117. R. Hill, *J. Mecha. Phys. Solids*, **13**, 189 (1967)
118. J.J. Herman, *Proc. K. Ned. Akad. Wetser., B. Phys. Sci.*, **B70-1**, (1967)

119. J.C. Halpin and N.S.W. Tsai, TR-67-423, Air Force Mater. Laboratories (1967)
120. V.R. Riley, Polym. Conf. Series, Univ. Utah, Salt Lake City, Utah, (1970)
121. S.W. Tsai, J.C. Halpin, and N.J. Pagano, Composite Material Workshop, Technomic, Stamford, Conn., (1968)
122. J.K. Lees, Polym. Eng. Sci., 8, 186 (1968)
123. J.C. Seferis, R.L. McCullough, and R.J. Samuels, Polym. Eng. Sci., 16, 5, 334 (1976)

LIST OF SYMBOLS

SYMBOL	DESCRIPTION
A_{\parallel}	Absorbance for linearly polarized light parallel to the chain direction.
A_{\perp}	Absorbance for linearly polarized light perpendicular to the chain direction.
A	Sample area, cm^2
A_f	Cross-sectional area of the fiber,
A_p	Projected area
$a(T_c)$	Rate of transformation
b	Width of the rectangular bar, mm
C_p	Specific heat at constant pressure, J/kg.K
$C_{p,s}$	Specific Heat in the solid state
$C_{p,l}$	Specific Heat in the liquid state
c_1	Indenter constant
D	Dichroic ratio
D_0	Dichroic Ratio of ideally oriented molecules
d	Length of long diagonal
E	Young Modulus, MPa
E_t	Tensile Modulus, MPa
E_f	Flexural Modulus, MPa
E_s	Young's Modulus of the skin layer, MPa
E_c	Young's Modulus of the core layer, MPa
E_M, E_{mn}	Modulus of the matrix, MPa
E_f, E_{max}	Modulus of the fibers, MPa
E_{α}	Local Modulus, MPa
$E(z)$	Young Modulus for the composite, MPa
E'	Storage Modulus (MPa)
E''	Loss Modulus (MPa)
e	Bagley correction factor
f	Orientation function
f_c	Orientation function of the crystalline band
F/Y	Initial slope of the load deflection record
G	Shear Modulus, MPa
h	Thickness of the rectangular bar, mm
h_c	Thickness of the core layer, mm
h_s	Thickness of the skin layer, mm
I	Second moment of area
I_p	Axial orientation function of p_{th} phase

SYMBOL	DESCRIPTION
K	Crystallization rate constant
k	Thermal conductivity, (J/ m.s °C)
k_s	Thermal Conductivity in the solid state
k_l	Thermal Conductivity in the liquid state
k_B	Boltzmann constant, 1.38×10^{-16} erg/rod°K
L	Fiber or crystal length, nm
i	Number of fiber plies
M	Bending moment
n	Avrami exponent
\mathbf{n}	Unit vector called the director
n_p	Normalized density function of p_{cb} phase
P	Pressure
p_f	Probability factor
P_L	Load, g
p	Pitch
Q_1, Q_2	Thermal fluxes on each side of the cavity cell
q	Heat flux, (J/ m ² .s)
q_0	Wave vector
R	Gas constant
R_1	Mean distance between fibers or crystals, nm
R_0	Radius of the fibers or crystals, nm
S	Order parameter
S_p	Support span, mm
T	Absolute temperature, °K
T_c	Crystallization temperature, °C
T_m	Melting temperature of the copolymer, °C
T_m°	Equilibrium melting temperature, °C
$\Delta T_1, \Delta T_2$	Thermal gradients, °C
t	Time, seconds
t_c	Crystallization time, seconds
ΔH_f	Heat of fusion, J/g
ΔH_f°	Heat of fusion at equilibrium temperature, J/g
w	Displacement of the neutral axis in the z-direction
$\Delta X_1, \Delta X_2$	Sample thickness, mm
x,y,z	coordinates
\dot{x}	Rate of crystallization
x	Degree of crystallization, %

SYMBOL

DESCRIPTION

GREEK LETTERS

α	Thermal diffusivity, (m ² /s)
α_s	Thermal Diffusivity in the solid state
α_l	Thermal Diffusivity in the liquid state
α_t	Transition Moment Angle
β_1, β_2	Cooling rates, °C/min
ρ	Density, g/cm ³
ρ_s	Density in the solid state
ρ_l	Density in the liquid state
θ	Angle (Theta)
$\varphi = h/h_c$	Dimensionless constant
ΔH°_m	Heat of transition
ΔS°_m	Entropy of transition
σ_e	Surface free energy
ω	Angular frequency
ϕ	Phase Angle
τ, τ_0	Stress and initial stress respectively
ϵ, ϵ_0	Strain and initial strain respectively
η_L	Cox's fiber length efficiency factor
η_α	Krenchel fiber orientation efficiency factor
η	Viscosity, Pa.s
γ	Shear rate, s ⁻¹
Tan δ	Loss Tangent

SYMBOL

DESCRIPTION

LCP	Liquid Crystal Polymer
F	Flow direction
HK	Knoop Hardness Number
PC1	Pressure Transducer No.1
PC2	Pressure Transducer No.2
PN	Nozzle Pressure
PH	Hydraulic Pressure
V	Velocity
TN	Nozzle (Melt) Temperature
TM	Mold Temperature
LD	Linear Displacement

APPENDIX A.1

THERMAL PROPERTIES

A.1.1: Specific Heat Data

Comparison of C_p of LCP2000 to C_p data reported in the literature (100), on similar polymer but with different compositions.

TEMPERATURE (°C)	75HBA/25HNA (1) C_p (J/mol°C)	70HBA/30HNA (2) C_p (J/mol°C)	58HBA/42HNA(1) C_p (J/mol°C)
20	-	147.5	-
27	151.1	-	159.0
40	-	148.2	-
47	155.8	-	164.1
50	-	153.9	-
57	161.3	-	169.8
60	-	159.8	-
67	166.9	-	175.4
70	-	167.1	-
77	173.0	-	182.1
80	-	-	-
85	-	174.8	-
87	179.3	-	189.0
90	-	180.3	-
95	-	-	-
97	185.3	-	196.8
100	-	188.4	-
105	-	193.8	-
107	192.3	-	206.0
110	-	198.8	-
117	197.0	-	211.7
120	-	205.1	-
127	200.5	-	215.8
130	-	210.2	-
137	204.0	-	220.8
140	-	214.9	-
147	207.6	-	225.2
150	-	220.6	-
157	211.3	-	229.6
160	-	227.4	-
167	214.4	-	234.2
170	-	232.1	-
177	218.5	-	238.5
180	-	-	-
187	221.5	-	243.0

Cont'd

TEMPERATURE (°C)	75HBA/25HNA (1) C _p (J/mol°C)	70HBA/30HNA (2) C _p (J/mol°C)	58HBA/42HNA (1) C _p (J/mol°C)
190	-	236.9	-
197	225.6	-	247.6
200	-	242.3	-
210	-	246.9	-
217	229.3	-	252.2
220	-	250.9	-
227	245.4	-	253.6
230	-	256.3	-
237	246.5	-	256.0
240	-	260.7	-
247	247.6	-	258.4
250	-	264.7	-
257	248.7	-	260.7
260	-	268.7	-
267	249.8	-	263.1
270	-	271.8	-
277	250.0	-	265.5
280	-	275.3	-
287	251.9	-	267.9
290	-	280.8	-
297	253.0	-	270.3
300	-	283.1	-
307	254.1	-	272.7
310	-	287.8	-
317	255.2	-	275.1
320	-	291.7	-
327	256.3	-	277.5

(1): Ref. 100

(2): This work

A.1.2: Thermal Conductivity Data

TEMPERATURE (°C)	THERMAL CONDUCTIVITY (J/m.sec°C)
30	0.237
40	0.240
50	0.242
60	0.242
70	0.244
80	0.245
90	0.246
100	0.245
110	0.242
120	0.242
130	0.242
140	0.245
150	0.245
160	0.246
170	0.249
180	0.250
190	0.251
200	0.251
210	0.252
220	0.252
230	0.252
240	0.251
250	0.251
260	0.252
270	0.253
280	0.252
290	0.248
300	0.249
310	0.249
320	0.251

A.1.3 Thermal Diffusivity Data

TEMPERATURE (°C)	THERMAL DIFFUSIVITY (m ² /sec)E+7
30	
40	1.932
50	
60	1.936
70	
80	1.942
90	
100	1.941
110	
120	1.940
130	
140	1.943
150	
160	1.943
170	
180	1.947
190	
200	1.946
210	
220	1.946
230	
240	1.946
250	
260	1.948
270	
280	1.949
290	
300	1.942
310	
320	1.940

APPENDIX A.2

PRESSURE-VOLUME-TEMPERATURE DATA

TEMPERATURE = 300 °C		TEMPERATURE = 320 °C	
PRESSURE (N/m ²)E+7	DENSITY (g/cm ³)	PRESSURE (N/m ²)E+7	DENSITY (g/cm ³)
82.75	1.333	79.94	1.318
117.11	1.337	131.14	1.323
155.68	1.341	187.94	1.327
208.98	1.345	255.26	1.331
269.28	1.349	298.74	1.335
308.56	1.353	371.67	1.339
371.67	1.357	453.02	1.344
441.80	1.362	528.75	1.349
516.13	1.366	621.32	1.353
593.27	1.370	659.19	1.357
673.21	1.374	743.34	1.362
715.29	1.379	827.49	1.366
799.44	1.383	918.65	1.371
883.59	1.387	1009.8	1.375
981.77	1.392		

APPENDIX A.3

MELTING AND CRYSTALLIZATION BEHAVIOR

A.3.1: Melting of Isothermally Crystallized Samples

MELTING TEMPERATURE (°C)		
CRYSTALLIZATION TEMPERATURE (°C)	PEAK I	PEAK II
160	276.0	
170	276.5	
185	276.2	260.4
200	276.3	266.6
210		274.5
220		279.8
230		284.5
235		288.0
240		293.5
245		296.3
250		300.1
255		303.0

A.3.2: Effect of Cooling Rates on Heat of Fusion

COOLING RATES		HEAT OF FUSION ΔH_f	
X_R (°C/min)	Experimental (J/g)	Calculated (J/g)	
0.1	11.21	10.736	
0.2	9.81	10.113	
0.4	8.73	9.125	
0.8	7.77	7.788	
1.6	6.59	6.323	
3.2	5.02	5.046	
6.4	4.39	4.136	
12.8	3.64	3.578	
25.6	3.32	3.265	
51.2	2.89	3.099	
102.4	2.89	3.014	

A.3.3: Effect of Cooling Rates on Melting Temperature

COOLING RATES (°C/min)	MELTING TEMPERATURE (°C)	CRYSTALLIZATION TEMPERATURE (°C)
0.0		
0.1	293.3	
0.2	289.6	
0.4	284.4	253.0
0.8	278.8	250.5
1.6	275.6	245.9
3.2	274.8	242.1
6.4	274.4	237.4
12.8	275.3	232.7
25.6	274.3	228.7
51.2	275.5	222.4
102.4		211.1

A.3.4: Comparison of Data Obtained Experimentally

	THIS WORK	LITERATURE (°)
HNB/HNA (mol%)	70/30	58/42
T_m (C)	300.5, 372	--
ΔH_m (J/g)	13.59	12.91
ΔS_m (J/mol.K)	3.2	3.19
σ_e (ergs/cm ²)	4.2	--

° : Ref. 91

APPENDIX A.4

KINETICS OF CRYSTALLIZATION

A.4.1: Variation of $\ln(\dot{x}/1-x)$ with Temperature at Different Cooling Rates.

$\ln(\dot{x}/1-x)$			
TEMPERATURE (°C)	4 °C/min	7 °C/min	10 °C/min
238			-6.164
239		-6.012	-6.527
240		-6.198	-6.848
241		-6.564	-7.022
242		-6.917	-7.551
243		-7.243	-7.859
244	-6.987	-7.536	-8.102
245	-7.321	-7.896	-8.430
246	-7.736	-8.171	-8.711
247	-8.123	-8.643	-9.117
248	-8.393	-8.807	-9.404
249	-8.783	-9.243	-9.629
250	-9.003	-9.540	-9.911

A.4.2: Variation of $\ln K$ with Temperature at Different Cooling Rates.

$\ln K$			
TEMPERATURE (K)	4°C/min	7°C/min	10°C/min
518	-13.79	-13.69	-13.72
519	-13.59	-13.44	-13.68
520	-13.47	-13.43	-13.55
521	-13.22	-13.09	-13.28
522	-12.92	-12.93	-13.11
523	-12.69	-12.68	-12.89

A.4.3: Variation of $\ln(a)$ as a Function of temperature.

CRYSTALLIZATION TEMPERATURE (K)	$\ln(a)$
503	0.677
498	0.634
493	0.609
483	0.591
473	0.567
463	0.548

APPENDIX A.5

DYNAMIC MECHANICAL MEASUREMENTS

A.5.1: Loss Processes of a Quenched Sample at 3.5 Hz.

TEMPERATURE (°C)	TAN δ	STORAGE MODULUS (MPa)	LOSS MODULUS (MPa)
-132	0.0000	1809	0.00
-129	0.0010	1744	1.74
-126	0.0010	1715	1.72
-121	0.0020	1779	3.56
-116	0.0020	1780	3.56
-111	0.0035	1718	6.01
-106	0.0045	1690	7.60
-101	0.0050	1752	8.76
-96	0.0060	1691	10.50
-91	0.0070	1663	11.64
-86	0.0080	1692	13.54
-81	0.0090	1665	14.99
-76	0.0110	1666	18.32
-71	0.0115	1640	18.86
-66	0.0125	1641	20.51
-61	0.0120	1671	20.05
-56	0.0155	1590	24.65
-51	0.0160	1591	25.46
-46	0.0170	1567	26.64
-41	0.0180	1544	27.79
-36	0.0180	1545	27.81
-31	0.0185	1499	27.74
-36	0.0190	1457	27.67
-21	0.0210	1501	31.52
-16	0.0220	1480	32.55
-11	0.0235	1481	34.80
-6	0.0260	1419	36.89
-1	0.0283	1421	40.21
4	0.0320	1423	45.53
9	0.0350	1365	47.77
14	0.0390	1312	51.18
19	0.0425	1313	55.79

Cont'd

TEMPERATURE (°C)	TAN δ	STORAGE MODULUS (MPa)	LOSS MODULUS (MPa)
24	0.0455	1280	58.26
29	0.0480	1219	58.53
34	0.0505	1192	60.20
39	0.0515	1126	58.00
44	0.0525	1091	57.26
49	0.0540	1047	56.53
54	0.0555	1007	55.87
59	0.0550	960	52.81
64	0.0530	902	47.79
69	0.0525	879	46.14
74	0.0500	823	41.16
79	0.0520	786	40.86
84	0.0540	741	39.99
89	0.0580	686	39.79
94	0.0615	631	38.82
99	0.0660	575	37.94
104	0.0690	530	36.60
109	0.0680	483	32.87
114	0.0640	450	28.80
120	0.0570	411	23.43
124	0.0552	389	21.50
129	0.0480	378	18.16
134	0.0435	363	15.77
139	0.0410	345	14.13
144	0.0400	332	13.26
149	0.0395	324	12.78
154	0.0380	307	11.67
159	0.0380	294	11.17
164	0.0390	283	11.04
169	0.0400	277	11.10
174	0.0420	265	11.12
179	0.0430	251	10.80
184	0.0455	247	11.23
189	0.0480	246	11.31
194	0.0510	223	11.36
199	0.0550	211	11.59
204	0.0600	196	11.73
209	0.0650	183	11.89

A.5.2: Loss Processes of an Annealed Sample (250°C for 10 Hours)
at 3.5 Hz.

TEMPERATURE (°C)	TAN δ	STORAGE MODULUS (MPa)	LOSS MODULUS (MPa)
-116	0.0010	2129	2.13
-111	0.0020	2055	4.11
-106	0.0030	2095	6.29
-101	0.0040	2098	8.39
-96	0.0045	2098	9.44
-91	0.0055	2026	11.14
-86	0.0060	2063	12.38
-81	0.0075	2063	15.47
-76	0.0090	2028	18.26
-71	0.0100	1994	19.94
-66	0.0110	2030	22.33
-61	0.0120	2032	24.38
-56	0.0130	1964	25.54
-51	0.0140	1966	27.53
-46	0.0143	1968	28.15
-41	0.0150	1969	29.54
-36	0.0160	1971	31.53
-31	0.0165	1940	32.01
-26	0.0165	1879	31.01
-21	0.0180	1881	33.85
-16	0.0190	1853	35.20
-11	0.0200	1827	36.54
-6	0.0215	1801	38.71
-1	0.0240	1775	42.61
4	0.0275	1726	47.46
9	0.0300	1704	51.11
14	0.0335	1681	56.31
19	0.0365	1681	61.37
24	0.0400	1615	64.58
29	0.0420	1593	66.92
34	0.0460	1660	76.37
39	0.0470	1496	70.30

Cont'd

TEMPERATURE (°C)	TAN δ	STORAGE MODULUS (MPa)	LOSS MODULUS (MPa)
44	0.0520	1443	75.03
49	0.0540	1394	75.27
54	0.0555	1332	73.94
59	0.0550	1276	70.18
64	0.0530	1165	61.72
69	0.0540	1165	62.92
74	0.0550	1103	60.67
79	0.0550	1045	57.47
84	0.0580	969	56.21
89	0.0610	918	55.99
94	0.0660	841	55.49
99	0.0710	781	55.47
104	0.0770	717	55.21
109	0.0770	640	49.29
114	0.0750	571	42.79
119	0.0720	524	37.71
124	0.0670	486	32.58
129	0.0610	463	28.24
134	0.0565	440	24.83
139	0.0530	422	22.36
144	0.0500	401	20.06
149	0.0480	381	18.27
154	0.0470	362	17.03
159	0.0460	352	16.19
164	0.0460	328	15.09
169	0.0460	324	14.91
175	0.0480	306	14.67
179	0.0490	301	14.72
184	0.0505	282	14.38
189	0.0530	263	13.94
194	0.0570	244	13.93
199	0.0600	220	13.21
204	0.0645	195	12.58
209	0.0690	173	11.91

A.5.3: Loss Processes of a Quenched Sample at 11 Hz.

TEMPERATURE (°C)	TAN δ	STORAGE MODULUS (MPa)	LOSS MODULUS (MPa)
-133	0.0000	1841	0.00
-128	0.0010	1775	1.78
-125	0.0015	1745	2.62
-120	0.0015	1811	2.72
-115	0.0020	1780	3.56
-110	0.0035	1689	5.91
-105	0.0040	1690	6.76
-100	0.0040	1783	7.13
-95	0.0060	1720	10.32
-90	0.0070	1636	11.46
-85	0.0075	1692	12.69
-80	0.0085	1693	14.39
-75	0.0100	1666	16.66
-70	0.0110	1667	18.33
-65	0.0120	1668	20.01
-60	0.0125	1727	21.59
-55	0.0150	1616	24.23
-50	0.0155	1617	25.06
-45	0.0170	1617	27.49
-40	0.0180	1592	28.66
-35	0.0190	1569	29.80
-30	0.0205	1522	31.20
-25	0.0190	1499	28.49
-20	0.0210	1523	31.99
-15	0.0220	1501	33.03
-10	0.0225	1503	33.81
-5	0.0250	1460	36.49
0	0.0270	1462	39.46
5	0.0295	1464	43.17
10	0.0330	1402	46.28
15	0.0370	1383	51.18
20	0.0400	1347	53.90
25	0.0440	1313	57.78
30	0.0470	1265	59.44
35	0.0510	1250	63.76

Cont'd

TEMPERATURE (°C)	TAN δ	STORAGE MODULUS (MPa)	LOSS MODULUS (MPa)
40	0.0570	1178	67.12
45	0.0560	1139	63.77
50	0.0600	1091	65.46
55	0.0630	1058	66.66
60	0.0635	1007	63.93
65	0.0620	960	59.54
70	0.0600	894	53.62
75	0.0590	857	50.57
80	0.0580	817	47.36
85	0.0595	780	46.39
90	0.0620	719	44.60
95	0.0655	659	43.19
100	0.0690	605	41.75
105	0.0705	553	39.00
110	0.0700	502	35.16
115	0.0669	470	31.47
121	0.0600	434	26.01
125	0.0550	413	22.70
130	0.0505	394	19.90
135	0.0460	373	17.16
140	0.0430	358	15.38
145	0.0405	346	14.01
150	0.0390	337	13.15
155	0.0380	324	12.29
160	0.0375	303	11.35
165	0.0375	291	10.92
170	0.0380	291	11.04
175	0.0390	279	10.89
180	0.0400	265	10.61
185	0.0420	256	10.75
190	0.0435	245	10.64
195	0.0460	232	10.66
200	0.0500	216	10.78
205	0.0535	204	10.89
210	0.0580	189	10.96

A.5.4: Loss Processes of an Annealed Sample (250°C for 10 Hours)
at 11 Hz.

TEMPERATURE (°C)	TAN δ	STORAGE MODULUS (MPa)	LOSS MODULUS (MPa)
-115	0.0005	2129	1.06
-110	0.0010	2130	2.13
-105	0.0020	2173	4.35
-100	0.0030	2136	6.41
-95	0.0040	2098	8.39
-90	0.0045	2098	9.44
-85	0.0055	2100	11.55
-80	0.0060	2100	12.60
-75	0.0075	2064	15.48
-70	0.0085	2064	17.54
-65	0.0095	2065	19.62
-60	0.0105	2068	21.71
-55	0.0120	2032	24.38
-50	0.0130	2034	26.44
-45	0.0140	2002	28.02
-40	0.0145	2003	29.04
-35	0.0150	2004	30.07
-30	0.0160	1972	31.55
-25	0.0165	1941	32.03
-20	0.0170	1942	33.02
-15	0.0180	1913	34.43
-10	0.0190	1856	35.26
-5	0.0200	1857	37.14
0	0.0220	1830	40.26
5	0.0250	1804	45.11
10	0.0280	1807	50.60
15	0.0305	1755	53.53
20	0.0340	1730	58.83
25	0.0370	1683	62.27
30	0.0410	1660	68.05
35	0.0450	1594	71.73
40	0.0480	1574	75.57
45	0.0530	1516	80.35
50	0.0570	1461	83.30
55	0.0590	1394	82.25

Cont'd

TEMPERATURE (°C)	TAN δ	STORAGE MODULUS (MPa)	LOSS MODULUS (MPa)
60	0.0600	1332	79.94
65	0.0600	1276	76.53
70	0.0600	1212	72.71
75	0.0595	1145	68.12
80	0.0600	1092	65.53
85	0.0620	1018	63.13
90	0.0640	978	62.56
95	0.0680	891	60.56
100	0.0730	818	59.74
105	0.0770	753	57.97
110	0.0775	672	52.11
115	0.0760	608	46.20
120	0.0730	563	41.09
125	0.0675	511	34.49
130	0.0630	479	30.20
135	0.0575	465	26.73
140	0.0530	444	23.50
145	0.0500	424	21.18
150	0.0480	402	19.31
155	0.0460	384	17.68
160	0.0445	366	16.28
165	0.0440	345	15.18
170	0.0440	333	14.65
176	0.0450	322	14.48
180	0.0460	309	14.21
185	0.0470	295	13.87
190	0.0500	271	13.53
195	0.0530	253	13.42
200	0.0560	235	13.14
205	0.0610	205	12.50
210	0.0660	179	11.81

APPENDIX A.6

RHEOLOGICAL DATA

A.6.1: Shear Viscosity Data at 300°C.

FORCE DATA (RAW DATA) IN KG

APP. GAMA	L/D=100.0	L/D=80.0	L/D=40.0	L/D=20.0
0.05	47.50	25.00	13.70	11.00
0.10	86.00	39.00	17.20	15.80
0.20	125.00	57.00	21.50	21.50
0.50	240.00	104.00	37.00	26.20
1.00	300.00	160.00	60.00	52.00
2.00	410.00	245.00	110.00	74.00
5.00	590.00	415.00	190.00	122.00

PRESSURE DATA (PD) IN MPA

APP. GAMA	L/D=100.0	L/D=80.0	L/D=40.0	L/D=20.0
13.67	6.54	3.44	1.86	1.51
27.34	11.84	5.37	2.37	2.17
54.68	17.20	7.84	2.96	2.96
136.70	33.03	14.31	5.09	3.61
273.40	41.29	22.02	8.26	7.16
546.81	56.42	33.72	15.14	10.18
1367.02	81.19	57.11	26.15	16.79

SHEAR STRESS DATA (TAU) IN MPA

APP. GAMA	L/D=100.0	L/D= 80.0	L/D= 40.0	L/D= 20.0
13.7	0.0163	0.0108	0.0118	0.0189
27.3	0.0296	0.0168	0.0148	0.0272
54.7	0.0430	0.0245	0.0185	0.0370
136.7	0.0826	0.0447	0.0318	0.0451
273.4	0.1032	0.0688	0.0516	0.0895
546.8	0.1411	0.1054	0.0946	0.1273
1367.0	0.2030	0.1785	0.1634	0.2099

CONSISTENCY INDEX, k= 3236 POWER LAW INDEX, n= 0.51

TRUE GAMA(1/s)	TRUE TAU(MPa)	MEAS.VIS(Pa.s)	CALC' VIS
16.4	0.0145	883.17	898.43
32.7	0.0221	674.86	653.83
65.4	0.0308	469.84	475.83
163.6	0.0511	312.00	312.61
327.2	0.0783	239.19	227.50
654.4	0.1171	178.90	165.56
1636.1	0.1887	115.33	108.77

A.6.2: Extrudate Swell at two Different Shear Rates (T=300°C)

TIME (sec)	Shear Rate s ⁻¹ 26	Shear Rate s ⁻¹ 104
16	0.99	1.02
32	0.99	1.01
48	0.99	1.01
64	0.99	1.00
80	0.99	1.01
96	0.99	1.01
112	0.99	1.01
128	0.99	1.01
144	0.99	1.00
160	0.99	1.01
176	0.99	1.01
192	0.99	1.01
208	0.99	1.02
224	0.99	0.99
240	0.99	1.01
256	0.99	1.01
272	0.99	1.01
288	0.99	1.01
304	0.99	1.01
320	0.99	1.01
336	0.99	1.00
352	1.00	1.00
368	0.99	1.00
384	0.99	1.02
400	0.99	1.00
416	0.99	1.01
432	0.99	1.01
448	0.99	1.01
464	0.99	1.01
480	0.99	1.01
496	0.99	1.01
512	0.99	1.01
528	1.00	1.01
544	0.99	1.01
560	0.99	1.00
576	0.99	1.00
592	0.99	1.01
608	0.99	1.03
624	0.99	1.01
640	1.00	1.00
656	0.99	1.01
672	0.99	1.01
688	0.99	1.00
704	0.99	1.01
720	0.99	1.00

APPENDIX A.7

TYPICAL OUTPUT FOR VARIABLE-TIME DATA

TIME (sec)	PC1	PC2	PN	PH	V	TN	TM	ID
0.01	29.28	32.16	0	0	0	330.17	40.63	0
0.02	34.32	31.44	0	0	0	330.43	40.74	0
0.03	32.88	29.28	0	0	0	330.43	40.74	0
0.04	31.44	34.32	0	0	0	330.43	40.97	0
0.05	28.56	32.88	0	0	0	330.34	40.86	0
0.06	32.16	31.44	0	0	0	329.46	40.86	0
0.07	31.44	28.56	0	0	0	329.99	40.63	0
0.08	32.88	32.16	0	0	0	329.99	40.74	0
0.09	30.72	31.44	0	0	0	329.99	40.74	0
0.10	30.00	32.88	0	0	0	329.73	40.97	0
0.11	30.00	30.72	0	0	0	329.99	40.86	0
0.12	30.00	30.00	0	0	0	308.96	40.67	0
0.13	30.00	30.00	0	0	0	329.73	40.51	0
0.14	32.88	30.00	0	0	0	329.73	40.86	0
0.15	29.28	30.00	0	0	0	329.81	40.86	0
0.16	30.72	32.88	0	0	0	329.46	40.86	0
0.17	31.44	29.28	0	0	0	329.73	40.97	0
0.18	30.00	30.72	0	1.74	0.04	329.64	40.74	0
0.19	30.00	31.44	0	13.94	0.54	329.64	40.97	0
0.20	31.44	30.00	0	28.22	1.75	329.73	40.74	0
0.21	29.28	30.00	0	21.23	2.51	329.73	40.63	0
0.22	30.00	31.44	0	08.99	2.89	329.64	40.74	0
0.23	30.72	29.28	0	08.11	2.93	329.64	40.97	0
0.24	30.00	30.00	0	14.53	2.85	329.46	40.74	0
0.25	30.00	30.72	0	12.78	2.67	329.37	40.74	0.11
0.26	29.28	30.00	0	09.28	2.31	329.73	40.74	0.18
0.27	31.44	30.00	0	08.11	2.13	329.28	40.51	0.26
0.28	30.72	29.28	0	09.28	2.04	329.28	40.86	0.31
0.29	32.16	31.44	0	11.90	2.07	329.64	40.86	0.38
0.30	30.72	30.72	0	11.61	2.18	329.37	40.74	0.44
0.31	30.72	32.16	0	10.74	2.31	329.64	40.63	0.51
0.32	30.00	30.72	0	10.15	2.55	329.46	40.97	0.56
0.33	32.88	30.72	0	12.49	2.85	329.28	40.74	0.63
0.34	30.72	30.00	02.26	11.61	3.11	329.37	40.86	0.69
0.35	31.44	32.88	06.77	11.61	3.17	329.28	40.74	0.78
0.36	29.28	30.72	06.77	11.61	3.18	329.28	40.74	0.85
0.37	30.00	31.44	13.54	11.03	3.17	329.28	40.97	0.93
0.38	30.00	29.28	20.31	11.61	3.06	329.28	40.86	1.00
0.39	31.44	30.00	20.31	13.36	3.01	329.28	40.74	1.12
0.40	29.28	30.00	22.56	12.78	3.01	329.28	40.97	1.14
0.41	31.44	31.44	29.33	12.49	3.01	329.28	40.86	1.23
0.42	30.72	29.28	31.59	12.19	3.11	329.20	40.97	1.28
0.43	31.44	31.44	29.33	15.11	3.20	329.28	40.86	1.38
0.44	31.44	30.72	38.36	15.69	3.28	329.46	40.86	1.43
0.45	30.72	31.44	42.87	17.44	3.34	329.28	40.74	1.48
0.46	31.44	31.44	49.64	17.15	3.44	329.28	40.86	1.52
0.47	31.44	30.72	51.90	16.27	3.47	329.37	40.63	1.60
0.48	30.00	31.44	60.92	18.61	3.46	329.28	40.74	1.64
0.49	30.00	31.44	65.44	19.48	3.38	329.28	40.97	1.72
0.50	30.00	30.00	74.46	20.06	3.28	329.37	40.63	1.76

0.51	31.44	30.00	76.72	21.81	3.13	329.28	40.74	1.84
0.52	29.28	30.00	78.97	25.60	2.96	329.28	40.86	1.87
0.53	31.44	31.44	99.28	28.81	2.90	329.28	40.74	1.93
0.54	30.00	29.28	101.54	32.59	2.98	329.28	40.63	1.98
0.55	31.44	31.44	108.31	33.18	3.29	329.28	40.74	2.04
0.56	30.72	30.00	121.85	27.06	3.74	329.28	40.97	2.07
0.57	32.16	31.44	133.13	24.73	3.83	329.28	40.74	2.17
0.58	29.28	30.72	146.67	34.34	3.63	329.28	40.74	2.23
0.59	30.00	32.16	164.72	42.79	3.27	329.28	40.63	2.29
0.60	30.00	29.28	173.74	41.34	2.95	329.28	40.97	2.34
0.61	30.00	30.00	191.79	43.67	2.78	329.28	40.74	2.39
0.62	30.00	30.00	207.59	48.04	3.01	329.28	40.97	2.44
0.63	31.44	30.00	234.67	47.17	3.53	329.02	40.63	2.50
0.64	31.44	30.00	254.97	44.83	3.85	329.28	40.97	2.56
0.65	30.00	31.44	295.59	49.21	3.77	329.28	40.74	2.62
0.66	31.44	31.44	318.15	54.45	3.45	329.28	40.74	2.68
0.67	30.00	30.00	345.23	56.78	3.06	329.28	40.74	2.73
0.68	31.44	31.44	363.28	58.24	2.93	329.28	40.74	2.78
0.69	31.44	30.00	381.33	61.45	3.07	328.75	41.09	2.82
0.70	30.00	31.44	403.90	65.82	3.39	329.37	40.97	2.89
0.71	30.72	31.44	433.23	71.65	3.57	329.28	40.63	2.94
0.72	30.72	30.00	467.08	74.56	3.48	329.28	40.97	3.00
0.73	29.28	30.72	478.36	75.73	3.33	329.20	40.74	3.05
0.74	32.16	30.72	498.67	76.31	3.24	329.46	40.74	3.11
0.75	30.00	29.28	512.21	78.06	3.32	329.28	40.74	3.15
0.76	31.44	32.16	518.97	81.26	3.44	329.28	40.97	3.23
0.77	30.72	30.00	537.03	85.05	3.46	329.28	40.74	3.27
0.78	30.72	31.44	555.08	88.55	3.41	329.20	40.74	3.34
0.79	31.44	30.72	568.62	89.42	3.38	329.28	40.74	3.37
0.80	30.72	30.72	575.38	89.13	3.40	329.28	40.97	3.43
0.81	30.72	31.44	584.41	90.30	3.46	329.28	41.32	3.47
0.82	31.44	30.72	595.69	92.63	3.46	329.28	42.02	3.53
0.83	31.44	30.72	609.23	94.09	3.43	329.28	42.36	3.59
0.84	31.20	31.44	604.72	94.96	3.42	329.28	42.83	3.63
0.85	31.93	31.44	616.00	96.13	3.42	329.20	43.40	3.69
0.86	37.04	31.44	616.00	97.29	3.45	329.28	43.98	3.75
0.87	41.42	31.44	622.77	97.58	3.49	329.37	44.67	3.79
0.88	45.08	31.44	622.77	98.75	3.47	329.28	44.90	3.86
0.89	45.08	31.44	629.54	97.00	3.47	329.28	45.59	3.90
0.90	48.73	31.44	629.54	99.33	3.47	329.28	45.94	3.95
0.91	50.92	32.16	636.31	99.91	3.48	329.37	46.05	4.00
0.92	53.84	31.44	640.82	101.08	3.50	329.28	46.51	4.07
0.93	58.22	30.00	647.59	101.37	3.50	329.37	46.51	4.11
0.94	61.14	32.16	656.62	103.41	3.43	329.28	46.05	4.17
0.95	62.61	29.28	661.13	104.29	3.43	329.28	47.43	4.23
0.96	66.99	31.44	656.62	104.29	3.44	329.28	47.66	4.29
0.97	71.37	32.88	667.90	104.87	3.43	329.28	47.66	4.35
0.98	74.29	31.44	672.41	107.49	3.45	329.28	48.12	4.40
0.99	78.68	36.48	672.41	107.78	3.49	329.28	48.23	4.57
1.00	81.60	39.36	685.95	107.20	3.48	329.28	48.35	4.61
1.01	83.79	38.64	685.95	108.66	3.45	328.75	48.92	4.83
1.02	87.44	42.97	699.49	109.82	3.49	329.28	49.03	5.56
1.03	91.09	44.41	710.77	110.41	3.47	329.37	49.26	7.26
1.04	95.48	47.29	713.03	112.74	3.44	329.37	49.38	6.79
1.05	98.40	49.45	717.54	113.61	3.42	329.28	49.49	6.11
1.06	104.24	53.77	722.05	114.19	3.47	329.37	49.49	5.65

1.07	107.16	55.21	731.08	114.49	3.48	329.37	49.83	5.12
1.08	110.82	56.65	740.10	113.90	3.44	329.28	49.83	5.26
1.09	110.82	60.26	742.36	114.19	3.44	329.28	50.18	5.11
1.10	115.20	61.70	755.90	116.53	3.41	329.28	50.18	5.14
1.11	121.77	65.30	755.90	117.40	3.45	329.20	50.52	5.14
1.12	124.69	69.62	771.69	116.53	3.44	329.28	50.63	5.18
1.13	126.89	71.78	764.92	119.73	3.43	329.28	50.75	5.30
1.14	132.73	73.22	771.69	119.73	3.44	329.20	51.09	5.51
1.15	137.11	77.55	778.46	119.73	3.41	329.28	50.86	5.48
1.16	140.03	78.99	782.97	121.19	3.41	329.28	50.86	5.48
1.17	142.96	83.31	785.23	122.65	3.44	329.37	51.09	5.65
1.18	148.80	86.19	795.51	124.39	3.45	329.28	51.09	5.62
1.19	151.72	89.79	796.51	125.85	3.42	329.28	51.43	5.43
1.20	159.03	91.96	798.77	124.39	3.51	329.28	51.32	5.47
1.21	169.25	96.28	801.03	123.52	3.45	329.28	51.66	5.51
1.22	183.86	102.04	812.31	123.81	3.49	329.28	52.00	5.58
1.23	201.39	112.13	812.31	124.39	3.47	329.37	51.77	5.61
1.24	226.23	126.54	825.85	125.27	3.38	329.28	52.00	5.66
1.25	265.67	143.11	837.13	128.77	3.45	329.64	51.77	5.72
1.26	332.87	169.04	852.92	127.60	3.45	329.28	52.00	5.75
1.27	450.48	211.55	880.00	131.39	3.31	329.28	52.23	5.80
1.28	654.27	282.87	918.36	137.51	3.26	329.28	52.23	5.81
1.29	905.55	415.43	981.54	144.50	3.23	329.46	52.45	5.90
1.30	1137.83	634.45	1096.62	156.74	3.06	329.28	52.45	5.94
1.31	1316.79	899.57	1254.56	178.31	2.95	329.37	52.34	5.96
1.32	1487.72	1132.99	1403.49	202.50	3.07	329.37	52.45	6.01
1.33	1637.46	1311.66	1529.85	219.11	3.06	329.28	52.91	6.03
1.34	1750.68	1483.12	1703.59	237.76	2.92	328.75	52.68	6.06
1.35	1833.22	1632.26	1861.54	261.66	3.07	329.28	52.34	6.11
1.36	1885.81	1736.72	1994.67	282.64	3.09	329.46	52.79	6.14
1.37	1922.34	1813.81	2089.44	295.46	3.15	329.28	53.13	6.19
1.38	1925.99	1866.40	2154.87	300.71	3.16	329.37	53.25	6.23
1.39	1938.41	1893.05	2202.26	306.25	3.20	329.28	53.25	6.27
1.40	1944.98	1900.26	2233.85	313.24	3.24	329.28	53.13	6.34
1.41	1955.94	1906.02	2256.41	317.32	3.22	329.28	53.25	6.39
1.42	1964.70	1909.62	2276.72	318.49	3.25	329.28	53.25	6.43
1.43	1974.20	1920.43	2308.31	322.57	3.25	329.28	53.47	6.45
1.44	1987.35	1929.08	2315.08	325.19	3.22	329.46	53.59	6.52
1.45	1991.73	1939.16	2335.38	326.94	3.23	329.64	53.47	6.56
1.46	1999.76	1955.01	2351.18	331.02	3.25	329.73	53.81	6.62
1.47	2005.61	1957.17	2366.97	334.51	3.27	329.73	53.81	6.64
1.48	2001.96	1962.22	2385.03	334.51	3.30	329.81	53.81	6.71
1.49	2014.67	1968.70	2398.56	335.10	3.23	329.81	53.81	6.74
1.50	2033.56	1964.38	2396.31	335.39	3.27	329.46	54.15	6.81
1.51	2038.67	1957.89	2414.36	337.43	3.26	329.99	53.93	6.85
1.52	2040.67	1950.69	2400.82	339.18	2.58	329.46	53.93	6.91
1.53	2032.56	1893.05	1999.18	476.15	0.06	329.81	54.04	6.94
1.54	2001.96	1819.57	1807.38	900.47	0	330.08	54.15	6.94
1.55	1993.92	1756.17	1651.69	1127.2	0	329.73	54.04	6.95
1.56	1945.71	1715.11	1529.85	1127.2	0	329.99	54.27	6.95
1.57	1833.95	1673.32	1439.59	1127.2	0	329.73	54.38	6.95
1.58	1753.60	1644.50	1378.67	1068.3	0	329.73	54.27	6.93
1.59	1704.66	1615.69	1320.00	910.96	0	329.73	54.15	6.94
1.60	1663.76	1589.03	1272.62	1007.7	0	329.81	54.49	6.94
1.61	1636.00	1558.77	1232.00	974.20	0	329.73	54.49	6.92
1.62	1596.55	1535.00	1191.38	823.53	0	329.64	54.38	6.91

1.62	1568.80	1501.14	1150.77	761.17	0	329.64	54.15	6.91
1.64	1538.12	1471.60	1121.44	755.05	0	329.81	54.72	6.90
1.65	1511.09	1437.02	1092.10	716.87	0	329.73	54.72	6.91
1.66	1478.22	1408.20	1065.03	777.49	0	329.64	54.95	6.91
1.67	1442.43	1374.34	1042.46	1127.2	0	329.64	54.49	6.90
1.68	1411.75	1345.52	1017.64	1127.2	0	329.73	54.72	6.90
1.69	1379.61	1320.31	988.31	1127.2	0	329.64	54.72	6.90
1.70	1345.28	1290.05	968.00	920.29	0	328.75	54.72	6.91
1.71	1318.98	1264.83	952.21	940.10	0	328.75	54.72	6.92
1.72	1288.30	1240.34	922.87	1074.2	0	329.64	54.72	6.90
1.73	1262.74	1212.96	916.10	937.77	0	329.46	54.72	6.90
1.74	1235.71	1189.91	891.28	779.53	0	329.64	55.06	6.89
1.75	1212.34	1166.85	873.23	761.75	0	329.64	54.83	6.90
1.76	1186.04	1145.96	857.44	769.91	0	329.28	54.95	6.89
1.77	1160.47	1124.35	837.13	708.13	0	329.46	54.95	6.91
1.78	1136.37	1104.89	821.33	645.76	0	329.37	54.95	6.88
1.79	1117.38	1086.16	810.05	920.58	0	329.64	55.06	6.90
1.80	1096.93	1071.03	798.77	1127.2	0	329.28	55.06	6.88
1.81	1076.47	1053.74	782.97	1127.2	0	328.75	55.18	6.91
1.82	1057.48	1042.94	773.95	1122.3	0	338.04	55.17	6.90
1.83	1044.33	1026.37	753.64	882.69	0	337.51	55.51	6.89
1.84	1025.34	1127.95	753.64	997.22	0	336.80	55.06	6.89
1.85	1013.65	1000.43	749.13	804.30	0	336.27	55.17	6.90
1.86	996.85	986.02	740.10	386.10	0	335.39	55.40	6.90
1.87	987.36	973.05	731.08	128.77	0	334.94	55.29	6.89
1.88	971.29	964.41	728.82	093.21	0	334.68	55.40	6.89
1.89	958.14	955.76	722.05	127.89	0	334.32	55.06	6.91
1.90	944.26	942.07	715.28	111.28	0	333.71	54.95	6.90
1.91	934.77	932.71	710.77	69.02	0	333.53	55.17	6.91
1.92	925.27	924.78	706.26	81.85	0	333.17	55.40	6.90
1.93	914.31	919.74	699.49	100.5	0	332.82	55.40	6.90
1.94	907.01	909.65	690.46	76.31	0	332.64	55.51	6.90
1.95	898.24	893.80	652.10	51.25	0	332.20	55.51	6.92
1.96	890.21	862.83	588.92	52.12	0	332.11	55.63	6.97
1.97	880.71	823.20	537.03	55.33	0	331.85	55.63	6.88
1.98	866.10	779.25	494.15	43.38	0	331.67	55.17	6.88
1.99	836.88	746.84	462.56	34.93	0	331.23	55.51	6.87
2.00	795.98	709.37	424.21	34.05	0	331.23	55.51	6.87
2.01	753.61	673.35	390.36	30.55	0	331.14	55.63	6.86
2.02	714.90	636.61	358.77	27.43	0	331.14	55.63	6.86
2.03	679.11	602.03	333.95	18.90	0	330.70	55.63	6.84
2.04	643.32	578.25	318.15	19.19	0	330.96	55.63	6.84
2.05	603.14	558.08	311.38	20.35	0	330.70	55.74	6.84
2.06	571.73	538.63	295.59	18.02	0	330.70	55.51	6.82
2.07	543.97	523.50	286.56	14.82	0	330.70	55.74	6.83
2.08	525.71	506.93	275.28	12.78	0	330.43	55.63	6.83
2.09	505.99	494.68	266.26	13.36	0	330.34	55.74	6.81
2.10	490.65	480.99	266.26	13.36	0	330.34	55.63	6.83
2.11	476.04	471.63	257.23	12.19	0	330.34	55.63	6.82
2.12	462.16	461.54	254.97	12.49	0	330.34	55.96	6.83
2.13	449.75	453.62	252.72	12.49	0	329.99	55.74	6.82
2.14	439.52	446.41	248.21	12.49	0	330.17	55.63	6.83
2.15	429.29	440.65	245.95	11.03	0	330.08	55.74	6.81
2.16	424.91	432.72	245.95	11.32	0	330.08	55.63	6.83
2.17	414.68	429.12	248.21	11.90	0	329.73	55.96	6.81
2.18	411.03	424.08	243.69	12.78	0	329.81	55.74	6.81

2.19	401.54	419.76	245.95	12.49	0	329.73	55.96	6.81
2.20	397.15	417.59	245.95	13.36	0	329.73	55.74	6.81
2.21	393.50	413.99	245.95	12.78	0	329.81	55.96	6.80
2.22	389.12	409.67	248.21	13.94	0	329.81	55.74	6.81
2.23	385.47	404.63	248.21	14.82	0	329.99	55.96	6.81
2.24	382.54	403.19	248.21	14.82	0	329.81	55.96	6.81
2.25	379.62	400.30	252.72	15.40	0	329.73	55.96	6.81
2.26	377.43	398.14	245.95	16.27	0	329.73	55.96	6.81
2.27	374.51	395.26	245.95	15.69	0	329.73	55.74	6.81
2.28	373.78	393.82	245.95	16.27	0	329.73	55.63	6.81
2.29	369.40	383.78	250.46	15.40	0	329.73	56.08	6.81
2.30	368.67	388.06	250.46	16.27	0	329.73	56.08	6.81
2.31	364.28	385.89	248.21	15.69	0	329.73	55.96	6.81
2.32	363.55	383.73	248.21	15.98	0	329.46	55.96	6.81
2.33	362.09	380.85	243.69	16.57	0	329.73	55.96	6.81
2.34	359.17	377.97	250.46	15.98	0	329.28	56.19	6.81
2.35	356.25	375.81	241.44	15.98	0	329.73	55.96	6.81
2.36	354.06	375.09	248.21	16.57	0	329.64	55.96	6.81
2.37	352.60	371.49	248.21	15.69	0	329.64	55.96	6.81
2.38	350.40	371.49	243.69	16.27	0	329.64	55.96	6.80
2.39	349.67	370.05	245.95	16.27	0	329.28	56.53	6.81
2.40	346.75	367.88	241.44	16.27	0	329.28	55.96	6.81
2.41	346.75	365.72	241.44	16.27	0	329.28	56.08	6.81
2.42	342.37	363.56	245.95	16.27	0	329.28	56.19	6.81
2.43	341.64	362.12	248.21	16.27	0	329.64	56.30	6.82
2.44	340.91	359.96	241.44	16.27	0	329.37	55.96	6.80
2.45	339.45	359.96	243.69	16.57	0	329.55	55.96	6.81
2.46	334.33	356.36	248.21	15.98	0	329.46	55.96	6.80
2.47	335.06	356.36	241.44	16.27	0	329.28	56.19	6.81
2.48	333.60	354.20	245.95	16.27	0	329.28	56.30	6.80
2.49	333.60	354.20	243.69	16.27	0	329.64	56.30	6.81
2.50	331.41	352.03	239.18	16.27	0	329.37	56.30	6.81
2.51	329.95	350.59	239.18	16.27	0	329.46	56.19	6.82
2.52	328.49	350.59	239.18	16.27	0	329.46	56.19	6.80
2.53	328.49	349.15	236.92	16.27	0	329.46	56.30	6.81
2.54	326.30	348.43	236.92	16.27	0	329.37	55.96	6.80
2.55	326.30	346.27	236.92	16.27	0	329.37	56.30	6.81
2.56	324.84	345.55	239.18	15.98	0	329.46	56.08	6.80
2.57	323.38	344.83	236.92	16.27	0	329.64	56.19	6.81
2.58	321.92	344.83	241.44	16.27	0	329.28	56.53	6.80
2.59	321.19	342.67	234.67	16.86	0	329.28	56.08	6.81
2.60	319.72	342.67	236.92	16.57	0	329.37	56.30	6.80
2.61	321.19	342.67	236.92	16.57	0	329.46	56.19	6.81
2.62	320.46	339.79	230.15	17.15	0	329.28	56.42	6.81
2.63	318.99	339.79	230.15	16.57	0	329.28	56.53	6.81
2.64	317.53	337.63	232.41	17.15	0	329.28	55.96	6.81
2.65	317.53	339.07	239.18	15.69	0	329.28	56.30	6.81
2.66	317.53	336.91	230.15	16.86	0	329.28	56.08	6.81
2.67	315.34	336.91	230.15	16.86	0	329.28	56.53	6.81
2.68	313.15	334.74	232.41	16.86	0	329.37	56.42	6.81
2.69	313.88	333.30	234.67	16.86	0	329.28	56.30	6.81
2.70	312.42	333.30	227.90	16.27	0	329.28	56.53	6.81
2.71	312.42	334.02	230.15	16.57	0	329.28	56.30	6.80
2.72	312.42	333.30	230.15	16.27	0	329.46	56.30	6.81
2.73	311.69	333.30	230.15	16.57	0	329.64	56.64	6.80
2.74	310.23	331.14	230.15	17.15	0	329.28	56.42	6.81

2.75	309.50	331.14	225.64	16.86	0	329.28	56.53	6.80
2.76	308.77	329.70	225.64	16.27	0	329.28	56.53	6.81
2.77	308.04	326.82	227.90	16.57	0	329.28	56.53	6.80
2.78	308.77	329.70	230.15	17.15	0	329.28	56.53	6.81
2.79	305.85	328.26	225.64	17.15	0	329.28	56.53	6.80
2.80	307.31	328.26	225.64	16.57	0	329.46	56.53	6.81
2.81	305.85	326.82	230.15	15.69	0	329.28	56.30	6.80
2.82	305.85	325.38	223.38	16.57	0	329.28	56.53	6.81
2.83	305.85	326.82	225.64	17.15	0	329.37	56.42	6.80
2.84	305.85	325.38	225.64	16.57	0	329.28	56.53	6.81
2.85	304.39	325.38	225.64	16.86	0	329.28	56.64	6.80
2.86	305.12	325.38	223.38	16.57	0	329.37	56.53	6.81
2.87	303.65	323.94	225.64	16.86	0	329.28	56.53	6.80
2.88	303.65	321.78	221.13	16.86	0	329.37	56.53	6.81
2.89	303.65	323.94	225.64	16.57	0	329.37	56.30	6.81
2.90	302.19	322.50	223.38	16.86	0	329.28	56.42	6.81
2.91	302.19	321.78	223.38	16.57	0	329.28	56.53	6.81
2.92	300.73	320.33	221.13	16.57	0	329.28	56.53	6.81
2.93	300.00	322.50	223.38	16.27	0	329.28	56.64	6.80
2.94	300.00	322.50	221.13	16.57	0	329.28	56.53	6.81
2.95	300.00	320.33	221.13	16.57	0	329.28	56.64	6.81
2.96	300.00	321.78	223.38	17.15	0	329.46	56.53	6.81
2.97	297.81	320.33	223.38	16.27	0	329.28	56.53	6.80
2.98	300.00	319.61	205.33	16.86	0	329.28	56.42	6.80
2.99	298.54	318.17	205.33	16.27	0	329.28	56.64	6.81
3.00	300.00	317.45	216.62	16.57	0	329.28	56.64	6.81
3.01	297.81	318.17	221.13	17.15	0	329.28	56.53	6.81
3.02	297.81	318.17	223.38	16.27	0	329.37	55.96	6.80
3.03	297.81	317.45	209.85	16.57	0	329.28	56.87	6.81
3.04	296.35	316.73	218.87	16.27	0	329.46	56.64	6.81
3.05	297.08	316.01	221.13	16.57	0	329.28	56.53	6.81
3.06	297.08	316.73	216.62	16.57	0	329.28	56.53	6.80
3.07	296.35	315.29	214.36	16.27	0	329.37	56.75	6.81
3.08	296.35	316.01	216.62	16.27	0	329.28	56.87	6.81
3.09	295.62	316.01	209.85	17.15	0	329.37	56.64	6.81
3.10	295.62	314.57	218.87	16.86	0	329.28	56.75	6.80
3.11	294.89	316.01	209.85	16.27	0	329.64	56.53	6.81
3.12	294.89	316.01	212.10	16.27	0	329.46	56.53	6.80
3.13	294.16	316.01	212.10	17.15	0	329.28	56.87	6.81
3.14	293.43	313.85	209.85	16.86	0	329.28	56.87	6.80
3.15	294.16	313.13	214.36	16.27	0	329.28	56.64	6.81
3.16	294.16	312.41	212.10	15.69	0	329.37	56.87	6.80
3.17	292.70	311.69	216.62	16.27	0	329.28	56.64	6.81
3.18	291.97	310.25	212.10	17.15	0	329.28	56.64	6.80
3.19	291.97	310.97	209.85	17.15	0	329.46	56.64	6.81
3.20	291.97	310.25	214.36	16.57	0	329.20	56.87	6.80
3.21	290.51	311.69	216.62	16.57	0	329.28	56.53	6.81
3.22	291.97	310.97	214.36	16.27	0	329.37	56.64	6.80
3.23	289.78	310.97	212.10	16.27	0	329.28	56.64	6.81
3.24	291.24	310.25	212.10	16.27	0	329.28	56.53	6.80
3.25	289.78	310.25	209.85	16.27	0	329.28	56.64	6.81
3.26	288.32	308.09	212.10	15.98	0	329.28	56.53	6.80
3.27	287.59	310.25	207.59	16.57	0	329.28	56.64	6.81
3.28	289.78	308.09	214.36	16.27	0	329.28	56.53	6.81
3.29	288.32	308.09	207.59	16.27	0	329.28	56.53	6.80
3.30	288.32	308.09	209.85	15.98	0	329.37	56.64	6.81

Cont'd

3.31	288.32	308.09	205.33	16.27	0	329.28	56.64	6.81
3.32	287.59	308.09	207.59	16.27	0	329.28	56.87	6.81
3.33	287.59	308.09	212.10	16.27	0	329.28	56.64	6.81
3.34	286.12	305.21	209.85	16.27	0	329.28	56.75	6.81
3.35	286.12	307.37	207.59	15.69	0	329.28	56.64	6.80
3.36	285.39	305.93	205.33	16.57	0	329.37	56.75	6.81
3.37	286.12	305.21	212.10	16.27	0	329.28	56.87	6.80
3.38	286.12	305.93	207.59	16.27	0	329.28	56.87	6.81
3.39	285.39	305.21	205.33	16.27	0	329.28	56.87	6.80
3.40	284.66	304.49	205.33	16.27	0	329.28	56.87	6.81
3.41	286.12	305.21	205.33	15.69	0	329.28	56.87	6.80
3.42	284.66	304.49	203.08	16.27	0	329.28	56.87	6.81
3.43	285.39	305.21	200.82	16.27	0	329.20	56.64	6.80
3.44	284.66	303.76	205.33	16.27	0	329.28	56.53	6.81
3.45	284.66	303.04	209.85	16.27	0	329.28	56.53	6.81
3.46	282.47	303.76	207.59	16.27	0	329.28	56.87	6.79
3.47	283.93	303.04	205.33	16.27	0	329.28	56.87	6.80
3.48	283.20	302.32	203.08	15.98	0	329.28	56.75	6.81
3.49	282.47	300.88	203.08	16.27	0	329.28	56.53	6.80
3.50	282.47	300.88	200.82	16.27	0	329.28	56.53	6.82
3.51	282.47	302.32	205.33	15.98	0	329.28	56.87	6.79
3.52	282.47	301.60	205.33	14.82	0	329.28	56.87	6.81
3.53	282.47	298.72	200.82	15.69	0	329.28	56.64	6.80
3.54	282.47	300.88	200.82	16.27	0	329.28	56.64	6.81
3.55	281.01	300.88	200.82	15.98	0	329.28	56.75	6.80
3.56	280.28	299.44	200.82	16.27	0	329.28	56.53	6.81
3.57	281.01	299.44	200.82	15.40	0	329.28	56.87	6.80
3.58	282.47	300.16	198.56	15.69	0	329.28	56.75	6.81
3.59	280.28	298.72	205.33	16.27	0	329.28	56.87	6.81
3.60	278.82	298.72	203.08	16.27	0	329.28	56.53	6.81
3.61	278.82	298.72	205.33	15.69	0	329.28	56.87	6.80
3.62	278.82	296.56	203.08	15.69	0	329.28	56.75	6.81
3.63	279.55	298.72	200.82	15.98	0	329.28	56.87	6.80
3.64	275.90	296.56	203.08	15.69	0	329.28	56.87	6.81
3.65	278.09	297.28	203.08	16.27	0	329.28	56.87	6.79
3.66	278.82	297.28	203.08	15.69	0	329.55	56.75	6.81
3.67	276.63	296.56	200.82	16.27	0	329.28	56.87	6.80
3.68	278.09	296.56	200.82	16.57	0	329.28	56.75	6.81
3.69	276.63	295.12	205.33	15.69	0	329.28	56.53	6.80
3.70	277.36	296.56	200.82	15.69	0	329.28	56.64	6.80
3.71	276.63	295.12	196.31	15.98	0	329.28	56.87	6.81
3.72	276.63	295.84	198.56	15.69	0	329.28	56.87	6.80
3.73	276.63	294.40	196.31	15.40	0	329.28	56.87	6.81
3.74	276.63	292.24	198.56	15.69	0	329.28	56.87	6.80
3.75	275.17	292.96	194.05	15.40	0	329.28	56.87	6.81
3.76	275.90	293.68	196.31	15.69	0	329.28	56.87	6.81
3.77	274.44	293.68	198.56	15.40	0	329.28	56.87	6.81
3.78	275.90	292.96	198.56	16.27	0	329.28	56.98	6.81
3.79	275.17	292.96	196.31	15.69	0	329.28	56.98	6.81
3.80	274.44	292.96	198.56	15.69	0	329.28	56.98	6.81
3.81	274.44	292.24	194.05	15.98	0	329.37	56.87	6.79
3.82	273.71	287.92	198.56	15.40	0	329.28	56.75	6.80
3.83	275.17	292.96	194.05	15.69	0	329.28	56.98	6.81
3.84	272.98	291.52	196.31	15.69	0	329.28	57.09	6.80

APPENDIX A.8

DENSITY DATA

A.8.1: Density Measurement for Calibration Curve

FLOAT #	FLOAT DENSITY (g/cm ³)	POSITION (mm) at time, t	POSITION (mm) at t+24hours
1	1.10	42	42
2	1.15	160	160
3	1.20	257	257
4	1.25	356	355
5	1.30	447	446.5
6	1.35	534	534
7	1.40	619	618
8	1.45	708	708
9	1.50	803	803
10	1.55	904	904

A.8.2: Effect of Mold Temperature on Density Distribution

FRACTIONAL THICK. (mm)	LOW MOLD TEMP	HIGH MOLD TEMP
0.0	1.3828	1.3956
0.1	1.4017	1.3991
0.2	1.4017	1.3997
0.3	1.3970	1.3990
0.4	1.3954	1.3997
0.5	1.3959	1.3908
0.6	1.3948	1.3997
0.7	1.3960	1.3991
0.8	1.4028	1.3997
0.9	1.4028	1.4003
1.0	1.3997	1.3991
1.1	1.4028	1.3997
1.2	1.3994	1.4003
1.3	1.3994	1.4000
1.4	1.4017	1.3991
1.5	1.3995	1.3997
1.6	1.4006	1.4003

APPENDIX A.9

A.9.1: Effect of Position on Orientation Function Distribution

Thick (mm)	POSITION A			POSITION B			POSITION C		
	D	$\frac{D-1}{D+2}$	f	D	$\frac{D-1}{D+2}$	f	D	$\frac{D-1}{D+2}$	f
0.00	2.85	0.382	0.426	2.04	0.257	0.286	1.70	0.189	0.211
0.05	-	-	-	-	-	-	-	-	-
0.10	2.34	0.309	0.345	1.55	0.154	0.172	1.98	0.245	0.274
0.15	-	-	-	-	-	-	-	-	-
0.20	1.62	0.172	0.191	1.69	0.186	0.207	2.16	0.278	0.310
0.30	-	-	-	-	-	-	2.57	0.343	0.382
0.35	1.28	0.086	0.096	2.02	0.254	0.283	-	-	-
0.40	-	-	-	-	-	-	1.94	0.238	0.265
0.45	1.69	0.187	0.208	1.67	0.182	0.203	-	-	-
0.50	-	-	-	-	-	-	1.86	0.222	0.248
0.55	1.65	0.177	0.198	1.56	0.157	0.175	-	-	-
0.60	-	-	-	-	-	-	1.51	0.144	0.161
0.65	2.05	0.259	0.289	1.77	0.203	0.227	-	-	-
0.70	-	-	-	-	-	-	1.82	0.215	0.240
0.75	1.34	0.101	0.112	1.58	0.162	0.181	-	-	-
0.80	-	-	-	-	-	-	1.34	0.098	0.109
0.85	-	-	-	0.80	-0.071	-0.080	-	-	-
0.90	0.55	-0.177	-0.197	-	-	-	0.72	-0.103	-0.115
0.95	-	-	-	0.511	-0.195	-0.217	-	-	-
1.00	0.45	-0.225	-0.250	-	-	-	0.46	-0.218	-0.243
1.05	-	-	-	0.59	-0.157	-0.175	-	-	-
1.10	0.43	-0.233	-0.259	-	-	-	0.34	-0.283	-0.316
1.15	-	-	-	0.66	-0.127	-0.142	-	-	-
1.20	0.32	-0.296	-0.330	-	-	-	0.26	-0.326	-0.363
1.25	-	-	-	0.49	-0.206	-0.229	-	-	-
1.30	0.30	-0.307	-0.342	-	-	-	0.35	-0.275	-0.307
1.35	-	-	-	0.48	-0.212	-0.236	-	-	-
1.40	-	-	-	-	-	-	0.40	-0.251	-0.280
1.45	-	-	-	-	-	-	-	-	-
1.50	-	-	-	-	-	-	0.36	-0.271	-0.302
1.55	-	-	-	-	-	-	-	-	-
1.60	-	-	-	-	-	-	-	-	-

A.9.3: Effect of Mold Temperature on Orientation Function Distribution

<table border="1" style="width: 100%; text-align: center;"> <tr> <td style="width: 50%;">LOW MOLD TEMPERATURE</td> <td style="width: 50%;">HIGH MOLD TEMPERATURE</td> </tr> </table>							LOW MOLD TEMPERATURE	HIGH MOLD TEMPERATURE
LOW MOLD TEMPERATURE	HIGH MOLD TEMPERATURE							
THICK. (mm)	D	$\frac{D-1}{D+2}$	f	D	$\frac{D-1}{D+2}$	f		
0.00	4.42	0.532	0.594	2.24	0.293	0.327		
0.10	2.76	0.370	0.412	2.11	0.270	0.301		
0.20	2.36	0.312	0.348	1.90	0.230	0.256		
0.30	2.27	0.298	0.332	2.52	0.336	0.375		
0.40	2.27	0.297	0.332	2.07	0.263	0.293		
0.50	1.98	0.246	0.274	1.93	0.238	0.265		
0.60	2.23	0.291	0.324	1.80	0.211	0.236		
0.70	2.67	0.358	0.399	1.79	0.208	0.232		
0.80	3.03	0.403	0.450	1.74	0.198	0.221		
0.90	1.74	0.197	0.220	1.54	0.154	0.171		
1.00	1.01	0.004	0.004	1.42	0.122	0.136		
1.10	0.89	-0.040	-0.044	1.18	0.055	0.062		
1.20	1.25	0.076	0.085	1.14	-0.044	0.049		
1.30	0.64	-0.137	-0.153	0.92	-0.027	-0.030		
1.40	0.44	-0.229	-0.256	0.71	-0.108	-0.120		
1.50	0.45	-0.224	-0.249	0.38	-0.260	-0.290		
1.60				0.40	-0.252	-0.281		

A.9.4: Effect of Injection Pressure on Orientation Function Distribution

LOW INJECTION PRESSURE				HIGH INJECTION PRESSURE		
THICK. (mm)	D	$\frac{D-1}{D+2}$	f	D	$\frac{D-1}{D+2}$	f
0.00	3.86	0.488	0.544	2.87	0.384	0.428
0.10	2.61	0.350	0.390	2.27	0.297	0.331
0.20	2.18	0.282	0.314	1.81	0.212	0.237
0.30	1.59	0.164	0.183	1.89	0.228	0.254
0.40	1.40	0.118	0.132	1.99	0.248	0.277
0.50	1.28	0.085	0.095	2.30	0.303	0.337
0.60	1.48	0.139	0.155	1.70	0.189	0.211
0.70	1.20	0.061	0.068	1.52	0.147	0.164
0.80	0.91	-0.030	-0.034	1.24	0.075	0.083
0.90	1.34	0.102	0.114	1.05	0.018	0.020
1.00	0.81	-0.066	-0.074	0.69	-0.118	-0.129
1.10	0.29	-0.309	-0.344	0.64	-0.134	-0.150
1.20	0.82	-0.065	-0.072	0.44	-0.229	-0.256
1.30	0.72	-0.101	-0.113	0.38	-0.259	-0.289
1.40	0.67	-0.123	-0.137	0.34	-0.281	-0.314
1.50	0.47	-0.215	-0.240	0.34	-0.283	-0.316
1.60	0.63	-0.141	-0.157	0.36	-0.270	-0.301

A.9.5: Effect of Injection Speed on Orientation Function Distribution

LOW INJECTION SPEED				HIGH INJECTION SPEED		
THICK. (mm)	D	$\frac{D-1}{D+2}$	f	D	$\frac{D-1}{D+2}$	f
0.00	6.15	0.632	0.705	3.86	0.488	0.544
0.10	1.61	0.170	0.189	2.61	0.350	0.390
0.20	2.02	0.253	0.282	2.18	0.282	0.314
0.30	0.77	-0.084	-0.093	1.59	0.164	0.183
0.40	1.11	0.035	0.039	1.40	0.118	0.132
0.50	2.28	0.300	0.334	1.28	0.085	0.095
0.60	3.56	0.461	0.514	1.48	0.139	0.155
0.70	1.26	0.079	0.089	1.20	0.061	0.068
0.80	0.99	-0.004	-0.005	0.91	-0.030	-0.034
0.90	0.89	-0.038	-0.043	1.34	0.102	0.114
1.00	0.88	-0.043	-0.048	0.81	-0.066	-0.072
1.10	0.41	-0.247	-0.275	0.29	-0.309	-0.343
1.20	0.59	-0.159	-0.177	0.81	-0.065	-0.072
1.30	0.47	-0.212	-0.237	0.72	-0.101	-0.113
1.40	0.53	-0.184	-0.206	0.67	-0.123	-0.137
1.50	0.73	-0.097	-0.108	0.47	-0.215	-0.240
1.60	0.60	-0.152	-0.170	0.63	-0.141	-0.157

APPENDIX A.10

MICROHARDNESS DATA

A.10.1: Effect of Position on Microhardness Distribution

		POSITION A		POSITION B		POSITION C	
Thick (mm)	Indent (Filar units)	Indent (μm)	Indent (Filar units)	Indent (μm)	Indent (Filar units)	Indent (μm)	
0.00	322	147.6	309	141.6	301	138.0	
0.15	275	126.0	283	129.7	288	132.0	
0.30	284	130.2	285	130.6	275	126.0	
0.45	293	134.3	284	130.2	280	128.3	
0.60	269	123.3	281	128.8	275	126.0	
0.75	260.5	119.4	284	130.2	248	113.7	
0.90	241	110.5	254	116.4	232	106.3	
1.05	244	111.8	246	112.7	235	107.7	
1.20	234	107.2	250	114.6	243	111.4	
1.35	225	103.1	236.5	108.4	249	114.1	
1.50	227	104.0	232	106.3	242	110.9	
1.65	235	107.7	235.5	107.9	254	116.4	

1 Filar Unit = 0.4583 μm

A.10.2: Microhardness Distribution for Replicates

<table border="1" style="width: 100%; text-align: center;"> <tr> <td style="width: 50%;">SAMPLE #1</td> <td style="width: 50%;">SAMPLE #2</td> </tr> </table>					SAMPLE #1	SAMPLE #2
SAMPLE #1	SAMPLE #2					
Thickness (mm)	Indent. (Filar units)	Indent. (μm)	Indent. (Filar units)	Indent. (μm)		
0.00	346	158.6	333	152.6		
0.15	300	137.5	295	135.2		
0.30	289	132.5	283	129.7		
0.45	279	127.9	276	126.5		
0.60	275	126.0	269	123.3		
0.75	282	129.2	271	124.2		
0.90	274	125.6	275	126.0		
1.05	257.5	118.0	259	118.7		
1.20	245	112.3	240	110.0		
1.35	245	112.3	233	106.8		
1.50	242	110.9	234	107.2		
1.65	232	106.3	231	105.9		

A.10.3: Effect of Mold temperatures on Microhardness Distribution

LOW MOLD TEMPERATURE		HIGH MOLD TEMPERATURE		
Thick. (mm)	Indent. (Filar units)	Indentat. (μm)	Indent. (Filar units)	Indent. (μm)
0.00	298	136.6	278	127.4
0.15	273	125.1	270	123.7
0.30	269	123.3	275	126.0
0.45	273	125.1	266	121.9
0.60	268.5	123.1	261	119.6
0.75	296	135.7	273	125.1
0.90	303	138.9	242	110.9
1.05	273.5	125.4	240	110.0
1.20	235	107.7	230	105.4
1.35	226	103.6	232	106.3
1.50	231.5	106.1	248	113.7
1.65	240	110.0	250	111.6

A.10.4: Effect of Injection Pressure on Microhardness Distribution

		LOW INJECTION PRESSURE		HIGH INJECTION PRESSURE	
Thickness (mm)	Indentation (Filar units)	Indentation (μm)	Indentation (Filar units)	Indentation (μm)	
0.00	325	149.0	313	143.5	
0.15	296	135.7	283	129.7	
0.30	267	122.4	285	130.6	
0.45	264	121.0	284	130.2	
0.60	266	121.9	281	128.8	
0.75	239	109.5	284	130.2	
0.90	233.5	107.0	252	115.5	
1.05	227	104.0	246	112.7	
1.20	224	102.7	250	114.6	
1.35	230	105.4	236.5	108.4	
1.50	229	105.0	232	106.3	
1.65	228.5	104.7	235.5	107.9	

A.10.5: Effect of Injection Speed on Microhardness Distribution

LOW INJECTION SPEED	HIGH INJECTION SPEED
---------------------	----------------------

Thickness (mm)	Indentation (Filar units)	Indentation (μm)	Indentation (Filar units)	Indentation (μm)
0.00	346	158.6	313	143.5
0.15	300	137.5	283	129.7
0.30	289	132.5	285	130.6
0.45	266	121.9	284	130.2
0.60	275	126.0	281	128.8
0.75	297	136.1	284	130.2
0.90	274	125.6	252	115.5
1.05	257.5	118.0	246	112.7
1.20	245	112.3	250	111.6
1.35	245	112.3	236.5	108.4
1.50	242	110.9	232	106.3
1.65	232	106.3	235.5	107.9

APPENDIX A.11

FLEXURAL MODULUS DATA

A.11.1: Flexural Modulus Distribution Obtained for Longitudinal (1L) and Transverse (1T) Samples.

FRACTIONAL THICK. (mm)	SAMPLE (1L) (GPa)	SAMPLE (1T) (GPa)
0.00	7.917	1.971
0.14	6.425	2.136
0.27	5.661	2.625
0.39	5.493	2.961
0.48	5.584	2.627
0.58	6.081	3.113
0.66	5.078	3.903
0.78	4.864	3.955
0.90	3.466	4.199
0.99	3.219	4.124
1.08	2.954	4.351
1.20	2.912	4.569
1.33	2.771	4.937
1.40		
1.45		
1.50		
1.6		

A.11.2: Flexural Modulus Distribution Obtained for Longitudinal Samples (1L) and (2L).

FRACTIONAL THICK. (mm)	SAMPLE (1L) (GPa)	SAMPLE (2L) (GPa)
0.00	7.917	4.797
0.14	6.425	8.492
0.27	5.661	7.872
0.39	5.493	4.725
0.48	5.584	5.489
0.58	6.081	7.550
0.66	5.078	6.008
0.78	4.864	5.965
0.90	3.466	5.544
0.99	3.219	4.677
1.08	2.954	4.576
1.20	2.912	4.278
1.33	2.771	4.905
1.40		
1.45		
1.50		
1.6		

A.11.3: Effect of Mold Temperature on Flexural Modulus Distribution

	LOW MOLD TEMP.	HIGH MOLD TEMP.
FRACTIONAL THICK. (mm)	E_r (GPa)	E_r (GPa)
0.00	9.223	8.357
0.14	7.829	7.304
0.27	6.343	6.836
0.39	5.055	5.887
0.48	5.183	5.963
0.58	5.903	5.062
0.66	6.820	7.546
0.78	5.465	7.899
0.90	5.245	7.406
0.99	3.818	4.294
1.08	3.504	4.198
1.20	2.990	3.203
1.33	2.624	2.809
1.40		
1.45		
1.50		
1.6		

A.11.4: Effect of Injection Pressure on Flexural Modulus Distribution

	SLOW INJ. PRESS.	HIGH INJ. PRESS.
FRACTIONAL THICK. (mm)	E_t (GPa)	E_t (GPa)
0.00	8.017	6.697
0.14	7.349	5.467
0.27	5.408	6.122
0.39	5.859	6.978
0.48	5.228	6.618
0.58	5.422	5.534
0.66	3.896	5.379
0.78	2.862	5.341
0.90	2.971	5.911
0.99	3.038	4.072
1.08	2.454	2.420
1.20	2.372	2.277
1.33	2.388	
1.40		
1.45		
1.50		
1.6		

A.11.5: Effect of Injection Speed on Flexural Modulus Distribution

	SLOW INJ. SPEED	HIGH INJ. SPEED
FRACTIONAL THICK. (mm)	E_r (GPa)	E_r (GPa)
0.00	8.500	6.697
0.14	7.850	5.467
0.27	6.696	6.122
0.39	3.933	6.978
0.48	4.484	6.618
0.58	7.816	5.534
0.66	6.448	5.379
0.78	5.366	5.341
0.90	4.252	5.911
0.99	3.976	4.072
1.08	3.029	2.420
1.20	2.422	2.277
1.33	2.981	2.686
1.40		
1.45		
1.50		
1.6		

APPENDIX A.12

PREDICTIONS OF FLEXURAL MODULUS

A.12.1: Longitudinal Sample (1L)

		RILEY	COX
FRACTIONAL THICK. (mm)	EXPERIMENTAL E_t (GPa)	CALCULATED E_t (GPa)	CALCULATED E_t (GPa)
0.00	7.917	7.970	9.220
0.10		5.970	6.830
0.14	6.425		
0.20		5.593	6.378
0.27	5.661		
0.30		5.709	6.517
0.39	5.493		
0.40		5.846	6.680
0.48	5.584		
0.50		6.107	6.993
0.58	6.081		
0.60		5.409	6.158
0.66	5.078		
0.70		5.111	5.802
0.78	4.864		
0.80		4.635	5.233
0.90	3.466	4.270	4.796
0.99	3.219		
1.00		3.476	3.847
1.08	2.954		
1.10		3.370	3.721
1.20	2.912	2.855	3.105
1.30		2.704	2.924
1.33	2.771		
1.40		2.593	2.792
1.50		2.578	2.773
1.60		2.649	2.858

A.12.2: Transverse Sample (1T)

		RILEY	COX
FRACTIONAL THICK. (mm)	EXPERIMENTAL E_t (GPa)	CALCULATED E_t (GPa)	CALCULATED E_t (GPa)
0.00	1.971	2.327	2.472
0.10		2.970	2.854
0.14	2.136		
0.20		3.145	3.013
0.27	2.625		
0.30		3.088	2.962
0.39	2.961		
0.40		3.013	2.893
0.48	2.627		
0.50		2.902	2.791
0.58	3.113		
0.60		3.225	3.087
0.66	3.903		
0.70		3.397	3.245
0.78	3.955		
0.80		3.741	3.560
0.90	4.199	4.052	3.844
0.99	4.124		
1.00		5.011	4.723
1.08	4.351		
1.10		5.182	4.880
1.20	4.569	6.242	5.851
1.30		6.664	6.237
1.33	4.937		
1.40		7.026	6.569
1.50		7.026	6.569
1.60		6.839	6.397

APPENDIX A.13

DERIVATIONS

A.13.1: Derivation of function

$$\langle \cos^4 \theta \rangle = \frac{\int_{\pi/2}^{\pi/2} K \cos^n \theta \cos^4 \theta \sin \theta \, d\theta}{\int_{\pi/2}^{\pi/2} K \cos^n \theta \sin \theta \, d\theta}$$

$$\langle \cos^2 \theta \rangle = \frac{\int_{\pi/2}^{\pi/2} K \cos^n \theta \cos^2 \theta \sin \theta \, d\theta}{\int_{\pi/2}^{\pi/2} K \cos^n \theta \sin \theta \, d\theta}$$

$$\frac{\langle \cos^4 \theta \rangle}{\langle \cos^2 \theta \rangle} = \frac{\int_{\pi/2}^{\pi/2} K \cos^{n+4} \theta \sin \theta \, d\theta}{\int_{\pi/2}^{\pi/2} K \cos^{n+2} \theta \sin \theta \, d\theta}$$

If $\cos \theta = X$

$-\sin \theta \, d\theta = dX$

$$\frac{\langle \cos^4 \theta \rangle}{\langle \cos^2 \theta \rangle} = \frac{- \int_{X_1}^{X_0} X^{n+4} \, dX}{- \int_{X_1}^{X_0} X^{n+2} \, dX} = \frac{\left[\frac{X^{n+5}}{n+5} \right]_{X_1}^{X_0}}{\left[\frac{X^{n+3}}{n+3} \right]_{X_1}^{X_0}}$$

$$= \frac{\left[\frac{\cos^{n+5} \theta}{n+5} \right]_{\pi/2}^{\pi/2}}{\left[\frac{\cos^{n+3} \theta}{n+3} \right]_{\pi/2}^{\pi/2}} = \frac{n+3}{n+5}$$

$$\frac{\langle \cos^4 \theta \rangle}{\langle \cos^2 \theta \rangle} = \frac{n+3}{n+5}$$

$$\langle \cos^4 \theta \rangle = \frac{\int \cos^{n+2} \theta \sin \theta \, d\theta}{\int \cos^n \theta \sin \theta \, d\theta} = \frac{\int X^{n+2} \, dx}{\int X^n \, dx}$$

$$= \frac{\left[\frac{X^{n+3}}{n+3} \right]_{X_0}^{X_1}}{\left[\frac{X^{n+1}}{n+1} \right]_{X_0}^{X_1}} = \frac{\left[\frac{\cos^{n+3} \theta}{n+3} \right]_{\theta_0}^{\theta_1}}{\left[\frac{\cos^{n+1} \theta}{n+1} \right]_{\theta_0}^{\theta_1}}$$

$$= \frac{n+1}{n+3}$$

$$\langle \cos^2 \theta \rangle = \frac{n+1}{n+3} \quad (2) \quad \longrightarrow \quad n \langle \cos^2 \theta \rangle + 3 \langle \cos^2 \theta \rangle = n+1$$

$$n[\langle \cos^2 \theta \rangle - 1] = 1 - 3 \langle \cos^2 \theta \rangle$$

$$n = \frac{1 - 3 \langle \cos^2 \theta \rangle}{\langle \cos^2 \theta \rangle - 1} \quad (3)$$

Substituting (3) in (1)

$$\frac{\langle \cos^4 \theta \rangle}{\langle \cos^2 \theta \rangle} = \frac{\frac{1 - 3\langle \cos^2 \theta \rangle}{\langle \cos^2 \theta \rangle - 1} + 3}{\frac{1 - 3\langle \cos^2 \theta \rangle}{\langle \cos^2 \theta \rangle - 1} + 5} = \frac{1 - 3\langle \cos^2 \theta \rangle + 3\langle \cos^2 \theta \rangle - 3}{1 - 5\langle \cos^2 \theta \rangle + 5\langle \cos^2 \theta \rangle - 5}$$

$$\frac{\langle \cos^4 \theta \rangle}{\langle \cos^2 \theta \rangle} = - \frac{2}{2 \langle \cos^2 \theta \rangle - 4}$$

$$\langle \cos^4 \theta \rangle = \frac{\langle \cos^2 \theta \rangle}{2 \langle \cos^2 \theta \rangle - 4} \quad (4)$$

Then

$$f_p = 1/2 [3\langle \cos^2 \theta \rangle_p - 1];$$

$$\langle \cos^2 \theta \rangle = \frac{2 f_p + 1}{3}$$

$$g_p = 1/4 [5\langle \cos^4 \theta \rangle_p - 1];$$

$$\langle \cos^4 \theta \rangle = \frac{4 g_p + 1}{5}$$

Substituting in (4)

$$\frac{4 g_p + 1}{5} = \frac{\frac{2 f_p + 1}{3}}{2 - \frac{2 f_p + 1}{3}} = \frac{2 f_p + 1}{5 - 2 f_p}$$

$$g_p = \frac{5(2 f_p + 1)}{4(5 - 2 f_p)} - \frac{1}{4}$$

$$g_p = \frac{10 f_p + 5 - 5 + 2f_p}{4(5 - 2f_p)} = \frac{12 f_p}{4(5 - 2f_p)}$$

$$g_p = \frac{3f_p}{5 - 2f_p}$$

A.13.2: Calculation of Stiffness and Strength

Consider a symmetric three-ply beam shown schematically in Figure A1. The beam has width b , thickness h and consists of a central core with thickness h_c , and skins of thickness h_s , so that $h = 2h_s + h_c$. The core and skin Young's moduli along the beam axis are E_c and E_s , respectively and it is assumed that transverse strains arising from differences in Poisson's ratio are negligible. The core and skin densities are denoted by ρ_c and ρ_s , respectively.

If ρ is the total density, the total mass of the beam is:

$$bhl\rho = bl(h_c\rho_c + 2h_s\rho_s)$$

$$h\rho = h_c\rho_c + 2h_s\rho_s, \quad \text{if } \varphi = h_c/h$$

$$\rho = \rho_c\varphi + \rho_s(1 - \varphi)$$

The tensile modulus of the sandwich material E_t is:

$$E_t = E_c\varphi + E_s(1 - \varphi)$$

In order to calculate the flexural rigidity D , we assume that classical bending theory can be applied to the sandwich beam. Thus cross-sections which are plane and perpendicular to the neutral axis of the unloaded beam remain so when bending takes place. Also assume that transverse stresses parallel to the faces may be neglected. It can then be shown that D is given by:

$$D = E_c I_c + 2E_s I_s$$

where I_c and I_s are the moments of inertia of the core and skin cross-sections about the centroidal axis of the beam. With the notation of Fig. 4.12,

$$I_c = bh_c^3/12$$

$$I_s = bh_s^3/12 + (h_c + h_s)^2 bh_s/4$$

which gives the result:

$$D = bE_s [h_s^3/6 + h_s(h_c + h_s)^2/2] + bE_c h_c^3/12$$

Let E_f be the effective flexural modulus of the sandwich beam, then

$$D = bh^3 E_f / 12$$

$$bh^3 E_f / 12 = bE_s [h_s^3/6 + h_s(h_c + h_s)^2/2] + bE_c h_c^3/12$$

$$E_f = E_s/h^3 [2h_s^3 + 6h_s(h_c + h_s)^2] + E_c h_c^3/h^3, \quad \text{if } h_s = h - h_c$$

$$E_f = E_c \phi^3 + E_s(1 - \phi^3)$$

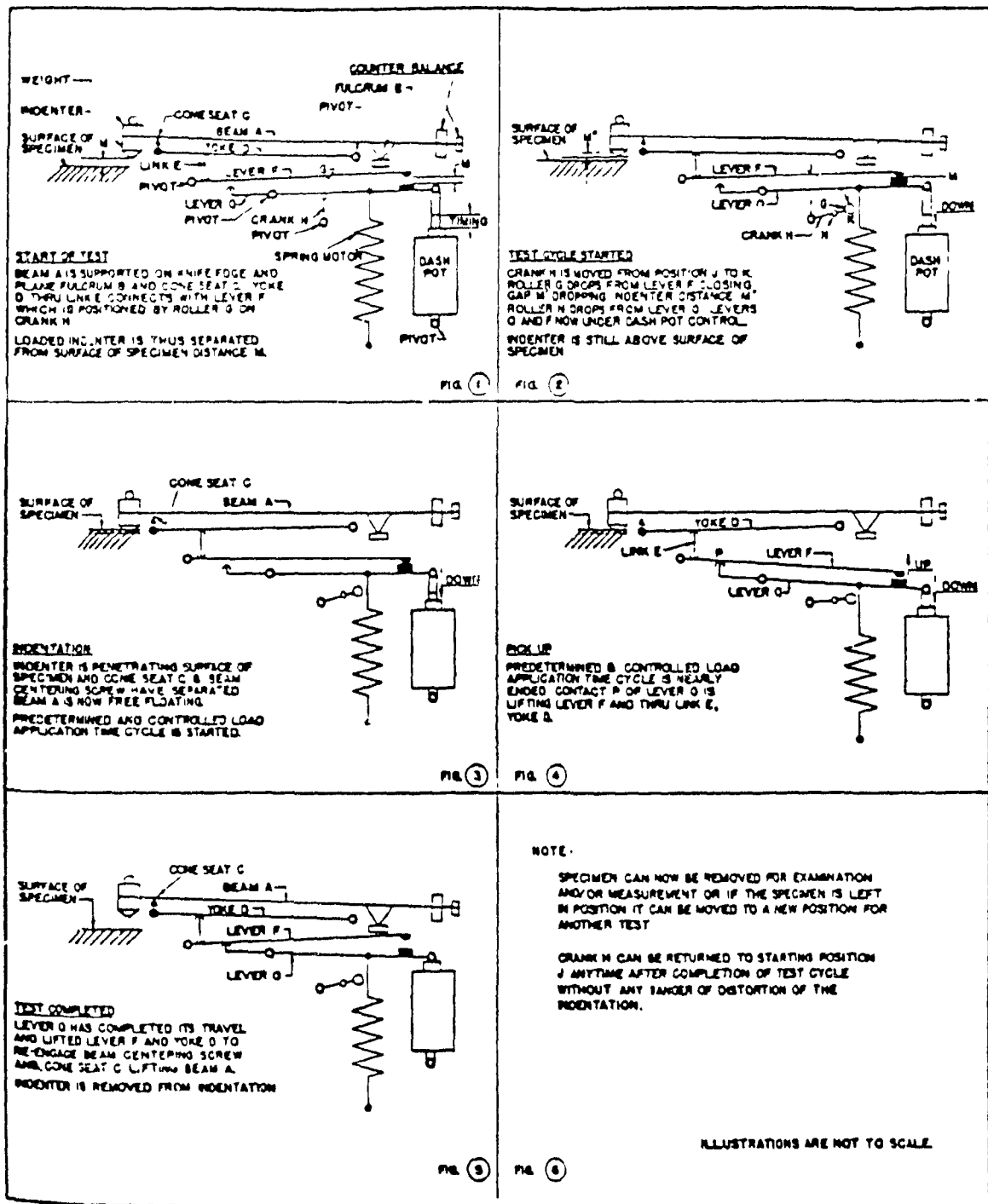


FIGURE A.13.3: Microhardness test: Steps for microhardness measurements.

THE KNOOP INDENTER

The Knoop Indenter is an accurately ground diamond forming a rhombic based pyramid, properly mounted for attaching to the beam. An indentation seen normal to specimen surface is rhombic in outline with diagonals having an approximate ratio of 7 to 1.

Depth of indentation is about 1/30 the length of long diagonal.

Perfect angles for Knoop Indenter are:

Included Longitudinal angle $172^{\circ} 30' 00''$

Included Transverse angle $130^{\circ} 00' 00''$

A CERTIFICATE OF TEST FOR THE KNOOP INDENTER is furnished by the manufacturer which records actual angles of indenter supplied and certifies that indenter complies with requirements of the National Bureau of Standards.

The INDENTER CONSTANT, which is used to calculate Knoop Hardness Number by formula, is the ratio of projected area of indentation to square of length of long diagonal. Its value is given by:

$$C = \frac{1}{2} \left(\frac{\cotangent A}{2} \times \frac{\tangent B}{2} \right)$$

where

A = Included Longitudinal edge angle

B = Included Transverse edge angle

C = 0.07028 for perfect indenter with angles of $172^{\circ} 30' 00''$ and $130^{\circ} 00' 00''$.

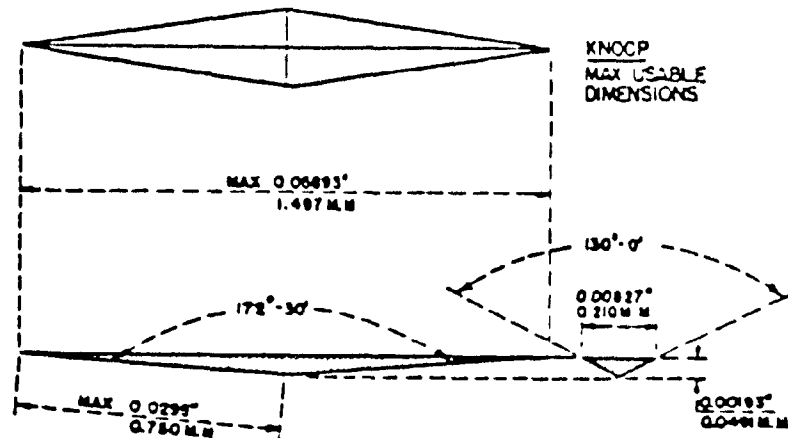


FIGURE A.13.4: The Knoop Indenter

APPENDIX A.14

ERROR ANALYSIS

A.14.1: Thermal Conductivity and Diffusivity

The thermal conductivity relative error in measurable quantities like current (1.5%), sample area (0.5%), sample thickness (0.5%), heater resistance (1.3%) and differential temperature (2.0%). The thermal conductivity error is 5.8%.

The thermal diffusivity error analysis is estimated from the sample thickness (0.5%) and the thermal penetration time (10%).

A.14.2: Density

The experimental errors were based on the float density (0.1%), float and sample position (0.1%) and temperature (0.1%).

$$\text{Density of LCP sample: } \rho_s = \rho_b + \frac{(\rho_b - \rho_a)(h_a - h_s)}{(h_a - h_b)}$$

$$\begin{aligned} \epsilon_{\rho S} = & \left\{ 1 + \left[\frac{(h_a - h_s)}{(h_a - h_b)} (-\rho_a) \epsilon_{\rho} \right]^2 + \left[\frac{(h_a - h_s)}{(h_a - h_b)} \rho_b \epsilon_{\rho} \right]^2 \right. \\ & + \left[\frac{(\rho_b - \rho_a)}{(h_a - h_b)} \epsilon (h_a - h_s) \right]^2 \\ & \left. + \left[\frac{(\rho_b - \rho_a)(h_a - h_s)}{(h_a - h_b)} \epsilon (h_a - h_s) \right]^2 \right\}^{1/2} \end{aligned}$$

$$\text{If } h_a = 0.533,$$

$$h_b = 0.62,$$

$$h_s = 0.613,$$

$$\text{and } \rho_a = 1.35$$

$$\rho_b = 1.40$$

Then the density error = 0.3%

A.14.3: Infrared Spectroscopy

Experimental errors for the dichroic ratio were estimated to be:

$$\text{Parallel absorption, } A_{\parallel} \quad 0.5$$

$$\text{Perpendicular absorption, } A_{\perp} \quad 0.5$$

$$\epsilon_D = \left\{ \left[\frac{1}{A_{\perp}} \cdot \epsilon_P \right]^2 + \left[-\frac{A_{\parallel}}{A_{\perp}} \cdot \epsilon_T \right]^2 \right\}^{1/2}$$

$$\epsilon_D = \left\{ \left[\frac{1}{(30.5)} \cdot (0.5) \right]^2 + \left[-\frac{(53.2)}{(30.5)^2} \cdot (0.5) \right]^2 \right\}^{1/2}$$

$$\epsilon_D = 0.023$$

The percent error = 1.3%

Similarly, the error on the orientation function from the dichroic ratio is estimated to be:

$$\text{Orientation function, } f = \frac{D - 1}{D + 2} \quad \text{or} \quad f = \frac{a}{b}$$

$$\epsilon_f = \left\{ \left[\frac{1}{b} \cdot \epsilon_a \right]^2 + \left[-\frac{a}{b^2} \cdot \epsilon_b \right]^2 \right\}^{1/2}$$

$$\epsilon_f = \left\{ \left[\frac{1}{(3.744)} \cdot (0.023) \right]^2 + \left[-\frac{(0.744)}{(3.744)^2} \cdot (0.023) \right]^2 \right\}^{1/2}$$

$$\epsilon_f = 0.00602$$

$$\text{The percent error} = \frac{0.00602}{0.19877} \times 100 = 3.03\%$$

A.14.4: Microhardness

The accuracy of the Tukon Microhardness method is a function of the accuracies of the test force, the indenter and measuring device. Under optimum conditions of these factors the accuracy can be expected to be equivalent of 4% of of the Tukon Hardness Number of the standardized reference hardness test blocks.

Fractional Thickness (mm)	HK Mean (mm)	95% confidence limit
0.00	158.6	± 7.2
0.15	137.5	± 4.5
0.30	132.5	± 6.3
0.45	127.9	± 5.4
0.60	126.0	± 8.1
0.75	129.2	± 3.6
0.90	125.6	± 2.7
1.05	118.0	± 4.9
1.20	112.3	± 3.6
1.35	112.3	± 1.8
1.50	110.9	± 4.5
1.65	106.3	± 6.3

A.14.5: Flexural Modulus

Scatter about the mean value was found to be less than 8%.

Fractional Thickness (mm)	E_r Mean (MPa)	95% Confid limits
1.6	7917	± 267
1.448	6425	± 304
1.335	5661	± 294
1.209	5493	± 76
1.08	5584	± 159
0.996	6081	± 302
0.912	5078	± 44
0.782	4864	± 211
0.677	3466	± 68
0.585	3219	± 108
0.484	2954	± 121
0.395	2912	± 91
0.267	2771	± 63